U.PORTO

FEUP FACULDADE DE ENGENHARIA
UNIVERSIDADE DO PORTO

Hemodynamics in the Left Coronary Artery – numerical and *in vitro* approaches

A thesis submitted in part fulfilment of the requirement for
the degree of Doctor in Chemical and Biological Engineering of the Faculty of
Engineering of the University of Porto
by

Erica Doutel Costa

João Bernardo Lares Moreira de Campos – Supervisor

João Mário Rodrigues Miranda – Co-supervisor

CEFT
Centro de Estudos de Fenómenos de Transporte
Transport Phenomena Research Center

Department of Chemical Engineering,
Faculty of Engineering, University of Porto, Portugal

May, 2016

This thesis was financially suported by Fundação para a Ciência e Tecnologia (Portugal) and FEDER under projects PTDC/EME-MFE/102974/2008, through the Operational Programe for Competitiveness Factors – COMPETE, ON.2 – O Novo Norte – Northe Portugal Regional Operational Program under projects: PEst-OE/EME/UI0532, NORTE-07-0124-FEDER-000025-RL2_5 Environment&Health and by CEFT.

UNIÃO EUROPEIA
Fundo Europeu
de Desenvolvimento Regional

Governo da República
Portuguesa

FCT
Fundação para a Ciência e a Tecnologia
MINISTÉRIO DA CIÊNCIA, TECNOLOGIA E ENSINO SUPERIOR

POPH
QUALIFICAR É CRESCER.

CEFT
Centro de Estudos de Fenómenos de Transporte
Transport Phenomena Research Center

ON.2
O NOVO NORTE
PROGRAMA OPERACIONAL
REGIONAL DO NORTE

Transport Phenomena Research Center
University of Porto – Faculty of Engineering
Rua Dr.Roberto Frias s/n, 4200-465 Porto

Agradecimentos / Acknowledgements

No desenvolvimento desta tese de doutoramento foram várias as pessoas que contribuíram de uma forma ou de outra para o seu sucesso.

Em primeiro lugar, quero aqui registar a minha satisfação por ter feito parte deste projeto. Sobretudo, aqui registo um especial e sincero agradecimento ao Professor João Moreira de Campos, por todo o valor que reconheceu em mim, pela sua orientação, motivação e competência e pelos seus conselhos e amizade. Muito mas muito obrigada Professor! Agradeço também ao meu coorientador, Doutor João Miranda pela sua preciosa ajuda, disponibilidade e paciência, assim como pelas famosas positivas discussões cujos conhecimentos transmitidos contribuíram para o meu enriquecimento científico.

Gostaria de agradecer igualmente à equipa médica do Centro Hospitalar de Vila de Nova de Gaia e Espinho, principalmente, ao Doutor Nuno Bettencourt e ao Daniel Leite, pela sua colaboração na cedência de imagens e informações médicas que valorizaram este trabalho.

Grata também à SOLIDtech, Ld, em especial ao Engº Lino, ao Joel e à Ana, obrigada pela dedicação e serviços de prototipagem prestados e pelo fabrico dos moldes de silicone, pois sem eles o trabalho teria outro rumo.

O meu muito obrigada ao Eng.º Nuno Viriato pela paciência e incansável ajuda ao longo destes anos nos problemas “demasiado simples” com o SolidWorks®.

Um singular agradecimento ao meu colega de trabalho, amigo e parceiro, João Carneiro, por toda a diversão e angústia partilhadas juntos, pelas hilariantes risadas e pelo constante apoio. Foi um prazer ter-te comigo nestes anos e adorei trabalhar contigo. Obrigada, pelo companheirismo, honestidade, paciência e amizade. És uma pessoa com uma enorme capacidade de trabalho, cuja curiosidade é o teu ponto forte. Reconheço aqui as tuas fortes competências e és o Biólogo mais Engenheiro que conheço! Desejo-te o maior sucesso para a tua tese e estarei sempre ao teu lado.

Aos meus colegas de trabalho do CEFT, Patrícia, Tânia, Vera, Renato, José Daniel, Soraia, Francisco, António, Samir, Ponmozhi, Filipe Direito, Filipe Celestino, Andreia, Luís, Joana e Ana, obrigada pelo ótimo ambiente de trabalho que me proporcionaram e pelas interessantes e divertidas conversas nas horas de descontração.

Queria agradecer aos meus “alfacinhas”, João Robalo, Joana do Vale e Filipa Marta, que apesar de estarem longe, estão sempre perto. Obrigada pelas inesquecíveis e compartilhadas férias que me ajudaram sempre a descontrair.

Às minhas grandes amigas do coração, Teresa Baltazar e Maria João, muito agradecida pelo seu constante apoio. Apesar do boicote ao nosso cafezinho semanal devido às nossas vidas, a amizade está sempre presente. Agradecida também aos amigos da vida e para a vida, Sara Paula, João Mendes, João Silva, Mário Pimentel, Catarina Nogueira, Ana Sofia, Sofia Silva, Vânia Paulo, Ali Emami, Viviana Pinto, Diana Olariu, Diogo Alves, Bruno Santos, Paula Dias, Marta Pimenta, Ana Duarte, António Leal, Isabel Gomes, André Maia e Ricardo Teixeira, pelos bons momentos e amizade.

Gostaria também de aqui registar a minha gratidão à minha família. Em particular à minha avó Tété e ao meu avô Doutel pela dedicação e constante amparo no meu percurso de vida. Aos meus avós Maria e Francisco Costa, que apesar de já não estarem entre nós me continuam a iluminar. Igualmente agradecida, aos meus tios Alexandra, Pedro, Sónia e Fernando, à minha afilhada Inês e aos primos Diogo Costa, Diogo Ribeiro e Lara pelos ternos momentos passados em família e pela persistente motivação. À minha segunda família, em especial aos meus sogros Lurdes e Fernando, e aos meus cunhados, Pedro e Rita, estarei sempre grata por todo o carinho e ajuda ao longo destes anos.

Aqui assinalo o meu peculiar agradecimento aos meus estimados pais, Luís Costa e Helena Doutel, pelo seu incondicional amor e apoio. Obrigada pela forma como me educaram, e por todos os valores que me incutiram. Sem isso não seria a pessoa que sou hoje. Ao meu querido irmão Gonçalo, deixo um carinho especial por me acompanhar sempre ao longo da vida e por tanto me valorizar.

Por fim, ao amor da minha vida, José Miguel, obrigada por seres o meu pilar, o meu incentivo e o meu porto de abrigo. Sem ti ao meu lado a vida não tinha o mesmo sabor.

A todos, o meu sincero e humilde agradecimento!

To my grandfather,

Almor Doutel

Preface

This dissertation is submitted for the degree of Doctor of Philosophy at University of Porto – Faculty of Engineering (FEUP). The present work was developed in Transport Phenomena Research Center, (CEFT), at the Chemical Department of FEUP. All CT scan images used in this work were provided through a collaboration with cardiovascular diagnosis and intervention unit from the Hospital Center of Vila de Nova de Gaia e Espinho. The work was supervised by Professor João Moreira de Campos and co-supervised by Dr. João Miranda from CEFT–FEUP.

From this PhD work resulted in a composition of five scientific articles, where two are already published (2nd and 4th chapters) and three are under review (3rd, 5th and 6th chapters).

Contents

Hemodynamics study in the Left Coronary Artery – Numerical and *in vitro* approaches

Abstract

Cardiovascular diseases are the leading cause of death in developed countries. Among them, atherosclerosis is characterized by plaque deposition at the arterial wall. These create an obstruction (stenosis) to blood flow. Atherosclerosis lesions usually occur at specific regions with complex vascular geometries, *i.e.* bifurcations and curvatures. This work studies the hemodynamics in the left coronary artery (LCA), in order to get a deeper understanding of which hemodynamic parameters most affect the development of this disease.

The hemodynamic studies were conducted using ideal models with realistic anatomical characteristics (designed using SolidWorks® software) and a patient-specific LCA, extracted from a computerized axial tomography. A numerical code was implemented using computational fluid dynamics (CFD). An experimental facility was constructed allowing the use of optical techniques, such as micro-particle image velocimetry (μPIV) and streak photography, to experimentally reproduce blood flow in the arterial models. The artificial arteries were fabricated using a newly developed fabrication method that enables the construction of flow phantoms with great accuracy and allows the use of optical techniques to characterize the flow.

The numerical and experimental velocity fields allow the observation of secondary flows, such as helical flows and vortexes, characterized by low velocities and low wall shear stress (WSS) zones. The uneven distribution of flow through the branches of LCA, contributes to the appearance of these secondary flows. Deviations from Murray's law[1] for flow partition were also analyzed, particularly how they influence the flow behaviour.

The WSS distribution and flow patterns were evaluated in healthy and stenotic models. For that, it was developed a numerical method for creating three-dimensional irregular stenosis. This method is based on the growth of stenosis through a diffusion model, based on previously identified areas as being prone to their appearance, *i.e.*, low WSS areas. The results showed that unique geometrical characteristics of the artery originate stenosis with specific shapes that rule the LCA hemodynamics. The influence of artery geometrical effects revealed that the non-planarity has a positive effect in helicity reducing the low WSS regions and therefore the atherosclerosis development. Numerical results of pulsatile blood flow assuming a non-Newtonian behaviour, reinforce the non-planarity effect in local hemodynamics.

Resumo

As doenças cardiovasculares são a principal causa de morte nos países desenvolvidos. Dentro dessas doenças, a aterosclerose é caracterizada pela deposição de substâncias gordas na parede arterial, a qual cria uma obstrução (estenose) ao escoamento de sangue. Geralmente, as lesões de aterosclerose ocorrem em regiões específicas com uma geometria vascular complexa, tais como bifurcações e curvaturas. Este trabalho estuda a hemodinâmica na artéria coronária esquerda (LCA), com o objetivo de melhor compreender quais os parâmetros hemodinâmicos que afetam o desenvolvimento desta doença.

Os estudos hemodinâmicos começaram por ser conduzidos em modelos simplificados de artérias com características anatómicas realistas (desenhados no SolidWorks®), seguindo-se o estudo num modelo de uma LCA de um paciente saudável, reconstruído a partir de uma tomografia axial computorizada. Foi implementado um código numérico para a simulação do escoamento recorrendo à dinâmica computacional de fluidos (CFD). Foi também construída uma instalação experimental que permitiu usar técnicas óticas, como a velocimetría por imagem de micropartículas (µPIV) e a visualização fotográfica, para reproduzir, experimentalmente, o escoamento sanguíneo nos modelos arteriais. Estes modelos foram construídos aplicando um novo método de fabrico desenvolvido para o efeito, o qual possibilita a sua construção com grande precisão e permite a utilização de técnicas óticas de caracterização do escoamento.

Os estudos numéricos e experimentais permitiram analisar o campo de velocidades em todo o domínio da LCA apresentando, na maioria dos casos, resultados congruentes. A análise do escoamento em diversas geometrias da LCA possibilitou a observação de zonas com escoamentos secundários como vórtices e escoamentos helicoidais, caracterizados por baixa velocidade e baixa tensão de corte na parede. A divisão não uniforme do fluxo através dos ramos arteriais potencia o aparecimento destes escoamentos secundários. Foram ainda analisados os desvios à lei de partição de Murray[1] e, em particular, de que forma estes desvios influenciam o escoamento na artéria.

Foram analisadas a distribuição da tensão de corte nas paredes e os padrões de escoamento em artérias saudáveis e com estenose. Para isso, foi desenvolvido um método numérico de criação de estenoses tridimensionais com forma irregular. Este método baseia-se no crescimento da estenose através de um processo difusivo com base em zonas previamente identificadas propícias ao aparecimento da estenose, ou seja, zonas de baixa tensão de corte na parede. Os resultados mostram que cada artéria tem as suas próprias características

geométricas, originando por isso estenoses diferentes de artéria para artéria com a sua própria hemodinâmica local. A influência das características geométricas das artérias revelou que o facto de estas não serem coplanares tem um efeito positivo no aumento de zonas com escoamento helicoidal, reduzindo o aparecimento de regiões com baixas tensões de corte na parede e diminuindo, portanto, o desenvolvimento da aterosclerose. Os resultados numéricos do escoamento sanguíneo oscilatório, assumindo um comportamento não-Newtoniano, reforçaram os efeitos da não - coplanaridade na hemodinâmica da artéria coronária esquerda.

---

[1] Murray, C.D., *The physiologtcal principle of minimom work I The vascular system and the cost of blood volume.* Proceedings of the National Academy of Sciences of the United States of America, 1926. **12**: p. 207-214.

Abbreviations

Abbreviation	Definition
2D	Two-dimensional
3D	Three-dimensional
CAD	Computer-aided design
CFD	Computational fluid dynamics
CHD	Coronary heart disease
CVD	Cardiovascular diseases
CT	Computer tomography
DICOM	Digital imaging and communications in Medicine
DMSO	Dimethyl sulfoxide
ECS	Endothelial cell surface
EDS	Energy Dispersive X-Ray Spectroscopy
ESS	Endothelial shear stress
LAD	Left anterior descending artery
LCA	Left coronary artery
LCx	Left circumflex artery
LDL	Low-density lipoprotein
LM	Left main stem
MRI	Magnetic resonance image
NA	Numerical aperture
µPIV	Micro-particle image velocimetry
PDMS	Poly(dimethylsiloxane)
PIV	Particle image velocimetry

PTV	Particle tracking velocimetry
RBCs	Red Blood Cells
RCA	Right Coronary Artery
RI	Ramus intermediate
SEM	Scanning Electron Microscopy
STL	Stereolithographic format
WSS	Wall shear stress

Chapter 1

> *"A curiosidade leva, por um lado,*
> *a escutar às portas, por outro, a*
> *descobrir a América."*
>
> **— Eça de Queiroz**

Introduction

1

Introduction

In the past two decades it has been observed a clear reduction in the mortality rate due to cardiovascular diseases (CVD) in the Portuguese population. Despite this trend, CVD are still the leading cause of death in Portugal. Figure 1.1 shows the percentage of deaths for each of the leading causes of mortality in Portugal from 1988 to 2012.

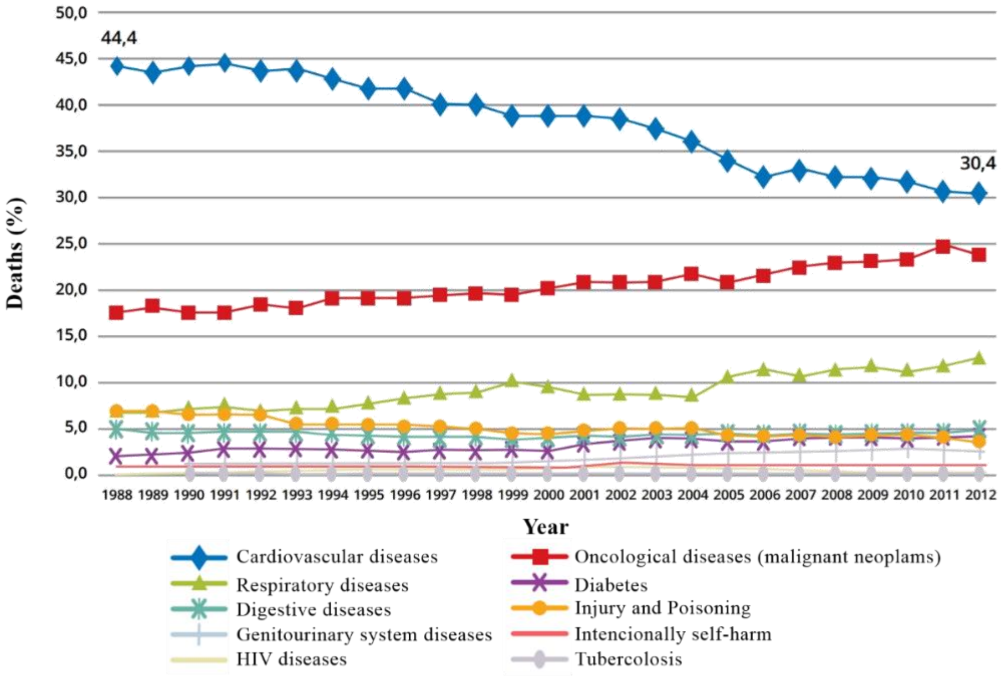

Figure 1.1. Percentage of deaths for each of the leading causes of mortality in Portugal (1988-2012)[1].

There are several pathologies contributing for the high mortality rate by CVD, such as rheumatic heart disease, hypertensive heart disease, cerebrovascular disease, coronary heart disease and others. In Europe, cardiovascular diseases cause almost two times as many deaths as cancer across the continent[2]. Townsend *et al.* [2] collected the most recent data covering the European region, showing that cardiovascular diseases are the largest cause of death (40% in men and 51% in women - Figure 1.2). Among cardiovascular diseases, the coronary heart disease accounts for 47% of deaths in men (Figure 1.2a) and 41% in women (Figure 1.2b). These fatalities led Europe to focus resources in the better understanding of CVD and aiming to its prevention.

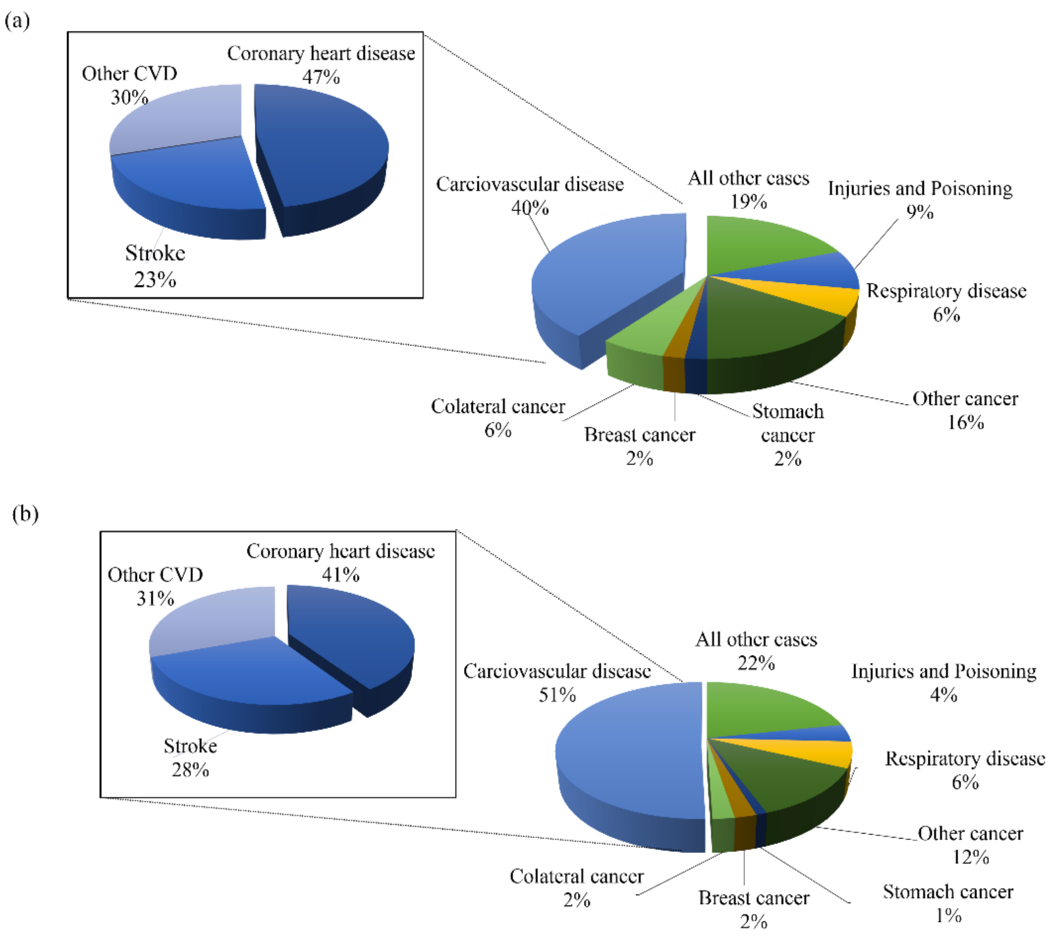

Figure 1.2. Major causes of death in Europe among men (a) and women (b), according to the World Health Organization (WHO) mortality database[2].

The coronary arteries, located on the surface of the heart itself, represent the only source of blood supply to the heart muscle (myocardium). The coronary heart disease is characterized by the narrowing of the coronary arteries, through the buildup of plaques, which decreases the blood supply to the heart. The plaque buildup can also originate blood clots formed in the arteries which may partially or completely block blood flow. When blood flow to the heart muscle is reduced or blocked a thrombosis or even a heart attack can occur.

Degenerative changes in coronary circulation can also lead to a progressive interruption on the supply of oxygen and nutrients to the cardiac muscle reducing the cardiac performance. In this thesis particular focus is given to the coronary artery disease.

1.1 Coronary artery disease and atherosclerosis

The typical coronary anatomy (Figure 1.3a) has been thoroughly studied and is described extensively in the literature[3-5]. Usually the two main coronary arteries correspond to the first two branches of the aorta: the right coronary artery (RCA) and the left coronary artery (LCA) and their ramifications extend to the heart apex (Figure 1.3b). The LCA is composed by the left main artery (LM), which is divided into two main branches: the left anterior descending artery (LAD), responsible for irrigating the left anterior region of the heart, and the left circumflex artery (LCx), which irrigates the posterior region.

Atherosclerosis is generally regarded as the primary cause of coronary artery disease, with results in abnormal changes in the coronary artery diameter[6]. Atherosclerotic lesions occur at specific regions of the arterial tree, particularly at regions with complex vascular geometries such as those seen in coronary arteries: bifurcations and curvatures[7-10]. In fact, the coronary arteries are the most sensitive sites for clinically significant atherosclerosis with progression to thrombosis events and subsequent myocardial infarction[11].

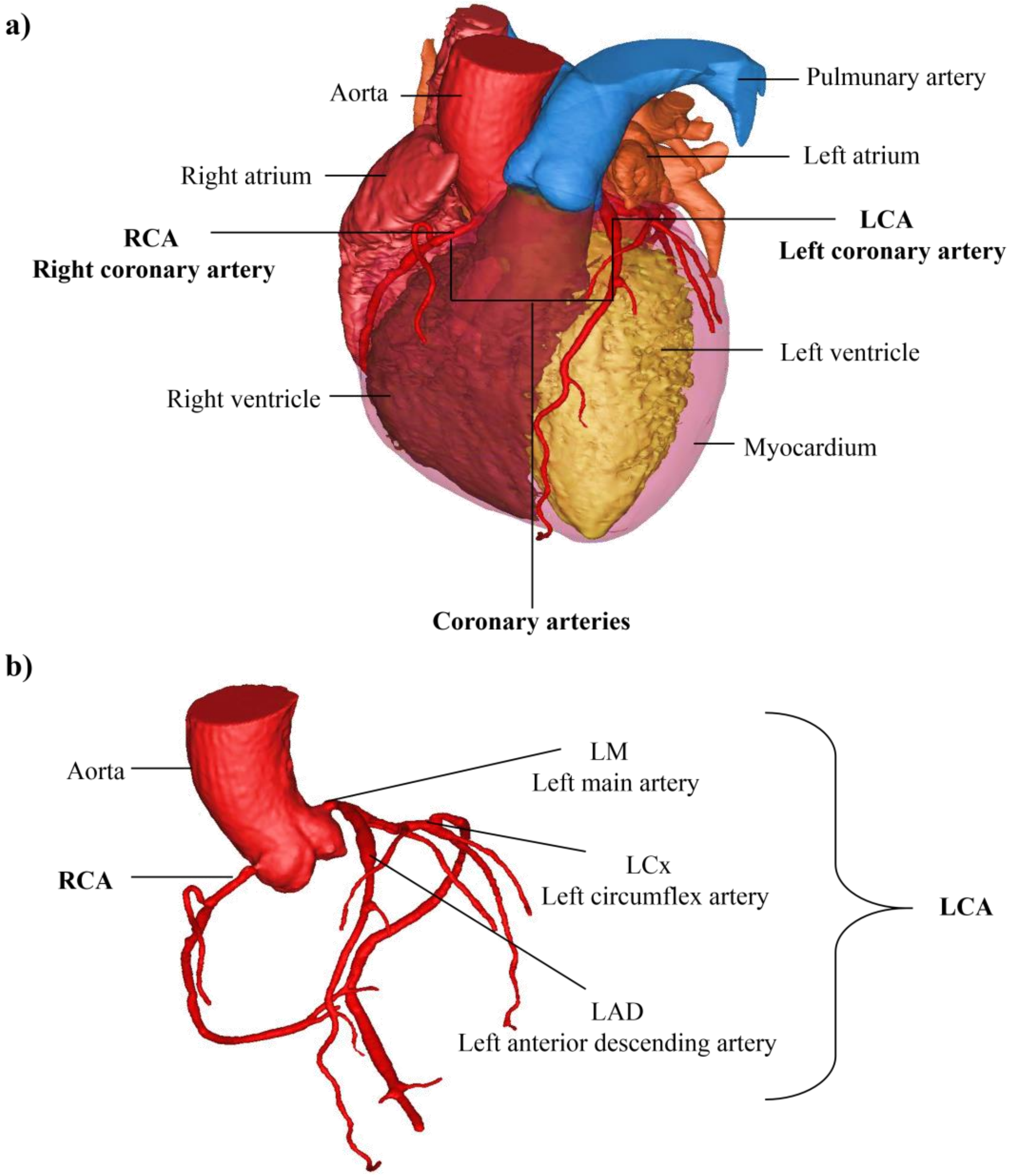

Figure 1.3. Volumetric reconstruction, using *Materialise Mimics*® software, from a healthy patient CT-scan: a) an heart showing the coronary circulatory system and b) coronary arteries representation (focus on the left coronary artery constitution).

1.1.1 Atherosclerosis

Atherosclerosis is a disease that affects millions of people world-wide, leading to heart muscle failure[7, 10, 12, 13]. The term comes from the Greek words *athero* – paste and *sclerosis* – hardness, and the disorder is characterized by a progressive narrowing and occlusion of the blood vessels[14]. When a local plaque forms inside a vessel causing a partial obstruction to the blood flow it is called stenosis. Atherosclerosis is a complex chronic inflammation in the large and medium arteries that is most frequently associated with hyperlipidemia (abnormally elevated levels of lipoproteins in the blood) and several other risk factors such as cigarette smoking, hypertension, diabetes mellitus, chronic infections, and genetic predisposition[15]. The mechanism of atherosclerosis development is complex and hemodynamic factors are determinant in the location of such disease[7, 8, 12].

Figure 1.4 represents the atherosclerosis progression in four stages[16]: the first stage represents the beginning of the disease (Figure 1.4a), when low-density lipoprotein (LDL) cholesterol and other molecules enter the artery wall, creating fatty streaks, often known as the first sign of atherosclerosis. When fatty deposits, constituted by LDL cholesterol, begin to buildup in the artery walls, they form a plaque (*i.e.* artery plaque), which can constrain blood flow – Figure 1.4b). Then, this plaque may continue to buildup, still non-obstructing the blood circulation; however, it becomes vulnerable to rupture (Figure 1.4c) resulting in the exposure of thrombogenic material into the artery interior originating the formation of a thrombus in the lumen. Finally, if the plaque does not rupture and the lesion continues to grow, it causes a severe narrowing of the artery restricting blood flow, also known as stenosis –Figure 1.4d.

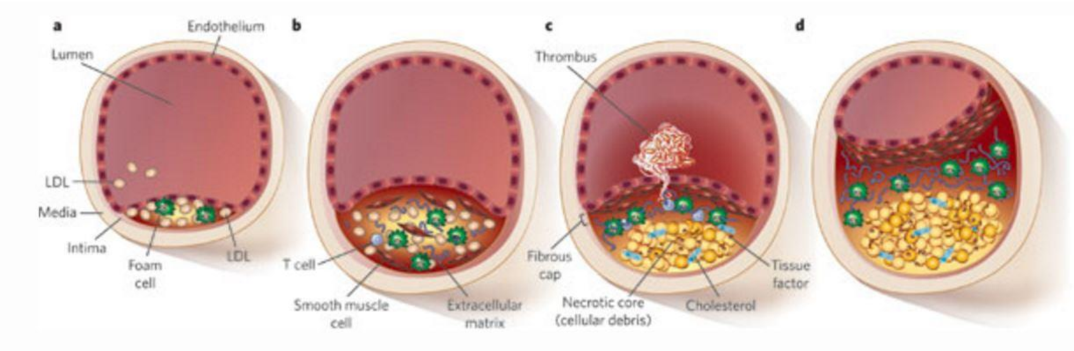

Figure 1.4. Atherosclerosis initiation and progression. Atherosclerosis development stages: a) lesion initiation, b) intermediate lesion, c) lesion vulnerable to rupture and finally d) advanced obstructive lesion. Adapted from Rader & Daugherty[16].

Thrombosis (blood coagulation) caused by the rupture of an atherosclerotic plaque is the most common cause of acute coronary syndromes such as myocardial infarction or unstable angina (chest pain). Figure 1.5 is an illustrative histological example indicating that a deadly thrombus can occupy 50% of the area of the coronary artery[17].

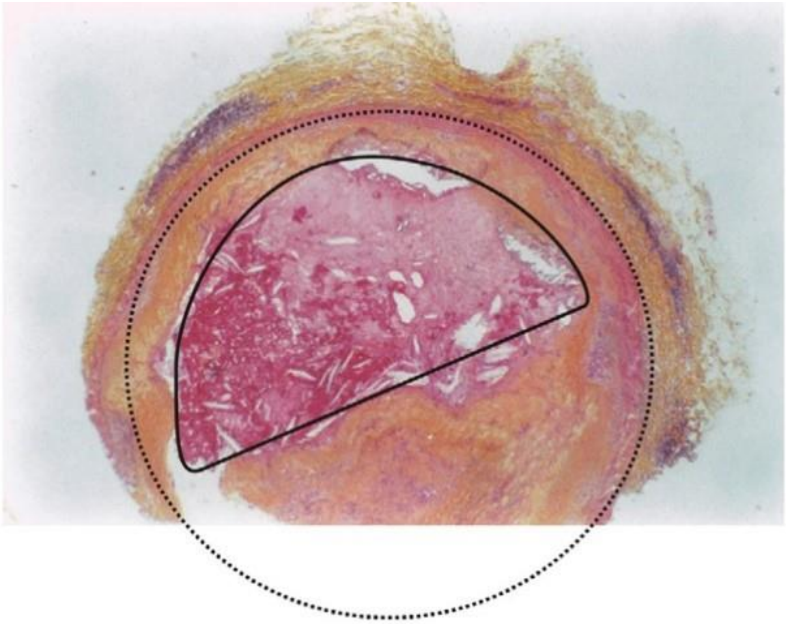

Figure 1.5. Histological image, presented by Brunette *et al.*[17], of 50% area occluded in coronary artery where a deadly thrombus formed in the remaining 50% lumen. The solid line approximates the thrombus external limit and the scattered line represents the external limit of the artery.

Several studies point out atherosclerotic lesions to specific locations in circulatory system, *i.e.* in the coronary bifurcations[18, 19]. These indicate that sites with arterial geometrical complexity, where disturbed flow patterns occur, are locations prone to lesions. Therefore, the use of realistic vascular geometries to determine the local flow field in the coronary artery is of vital importance for understanding the underlying development mechanisms of coronary artery diseases, namely atherosclerosis. The early diagnosis of coronary artery disease is particularly important for the reduction of mortality and non-lethal complications.

1.1.2 Left coronary artery morphology

Left coronary artery (LCA), together with the right coronary artery (RCA), the circumflex (LCx) and anterior descending (LAD) arteries are vessels considered in the classification of coronary artery disease[20, 21]. Figure 1.6 shows the distribution of the atherosclerotic occlusive lesions (red) in coronary arteries.

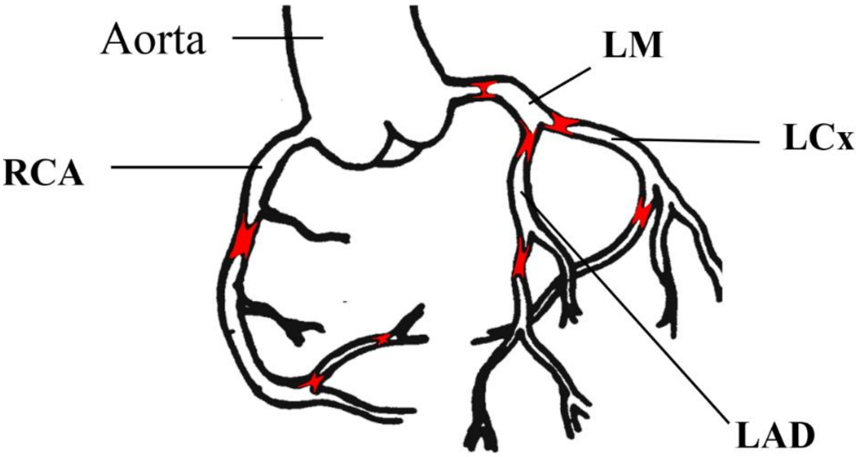

Figure 1.6. Distribution of atherosclerotic occlusive lesions (red) in human coronary arteries, reproduced from Debakey *et al.*[21].

The morphology of the artery is essential for understanding the development of atherosclerosis[18, 19, 22-24]. LCA was chosen to perform experimental and numerical hemodynamic studies. In this section a morphologic description of the artery under study is reported.

The LM can divide in several ways: it bifurcates, producing LAD and LCx; trifurcates, producing LAD, LCx and a ramus intermediate (RI); or tetrafurcates, producing LAD, LCx and two RIs. Table 1.1 shows the branching patterns of LCA analyzed by several authors from 1991 to 2013. The RIs present variability in their diameter and length, characteristics that are highly dependent on how many RIs exist[25, 26]. For some authors, the RI is the artery located in the angle formed by the LAD and LCx[25, 27], other authors use a broader approach and consider that RI has its origin in the vertex of the angle formed by the terminal branches of the LCA or in the initial millimeters of the LAD or LCx. Identification of the RI is important clinically. In its absence the irrigation is exclusively done by LAD and LCx branches; so in the case of occlusion of LAD and LCx much more area is affected. When RI is present, its origin is the site where atherosclerosis frequently occurs[28].

Table 1.1. Comparison of the branching pattern of LCA in past studies.

Author(s) and Year	Samples	Branching pattern				
		O	**B**	**T**	**Q**	**P**
Baptista *et al.* [25], 1991	100	2%	60%	38%	-	-
Cavalcanti *et al.* [4], 1995	100	1%	47%	40%	11%	1%
Reig *et al.* [27]; 2004	100	-	62%	38%		-
Ballesteros *et al.* [3]; 2008	154	-	52%	42%	5.8%	-
Hirak *et al.* [29], 2005	100	-	60%	35%	5%	-
Dombe *et al.*[28], 2012	64	1%	55%	36%	8%	-
Tomar *et al.* [30], 2013	50	-	76%	24%	-	-

O - One branch**;** **B** - Bifurcation; **T** - Trifurcation; **Q** – Quadrifurcation and **P** - Pentafurcation

Although Table 1.1 shows that previous studies have reported a wide variation in LM branching, there is a greater prevalence of the bifurcated anatomy [25, 27, 31]. Therefore, this PhD focus on the bifurcated branching pattern.

The LCA presents also wide morphological variability with regard to length, diameter and bifurcation angle. Table 1.2 reviews studies conducted by several authors from 1973 to 2013 on the LM morphology (diameter, length and bifurcation angle). In terms of LM length, two categories may be defined, using the criteria of extreme values[32]: a short LM, where the length is inferior to 5 mm, and a long LM, where the length is superior to 5 mm. A short LM has been considered as a risk factor in the development of atherosclerosis, since, during systole, a certain degree of twisting of the terminal branches increases the mechanical effort undergone by its walls, leading to greater atherosclerotic degeneration[33].

The LM average diameter range (see Table 1.2) is similar across several authors and ranges between 4 to 5 mm. Ballesteros *et al.*[3] observed a high frequency of values of small LM diameters (3.6 mm) in population under study. These regions have disturbed flow owing to the topology of the vascular tree, which is found in areas of branching or high vessel curvature.

Table 1.2. Comparison of the morphology with regard to length, diameter and bifurcation angle (between LAD and LCx) of the left main stem (LM).

Author/Year	**Samples**	**Diameter (mm)**	**Length (mm)**	**Bifurcation angle**
McAlpin *et al.*[32], 1973	100	4.7±1.2	6-15	-
Fox *et al.*[34], 1973	100	-	9-10	-
R. Kalpana *et al.*[35], 2003	100	-	6-15	-
Reig *et al.* [27], 2004	100	4.9±0.8	10.8±5.5	86.7º ±28.8º
Pflederer *et al.*[36], 2006	100			80º ± 27º
Ballesteros *et al.*[3], 2008	154	3.6±0.6	6.5±2.6	-
Kawasaki *et al.*[37] ,2009	209	-	-	72º ± 22º
Dombde *et al.*[28], 2012	64	4.7±1.0	11.2±0.4	-
Tomar *et al.*[30], 2013	50	-	7.1± 3.0	-

The impact of the bifurcation angle, between LAD and LCx branches, on plaques buildup and coronary heart disease development is a hot research topic; the bifurcation angle might have an effect on plaque size and plaque development. Previous studies have reported that a wider bifurcation angle might be related to the appearance of disturbed flow regions prone to atherosclerosis development, whereas a narrow angle might minimize this effect[38, 39]. Previous studies investigating the typical distribution of coronary bifurcation angle[27, 36] considered 80º as the angle above which the risk of atherosclerosis development is significant. Besides, non-calcified plaques have been described to be associated with higher bifurcation angles[40]. This strong relationship between the angle of the left coronary artery and the presence of plaques within the left coronary bifurcation must be used as guidance for analysis of potential effects of hemodynamics on the local characteristics and distribution of plaques[41, 42]. Therefore, morphological variations of the left coronary artery (LCA) are of the highest importance in determining areas related to arterial occlusive disease, in hemodynamic procedures and finally in terms of academic value [35, 43, 44].

1.2 Hemodynamics fundamentals

Westerhof *et al.*[45] stated that: "*Hemodynamics makes it possible to characterize, in a quantitative way, the function of the heart and arterial system, thereby producing information about what genetic and molecular processes are of importance for cardiovascular function*".

In 1872, Edward Rindfleisch[46] was the first researcher to correlate atherosclerosis with the hemodynamic environment by observing that plaques were found in specific locations. He believed that those locations were correlated with strong forces exerted by the blood flow on the arterial wall. In 1960, a century later, contrarily to Rindfleisch suppositions, Caro *et al.*[22] showed that regions prone to lesions are susceptible to intimal thickening due to migration and proliferation of vascular smooth muscle cells; this phenomenon, correlates the hemodynamic environment with low wall shear stress (WSS). Since then, many other studies have proven this theory, demonstrating that plaque formation in human coronary arteries is located in regions of reduced values of pressure, blood velocity, and wall shear stresses[18, 47]. Ku *et al.*[8] performed a closer analysis of the branch points showing that the flow dividers – regions of high shear stress– were relatively protected from these lesions. In contrast, there was a predilection for atherosclerosis at the curvatures and lateral walls of the branch points with low WSS.

The locations of lesions are subject to abnormal blood flow behaviours resulting in changes in the hemodynamic environment[8, 48]. Blood vessels are constantly exposed to several types of hemodynamics forces (including hydrostatic pressure, cyclic stretch and shear stress)[49] as illustrated in Figure 1.7.

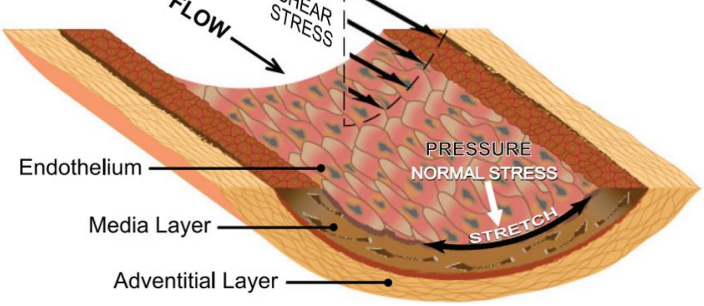

Figure 1.7. Diagram of WSS (parallel to the endothelial cell surface (ECS)) and the normal stress (perpendicular to the ECS) by blood flow [49].

1.2.1 Blood Viscosity

A fluid is defined as a substance that moves and deforms continuously as long as a shear stress is applied[50]. On the other hand, it is possible to define another class of materials, known as elastic solids, which may experience small deformations when exposed to a shear stress, but will not flow, *i.e.* will not deform continuously. Later, a hybrid concept, which comprises the elastic and viscous behaviours of materials was introduced, the so-called viscoelastic material.

For a Newtonian fluid, the applied shear stress (τ_w) is proportional to the resulting deformation rate ($\dot{\gamma}$), in accordance with Newton's law of viscosity:

$$\tau_w = \mu \cdot \dot{\gamma} \tag{1.1}$$

When the relation between shear stress and deformation rate is non-linear, the fluids are called non-Newtonian; typical examples include polymeric solutions, melts, colloidal suspensions and blood[19, 51].

The blood is a complex biphasic liquid suspension of 55–60 % of liquid medium (plasma) and 40–45 % of elements such as red blood cells (RBCs), white blood cells, and platelets[52]. Thus, its viscosity is mainly determined by viscous properties of the plasma, by the fraction of RBCs in the blood, and also by the properties of its constitution elements. Blood is a non-Newtonian fluid and exhibits a complex rheological behaviour, such as shear-thinning viscosity, some elasticity and thixotropic behaviour[53]. The presence and interactions between cellular elements, mainly RBCs, which are the most abundant component and whose mechanical properties are inherent to the blood microstructure contribute to its complex behaviour[45]. Figure 1.8 shows the shear viscosity of plasma and blood, calculated from the tangent of the shear stress as a function of the shear rate. Generally in most physiological conditions, the shear viscosity of the blood is about three fold higher than the viscosity of water[14].

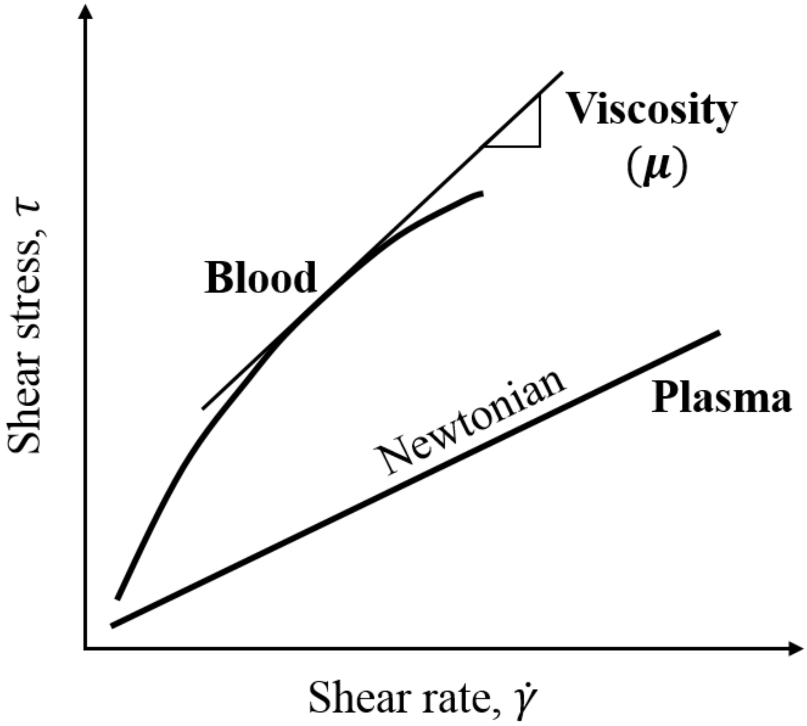

Figure 1.8. Viscosity of plasma and blood.

The blood viscosity depends on the shear stress applied. Specifically, under high shear stresses blood viscosity decreases, due to the deformation of RBCs, while under low shear stresses the RBCs aggregate with each other and form stacked coin structures. This process is reversible and, as the shear rate increases, the larger group of stacked coin structures breaks up into smaller ones; at higher values, the suspension can be seen as a monodispersed RBC suspension[54-56]. Sousa *et al.*[57] measured *in vivo* blood viscosity and at 37°C, for high shear rates (100-300 s^{-1}), the viscosity is about 3.5 cP, while it increases rapidly up to 30 cP as shear rate decreases to less than 2 s^{-1} as shown in Figure 1.9. The other key component of blood is plasma, whose infinite shear viscosity plateau[52, 58, 59], in normal conditions, varies from 1.10 cP to ~ 1.35 cP at 37°C.

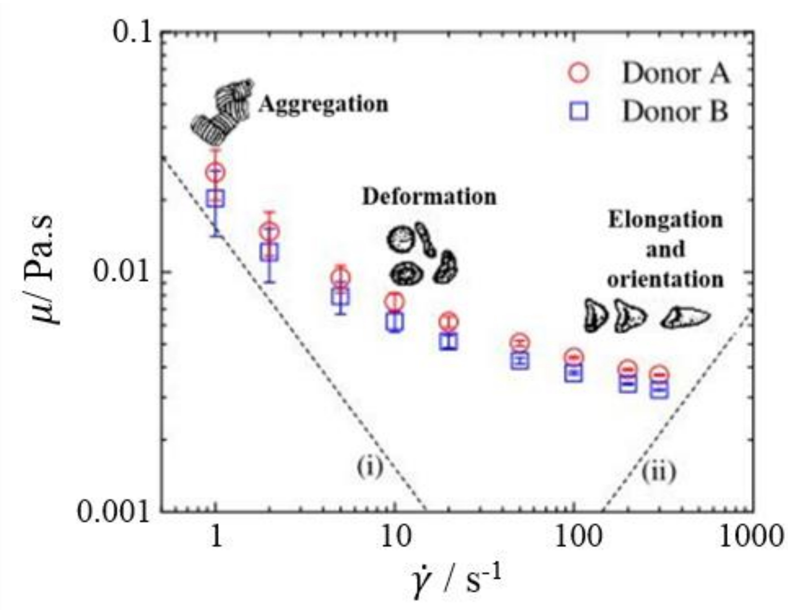

Figure 1.9. Steady-shear viscosity as a function of the shear rate measured at 37◦C, for two healthy donors, A and B. Adapted from Sousa *el al.*[57].

The size of blood vessels also determines blood viscosity. In small blood vessels, as capillaries and arterioles, and at high velocities, the blood viscosity decreases with the decreasing of the blood vessel diameter (Figure 1.10).

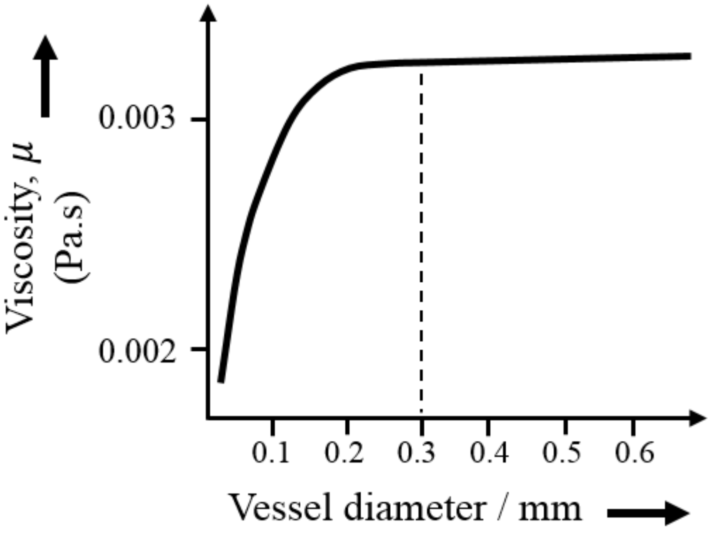

Figure 1.10. Viscosity as function of blood vessel diameter[60].

This effect is also known as the Fahraeus-Lindqvist effect, and it occurrence is observed at blood vessels smaller than 0.3 mm in diameter[60] – Figure 1.10. In medium and large arteries, the shear rates are higher than 100 s^{-1} and so blood viscosity is almost constant[19, 45, 51] (Figure 1.9). These are, perhaps, the reasons why blood is most often assumed to be a Newtonian fluid in simulations of blood flow, which is an accurate approximation at large Reynolds numbers and in large and medium blood vessels. However, in transient studies, especially when the flow stops, there are periods of time where the shear rate is below 100 s^{-1} and non-Newtonian effects can become important[51].

1.2.2 Reynolds number

Flow rate is a purely quantitative value indicating the volume of blood passing through a vessel per a unit of time. Another approach is the qualitative description of the blood flow. Flow can be either laminar or turbulent and the Reynolds number helps to predict the transition between laminar and turbulent regimes. The Reynolds number is the ratio between inertial and viscous forces exerted on an element of fluid and it is defined as:

$$Re = \frac{inertial\ forces}{viscous\ forces} = \frac{\rho v D}{\mu} \tag{1.2}$$

where ρ is the fluid density, v the fluid velocity and D the vessel diameter.

The blood flow Reynolds number ranges from 1, for small arterioles, and goes up to 4000 in the aorta[18]. Laminar flow ($Re < 2000$) is described by a parabolic velocity profile, which means that the fastest molecules are at the center of the vessel and the velocity decreases in the wall direction – from the center to the walls[14]. The turbulent flow ($Re > 4000$) takes place every time the blood velocity is too high. In the transition region ($2000 < Re < 4000$), the flow can oscillate chaotically between laminar and turbulent.

1.2.3 Blood pressure

From an engineering perspective, the human cardiovascular system can be described as a pump that forces fluid through a complex vessel system comprised of arteries and veins. When the heart beats, mechanical energy is supplied to the blood and its pressure rises. The highest blood pressure (systolic pressure) occurs during heartbeat; the lowest value corresponds to the resting pressure experienced between heart beats (diastolic) - Figure 1.11.

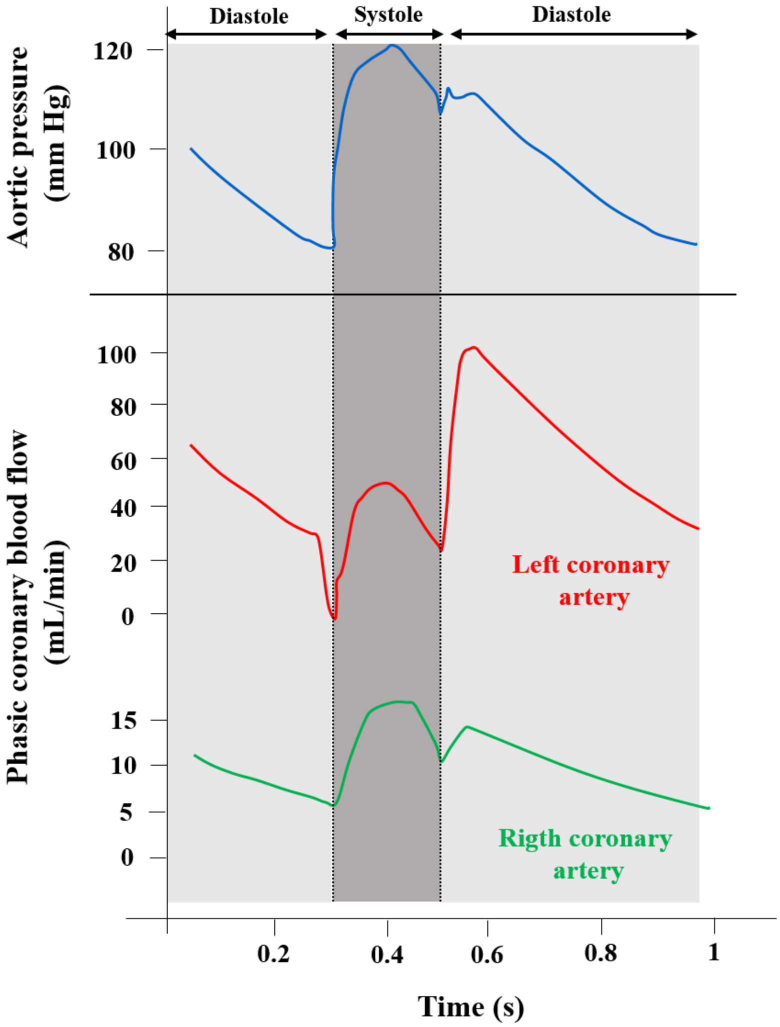

Figure 1.11. Illustration of the phasic blood flows of right and left coronary arteries in relation to aortic pressure. Adapted from Koeppen *et al.*[60]

A single cardiac cycle comprises both phases: diastole and systole. During the systole the left and right ventricles contract and eject blood into the aorta and pulmonary arteries. In this period the atrioventricular valves are closed and no blood enters the ventricles. Conversely, during the diastole, the ventricles are relaxed and blood passively flows from the left and right atriums into the left and right ventricles, respectively.

Coronary blood flow rate varies directly with the pressure along the coronary microcirculation, which can be essentially considered as the aortic pressure, since coronary venous pressure is near zero. However, since the coronary circulation irrigates the heart, during systole the coronary arteries are compressed by the contraction of the myocardium, impeding blood to circulate, therefore most of the coronary flow occurs during diastole, where the flow increases (note that this is the opposite of all other vascular routes in the body) - Figure 1.11.

1.2.4 Wall shear stress – WSS

Wall shear stress is the tangential force that blood exerts in the flow direction on the surface of the vascular wall as illustrated in Figure 1.12. For Newtonian fluids, the wall shear stress is proportional to the velocity gradient at the wall of the tube:

$$\tau_w = -\mu \left.\frac{\partial v}{\partial r}\right|_{r=R} \tag{1.3}$$

where v is the fluid velocity flowing in a straight tube with a certain radius (R) and μ is the fluid viscosity.

Endothelial cells are specialized in sensing and processing these forces in a complex manner that triggers and controls adaptation, atherosclerotic inflammation and remodeling[61]. Luminal remodeling changes vascular geometry and in turn alters local flow fields and WSS. Thus, vascular geometry and local WSS are held as important risk-factors in coronary artery disease. Because the coronary vessels are very small in diameter (few millimeters) and difficult to access, the established method to evaluate this risk-factor is flow simulation by computational fluid dynamics (CFD), based on three-dimensional (3D) luminal reconstructions[62, 63].

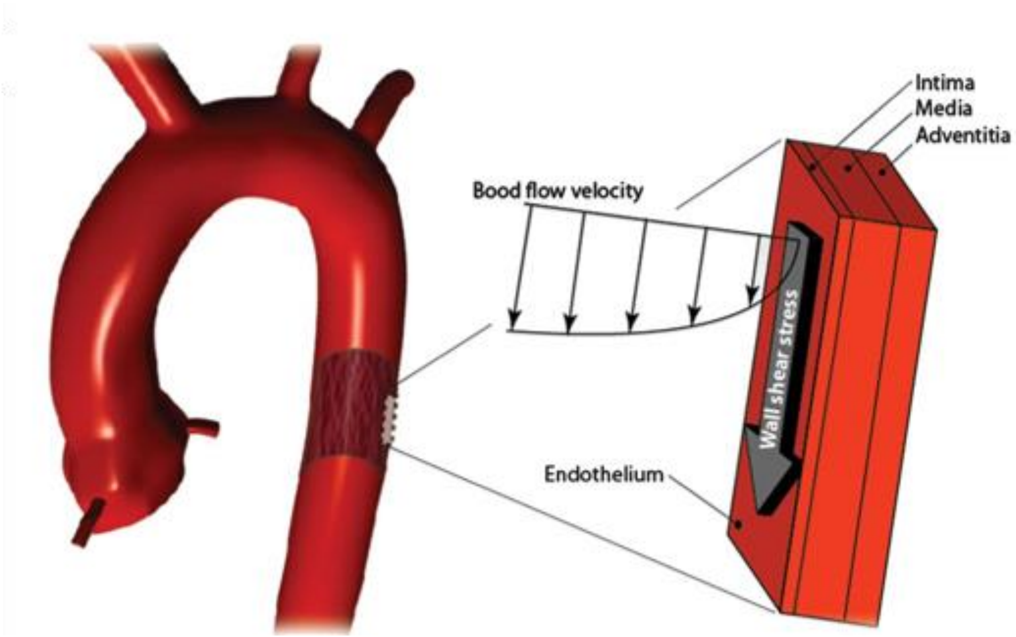

Figure 1.12. Illustration of wall shear stress as a consequence of blood flow over the endothelial layer. Adapted from Back *et al.*[64].

Local hemodynamic factors, in particular low endothelial shear stress (ESS), play a major role in the atherosclerosis location, underlining the importance of studying the WSS magnitude and distribution in coronary arteries[65]. However, the endothelium is in direct contact with the blood flow and thereby constantly exposed to the mechanical forces that blood applies.

Over the last century, researchers have been using the physical principles that rule the vessel branching system to better understand its architecture and blood flow. One of such principles is Murray's Law, which restricts the size and the flow distribution in a vessel bifurcation based on the minimization of the energy to maintain and pump the blood[66, 67]. Murray's law maintains an important role in hemodynamics studies as a guiding theoretical principle, and it is assumed that vessel systems that deviate from Murray's Law are more prone to health problems[68]. In this way, the information given by WSS and, in particular, its distribution across blood vessels gives valuable knowledge about the risk of atherosclerosis initiation. In this thesis, in **Chapter 4**, particular emphasis is given to the study of deviations from Murray's law and how these influence the sites prone to atherosclerosis development.

1.3 Flow Characterization

The study of fluid flow in the vascular system requires a combination of *in vivo*, *in vitro* and numerical studies. When considering experimental methods for quantifying pressure and velocity fields, it is important to distinguish between *in vitro* and *in vivo* methods. *In vitro* methods (used in replica models) are considerably more flexible due to the fact that they use technologies that are unviable and/or non-ethical to use *in vivo* (in human or animal studies). For example, one of the most popular technologies to measure velocity fields are laser based methods. However, these methods need transparent models and so they are impossible to use *in vivo* models due to its opacity.

The main objective in a hemodynamic study, through either computational or experimental investigation methods, is to describe pressure and velocity fields as accurately as possible. The most elemental method of experimental investigation is flow visualization. Flow visualization techniques are of great importance in order to understand fluid flow behaviour when spatial and temporal gradients exist. It allows a qualitative or quantitative analysis by the assessment of different flow phenomena.

1.3.1 *In vivo* techniques

Non-invasive *in vivo* approaches include several techniques such as: computed tomography (CT), ultrasound, Doppler echocardiography and magnetic resonance imaging, among others. The CT is widely used for evaluation of the artery anatomy[69]. The radiation involved in a CT scan prevents it from being used routinely for research purposes. Doppler echocardiography uses ultrasound techniques and is usually employed for obtaining the in-plane velocity component, allowing velocity profiles determination and flow quantification. However, because they require an acoustic window, they cannot be performed through air or bones, a limitation to the image acquisition in the vicinity of the lungs, ribs, and cranium. Magnetic resonance imaging is a unique imaging technique that allows the acquisition of both the three-dimensional anatomy and the velocity fields throughout the cardiac cycle, being therefore an important technique for clinical and research investigations in cardiovascular fluid mechanics.

Several authors have performed different studies using *in vivo* approaches in order to have a deeper understanding of coronary artery diseases. Williams *et al.*[70] implemented a new method for measuring WSS in coronary arteries using simultaneously acquired pressure and intravascular ultrasound measurements in the coronary luminal area. They developed a new method, over physiological conditions, for determining coronary artery mechanical properties [70]. The position of a stenosis in the LAD was examined *in vivo* by Kimura *et al.*[71]. They used intravascular ultrasound images from patients with atherosclerosis in the LAD and demonstrated that the lesion is usually located on the lateral wall, opposite to the entrance of the LCx[71]. Fayad *et al.*[72] demonstrated that *in vivo* MRI can provide high-spatial-resolution images of the coronary artery wall in normal and diseased human arteries. They have combined the high-resolution MRI and genetically engineered animals to investigate the progression and regression of atherosclerotic lesions, thus demonstrating that this combination is a valuable tool for the advancement of atherosclerosis understanding[73].

Although there are steady advances in *in vivo* studies, the ethical and practical conditions are still limiting factors. The subsequent section will give a brief literature overview of the *in vitro* studies with a focus on optical techniques commonly used in the experimental studies. A major emphasis on µPIV system is given, since this technique was used throughout this thesis.

1.3.2 *In vitro* techniques

Over the years, several *in vitro* methods have been applied in an effort to understand the blood flow. The development of experimental optical techniques has contributed for the understanding of blood flow in macro and microcirculation.

The *in vitro* blood flow has been investigated using several image techniques including: video microscopy and image analysis[74], laser-Doppler anemometry[75] and particle-based methods such as Particle tracking velocimetry (PTV)[76], particle image velocimetry (PIV)[17, 77], micro-particle image velocimetry (µPIV)[78, 79] and stereo-PIV.

The advances of optics, computation power and digital image processing techniques allowed combining the high spatial and temporal resolutions of an inverted microscope with the traditional particle image velocimetry (PIV) system[80].

PIV is an imaging technique used for the characterization of flow kinematics, which relies on the acquisition of the local velocity, v, using the experimental average displacement of tracer particles (Δx), in a sampling window over a known period of time (Δt)[80, 81].

$$v = \frac{\Delta x}{\Delta t} \tag{1.4}$$

In other words, particle distributions are recorded at two instants and the flow motion is determined from the change of the spatial particle distribution over time. µPIV technique is based on the same measurement principle, but with specific characteristics such as the scale range, the imaging set up and the flow illumination concept. In the last 20 years this image technique has become the standard tool for measuring fluid velocities at micro/mili scales. This technique is very flexible allowing the analysis of regions ranging from a few micrometers up to several millimeters by choosing the appropriate magnification; the flow velocities can also be acquired from nanometers per second to meters per second by adjusting the timing of the measurement devices to the flow under study[82]. One main difference between PIV and µPIV methods is the light used: in macroscopic experiments a laser light sheet is used to illuminate the tracer particles within the plane of the flow under study while in µPIV experiments a laser light is reflected through a dichroic mirror, travels through an objective lens that focuses on the region of interest, and illuminates a regional volume[82].

The main conventional µPIV system components are: a microscope, a high resolution objective lens, optical filters, a high power light source for flow illumination and a high speed camera. Figure 1.13 shows an illustration of a conventional µPIV setup.

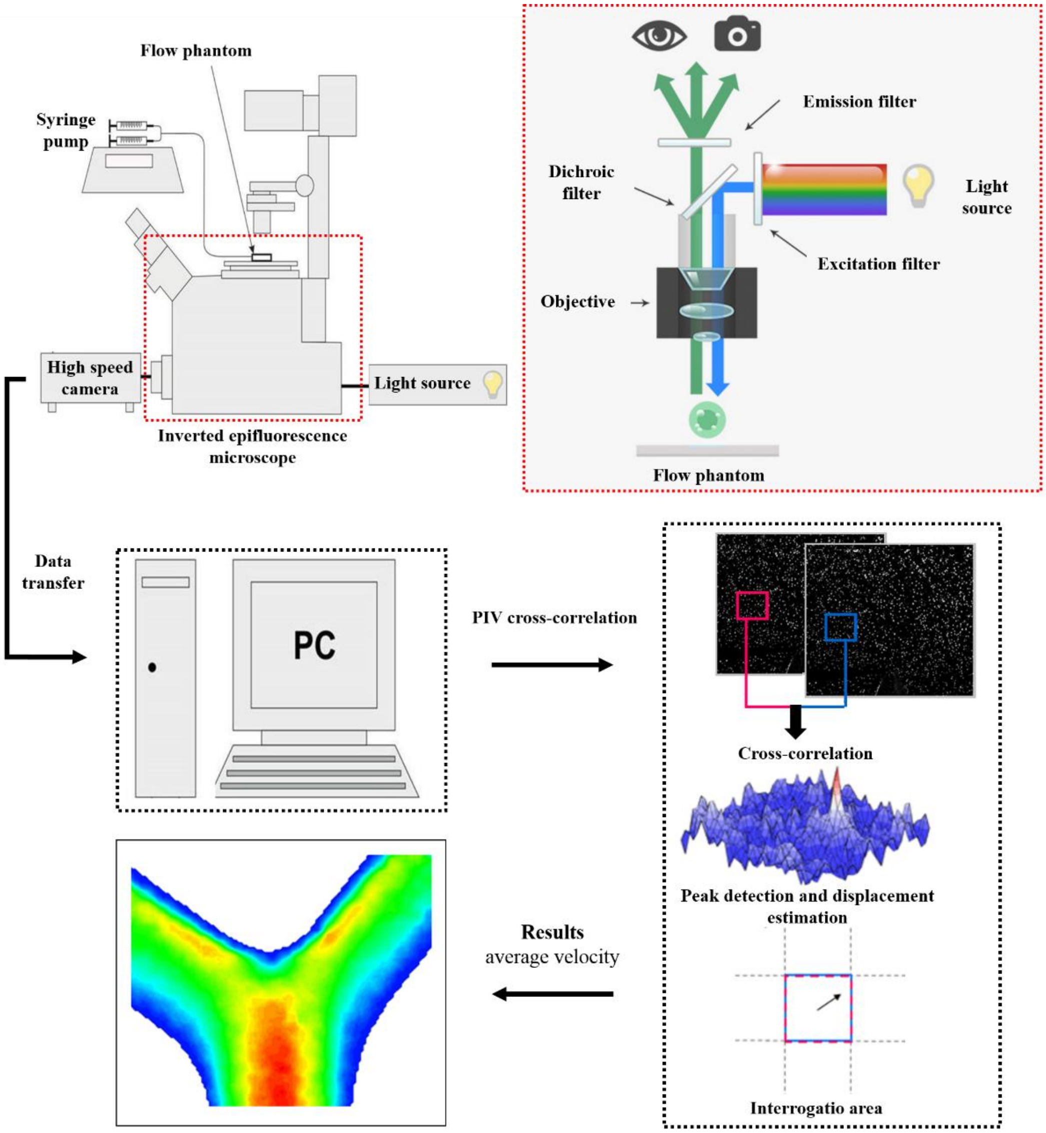

Figure 1.13. µPIV experimental setup and PIV cross-correlation method[82, 83].

The basic principle of µPIV technique is that a laser source is used to illuminate the whole flow volume, in which the flowing fluid is seeded with small fluorescent particles to visualize and measure the flow. The emitted light by the source is reflected by a dichromatic mirror inside the inverted microscope, and then is transmitted through the objective lens and illuminates the flow volume. When the light hits the fluorescent tracer particles, it disperses and travels back to the dichromatic mirror, which filters out all reflected light capturing only the emitted light from the particles[82, 83]. Then, the resulting images are recorded in two successive images by a high speed camera. The synchronization between the pulsed light source and the camera is done in a way that the time interval between the two images acquired are independent of the camera frame rate, allowing the user to adjust the time interval according to the flow conditions[82]. After the images are recorded, PIV cross-correlation is applied. The images are divided into small search areas (*i.e.* interrogation areas) typically 32 × 32 pixels. The cross-correlation is then applied to each interrogation area for obtaining a correlation plane. Finally, the peak detection and displacement estimation are applied to obtain the most probable local displacement in each interrogation area. At this instant, given the size of a pixel in the image of the flow field and the time separation between the two images, the velocity can be calculated[81-83].

Several factors affect the µPIV system resolution, such as the density and size of the tracer particles, the size and optical characteristics of the flow phantom and image quality and also the out-of-focus particle images from volume illumination. µPIV illumination leads to high background noise caused by the out-of-focus particles because both, focused and unfocused particles, appear in the image. Wereley and Meinhart[81] executed µPIV experiments using a large number of acquisition images in order to perform a collective average correlation. Using all the pairs of images, they were able to improve the resolution and velocity accuracy of the µPIV measurements by reducing the background noise. The distance above and below the focal plane under study, in which unfocused particles contribute to the correlation function, is defined as the total measurement depth, i.e., the thickness of the measurement "plane", δ_{z_m}[81, 84]:

$$\delta_{z_m} = \frac{3n\lambda_0}{NA^2} + \frac{2.16d_p}{tan\theta} + d_p \qquad (1.5)$$

and can be calculated as the sum of three different effects: the effect by diffraction $\left(\frac{3n\lambda_0}{\mathrm{NA}^2}\right)$, the effect caused by geometrical optics $\left(\frac{2.16d_p}{\tan\theta}\right)$ and the effect due to the finite size of the particle (d_p). NA is the numerical aperture, λ_0 the wavelength in vacuum being imaged $\left(\tan\theta \cong \sin\theta \cong \frac{\mathrm{NA}}{n}\right)$ and n the refractive index.

There are numerous applications using µPIV system to measure 2D flow fields in simplified geometries as well as in more complex cases. The range of applications is wide and the focus can be either technological or for fundamental interests in fluid-mechanics. Although µPIV is a well-established technique and the offering of commercial µPIV systems are reliable, there is a huge contribution in finding novel methods or applications.

The extension of µPIV into three dimensional space has been accomplished by a number of techniques, including scanning multiple 2D slices[85], digital holography[86] and stereo imaging[87]. While traditional µPIV only is able to measure two components of the velocity, stereo PIV allows to measure all the three velocity components in a single 2D plane[87]. Nevertheless its application to the µPIV setup is extremely more complex than its application to the macroscale PIV due to conflicts between the spatial resolution and the accuracy of the out-of-plane velocity components. Lindken *et al.*[88] performed the first successful stereo µPIV experiments investigating the 3D flow in a T-shaped micromixer.

In the literature, several researchers have been working on patient-specific *in vitro* techniques that allow experimental studies of blood flow in realistic configurations[89-91]. First of all, *in vitro* studies require the construction of a model of the blood vessel (flow phantom) under study. The model must be transparent to the wavelength of the light used and its half thickness must be smaller than the focal distance of the objective lens used[92]. Geoghegan *et al.*[93] provided a complete description of a method to convert medical imaging data into phantoms. Figure 1.14a), shows a rigid phantom of a carotid artery bifurcation developed by Geoghegan *et al.*[93]. In another interesting study, Irwan *et al.*[94] tested a flow sequence on a moving anthropomorphic silicone heart phantom (Figure 1.14b), where the coronary arteries were filled with a contrast solution. The clinical relevance of this phantom was validated by comparing the myocardial relaxation times of the wall of the phantom's silicone to those of humans. Kabinejadian *et al.*[95] developed and evaluated a novel carotid stent design based on a CT Scan; this model, shown in Figure 1.14c), was tested in a real scale poly(dimethylsiloxane) (PDMS) replica of an anatomical geometry of a healthy carotid artery.

Models of complex geometries, as the ones shown in Figure 1.14, are typically constructed by direct rapid prototyping from a 3D computational representation of the blood vessel[90, 91, 96] or by casting in a mold produced by rapid prototyping[96, 97]. However, comprehensive 3D flow and shear stress measurements in models that mimic the left coronary artery and its branches are still missing. Some work in this direction has been undertaken by Vétel *et al.*[98], who used multi-plane Stereo-PIV to describe complex and coherent 3D Lagrangian structures and also by Brunette *et al.*[17], who applied a 2D PIV scanning technique to reconstruct the flow field in a stenotic coronary artery. Gaillard *et al.*[99] developed an *in vitro* model in which the authors were able to mimic the coronary circulation enabling the quantification of the effects of aortic valve stenosis on a normal left coronary artery with mathematical model validation.

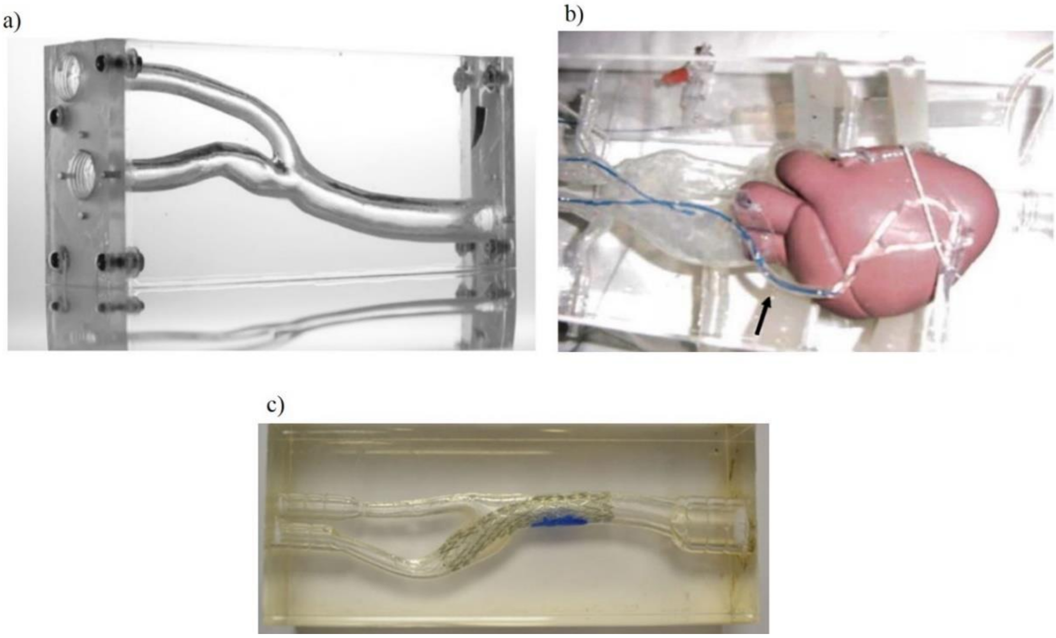

Figure 1.14. Photographs of several phantoms found in literature: a) Rigid phantom of a carotid artery bifurcation, fabricated by Geoghegan *et al.*[93] b) Moving heart phantom with coronary arteries and a blue wire as a catheter in the study of Irwan *et al.*[94] c) Kabinejadian *et al.*[95] planar model with a stent inserted.

Several investigations have emerged studying the blood flow in realistic configurations[97]. Kabinejadian *et al.*[100] used an *in vitro* coronary PDMS model to design a novel coupled sequential anastomosis (back route for blood flow if one branch is blocked or compromised), Figure 1.15. The flow field inside the phantom models of the coronary artery bypass grafts with different designs was investigated under pulsatile flow conditions using PIV (some results can be observed in Figure 1.15). This *in vitro* investigation, that complemented previous computational studies[101, 102], is a perfect example on how *in vitro* and computational hemodynamic studies can give helpful insights for future clinical applications

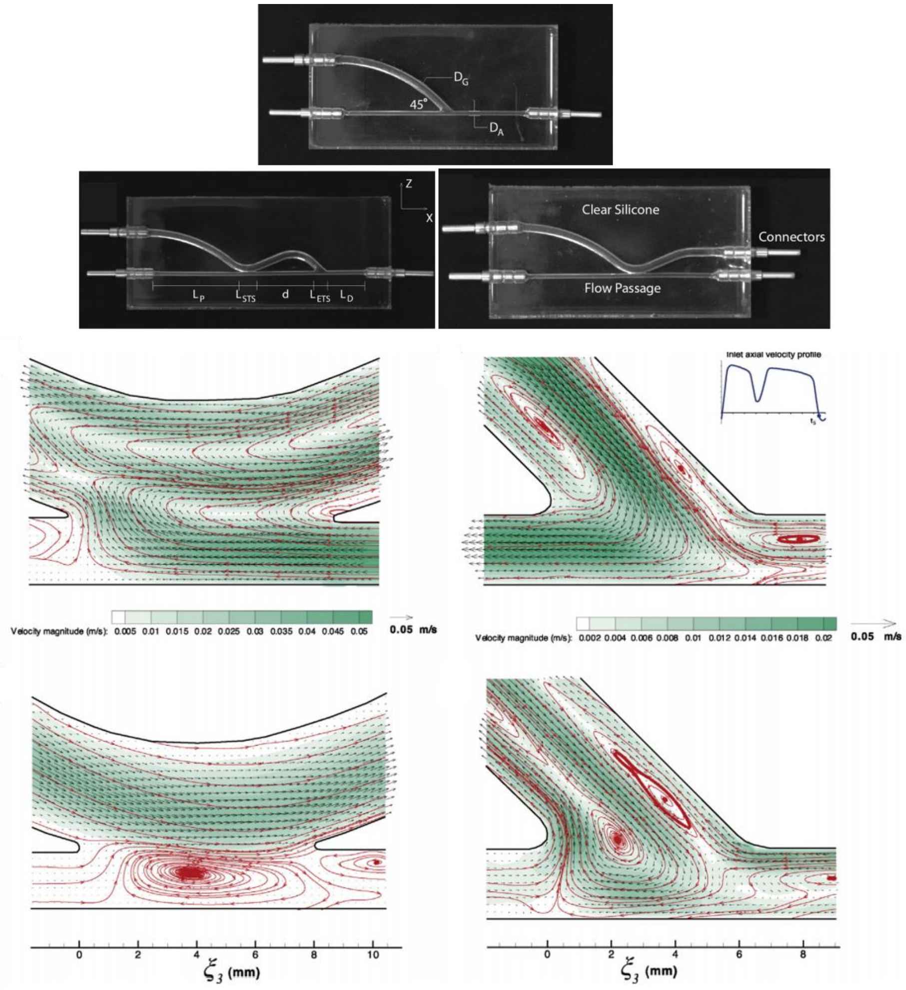

Figure 1.15. PDMS models of different sequential anastomoses configurations (top) and (bottom) measured flow field by PIV technique showing the velocity vectors pointing out to some larger vortices in the different models configurations[100].

1.3.3 Computational Fluid Dynamics (CFD)

Fluid dynamics studies have been used to complement and advance the understanding of cardiovascular diseases. The fluid dynamics equations are mathematical statements of the conservation laws in physics for describing the transport of mass, momentum, and energy through a physical domain[103]. These equations are applied to the computational domains representing the fluid component and they are fundamental to perform a correct blood flow simulation. Differential equations translate the various physical phenomena, including fluid dynamics, chemistry, physics and engineering, and more recently, areas such as medicine and biology. Generally, mathematical models do not have an analytical solution, therefore requiring its numerical resolution. To fill this gap, computational fluid dynamics (CFD) became a popular methodology to solve problems that involve fluid flow and heat/mass transfer. Much of the numerical investigations were performed using several commercial CFD software[41, 104], even though some authors have developed their own numerical code[105, 106]. Briefly, CFD comprises a series of steps, in which the classical equations of fluid flow, and other auxiliaries, are approximated by algebraic equations solved numerically, in sequence or in parallel[103, 107, 108]. CFD is a research field that may lead to the everyday use of computer techniques for diverse biomedical engineering applications.

The starting point of any numerical method is the description of the mathematical model, *i.e.* the definition of the differential equations and the implementation of the boundary conditions to apply on incompressible/compressible, inviscid/viscous, laminar/turbulent, 2D or 3D, *etc*. studies. Then, it is necessary a spatial discretization where the differential equations are solved. Finally the solution is determined for all points in the domain and, sometimes, as function of time[107, 108].

In the spatial discretization step, each geometry is divided into a number of small elements, or grid cells, covering the domain under study. In each element, the equations are solved to yield their corresponding values of variables under study such as, velocity, pressure, temperature or others. This methodology allows calculating changes or interpolation between cells. The type of mesh created in the study domain is highly dependent on which are the variables being evaluated; *i.e.* when assessing wall shear stress, the flow near the walls has particularly interest, therefore the mesh in these regions should be refined. There are several mesh strategies based on different grid elements that can be applied to a given geometry, such as mapping, triangular, paved, triangular with prism layers and several multi-block types. Figure 1.16 shows such meshing strategies in the artery model[103].

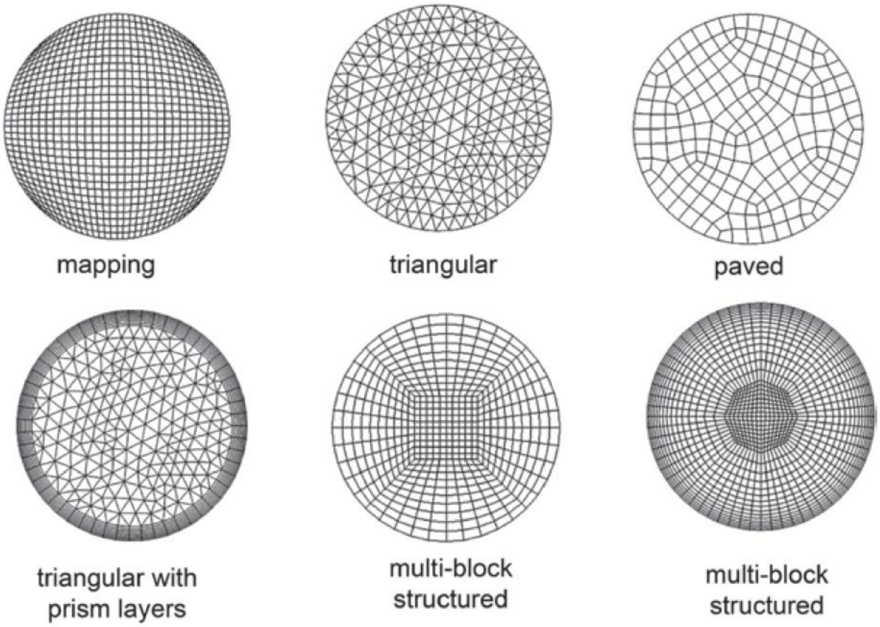

Figure 1.16. Cross-sectional view of an artery vessel using different mesh strategies. Adapted from Tu *et al.*[103].

The number of elements in the mesh influences the accuracy and computational resources. Although a highly refined mesh may give very accurate results, its simulation time may be unreasonable. Therefore mesh independence studies are carried out to assure a compromise between accuracy and computational resources. To do so, flow results are checked using different refinement meshes, and the mesh is considered adequate when the results are almost unchanged with decreasing cell size[103].

Hemodynamic analysis of coronary artery disease, either experimental or numerical, has been typically performed using one of two approaches: idealized models [17, 41, 79, 106] with idealized shapes or realistic coronary arteries[6, 38, 95, 109] models extracted from patient's medical data. A good predictor for coronary atherosclerotic lesion location is its anatomical geometry complexity, such as branching, irregular shape and large tortuosity present in the coronary arteries[110, 111]. Further in this thesis (**Chapter 6**), a link between arterial geometrical features, and particular geometrical non-planarity, with plaque distribution that might lead to atherosclerosis initiation is evaluated.

Chaichana *et al.*[41] performed an interesting study on the hemodynamic effect of variations in the angulations of the left coronary artery, simulating blood flow in twelve LCA models, in which four are patient-specific geometries created from CT scans and eight are fully design idealized models - Figure 1.17.

This study showed a strong relation between hemodynamics and LCA angulations. Consistent observations between idealized and patient-specific LCA models demonstrated that for particular parameters, in this case the bifurcation angle, the idealized models help to understand their impact in hemodynamics. Nevertheless, hemodynamic profiles generated in individual patients are complex with different own shape characteristics influencing the own hemodynamics from patient to patient. In this thesis, although idealized arterial models were initially used as proof of concept for the phantoms fabrication (**Chapter 2, 3** and **4**), patient-specific arteries were also considered, particularly when drawing important conclusions for the link between LCA geometrical characteristics and atherosclerosis (**Chapters 5** and **6**).

The development of modern and better imaging technologies, especially magnetic resonance imaging and computed tomography, allowed a quantification of arterial blood flow in patient-specific geometrical models[103, 112-114]. The non-invasive *in vivo* techniques as MRI and CT scans can be applied at arterial sites where vascular anatomy typically exhibits great individual variability and complexity and by medical imaging softwares (*e.g.* Mimics® software), the realistic geometry of patients can be post-processed and converted to numerical meshes to perform numerical simulation. Mimics® software has been used in this work for extracting real LCA geometries provided by a medical team from the *Hospital Center of Vila Nova de Gaia e Espinho*.

Idealized models

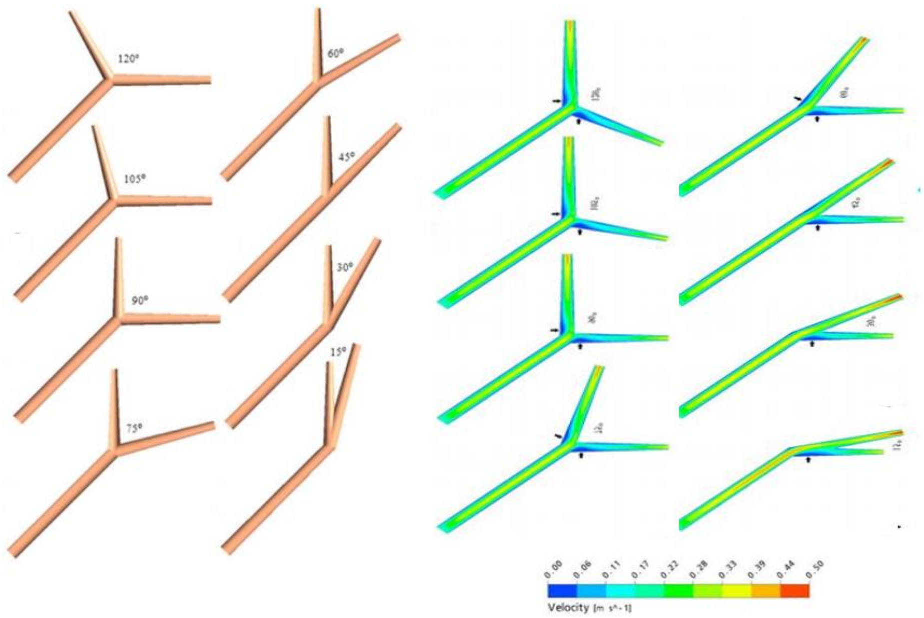

Patient-specific models

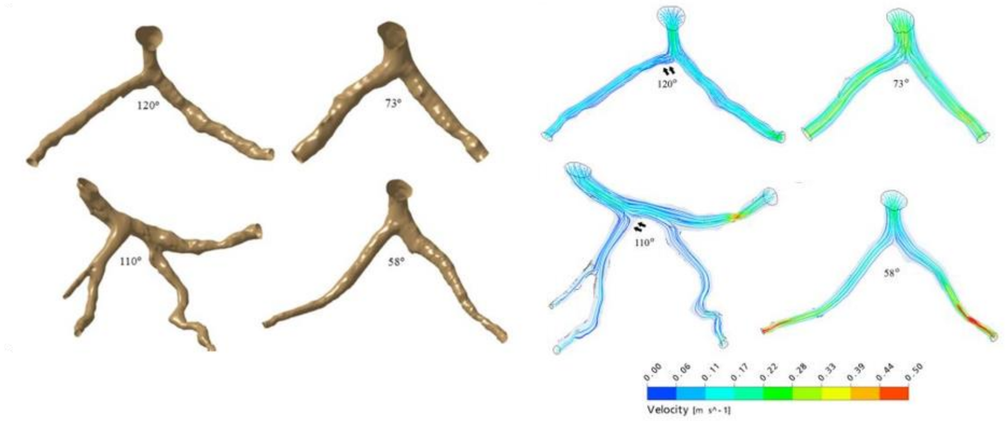

Figure 1.17. Idealized and patient-specific LCA models used by Chaichana *et al.*[41] , with their respective velocity fields calculated using CFD.

Campbell *et al.*[115] performed a three-dimensional numerical study using a model of the carotid artery constructed from MRI or CT images; Marshall *et al.*[116] demonstrated that coupling MRI measurements and CFD allows predicting the stenosis location.

CFD flow equations were used to numerically analyse the wall shear stress gradient distribution over the normal human LCA by Farmakis *et al.*[117]. Antiga *et al.*[118] developed a methodology for patient-specific model reconstruction, on geometric bifurcations, using CT angiography of carotid bifurcations from two patients affected by severe atherosclerotic plaques.

Ultimately, CFD simulations of flow conditions leading to atherosclerosis can allow the development of appropriate treatment solutions. Up to now, the use of stents is the most used treatment for atherosclerotic lesions[119-121]. However, the stent introduction alters the local hemodynamics and in combination with the arterial wall displacement can lead to its detachment and even to embolism[122]. Thus, the understanding of local hemodynamics before and after stent implementation is of vital importance in reducing future medical interventions as well as restenosis or occlusion that might occur unexpectedly.

Computational hemodynamics is in constant evolution, and is becoming increasingly more valuable, particularly when combined with experimental studies that validate its numerical results. In this thesis, CFD has been used extensively, in combination with experimental flow measurements, not only for the validation of the numerical code but also for predicting critical areas for the atherosclerosis development.

1.4 Thesis Outline

The work developed in this thesis aims to the better understanding of atherosclerosis by experimental and numerical studies of hemodynamics in the LCA, which includes the circumflex (LCx) and the anterior descending (LAD) arteries. For that, a multi-stage approach was developed to create and replicate 3D models of arteries. Figure 1.18 illustrates the **outline** of this PhD thesis. Two types of artery models were used: idealized geometries based on LCA morphological characteristics and patient-specific LCAs obtained from CT scan images.

The idealized geometrical LCA's were fully designed in SolidWorks® software and then converted to STL file. This file type enabled the use of rapid prototyping, by stereolithography, and also to generate a mesh to perform numerical simulations at the same experimental conditions. Once having the LCA prototype, a novel, low cost and fast fabrication process, described in **Chapter 2**, was developed to construct a flow phantom which allowed the use of optical experimental techniques such as µPIV and streak photography. The flow phantoms are made of poly(dimethylsiloxane) (PDMS) which is a suitable material for hemodynamic studies using optical techniques. The developed method, entitled as lost-sucrose casting, is described and tested against the commonly used lost-wax casting process.

The flow fabrication process described in **Chapter 2**, allowed in **Chapter 3**, to combine numerical (CFD) and experimental methods (µPIV and streak photography) to study the flow in a coronary bifurcation. The results show evidence of secondary flows in the bifurcations, such as helical flow and vortexes and allowed to validate the numerical models used. The secondary flows have been hinted previously in the literature, mainly in CFD studies, however our main contribution is the experimental observation and detailed characterization for understanding blood flow in the left coronary artery bifurcation. **Chapter 4** analyses how deviations from Murray's law influence indicators relevant to atherosclerosis development. CFD is used to evaluate the size of low wall shear stress regions and other indicators associated with atherosclerosis, in several shaped ideal LCA artery models.

The CT scan images of several patients were collected in a local cardiovascular diagnosis and intervention unit (*Hospital Center of Vila Nova de Gaia e Espinho*). The clinical data was processed in Mimics® software (C&V and FEA modules) from *Materialise*. The region of interest (LCA) was identified and after post-processing and segmentation a 3D voxel volume were converted into a STL (stereolithography) file. This allowed using real patient-specific LCA models to study its hemodynamics. Using the regions prone to atherosclerosis identified in **Chapter 4**, **Chapter 5** discloses a method to produce artificial realistic stenosis on realistic positions in the arteries. The method is based on the growth of the stenosis by a diffusional process and the size of the stenosis can be controlled by the Fourier number. The stenosis emerges in previously identified regions prone to atherosclerosis, i.e. regions of low wall shear stress.

Finally, the main goal was to develop and validate an integrated framework for patient-specific blood flow analysis in which it could be possible to get some insight about atherosclerosis in LCA. **Chapter 6** represents this achievement. In this chapter a complete hemodynamic study is presented, considering stenotic and non-stenotic LCA by *in vitro* experiments and also by CFD. Patient-specific and approximated idealized LCA models were used to study the influence of non-planarity in the hemodynamics. The methodology developed for creating irregular stenosis, in the previous chapter, was used to correlate flow patterns between healthy and stenotic arteries with some geometrical irregularities. Physiological conditions as pulsatile blood flow and non-Newtonian behaviour in patient-specific LCA were also evaluated by CFD. The results allowed identification of wall areas prone to atherosclerosis development and regions of high helical flow and also to draw important conclusions about generic arterial geometries.

The scientific contribution from this thesis is summed up in **Chapter 7**, where the main conclusions are disclosed, along with suggestions for future work.

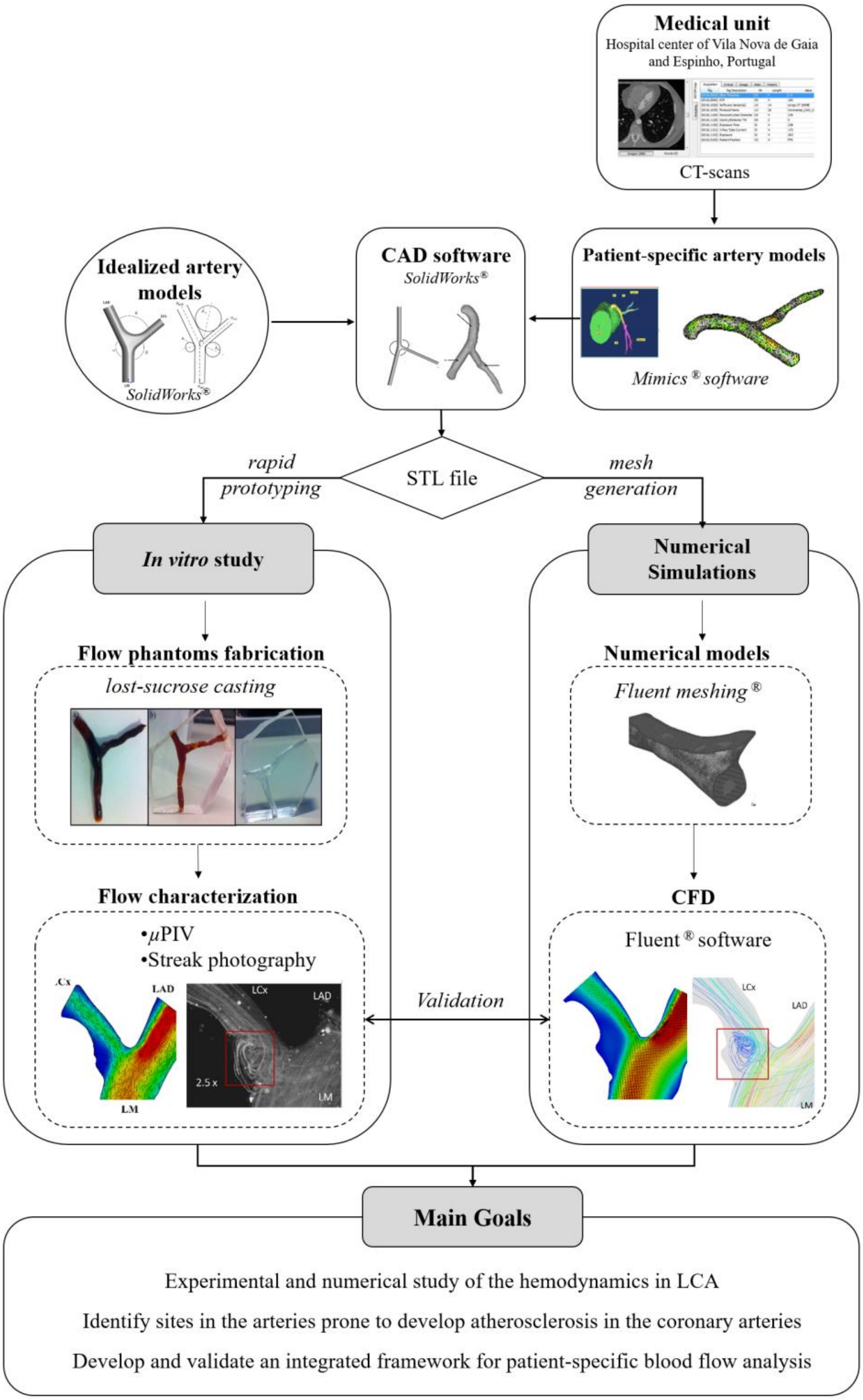

Figure 1.18. Schematic overview of the developed multi-stage approach used to accomplish the main goal of the thesis.

Notation

Symbols	**Definition**
D	Diameter
Δt	Period of time
Δx	Experimental average displacement of tracer particles
μ	Viscosity
R	Radius
ρ	Fluid density
$\dot{\gamma}$	Deformation rate - shear rate
τ_w	Wall shear stress
v	Velocity
NA	Numerical aperture
n	Refractive index
d_p	Size of tracer particles
δ_{z_m}	Thickness of the measurement "plane"
λ_0	Wavelength in a vacuum

References

1. DGS, *Portugal: Doenças Cérebro-Cardiovasculares em números - 2014*, 2014. p. 106-106.
2. Nichols, M., N. Townsend, P. Scarborough and M. Rayner, *Cardiovascular disease in Europe 2014: epidemiological update.* Eur Heart J, 2014. **35**(42): p. 2950-9.
3. Ballesteros, L.E. and L.M. Ramirez, *Morphological expression of the left coronary artery: a direct anatomical study.* Folia Morphol (Warsz), 2008. **67**(2): p. 135-42.
4. Cavalcanti, J.S., M. de Lucena Oliveira, A.V. Pais e Melo, Jr., *et al.*, *[Anatomic variations of the coronary arteries].* Arq Bras Cardiol, 1995. **65**(6): p. 489-92.
5. Loukas, M., C. Groat, R. Khangura, *et al.*, *The normal and abnormal anatomy of the coronary arteries.* Clin Anat, 2009. **22**(1): p. 114-28.
6. Wellnhofer, E., J. Osman, U. Kertzscher, *et al.*, *Flow simulation studies in coronary arteries--impact of side-branches.* Atherosclerosis, 2010. **213**(2): p. 475-481.
7. VanderLaan, P.A., C.A. Reardon and G.S. Getz, *Site specificity of atherosclerosis: site-selective responses to atherosclerotic modulators.* Arterioscler Thromb Vasc Biol, 2004. **24**(1): p. 12-22.
8. Ku, D.N., D.P. Giddens, C.K. Zarins and S. Glagov, *Pulsatile flow and atherosclerosis in the human carotid bifurcation. Positive correlation between plaque location and low oscillating shear stress.* Arteriosclerosis, 1985. **5**(3): p. 293-302.
9. Berk, B.C., *Atheroprotective signaling mechanisms activated by steady laminar flow in endothelial cells.* Circulation, 2008. **117**(8): p. 1082-9.
10. Texon, M., *The Hemodynamic Concept of Atherosclerosis.* Bull N Y Acad Med, 1960. **36**(4): p. 263-74.
11. Lee, R.T., A.J. Grodzinsky, E.H. Frank, *et al.*, *Structure-dependent dynamic mechanical behavior of fibrous caps from human atherosclerotic plaques.* Circulation, 1991. **83**(5): p. 1764-70.
12. Chatzizisis, Y.S., A.U. Coskun, M. Jonas, *et al.*, *Role of endothelial shear stress in the natural history of coronary atherosclerosis and vascular remodeling: molecular, cellular, and vascular behavior.* J Am Coll Cardiol, 2007. **49**(25): p. 2379-93.
13. Murray, C.J. and A.D. Lopez, *Mortality by cause for eight regions of the world: Global Burden of Disease Study.* Lancet, 1997. **349**(9061): p. 1269-76.
14. Waite, L. and J.M. Fine, *Applied Biofluid Mechanics*. 2007: McGraw-Hill Education.
15. Frohlich, J., M. Dobiasova, S. Lear and K.W. Lee, *The role of risk factors in the development of atherosclerosis.* Crit Rev Clin Lab Sci, 2001. **38**(5): p. 401-40.
16. Rader, D.J. and A. Daugherty, *Translating molecular discoveries into new therapies for atherosclerosis.* Nature, 2008. **451**(7181): p. 904-13.

17. Brunette, J., R. Mongrain, J. Laurier, *et al.*, *3D flow study in a mildly stenotic coronary artery phantom using a whole volume PIV method.* Med Eng Phys, 2008. **30**(9): p. 1193-200.
18. Ku, D.N., *Blood flow in arteries.* Annual Review of Fluid Mechanics, 1997. **29**: p. 399-434.
19. Berger, S.A. and L.D. Jou, *Flows in stenotic vessels.* Annual Review of Fluid Mechanics, 2000. **32**(1): p. 347-382.
20. Corbineau, H., H. Lebreton, T. Langanay, *et al.*, *Prospective evaluation of coronary arteries: influence on operative risk in coronary artery surgery.* Eur J Cardiothorac Surg, 1999. **16**(4): p. 429-34.
21. Debakey, M.E., G.M. Lawrie and D.H. Glaeser, *Patterns of Atherosclerosis and Their Surgical Significance.* Annals of Surgery, 1985. **201**(2): p. 115-131.
22. Caro, C.G., J.M. Fitz-Gerald and R.C. Schroter, *Atheroma and arterial wall shear. Observation, correlation and proposal of a shear dependent mass transfer mechanism for atherogenesis.* Proc R Soc Lond B Biol Sci, 1971. **177**(1046): p. 109-59.
23. Cavalcanti, S., *Hemodynamics of an artery with mild stenosis.* J Biomech, 1995. **28**(4): p. 387-99.
24. Gibson, C.M., L. Diaz, K. Kandarpa, *et al.*, *Relation of vessel wall shear stress to atherosclerosis progression in human coronary arteries.* Arterioscler Thromb, 1993. **13**(2): p. 310-5.
25. Baptista, C.A., L.J. DiDio and J.C. Prates, *Types of division of the left coronary artery and the ramus diagonalis of the human heart.* Jpn Heart J, 1991. **32**(3): p. 323-35.
26. Ortale, J.R., J.M. Filho, A. Maria, *et al.*, *Anatomy of the lateral , diagonal and anterosuperior arterial branches of the left ventricle of the human heart.* 2005. **20**(2): p. 149-158.
27. Reig, J. and M. Petit, *Main trunk of the left coronary artery: anatomic study of the parameters of clinical interest.* Clin Anat, 2004. **17**(1): p. 6-13.
28. Dombe, D.D., T. Anitha, S.D. Dombe and M.V. Ambiye, *Clinically relevant morphometric analysis of left coronary artery.* International Journal of Biological and Medical Research (IJBMR), 2012. **3**: p. 1327-1330.
29. Das, H., G. Das, D.C. Das and K. Talukdar, *A Study of Coronary Dominance in the Population of Assam.* Journal of Anatomical Society of India, 2010. **59**(2): p. 187-191.
30. Tomar, S., P.K. Sharma, P. Manik and A.K. Srivastava, *Normal and variant anatomy of Left Coronary Artery: 64-Slice Multi Detector Computed Tomography (MDCT) Coronary Angiographic Depiction in North Indian population.* International Journal of Scientific and Research Publications (IJSRP). **3**(8).
31. Angelini, P., *Coronary artery anomalies: an entity in search of an identity.* Circulation, 2007. **115**(10): p. 1296-305.
32. MacAlpin, R.N., A.S. Abbasi, J.H. Grollman, Jr. and L. Eber, *Human coronary artery size during life. A cinearteriographic study.* Radiology, 1973. **108**(3): p. 567-76.

33. Gazetopoulos, N., P.J. Ioannidis, A. Marselos, *et al.*, *Length of main left coronary artery in relation to atherosclerosis of its branches. A coronary arteriographic study.* Br Heart J, 1976. **38**(2): p. 180-5.
34. Fox, C., M.J. Davies and M.M. Webb-Peploe, *Length of left main coronary artery.* Br Heart J, 1973. **35**(8): p. 796-8.
35. Kalpana, R., *A study on principal branches of coronary artery in humans.* J Anat. Soc. India 52(2) 137-140 (2003), 2003.
36. Pflederer, T., J. Ludwig, D. Ropers, *et al.*, *Measurement of coronary artery bifurcation angles by multidetector computed tomography.* Invest Radiol, 2006. **41**(11): p. 793-8.
37. Kawasaki, T., H. Koga, T. Serikawa, *et al.*, *The bifurcation study using 64 multislice computed tomography.* Catheter Cardiovasc Interv, 2009. **73**(5): p. 653-8.
38. Sun, Z. and Y. Cao, *Multislice CT angiography assessment of left coronary artery: correlation between bifurcation angle and dimensions and development of coronary artery disease.* Eur J Radiol, 2011. **79**(2): p. e90-5.
39. Rodriguez-Granillo, G.A., M.A. Rosales, E. Degrossi, *et al.*, *Multislice CT coronary angiography for the detection of burden, morphology and distribution of atherosclerotic plaques in the left main bifurcation.* Int J Cardiovasc Imaging, 2007. **23**(3): p. 389-92.
40. Papadopoulou, S.L., S. Brugaletta, H.M. Garcia-Garcia, *et al.*, *Assessment of atherosclerotic plaques at coronary bifurcations with multidetector computed tomography angiography and intravascular ultrasound-virtual histology.* Eur Heart J Cardiovasc Imaging, 2012. **13**(8): p. 635-42.
41. Chaichana, T., Z. Sun and J. Jewkes, *Computation of hemodynamics in the left coronary artery with variable angulations.* J Biomech, 2011. **44**(10): p. 1869-78.
42. Kimura, B.J., R.J. Russo, V. Bhargava, *et al.*, *Atheroma morphology and distribution in proximal left anterior descending coronary artery: in vivo observations.* J Am Coll Cardiol, 1996. **27**(4): p. 825-31.
43. Baptista, C.A., L.J. DiDio and G. Teofilovski-Parapid, *Variation in length and termination of the ramus circumflexus of the human left coronary artery.* Anat Anz, 1990. **171**(4): p. 247-53.
44. Reig, J., A. Jornet and M. Petit, *Patterns of the coronary artery irrigation in the left ventricle.* Surg Radiol Anat, 1993. **15**(4): p. 309-14.
45. Westerhof, N., N. Stergiopulos and M.I.M. Noble, *Snapshots of Hemodynamics: An Aid for Clinical Research and Graduate Education*. 2010: Springer US.
46. Rindfleisch, E. and W.C. Kloman, *A Textbook of Pathological Histology : An Introduction to the Study of Pathological Anatomy (1871)*. 1871, Whitefish MT, United States: Kessinger Publishing.
47. Malek, A.M., S.L. Alper and S. Izumo, *Hemodynamic shear stress and its role in atherosclerosis.* JAMA, 1999. **282**(21): p. 2035-42.
48. Grottum, P., A. Svindland and L. Walloe, *Localization of atherosclerotic lesions in the bifurcation of the main left coronary artery.* Atherosclerosis, 1983. **47**(1): p. 55-62.

49. Chiu, J.J. and S. Chien, *Effects of disturbed flow on vascular endothelium: pathophysiological basis and clinical perspectives.* Physiol Rev, 2011. **91**(1): p. 327-87.
50. White, F.M., *Fluid Mechanics*. Vol. 6th Ed. 2008, Boston: McGraw-Hill.
51. Pedley, T.J., *The Fluid Mechanics of Large Blood Vessels*. 1980: Cambridge University Press.
52. Robertson, A., A. Sequeira and M. Kameneva, *Hemorheology*, in *Hemodynamical Flows*. 2008, Birkhäuser Basel. p. 63-120.
53. Gijsen, F.J.H., E. Allanic, F.N. van de Vosse and J.D. Janssen, *The influence of the non-Newtonian properties of blood on the flow in large arteries: unsteady flow in a 90° curved tube.* Journal of Biomechanics, 1999. **32**(7): p. 705-713.
54. Brust, M., *Rheological Properties of Red Blood Cells*. 2013.
55. Brust, M., O. Aouane, M. Thiebaud, *et al.*, *The plasma protein fibrinogen stabilizes clusters of red blood cells in microcapillary flows.* Sci Rep, 2014. **4**: p. 4348.
56. Brust, M., C. Schaefer, R. Doerr, *et al.*, *Rheology of human blood plasma: viscoelastic versus Newtonian behavior.* Phys Rev Lett, 2013. **110**(7): p. 078305.
57. Sousa, P.C., J. Carneiro, R. Vaz, *et al.*, *Shear viscosity and nonlinear behavior of whole blood under large amplitude oscillatory shear.* Biorheology, 2013. **50**(5-6): p. 269-82.
58. Wagner, C., P. Steffen and S. Svetina, *Aggregation of red blood cells: From rouleaux to clot formation.* Comptes Rendus Physique, 2013. **14**(6): p. 459-469.
59. Kim, Y., K. Kim and Y. Park, *Measurement Techniques for Red Blood Cell Deformability: Recent Advances*. Blood Cell - An Overview of Studies in Hematology. 2012.
60. Koeppen, B.M. and B.A. Stanton, *Berne & Levy Physiology, Updated Edition*. 2009: Elsevier Health Sciences.
61. Chien, S., *Mechanotransduction and endothelial cell homeostasis: the wisdom of the cell.* Am J Physiol Heart Circ Physiol, 2007. **292**(3): p. H1209-24.
62. Gimbrone, M.A., Jr., J.N. Topper, T. Nagel, *et al.*, *Endothelial dysfunction, hemodynamic forces, and atherogenesis.* Ann N Y Acad Sci, 2000. **902**: p. 230-9; discussion 239-40.
63. Stone, P.H., A.U. Coskun, S. Kinlay, *et al.*, *Effect of endothelial shear stress on the progression of coronary artery disease, vascular remodeling, and in-stent restenosis in humans: in vivo 6-month follow-up study.* Circulation, 2003. **108**(4): p. 438-44.
64. Back, M., T.C. Gasser, J.B. Michel and G. Caligiuri, *Biomechanical factors in the biology of aortic wall and aortic valve diseases.* Cardiovasc Res, 2013. **99**(2): p. 232-41.
65. Chatzizisis, Y.S., M. Jonas, A.U. Coskun, *et al.*, *Prediction of the localization of high-risk coronary atherosclerotic plaques on the basis of low endothelial shear stress: an intravascular ultrasound and histopathology natural history study.* Circulation, 2008. **117**(8): p. 993-1002.

66. Murray, C.D., *The physiologtcal principle of minimom work I The vascular system and the cost of blood volume.* Proceedings of the National Academy of Sciences of the United States of America, 1926. **12**: p. 207-214.
67. Gafiychuk, V.V. and I.A. Lubashevsky, *On the principles of the vascular network branching.* J Theor Biol, 2001. **212**(1): p. 1-9.
68. Schoenenberger, A.W., N. Urbanek, S. Toggweiler, *et al.*, *Deviation from Murray's law is associated with a higher degree of calcification in coronary bifurcations.* Atherosclerosis, 2012. **221**(1): p. 124-30.
69. Rogers, E.W., H. Feigenbaum, A.E. Weyman, *et al.*, *Evaluation of left coronary artery anatomy in vitro by cross-sectional echocardiography.* Circulation, 1980. **62**(4): p. 782-7.
70. Williams, M.J., R.A. Stewart, C.J. Low and G.T. Wilkins, *Assessment of the mechanical properties of coronary arteries using intravascular ultrasound: an in vivo study.* Int J Card Imaging, 1999. **15**(4): p. 287-94.
71. Kimura, B.J., R.J. Russo, M.B. McDaniel, *et al.*, *Atheroma Morphology and Distribution in Proximal Left Anterior Descending Coronary Mery : In Vivo Observations.* **27**(4).
72. Fayad, Z.A., V. Fuster, J.T. Fallon, *et al.*, *Noninvasive In Vivo Human Coronary Artery Lumen and Wall Imaging Using Black-Blood Magnetic Resonance Imaging.* Circulation, 2000. **102**(5): p. 506-510.
73. Fayad, Z. and V. Fuster, *Clinical imaging of the high-risk or vulnerable atherosclerotic plaque.* Circulation Research, 2001. **89**.
74. G., B. and H.J. W., *Detailed Characteristics of the Flow of Blood In Vitro.* Transactions of the Society of Rheology, 1963. **7**(1): p. 209-230.
75. Einav, S., H.J. Berman, R.L. Fuhro, *et al.*, *Measurement of velocity profiles of red blood cells in the microcirculation by laser doppler anemometry (LDA).* Biorheology, 1975. **12**(3-4): p. 207-10.
76. Adrian, R.J., *Particle-Imaging Techniques for Experimental Fluid Mechanics.* Annual Review of Fluid Mechanics, 1991. **23**(1): p. 261-304.
77. Zhang, J.M., L.P. Chua, D.N. Ghista, *et al.*, *Validation of numerical simulation with PIV measurements for two anastomosis models.* Med Eng Phys, 2008. **30**(2): p. 226-47.
78. Lima, R., S. Wada, K. Tsubota and T. Yamaguchi, *Confocal micro-PIV measurements of three-dimensional profiles of cell suspension flow in a square microchannel.* Measurement Science and Technology, 2006. **17**(4): p. 797-808.
79. Sugii, Y., R. Okuda, K. Okamoto and H. Madarame, *Velocity measurement of both red blood cells and plasma of in vitro blood flow using high-speed micro PIV technique.* Measurement Science and Technology, 2005. **16**(5): p. 1126-1130.
80. A.;, T.C. and D.M. T., *Experimental and computacional methods in cardiovascular fluid mechanics.* Annual Review of Fluid Mechanics, 2004. **36**(1): p. 197-231.
81. Wereley, S.T. and C.D. Meinhart, *Recent Advances in Micro-Particle Image Velocimetry.* Annual Review of Fluid Mechanics, 2010. **42**(1): p. 557-576.

82. Lindken, R., M. Rossi, S. Grosse and J. Westerweel, *Micro-Particle Image Velocimetry (microPIV): recent developments, applications, and guidelines.* Lab Chip, 2009. **9**(17): p. 2551-67.
83. Garcia, V., R. Dias and R. Lima, *In Vitro Blood Flow Behaviour in Microchannels with Simple and Complex Geometries.* 2002.
84. Christopher, J.B., G.O. Michael and A.D. Gorby, *Validation of an analytical solution for depth of correlation in microscopic particle image velocimetry.* Measurement Science and Technology, 2004. **15**(2): p. 318.
85. Pommer, M.S. and S.B.M.E. University of California, *Fluid Mechanic Manipulations on Cells*. 2007: University of California, Santa Barbara.
86. Yang, C.T. and H.S. Chuang, *Measurement of a microchamber flow by using a hybrid multiplexing holographic velocimetry*. Experiments in Fluids, 2005. **39**(2): p. 385-396.
87. Prasad, A.K., *Stereoscopic particle image velocimetry.* 2000. **29**(February).
88. Lindken, R., J. Westerweel and B. Wieneke, *Stereoscopic micro particle image velocimetry.* Experiments in Fluids, 2006. **41**(2): p. 161-171.
89. Burgmann, S., S. Grosse, W. Schroder, *et al.*, *A refractive index-matched facility for fluid-structure interaction studies of pulsatile and oscillating flow in elastic vessels of adjustable compliance.* Experiments in Fluids, 2009. **47**(4-5): p. 865-881.
90. de Zelicourt, D., K. Pekkan, H. Kitajima, *et al.*, *Single-step stereolithography of complex anatomical models for optical flow measurements.* J Biomech Eng, 2005. **127**(1): p. 204-7.
91. de Zelicourt, D.A., K. Pekkan, L. Wills, *et al.*, *In vitro flow analysis of a patient-specific intraatrial total cavopulmonary connection.* Ann Thorac Surg, 2005. **79**(6): p. 2094-102.
92. Sousa, P.C., F.T. Pinho, M.S.N. Oliveira and M.A. Alves, *Efficient microfluidic rectifiers for viscoelastic fluid flow.* Journal of Non-Newtonian Fluid Mechanics, 2010. **165**(11-12): p. 652-671.
93. Geoghegan, P.H., N.A. Buchmann, C.J.T. Spence, *et al.*, *Fabrication of rigid and flexible refractive-index-matched flow phantoms for flow visualisation and optical flow measurements.* Experiments in Fluids, 2012. **52**(5): p. 1331-1347.
94. Irwan, R., I.K. Russel and P.E. Sijens, *Fast 3D coronary artery contrast-enhanced magnetic resonance angiography with magnetization transfer contrast, fat suppression and parallel imaging as applied on an anthropomorphic moving heart phantom.* Magn Reson Imaging, 2006. **24**(7): p. 895-902.
95. Kabinejadian, F., F. Cui, Z. Zhang, *et al.*, *A novel carotid covered stent design: in vitro evaluation of performance and influence on the blood flow regime at the carotid artery bifurcation.* Ann Biomed Eng, 2013. **41**(9): p. 1990-2002.
96. Buchmann, N.A., C. Atkinson, M.C. Jeremy and J. Soria, *Tomographic particle image velocimetry investigation of the flow in a modeled human carotid artery bifurcation*. Experiments in Fluids, 2011. **50**(4): p. 1131-1151.
97. Bale-Glickman, J., K. Selby, D. Saloner and O. Savas, *Experimental flow studies in exact-replica phantoms of atherosclerotic carotid bifurcations under steady input conditions.* J Biomech Eng, 2003. **125**(1): p. 38-48.

98. Vétel, J., A. Garon and D. Pelletier, *Lagrangian coherent structures in the human carotid artery bifurcation.* Experiments in Fluids, 2009. **46**(6): p. 1067-1079.

99. Gaillard, E., D. Garcia, L. Kadem, *et al.*, *Impact of aortic valve stenosis on left coronary artery flow: An in vitro study*, in *4th European Conference of the International Federation for Medical and Biological Engineering: ECIFMBE 2008 23–27 November 2008 Antwerp, Belgium*, J. Sloten, *et al.*, Editors. 2009, Springer Berlin Heidelberg: Berlin, Heidelberg. p. 1922-1925.

100. Kabinejadian, F., D.N. Ghista, B. Su, *et al.*, *In vitro measurements of velocity and wall shear stress in a novel sequential anastomotic graft design model under pulsatile flow conditions.* Med Eng Phys, 2014. **36**(10): p. 1233-45.

101. Kabinejadian, F., L.P. Chua, D.N. Ghista, *et al.*, *A novel coronary artery bypass graft design of sequential anastomoses.* Ann Biomed Eng, 2010. **38**(10): p. 3135-50.

102. Kabinejadian, F. and D.N. Ghista, *Compliant model of a coupled sequential coronary arterial bypass graft: effects of vessel wall elasticity and non-Newtonian rheology on blood flow regime and hemodynamic parameters distribution.* Med Eng Phys, 2012. **34**(7): p. 860-72.

103. Tu, J., K. Inthavong and K.K.L. Wong, *Computational Hemodynamics – Theory, Modelling and Applications*. 2015: Springer Netherlands.

104. Perktold, K. and G. Rappitsch, *Computer simulation of local blood flow and vessel mechanics in a compliant carotid artery bifurcation model.* J Biomech, 1995. **28**(7): p. 845-56.

105. Steinman, D.A., R. Frayne, X.D. Zhang, *et al.*, *MR measurement and numerical simulation of steady flow in an end-to-side anastomosis model.* J Biomech, 1996. **29**(4): p. 537-42.

106. Lee, D. and J.Y. Chen, *Pulsatile Flow Fields in a Model of Abdominal Aorta with Its Peripheral Branches.* Biomedical Engineering: Applications, Basis and Communications, 2003. **15**(05): p. 170-178.

107. Ferziger, J.H. and M. Perić, *Computational Methods for Fluid Dynamics*. 1996: Springer.

108. Fletcher, C., *Computational Techniques for Fluid Dynamics 1*. 1991: Springer Berlin Heidelberg.

109. Taylor, C.A. and C.A. Figueroa, *Patient-specific Modeling of Cardiovascular Mechanics.* Annual review of biomedical engineering, 2009. **11**: p. 109-134.

110. Shanmugavelayudam, S.K., D.A. Rubenstein and W. Yin, *Effect of Geometrical Assumptions on Numerical Modeling of Coronary Blood Flow Under Normal and Disease Conditions.* Journal of Biomechanical Engineering, 2010. **132**(6): p. 061004-061004.

111. Nosovitsky, V.A., O.J. Ilegbusi, J. Jiang, *et al.*, *Effects of Curvature and Stenosis-Like Narrowing on Wall Shear Stress in a Coronary Artery Model with Phasic Flow.* Computers and Biomedical Research, 1997. **30**(1): p. 61-82.

112. Calcagno, C., S. Ramachandran, D. Izquierdo-Garcia, *et al.*, *The complementary roles of dynamic contrast-enhanced MRI and 18F-fluorodeoxyglucose PET/CT for imaging of carotid atherosclerosis.* Eur J Nucl Med Mol Imaging, 2013. **40**(12): p. 1884-93.

113. Sanz, J. and Z.A. Fayad, *Imaging of atherosclerotic cardiovascular disease.* Nature, 2008. **451**(7181): p. 953-7.
114. Silvera, S.S., H.E. Aidi, J.H. Rudd, *et al.*, *Multimodality imaging of atherosclerotic plaque activity and composition using FDG-PET/CT and MRI in carotid and femoral arteries.* Atherosclerosis, 2009. **207**(1): p. 139-43.
115. Campbell, I.C., J. Ries, S.S. Dhawan, *et al.*, *Effect of inlet velocity profiles on patient-specific computational fluid dynamics simulations of the carotid bifurcation.* J Biomech Eng, 2012. **134**(5): p. 051001.
116. Marshall, I., S. Zhao, P. Papathanasopoulou, *et al.*, *MRI and CFD studies of pulsatile flow in healthy and stenosed carotid bifurcation models.* J Biomech, 2004. **37**(5): p. 679-87.
117. Farmakis, T.M., J.V. Soulis, G.D. Giannoglou, *et al.*, *Wall shear stress gradient topography in the normal left coronary arterial tree: possible implications for atherogenesis.* Curr Med Res Opin, 2004. **20**(5): p. 587-96.
118. Antiga, L., B. Ene-Iordache, L. Caverni, *et al.*, *Geometric reconstruction for computational mesh generation of arterial bifurcations from CT angiography.* Comput Med Imaging Graph, 2002. **26**(4): p. 227-35.
119. Barakat, A.I. and E.T. Cheng. *Numerical simulation of fluid mechanical disturbance induced by intravascular stents*. in *Proceedings of the 11th International Conference on Mechanics in Medicine and Biology*. 2000.
120. Chen, Z., Y. Fan, X. Deng and Z. Xu, *Swirling flow can suppress flow disturbances in endovascular stents: a numerical study.* ASAIO J, 2009. **55**(6): p. 543-9.
121. Chiastra, C., S. Morlacchi, D. Gallo, *et al.*, *Computational fluid dynamic simulations of image-based stented coronary bifurcation models.* J R Soc Interface, 2013. **10**(84): p. 20130193.
122. Richter, G.M., J.C. Palmaz, G. Noeldge and F. Tio, *Relationship between blood flow, thrombus, and neointima in stents.* J Vasc Interv Radiol, 1999. **10**(5): p. 598-604.

2

Chapter

> *"Everything is theoretically impossible, until it is done."*
>
> **— Robert A. Heinlein**

Fabrication of 3D mili-scale channels for hemodynamics studies[*]

---

[*] E. Doutel, J. Carneiro, MSN. Oliveira, JBLM. Campos, JM. Miranda
Fabrication of 3D mili-scale channels for hemodynamics studies, **Journal of Mechanics in Medicine and Biology**, 10.1142/s0219519415500049, 2015.

2

Fabrication of 3D mili-scale channels for hemodynamic studies

Abstract

3D mili-scale channel representing simplified anatomical models of blood vessels were constructed in poly(dimethylsiloxane) (PDMS). The objective was to obtain a sequential method to fabricate transparent PDMS models from a mold produced by rapid prototyping. For this purpose, two types of casting methods were compared, a known lost-wax casting method and a casting method using sucrose. The channels fabricated by both casting methods were analyzed by Optical Microscopy, Scanning Electron Microscopy (SEM), and Energy Dispersive X-ray Spectroscopy (EDS). The lost-wax method is not ideal since the channels become contaminated during the removal process. The models produced with the lost-sucrose casting method exhibit much better optical characteristics. These models are transparent with no visible contamination, since the removing process is done by dissolution at room temperature rather than melting. They allow for good optical access for flow visualization and measurement of the velocity field by micro-Particle Image Velocimetry (μPIV). The channels fabricated by the lost-sucrose casting method were shown to be suitable for future hemodynamic studies using optical techniques.

2.1. Introduction

Cardiovascular diseases are presently one of the leading causes of death in humans[1]. From clinical practice, it is known that specific sites in the human circulatory system are particularly sensitive to the development of cardiovascular diseases[2]. Local hemodynamics is crucial to understand the development and the complications derived from medical conditions like atherosclerosis[3, 4], aneurysms[5-8] and stenoses[9-11]. Some medical interventions, such as stent implantation and bypasses, can disturb regular hemodynamics[12-14] and their impact on fluid flow must be understood.

Fluid dynamics studies have been used to advance the understanding of cardiovascular diseases. For example, Shahcheraghi *et al.*[15] studied numerically three-dimensional and pulsatile blood flow in a human aortic arch and its three major branches, suggesting that the preferential development of lesions is in regions of extreme wall shear stresses and pressure. These results are in agreement with the numerical data of Kobayashi and Pereira[16]. Barakat and Cheng[17] presented a numerical simulation of fluid disturbance induced by intravascular stents. They demonstrated the existence of a region of flow separation immediately downstream the implemented stent.

The study of fluid flow of the vascular system requires a combination of numerical and *in vivo* and *in vitro* experimental studies. *In vivo* studies are only possible in very limited situations due to practical and ethical reasons. Numerical studies always require experimental validation due to the importance of turbulence, non-newtonian effects and, for microvessels, the particulate nature of blood. The velocity of blood flow *in vitro* has been studied using several techniques, including: video microscopy and image analysis[18], laser-Doppler anemometry[19] and particle-based methods such as Particle Tracking Velocimetry (PTV)[20], Particle Image Velocimetry (PIV)[21] and Micro-Particle Image Velocimetry (µPIV)[22]. µPIV was applied to the study of microcirculation[22-24], flows in vessels with less than 250 µm. Confocal µPIV[23] has become accepted as a reliable method for measuring velocity profiles of biological flows in vessels of small diameter with high spatial resolution. Lima *et al.*[24] demonstrated the ability of confocal µPIV to measure both homogeneous and non-homogeneous fluids, using red blood cell suspensions. *In vitro* studies require the construction of a model of the blood vessel under study. The model must be transparent in the wavelength of the light used and its half thickness must be smaller than the focal distance of the objective used.

Several researchers have been working on patient-specific *in vitro* techniques that allow experimental studies of blood flow in realistic configurations[3, 25-27]. Models of complex geometries are typically constructed by direct rapid prototyping from a 3D computational representation of the blood vessel[26, 27] or by casting in a mold produced by rapid prototyping[3].

There are several studies concerning the use of different sacrificial template materials for the fabrication of *in vitro* models including wax[28-30], cerrolow[31-33] (metallic alloy with a low temperature melting point– 320 to 352 K), isomalt[31] (sugar based material - 418 to 423 K melting point) gelatine, chocolate and plaster powder[34]. Sucrose[35] has been used as a sacrificial template material to fabricate 3D networks of cylindrical microchannels. The most commonly reported materials are wax and cerrolow, and in these cases the sacrificial mold is removed from the final mold by melting the material at high temperatures.

The major limitation of wax is that it is a very fragile material and so small diameter channels (less than 2 mm) cannot be produced[29, 31]. While most of the experimental work in this field has been done with vessel structures larger than 5 mm and microvessels smaller than 300 µm, there are very few studies on vessels with diameters in the range between 300 µm and 5 mm and fabrication techniques for this intermediate range would be very useful. Cerrolow has no size limitation, but is well known to leave residues in the vessels wall after melting[31, 33] which is not acceptable for quantitative measurement when optical access is required.

In this chapter, a multi-stage approach was developed to create and replicate simplified 3D models of arteries in the millimeter-scale range, with or without stenosis, using melted sucrose as casting material. The main difference relatively to other common casting methods and materials is that the removal process in which the sacrificial mold is destroyed is carried out by dissolving the sucrose in water at room temperature, rather than melting, which allows to produce transparent non-contaminated PDMS channels suitable for flow visualizations and optical flow measurements.

These studies were performed to ensure that the fabricated channels are suitable for hemodynamics studies, *i. e.*, are able to mimic realistically the geometry of an artery, are easily replicated and reproducible and exhibit ideal optical properties and no contamination.

This chapter is organized as follows. The fabrication process is described and discussed in detail in Section 2.2. In Section 2.3, the PDMS transparent channels are analyzed by Optical Microscopy, Scanning Electron Microscopy (SEM), and Energy Dispersive X-ray Spectroscopy (EDS). Flow dynamics studies conducted using flow visualization and µPIV techniques are presented in Section 2.4. We finalize with some concluding remarks in Section 2.5.

2.2. Fabrication of *in vitro* models

An overview of the fabrication process is illustrated Figure 2.1.

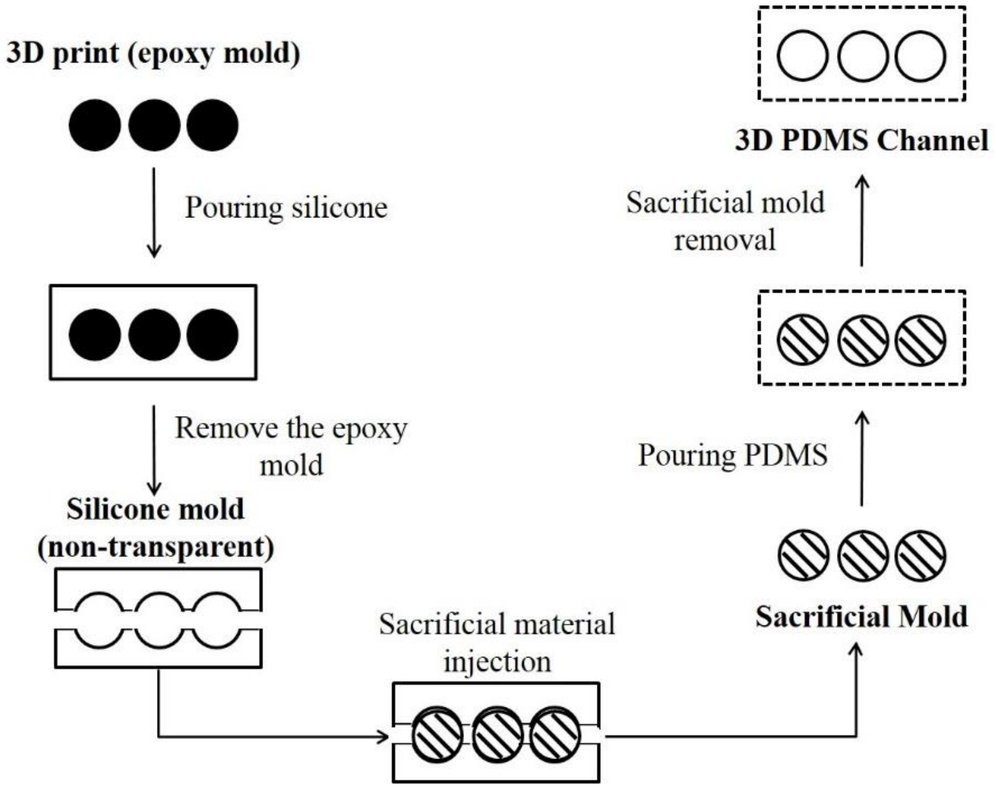

Figure 2.1. Schematic diagram of the fabrication process.

The geometry is created in Computer-aided design (CAD) and a first mold made of an epoxy-resin is then constructed by rapid prototyping by stereolithography. Afterwards, a negative version of the mold is fabricated in non-transparent silicone. This silicone mold is used to cast a sacrificial mold using materials such as wax and melted sucrose. The sacrificial mold is destroyed during the final step of fabrication, but the non-transparent silicone mold can be repeatedly used to replicate anatomical models maintaining identical geometry characteristics.

2.2.1. CAD and channel design

CAD models of the desired channels were designed using SolidWorks® software (SolidWorks, Concord, MA, USA). The models were then converted into stereolithography (STL) format, which is widely used for rapid prototyping and computer-aided design.

Based on the study of Chaichana *et al.*[36] we used as reference the dimensions of the left coronary artery (LCA). We started with the simple case of a straight channel with two different diameters, *d*, 2.5 mm and 3.5 mm, and evolved to a more complex case of a bifurcation channel, with one inlet (main branch) and two outlets (daughter branches); a 90º angle was considered between the two daughter branches of the channel. To achieve an approximated geometrical representation of the blood vessels, cross-sections of the daughter branches were made elliptical. These three CAD models are illustrated Figure 2.2.

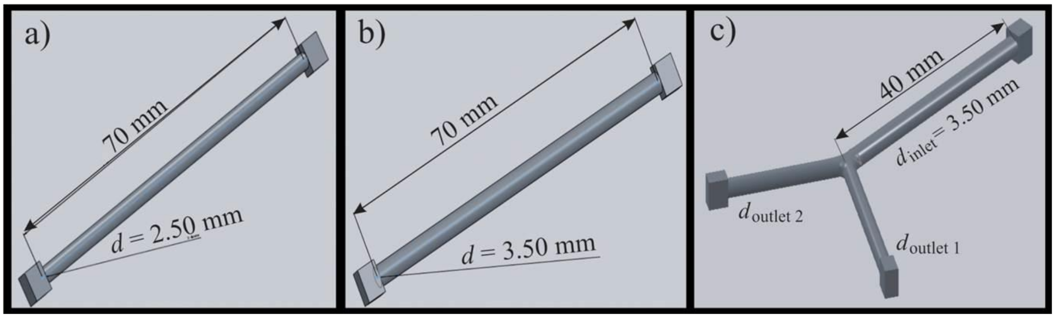

Figure 2.2. CAD models used in the rapid prototyping by stereolithography: a) straight channel with *d*=2.5 mm, b) straight channel with *d*=3.5 mm and c) bifurcated channel with a main branch diameter of 3.5 mm.

Parallelepiped blocks were introduced in the extremities of the designed CAD models. By adjusting the height of the blocks, the wall thickness of the final model can be controlled. A maximum thickness of 1 mm was considered in order to get a suitable focal distance to the middle plane of the channels. This technique can also be utile to assure a co-planar system, *i.e.*, a system where the middle planes of all the branches are coincident. In this case, the size of the parallelepiped blocks must compensate the differences in the diameters of the branches.

In addition, we also considered the inclusion of a stenosis, which can be located in different positions in the vessels and have different degrees of occlusion.

2.2.2. Rapid prototyping

The CAD models, shown in Figure 2.2, were used to construct epoxy resin molds by rapid prototyping using solid state stereolithography. The prototyping equipment used was an Accura® 55Plastic from 3D Systems® with a precision of 0.15 mm. The prototypes, shown in Figure 2.3a) and b), were used to construct a second mold in non-transparent silicone, Figure 2.3c), at SOLIDtech, Lda.

This second mold can be used to cast a negative sacrificial mold, using materials such as wax and sucrose.

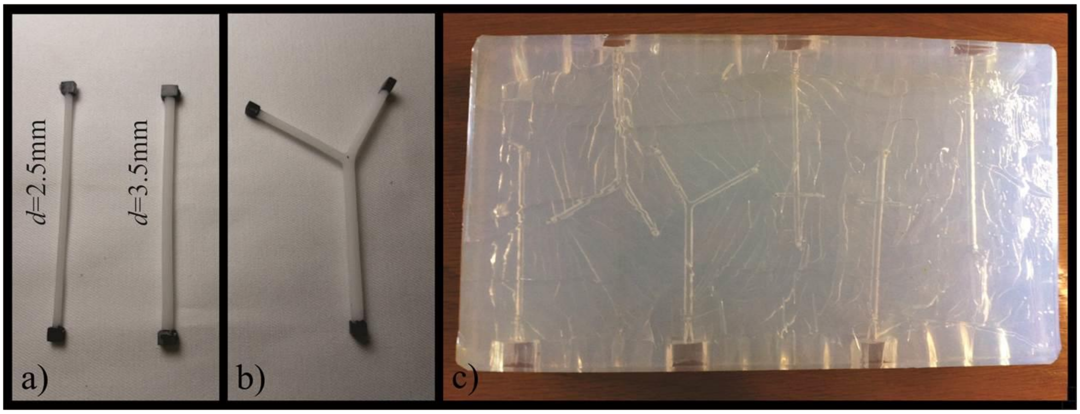

Figure 2.3. Epoxy resin mold made by stereolithography of: a) two straight channels, b) bifurcated channel and c) non-transparent silicone mold containing the various geometries.

2.2.3. Sacrificial mold and PDMS channel

Two alternative materials were considered for fabricating the sacrificial molds: wax and sucrose.

Lost-wax casting method

The lost-wax casting method is performed by injecting melted wax (353 K) into the silicone mold. In the present work, paraffin was used. The wax mold is taken from the non-transparent silicone and placed in a petri dish (Figure 2.4 a). To fabricate the final channels in transparent and elastic material, PDMS is mixed with curing agent in a 5:1 ratio. A Thinky Mixer® ARE-250 was used to prepare the PDMS/curing agent mixture. The mixture is then put into a desiccator connected to a vacuum pump to remove air bubbles. The PDMS is then transferred to the petri dish containing the sacrificial mold and cured at room temperature for 24h (Figure 2.4 b). The wax is removed by melting at 353 K for 20 min to obtain the final PDMS channels (Figure 2.4 c).

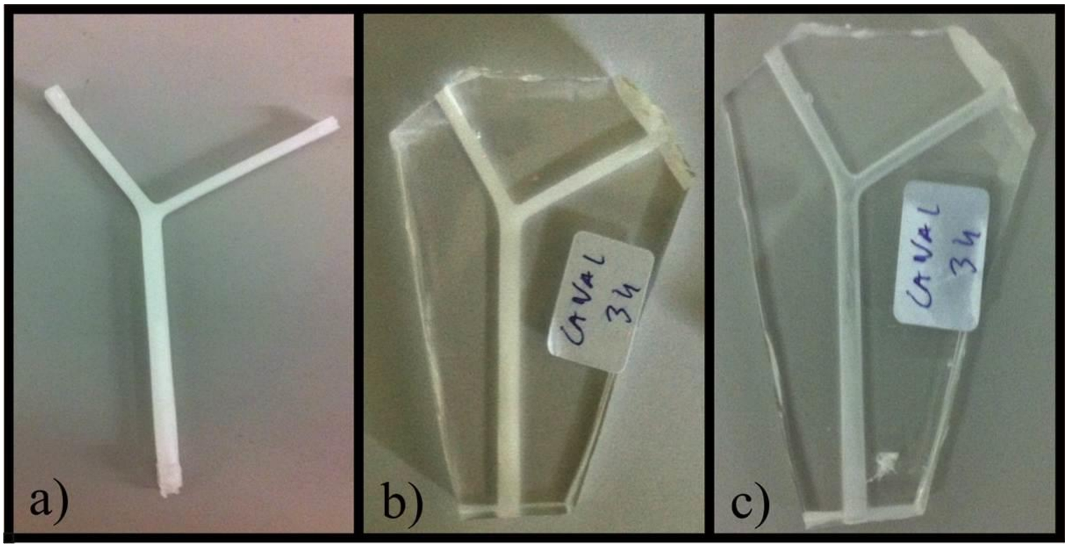

Figure 2.4. Fabrication technique of the final PDMS channels using the lost-wax casting method: a) negative mold made of paraffin, b) PDMS channel after the curing stage and before the wax removal step by melting and c) final 3D PDMS channel.

Lost-sucrose casting method

The fabrication procedure using sucrose is illustrated in Figure 2.5. The sucrose is caramelized at 433 K and injected, at this temperature, into the non-transparent silicone mold. Similarly to the lost-wax procedure, the final PDMS mili-scale channels are cured under the same experimental conditions. After the curing step the sucrose is removed by dissolution, in water at room temperature.

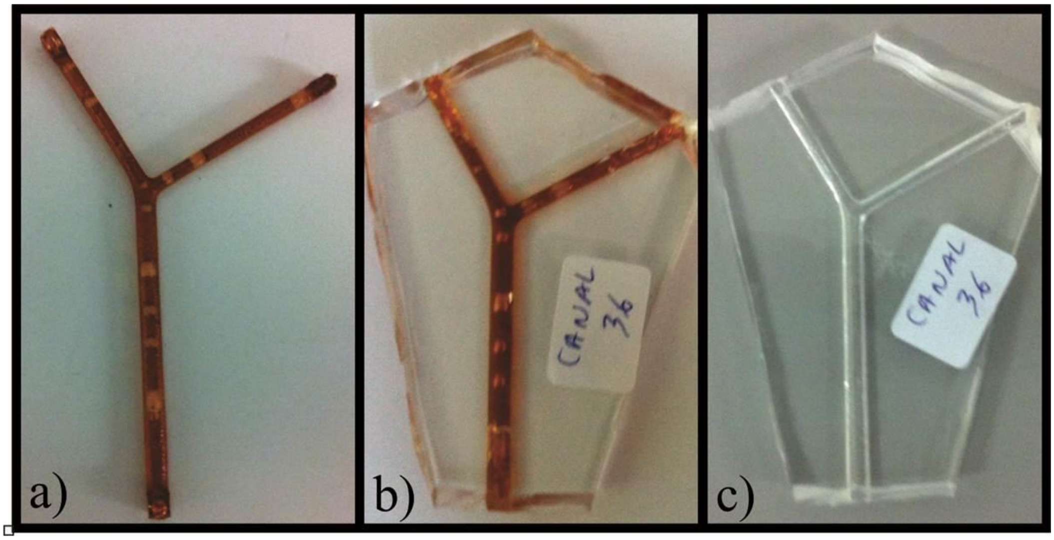

Figure 2.5. Fabrication technique of the final PDMS channels using the lost-sucrose casting method: a) negative mold made of sucrose, b) PDMS channel after the curing stage before the sucrose removal step by dissolution and c) final 3D PDMS channel.

2.2.4. Stenosis fabrication and its implementation in the channels

For the fabrication of channels with stenosis, a new approach was developed. The stenosis is independently fabricated and inserted into the transparent channel *a posteriori*. The procedure is illustrated in Figure 2.6. In Figure 2.6a) four different CAD models of stenoses are represented: with 25%, 50% and 75% bilateral occlusion and a 50% unilateral occlusion. Those CAD models (Figure 2.6 a) were used to fabricate the epoxy resin molds by rapid prototyping (Figure 2.6 b) and the non-transparent silicone mold containing different types of stenoses (Figure 2.6 c). The sacrificial mold is, in fact, the negative of the required stenosis, and is inserted into the main 3D PDMS transparent mili-scale channel in the exact position where the stenosis is to be created (Figure 2.6 d). After being positioned in the desired location liquid PDMS is injected using a syringe in the free surrounding space created between the negative mold of the stenosis and the channel walls (Figure 2.6 e). The PDMS is cured at room temperature and the sucrose negative mold is then removed by dissolving it in distilled water (Figure 2.6 f), yielding the final channels with the desired stenosis. In Figure 2.7 is represented, in detail, the diversity of 3D models, with the sucrose mold inside and after the dissolution process.

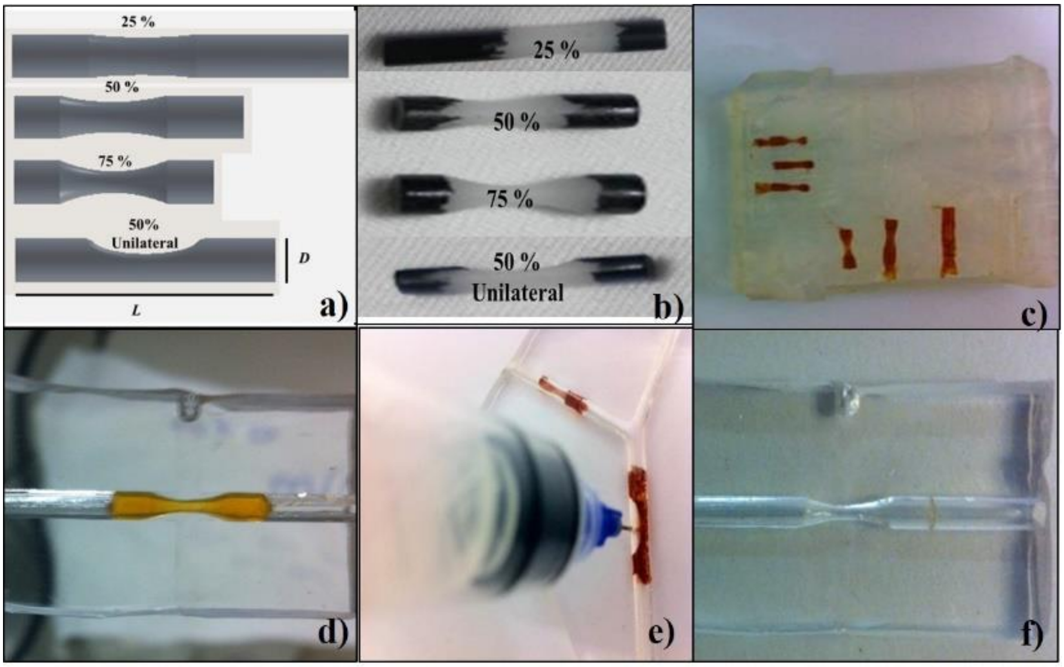

Figure 2.6. Stenoses fabrication and its implementation in the channels, using the lost-sucrose casting method: a) CAD models, b) epoxy resin molds, c) non-transparent silicone mold containing the different stenoses geometries, d) sacrificial sucrose mold in the desired position, e) injection of the PDMS and f) final 3D PDMS channel with the desired stenosis. The larger diameter of the stenoses models is the same as the diameter of the channels, 2.5 mm $\leq d \leq$ 3.5 mm. The length of the stenoses models varies between 5 mm and 15 mm.

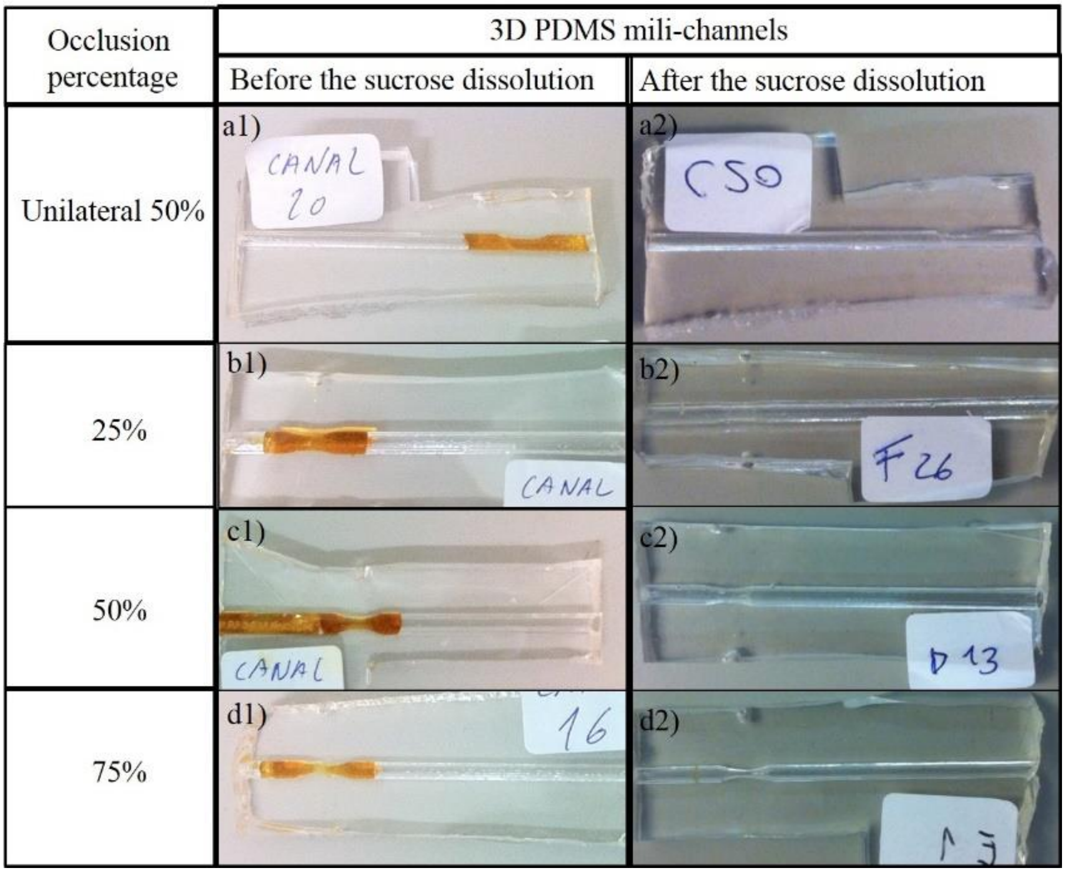

Figure 2.7. 3D PDMS mili-scale channels fabricated by the lost-sucrose casting method: a1 to d1) before the sucrose dissolution and a2 to d2) after the sucrose dissolution.

2.3. Characterization of the *in vitro* models

The PDMS channels fabricated by lost-wax and lost-sucrose methods were compared and characterized in terms of optical properties and structure. Refractometry and analyses by Scanning Electron Microscopy (SEM) and by Energy dispersive X-Ray Spectroscopy (EDS) were performed.

The simplest method to visualize the effect of optical distortion due to the curvature of the solid-liquid interface is to inject a fluid into the channels and placing them over a patterned surface such as the gridlines of a millimeter paper. Three different fluids were used for this purpose: air, water and a water/glycerol mixture. Table 2.1 shows the relevant properties of the materials used in this study.

The refractive index of the PDMS was measured in an ABBE® (WYA-1S) digital refractometer, at a controlled temperature of 293 K. A water/glycerol mixture was prepared using 39% (w/w) water and 61% (w/w) glycerol, in order to match the refractive index of the PDMS[37] which is essential to eliminate distortion given the curvature of the channel walls. The viscosity of the solution was measured with an Anton Paar® Physica MCR301 Rotational Rheometer.

Table 2.1. Relevant properties of the materials used in this study at a controlled temperature of 293K.

Materials	**Refractive index**	**Density kg.m^{-3}**	**Viscosity Pa·s**
Air	1.0003	1.2041	1.837×10^{-5}
Water	1.3321	998.21	1.002×10^{-3}
Water / glycerol	1.4125	1156.6	1.140×10^{-2}
PDMS	1.4125	-	-

Figure 2.8 shows the distortion of the gridlines of a sheet of millimeter paper as seen through the 3D mili-scale channels made by lost-wax casting method and by lost-sucrose casting method, when filled with air, water and the water/glycerol mixture.

Channels produced by the lost-sucrose casting method (Figure 2.8 a2 to c2) are clearly better in terms of transparency than those made using wax (Figure 2.8 a1 to c1). Air and water have a much lower refractive index than PDMS and therefore there is no refractive index matching and distortion of the gridlines is clear. On the other hand, the water/glycerol mixture matches the refractive index of the channels material showing no optical distortion. In the channels made by the lost-wax casting method the borders are clearly delimited by wax residues impregnated in the PDMS.

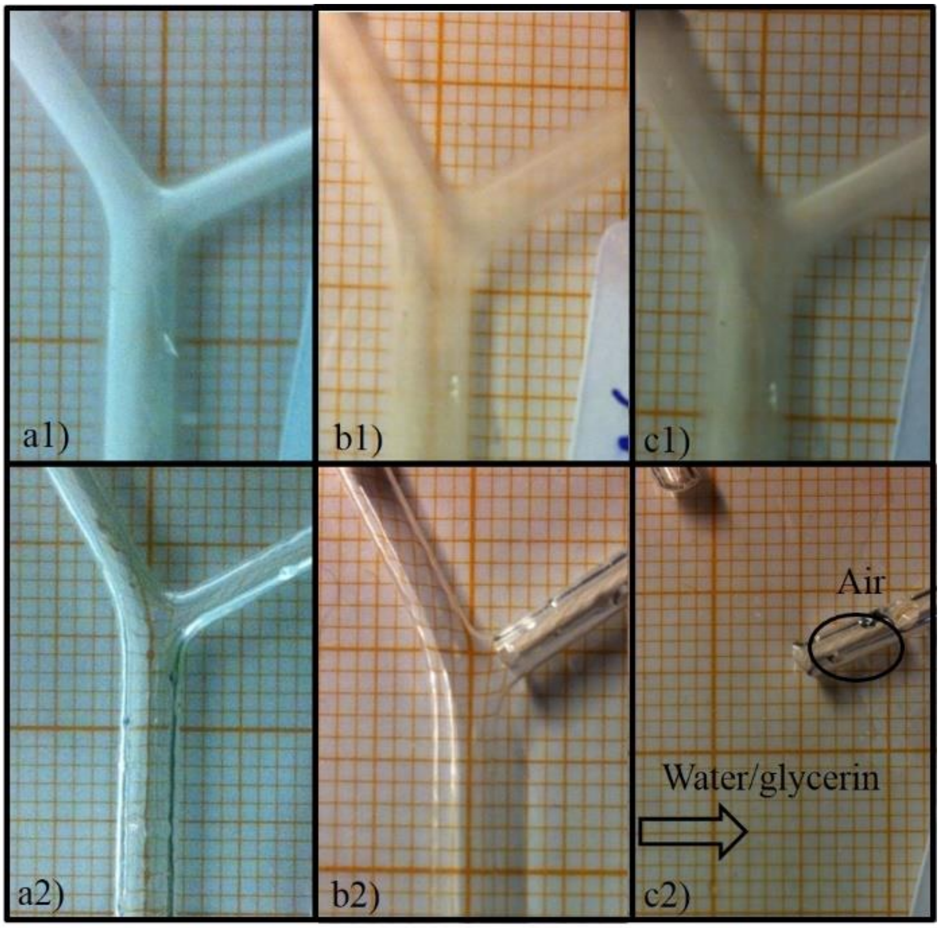

Figure 2.8. Distortion of gridlines seen through the 3D mili-scale PDMS channel, fabricated by lost-wax casting method (top) and by lost-sucrose casting method (bottom), when the channel is filled with: a) air, b) water and c) water/glycerol.

The surface of the mili-scale channels was analyzed using SEM and EDS techniques. The purpose of SEM and EDS analysis is to verify the possible contamination of the model surface by the sacrificial materials (wax and sucrose). SEM allows the detection of small clusters of contaminants over the otherwise smooth surface of PDMS. EDS is used to verify if the chemical composition of the surface differs from that of PDMS.

A SEM image of the surface of the channel obtained using the lost-wax casting method is shown in Figure 2.9 a). The EDS analysis was performed in two different areas: Z1 pointing out a structure that is contaminating the channel and Z2 representing a clean area. The EDS spectrum shown in Figure 2.9 b), indicates that the Z2 area is mostly constituted by silicon, which is one of the constitutive elements of PDMS. The Z1 area has a low silicon count and a high carbon counts indicating the presence of contamination in the PDMS.

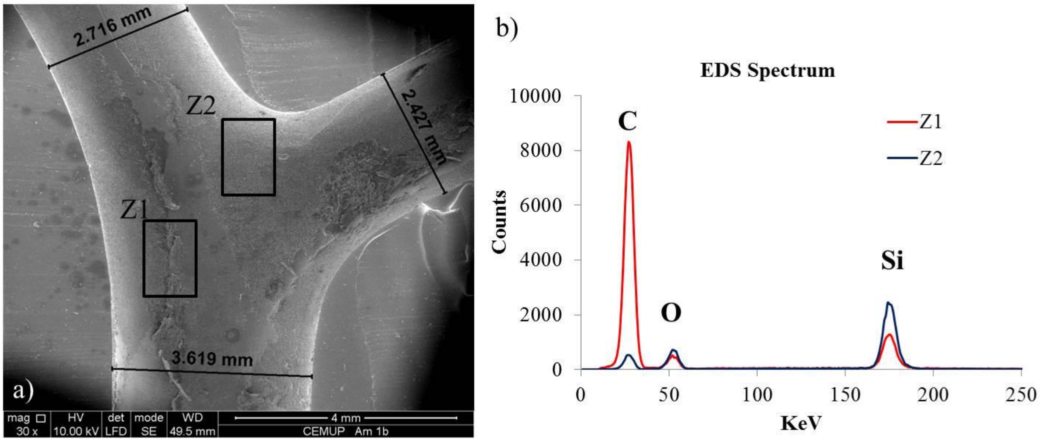

Figure 2.9. Surface analysis of a mili-channel fabricated by the lost-wax casting method: a) SEM image showing the location of the surfaces analysed and b) EDS Spectrum showing the different element counts in the Z1 and Z2 areas.

The mili-scale channels produced using the lost-sucrose casting method exhibit much less contamination, with a smooth surface as shown by SEM image in Figure 2.10 a). The corresponding EDS spectrum confirms silicon (Z3) as the most frequent element (Figure 2.10 b), as expected from the optical distortion analysis.

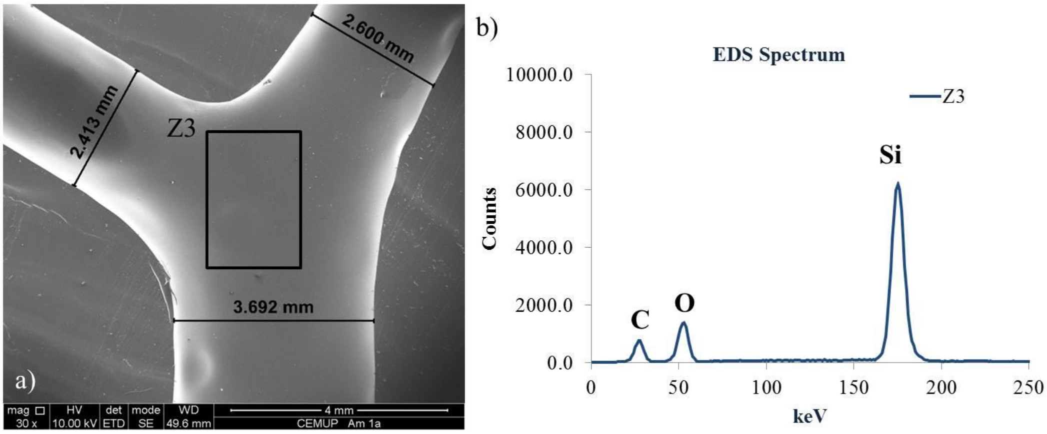

Figure 2.10. Surface analysis of a mili-channel fabricated by the lost-sucrose casting method: a) SEM image showing the location of the surface analysed and b) EDS Spectrum showing the different element counts in the Z3 area.

The results of SEM and EDS have shown that the lost-wax method leaves significant contamination observable by SEM with a change in the chemical composition of the surface detectable by EDS analysis. In the case of lost-sucrose casting method, there are no contaminants observable in the SEM images and the EDS analysis reveals that the surface has, as expected, the composition of PMDS.

Figure 2.11 shows the CAD model of a straight channel and a bifurcated one. The dimensions of the fabricated channels were evaluated by brightfield microscopy (DMI 5000M Leica Microsystems ®).

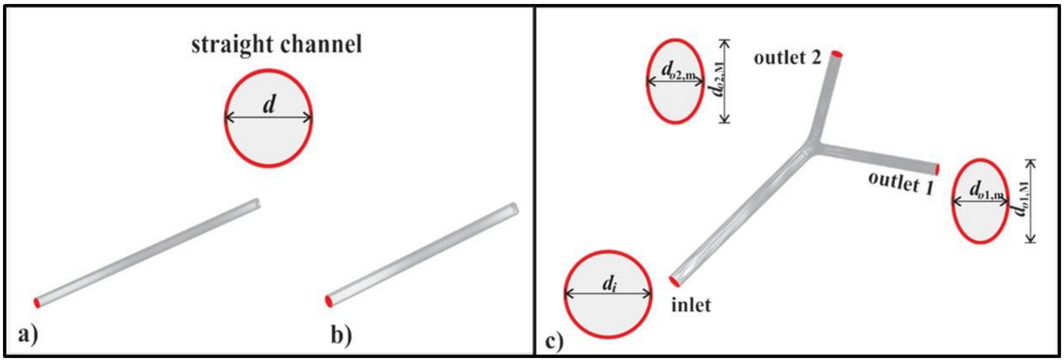

Figure 2.11. CAD models: a) straight channel with d = 2.50 mm; b) straight channel with d = 3.50 mm; c) bifurcated channel, with one inlet, d_i= 3.50 mm, and two outlets (daughter branches) with ellipse shaped cross-section (with major diameters $d_{o1,M} = d_{o2,M}$ = 3.50 mm and minor diameters $d_{o1,m} = d_{o2,m}$ = 2.78 mm).

Images of the corresponding cross-sections of the channels produced in PDMS are shown in Figure 2.12. The relevant dimension measured are shown in Table 2.2, the diameter of the two straight channels, d, the inlet diameter of the bifurcated channel, d_i, and the major and minor diameters of outlet 1 ($d_{o1,M}$ and $d_{o1,m}$) and outlet 2 ($d_{o2,M}$ and $d_{o2,m}$).

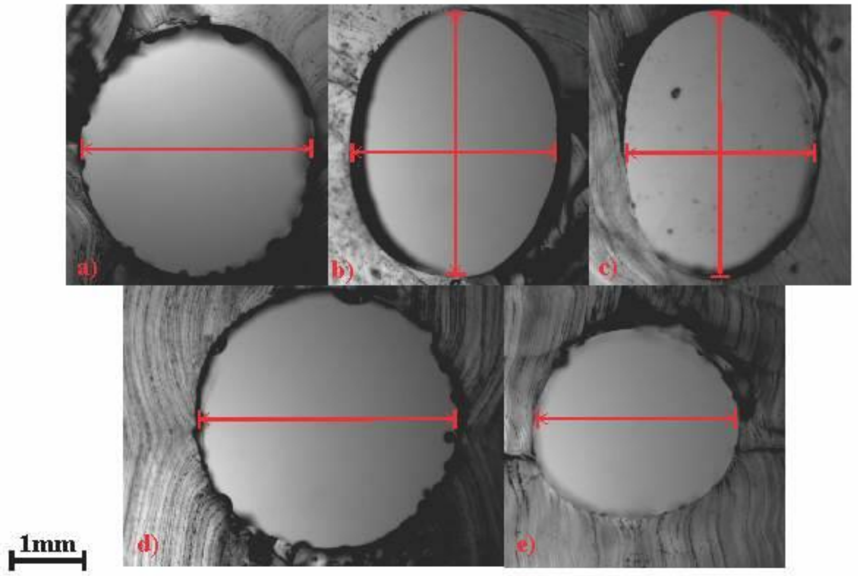

Figure 2.12. Brightfield visualization of the mili-scale channels cross-sections with corresponding diameters: a) inlet, b) outlet 1, c) outlet 2, d) and e) of two different straight channels.

For the paraffin channels, ten replicates were prepared and their dimensions compared with each other and with the nominal dimensions of the CAD model design. The same procedure was followed for the sucrose channels and fifteen replicates were analyzed. The accuracy of the casting methods was quantified by the mean error defined by:

$$\epsilon = \frac{\left(\bar{d} - d_{CAD}\right)}{d_{CAD}} \times 100 \tag{2.1}$$

where d_{CAD} is the reference diameter of the previous geometries designed in CAD software and $\bar{d}$ is the mean diameter of the samples defined by:

$$\bar{d} = \sum_{k=1}^{n} \frac{d_k}{n} \tag{2.2}$$

where d_k is the diameter of a given sample and n the number of samples.

The reproducibility of the method was assessed through the standard deviation of the samples defined by:

$$\sigma = \sqrt{\frac{\sum_{k=1}^{n}\left(d_k - \bar{d}\right)^2}{n-1}} \tag{2.3}$$

The geometrical deviation between the channels and the CAD model amounted to a maximum mean error (ϵ/ %) of 17.7% (minor axis of outlet 1) for paraffin and of 11.3% (minor axis of outlet 2) for sucrose. It can be concluded, from these values, that the real channels are excellent replicates of the CAD model design, especially if one consider the inherent error associated to the rapid prototyping by solid state stereolithography is approximately 0.15 mm.

The standard deviation varied from 0.07 to 0.31 mm for the paraffin channels and only 0.02 to 0.16 mm for the sucrose channels, showing the reproducibility of the channels made by lost-sucrose casting method.

Table 2.2. Evaluation of cross-sections dimensions of the final 3D PDMS mili-scale channels.

		Straight channel ***2.5***	**Straight channel** ***3.5***	**Bifurcated channel**				
				Inlet	***Outlet* 1**		***Outlet* 2**	
					Major axis	***Minor axis***	***Major axis***	***Minor axis***
CAD	d/mm	2.50	3.50	3.50	3.50	2.78	3.50	2.78
Paraffin	$\bar{d} \pm \sigma/mm$	2.64±0.31	3.67±0.07	3.7±0.11	3.69±0.19	2.36±0.15	3.45±0.16	2.50±0.23
	$\epsilon/\%$	5.41	4.61	5.28	5.15	17.70	1.45	11.02
Sucrose	$\bar{d} \pm \sigma/mm$	2.43±0.02	3.49±0.07	3.29±0.07	3.31±0.04	2.49±0.08	3.42±0.10	2.62±0.16
	$\epsilon/\%$	3.08	0.13	6.12	5.83	11.29	2.32	5.78

2.4. Flow Characterization

The final PDMS channels were used in flow visualization (section 2.4.1) and µPIV (section 2.4.2) studies to evaluate the ability of the lost-sucrose casting method to fabricate 3D mili-scale channels suitable for optical hemodynamic studies. The fluid used for flow visualization and µPIV was the water/glycerol (39%/61% *w/w*) mixture.

2.4.1. Flow visualizations

Flow visualization of the flow patterns were carried out using streak photography with exposure times of the order of 300 ms. For this purpose, the fluid was seeded with 20 ppm *w/w* of 1 µm fluorescent polystyrene tracer particles (Nile Red, Molecular Probes, Invitrogen, Ex/Em: 535/575 nm, density: 1.05 g/mL). A syringe pump was used to impose the flow rate in the mili-scale channels. The channels were placed on an inverted epifluorescence microscope (DMI 5000M, Leica Microsystems GmbH) and were continuously illuminated by a 100 W mercury lamp. A filter cube (Leica Microsystems GmbH, excitation filter BP of 530–545 nm, dichroic of 565 nm, and barrier filter of 610–675 nm) was used to filter the multichromatic light into the excitation light which reaches the geometries containing the seeded fluid via a microscope objective (2.5x, NA = 0.07) Figure 2.13 illustrates the experimental setup used for flow visualization and µPIV analysis.

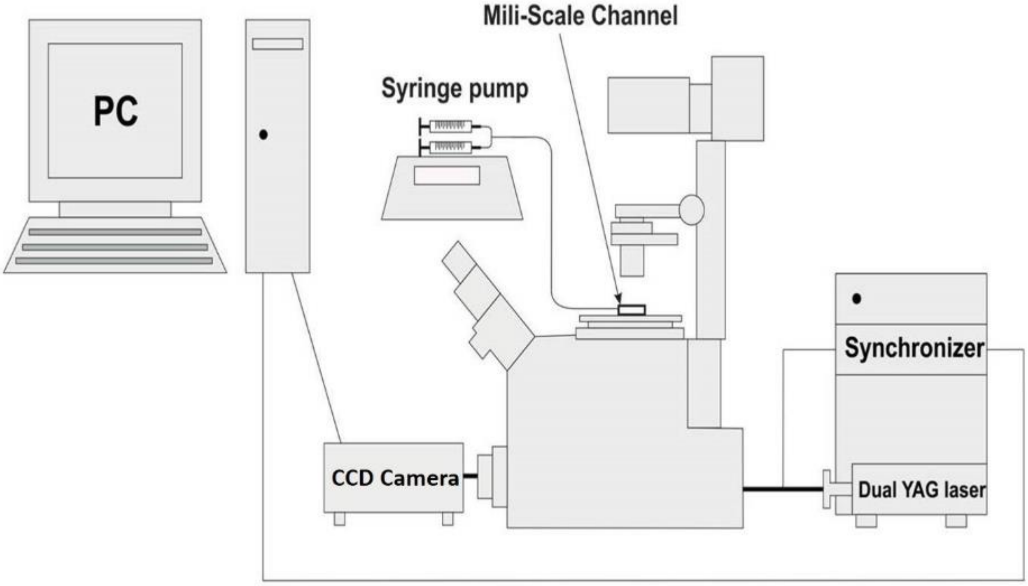

Figure 2.13. Setup for µPIV analysis.

The light emitted by the fluorescent tracer particles was imaged through the same objective into the camera DFC350 FX (Leica Microsystems GmbH) in order to capture the particle path-lines, as shown in Figure 2.14. All images presented here are centered at the midplane of the mili-scale channel. The flow visualization experiments were carried out at a controlled room temperature (T ~ 293 K) for a wide range of flow rates ($100 \leq Q \leq 1000$ mL h^{-1}).

The light emitted by the fluorescent tracer particles was imaged through the same objective into the camera DFC350 FX (Leica Microsystems GmbH) in order to capture the particle path-lines, as shown in Figure 2.14. All images presented here are centered at the midplane of the mili-scale channel. The flow visualization experiments were carried out at a controlled room temperature (T ~ 293 K) for a wide range of flow rates ($100 \leq Q \leq 1000$ mL h^{-1}).

Using an index-matched fluid eliminates most of the optical distortion caused by the channel curvature and reliable visualizations of the flow patterns can be performed. This visualization was a preliminary study to carry out a reliable µPIV analysis.

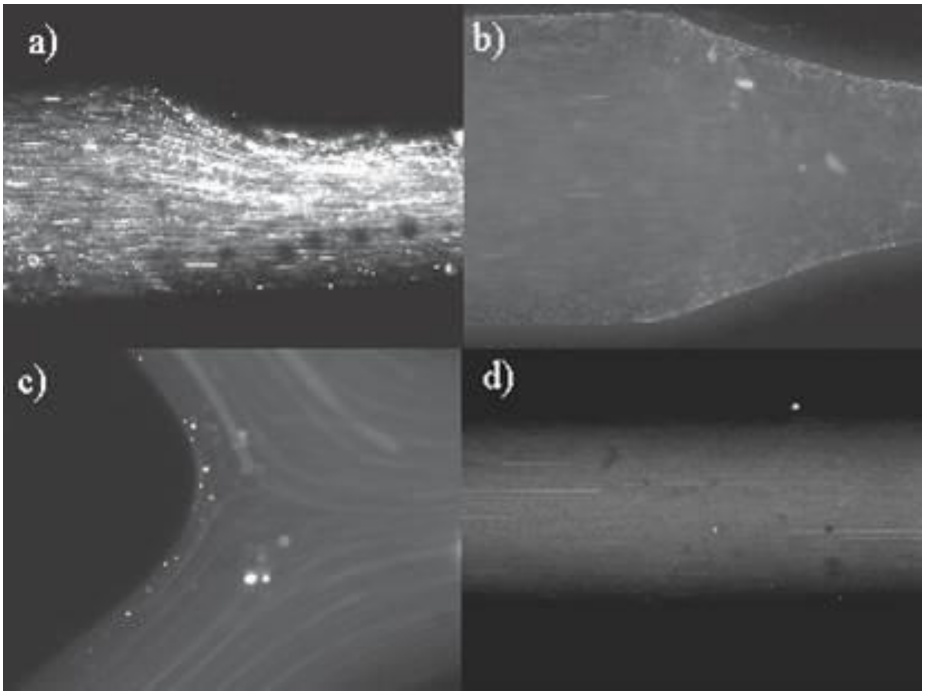

Figure 2.14. Flow visualization, using water/glycerol, in channels fabricated by the lost-sucrose casting method: a) Q = 100 mL.h^{-1} (50% unilateral occlusion), b) Q = 500 mL.h^{-1} (75% occlusion), c) Q = 200 mL.h^{-1} (bifurcated channel) and d) Q = 1000 mL.h^{-1} (straight channel without stenosis).

2.4.2. µPIV analysis

Measurements of the velocity field were carried out using µPIV. For that purpose, the fluid was seeded with the same fluorescent microparticles used in the flow visualization. The generic imaging setup used is similar to that described in the previous section except for the light source. The light source used for µPIV is a doubled pulsed Nd:YAG (yttrium aluminum garnet) laser (Dual Power 65-15, Dantec Dynamics) with a wavelength of 532 nm. The time interval between pulses was adjusted in the range of $100 \leq \Delta t$ [µs] ≤ 1000, such that particle displacement was about 25% the size of the interrogation area, which was selected according to the velocity of the flow and the objective used. For each flow rate, 100 pairs of images were acquired using a digital camera (Flow Sense 4M, Dantec Dynamics) with a resolution of 2048 x 2048 pixels and running in double frame mode. The images were post-processed to obtain the velocity vector map using DYNAMIC STUDIO V2.3 software (Dantec Dynamics) based on ensemble averaging the 100 pairs of images. All images were acquired at the midplane of the mili-scale channel.

Two different geometries were chosen for µPIV data analysis, a bifurcated channel with a stenosis in one of the daughter branches (25 % occlusion), Figure 2.15 to Figure 2.17, and a straight channel containing a stenosis (50 % occlusion), Figure 2.18 and Figure 2.19.

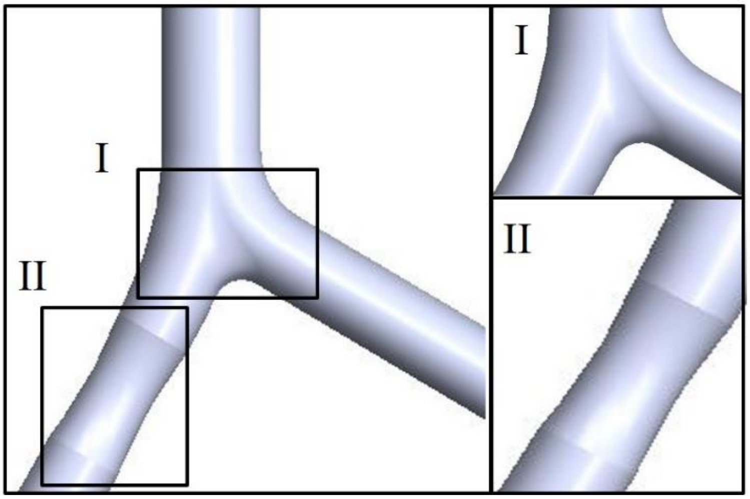

Figure 2.15. Bifurcated channel with a stenosis (25 % occlusion) for µPIV analysis. Details: I) the bifurcated area an II) the stenosis area.

Figure 2.16 shows the velocity field normalized by the mean velocity in the inlet channel. Note that the normalized velocity is lower in the daughter branch that contains the stenosis due to the higher pressure drop along that branch.

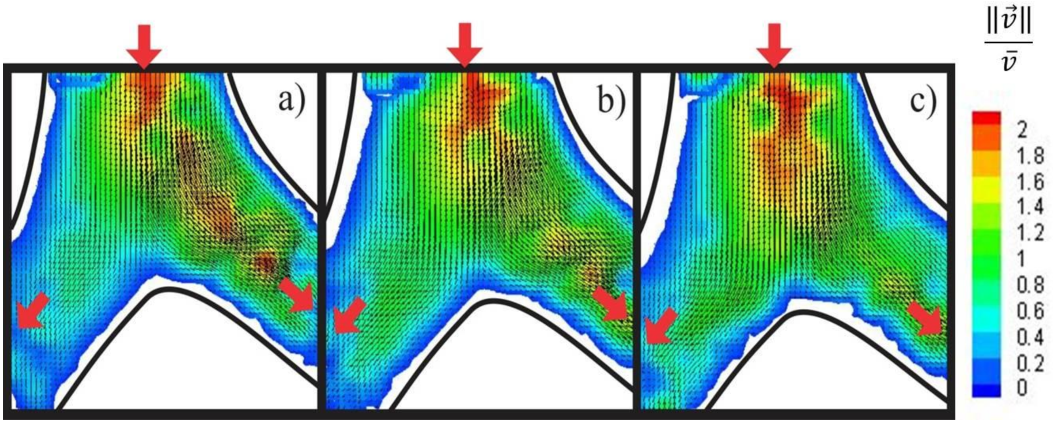

Figure 2.16. Normalized velocity field in the bifurcated 3D mili-scale channel at: a) Q = 600 mL.h^{-1}, b) Q = 1200 mL.h^{-1} and c) Q = 5000 mL.h^{-1}. The red arrows show the flow direction.

Figure 2.17 represents the velocity field normalized by the mean velocity in the stenotic branch of the bifurcated channel. As described above the red arrows show the flow direction.

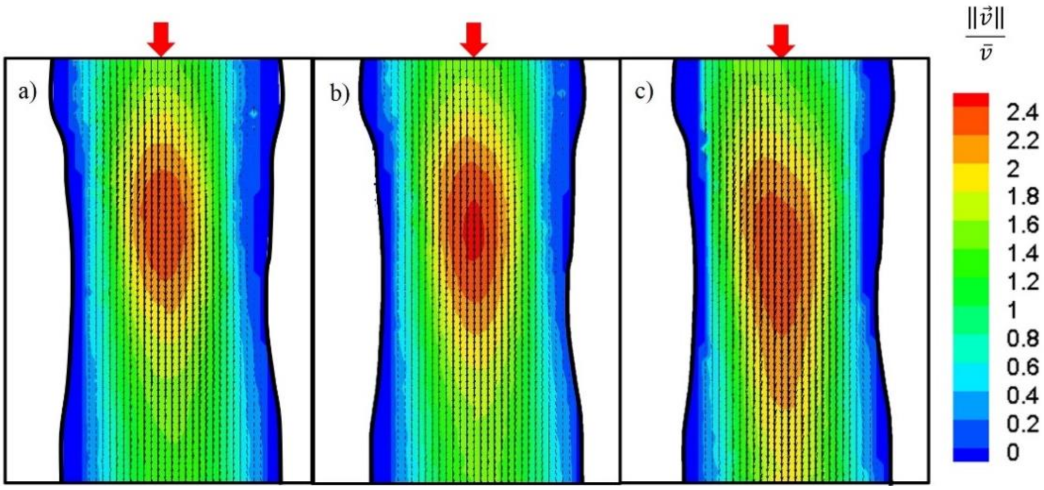

Figure 2.17. Normalized velocity field in the stenosis region (25% occlusion) at: a) Q = 600 mL.h^{-1}, b) Q = 1200 mL.h^{-1} and c) Q = 5000 mL.h^{-1}.

Figure 2.18 shows a straight channel containing the detail of a stenosis with a 50% occlusion. The rectangular regions represented, I and II, are those where the µPIV experiments were carried out.

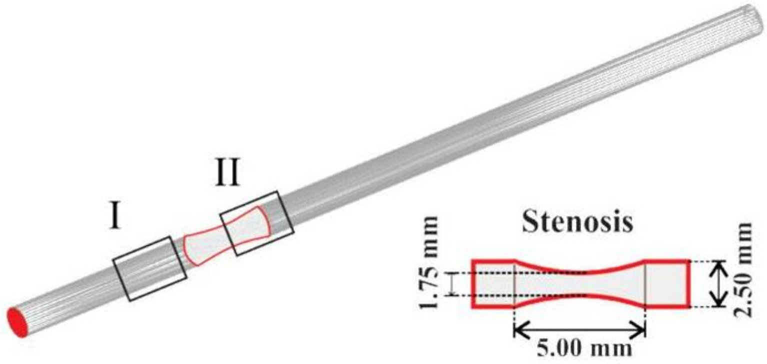

Figure 2.18. CAD representation of a straight channel containing a stenosis, highlighting the detail of stenosis with 50 % occlusion and two regions where the µPIV analysis was performed: I) upstream the stenosis and II) in the stenosis.

In Figure 2.19, the corresponding velocity fields are illustrated: I) region of the velocity field upstream of the stenosis (Figure 2.19a) and II) in the stenosis region (Figure 2.19b). For better understanding the velocity field was overlapped on a brightfield image at the same site where the µPIV was carried out.

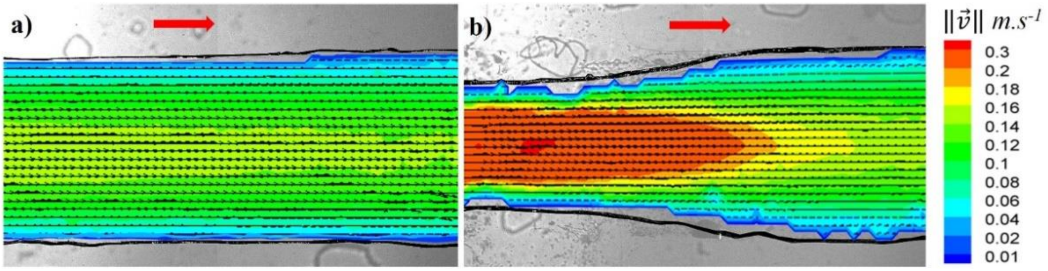

Figure 2.19. Velocity fields overlapped on brightfield images representing two different regions of the straight channel for Q = 1000 mL.h^{-1}: a) upstream of the stenosis and b) in the stenosis (50% occlusion). The red arrows represent the flow direction.

The mean velocity is higher in the stenosis due to the smaller diameter, as expected. The velocity profiles along the straight channel are shown in Figure 2.20. This representation shows that the flow, in the largest diameter area, is developed upstream the stenosis and starts accelerating as it approach the stenosis region. In the stenosis region the velocity profiles are more elongated and the peak velocity is higher as expected.

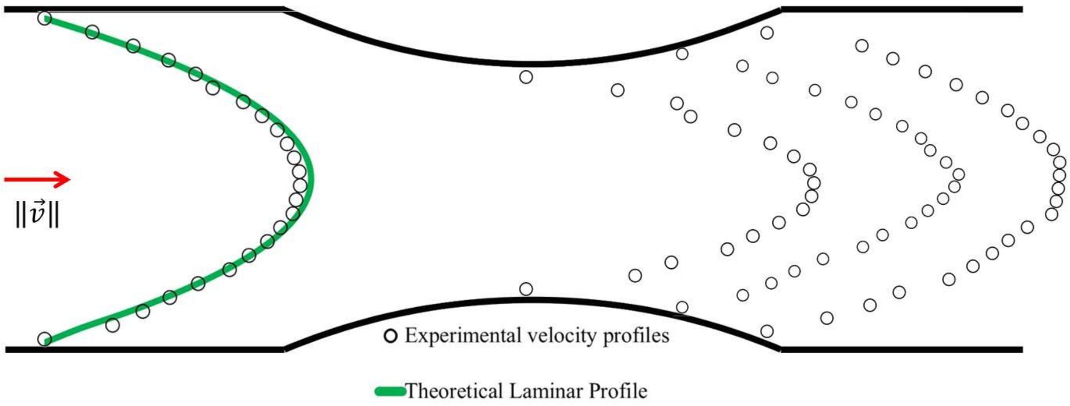

Figure 2.20. Experimental and theoretical (Q= 1047 mL.h^{-1}) velocity profiles measured along the midplane of the straight channel highlighting the stenosis region (50% occlusion).

2.5. Conclusions

The objective of this chapter was to find a good fabrication method of 3D mili-scale channels for hemodynamic studies. The most common methods for fabrication of *in vitro* models of mili-scale arteries rely on the use of sacrificial template techniques. However, the removal process of these materials is usually done by melting. This heat removal process is known to leave residues in the walls of the final model which compromise the optical experiments and jeopardize the credibility of the final results. One of the most employed methods in the literature, the lost-wax casting method, was tested and compared to a novel process created to surpass the known limitations of the usual fabrication methods. The developed process relies on the use of a material that could be removed without the need of high temperatures, but could be injected in any format silicon mold. The material used was sucrose, and the method was denominated the “lost-sucrose” casting method. It was shown that, for fabricating 3D PDMS mili-scale channels, the developed method not only fulfilled all the requirements for this type of process but also was better than the common methods found in literature. This method enables the fabrication of mili-scale channels with excellent optical properties, in terms of transparency and very low level of optical distortion.

These findings are explained by the much less level of contamination of the channels during the fabrication process with sucrose. The low level of contamination is explained by the removal process used. In the lost-sucrose casting method, the removal is by dissolution in water at room temperature while in the lost-wax casting method, as in other methods, typically removal is done by melting at high temperatures which leaves residues in the walls of the channels.

In terms of µPIV it was possible to study the velocity field and extract the velocity profiles along the 3D mili-scale channels. The µPIV technique is often used in micro and macro-channels and this study proves that it is possible to apply with accuracy this technique to the 3D mili-scale channels fabricated with the sucrose method.

This work will allow a more realistic approach for future hemodynamic studies that focus on atherosclerosis in mili-scale arteries.

Acknowledgments

The authors gratefully acknowledge the funding by Fundação para a Ciência e Tecnologia, FCT (Portugal), and FEDER under projects PTDC/EME-MFE/102974/2008 and PTDC/EME-MFE/099109/2008. SEM and EDS were performed at CEMUP facilities (funded by FCT projects REEQ/1062/CTM/2005 and REDE/1512/RME/2005).

Notation

Symbol	**Definition**
$\Delta\mathrm{t}$	Time interval
d	Diameter of the straight channel
d_{CAD}	CAD reference diameter
d_{i}	Inlet diameter
d_{k}	Diameter of a given sample
$\bar{d}$	Mean diameter of the samples
$d_{\mathrm{o1,m}}$	Diameter of the minor axis of Outlet 1
$d_{\mathrm{o1,M}}$	Diameter of the major axis of Outlet 1
$d_{\mathrm{o2,m}}$	Diameter of the minor axis of Outlet 2
$d_{\mathrm{o2,M}}$	Diameter of the major axis of Outlet 2
ϵ	Mean error
n	Number of samples
Q	Flow rate
T	Room temperature
σ	Standard deviation
$\lVert\vec{v}\rVert$	Velocity length
$\bar{v}$	Mean velocity

References

1. Lozano, R. and M. Naghavi and K. Foreman, *et al., Global and regional mortality from 235 causes of death for 20 age groups in 1990 and 2010: a systematic analysis for the Global Burden of Disease Study 2010.* Lancet, 2012. **380**(9859): p. 2095-128.
2. Chatzizisis, Y.S., A.U. Coskun, M. Jonas, *et al., Role of endothelial shear stress in the natural history of coronary atherosclerosis and vascular remodeling: molecular, cellular, and vascular behavior.* J Am Coll Cardiol, 2007. **49**(25): p. 2379-93.
3. Bale-Glickman, J., K. Selby, D. Saloner and O. Savas, *Experimental flow studies in exact-replica phantoms of atherosclerotic carotid bifurcations under steady input conditions.* J Biomech Eng, 2003. **125**(1): p. 38-48.
4. Shaaban, A.M. and A.J. Duerinckx, *Wall shear stress and early atherosclerosis: a review.* AJR Am J Roentgenol, 2000. **174**(6): p. 1657-65.
5. Zurauskas, E., J. Usinskiene, V. Gaigalaite, *et al., [Models of intracranial aneurysms for angiographic imaging modalities. A technical note].* Medicina (Kaunas), 2007. **43**(7): p. 562-7.
6. Baek, H., M.V. Jayaraman, P.D. Richardson and G.E. Karniadakis, *Flow instability and wall shear stress variation in intracranial aneurysms.* J R Soc Interface, 2010. **7**(47): p. 967-88.
7. Valen-Sendstad, K., K.A. Mardal, M. Mortensen, *et al., Direct numerical simulation of transitional flow in a patient-specific intracranial aneurysm.* J Biomech, 2011. **44**(16): p. 2826-32.
8. Ford, M.D. and U. Piomelli, *Exploring high frequency temporal fluctuations in the terminal aneurysm of the basilar bifurcation.* J Biomech Eng, 2012. **134**(9): p. 091003.
9. Brunette, J., R. Mongrain, J. Laurier, *et al., 3D flow study in a mildly stenotic coronary artery phantom using a whole volume PIV method.* Med Eng Phys, 2008. **30**(9): p. 1193-200.
10. Lorthois, S., J. Stroud-Rossman, S. Berger, *et al., Numerical simulation of magnetic resonance angiographies of an anatomically realistic stenotic carotid bifurcation.* Ann Biomed Eng, 2005. **33**(3): p. 270-83.
11. Shalman, E., M. Rosenfeld, E. Dgany and S. Einav, *Numerical modeling of the flow in stenosed coronary artery. The relationship between main hemodynamic parameters.* Computers in Biology and Medicine, 2002. **32**(5): p. 329-344.
12. Bertolotti, C., V. Deplano, J. Fuseri and P. Dupouy, *Numerical and experimental models of post-operative realistic flows in stenosed coronary bypasses.* J Biomech, 2001. **34**(8): p. 1049-64.
13. Ku, J.P., C.J. Elkins and C.A. Taylor, *Comparison of CFD and MRI flow and velocities in an in vitro large artery bypass graft model.* Ann Biomed Eng, 2005. **33**(3): p. 257-69.

14. Kabinejadian, F., F. Cui, Z. Zhang, *et al.*, *A novel carotid covered stent design: in vitro evaluation of performance and influence on the blood flow regime at the carotid artery bifurcation.* Ann Biomed Eng, 2013. **41**(9): p. 1990-2002.
15. Shahcheraghi, N., H.A. Dwyer, A.Y. Cheer, *et al.*, *Unsteady and three-dimensional simulation of blood flow in the human aortic arch.* J Biomech Eng, 2002. **124**(4): p. 378-87.
16. Kobayashi, M.H. and J.C. Pereira, *A computational method for solving arbitrary two-dimensional physiological flows.* J Biomech Eng, 1994. **116**(3): p. 315-7.
17. Barakat, A.I. and E.T. Cheng. *Numerical simulation of fluid mechanical disturbance induced intravascular stents*. in *CMMB-11: Int Conf Mechanics in Medicine and Biology*. 2000. Maui, Hawaii.
18. Braunmuller, S., L. Schmid and T. Franke, *Dynamics of red blood cells and vesicles in microchannels of oscillating width.* J Phys Condens Matter, 2011. **23**(18): p. 184116.
19. Einav, S., H.J. Berman, R.L. Fuhro, *et al.*, *Measurement of velocity profiles of red blood cells in the microcirculation by laser doppler anemometry (LDA).* Biorheology, 1975. **12**(3-4): p. 207-10.
20. Ravnic, D.J., Y.Z. Zhang, A. Tsuda, *et al.*, *Multi-image particle tracking velocimetry of the microcirculation using fluorescent nanoparticles.* Microvasc Res, 2006. **72**(1-2): p. 27-33.
21. Santiago, J.G., S.T. Wereley, C.D. Meinhart, *et al.*, *A particle image velocimetry system for microfluidics.* Experiments in Fluids, 1998. **25**(4): p. 316-319.
22. Sugii, Y., R. Okuda, K. Okamoto and H. Madarame, *Velocity measurement of both red blood cells and plasma of in vitro blood flow using high-speed micro PIV technique.* Measurement Science and Technology, 2005. **16**(5): p. 1126-1130.
23. Park, J.S., C.K. Choi and K.D. Kihm, *Optically sliced micro-PIV using confocal laser scanning microscopy (CLSM).* Experiments in Fluids, 2004. **37**(1): p. 105-119.
24. Lima, R., S. Wada, K. Tsubota and T. Yamaguchi, *Confocal micro-PIV measurements of three-dimensional profiles of cell suspension flow in a square microchannel.* Measurement Science and Technology, 2006. **17**(4): p. 797-808.
25. Burgmann, S., S. Grosse, W. Schroder, *et al.*, *A refractive index-matched facility for fluid-structure interaction studies of pulsatile and oscillating flow in elastic vessels of adjustable compliance.* Experiments in Fluids, 2009. **47**(4-5): p. 865-881.
26. de Zelicourt, D., K. Pekkan, H. Kitajima, *et al.*, *Single-step stereolithography of complex anatomical models for optical flow measurements.* J Biomech Eng, 2005. **127**(1): p. 204-7.

27. de Zelicourt, D.A., K. Pekkan, L. Wills, *et al.*, *In vitro flow analysis of a patient-specific intraatrial total cavopulmonary connection.* Ann Thorac Surg, 2005. **79**(6): p. 2094-102.
28. Gailloud, P., M. Muster, M. Piotin, *et al.*, *In vitro models of intracranial arteriovenous fistulas for the evaluation of new endovascular treatment materials.* AJNR Am J Neuroradiol, 1999. **20**(2): p. 291-5.
29. Wetzel, S.G., M. Ohta, A. Handa, *et al.*, *From patient to model: stereolithographic modeling of the cerebral vasculature based on rotational angiography.* AJNR Am J Neuroradiol, 2005. **26**(6): p. 1425-7.
30. Knox, K., C.W. Kerber, S.A. Singel, *et al.*, *Rapid prototyping to create vascular replicas from CT scan data: making tools to teach, rehearse, and choose treatment strategies.* Catheter Cardiovasc Interv, 2005. **65**(1): p. 47-53.
31. Allard, L., G. Soulez, B. Chayer, *et al.*, *Multimodality vascular imaging phantoms: a new material for the fabrication of realistic 3D vessel geometries.* Med Phys, 2009. **36**(8): p. 3758-63.
32. Cloutier, G., G. Soulez, S.D. Qanadli, *et al.*, *A multimodality vascular imaging phantom with fiducial markers visible in DSA, CTA, MRA, and ultrasound.* Med Phys, 2004. **31**(6): p. 1424-33.
33. Smith, R.F., B.K. Rutt and D.W. Holdsworth, *Anthropomorphic carotid bifurcation phantom for MRI applications.* J Magn Reson Imaging, 1999. **10**(4): p. 533-44.
34. Geoghegan, P.H., N.A. Buchmann, C.J.T. Spence, *et al.*, *Fabrication of rigid and flexible refractive-index-matched flow phantoms for flow visualisation and optical flow measurements.* Experiments in Fluids, 2012. **52**(5): p. 1331-1347.
35. Lee, J., J. Paek and J. Kim, *Sucrose-based fabrication of 3D-networked, cylindrical microfluidic channels for rapid prototyping of lab-on-a-chip and vaso-mimetic devices.* Lab Chip, 2012. **12**(15): p. 2638-42.
36. Chaichana, T., Z. Sun and J. Jewkes, *Computation of hemodynamics in the left coronary artery with variable angulations.* J Biomech, 2011. **44**(10): p. 1869-78.
37. Buchmann, N.A., C. Atkinson, M.C. Jeremy and J. Soria, *Tomographic particle image velocimetry investigation of the flow in a modeled human carotid artery bifurcation.* Experiments in Fluids, 2011. **50**(4): p. 1131-1151.

3

Chapter

> *"The voyage of discovery is not in seeking new landscapes*
> *but in having new eyes!"*
>
> **— Marcel Proust**

Experimental and numerical characterization of secondary flows in coronary bifurcations[*]

---

[*] E. Doutel, J. Carneiro, JBLM. Campos, JM. Miranda
Experimental and numerical characterization of secondary flows in a coronary bifurcation, **Journal of Experiments in Fluids**, March 2016, under review.

3

Experimental and numerical characterization of secondary flows in a coronary bifurcation

Abstract

Atherosclerosis initiation and progression are a direct consequence of local hemodynamics and can lead to plaque rupture and thrombosis, eventually causing myocardial infarction. Many studies describe that local blood flow patterns are responsible for the location and development of atherosclerosis. In coronary bifurcation diseases, quantitative information on local hemodynamic parameters, such as velocity and wall shear stress, can contribute to their better understanding. To investigate the local hemodynamics in the LCA bifurcation, an approach combining numerical (CFD) and experimental methods (µPIV and streak photography) was followed. A whole volume µPIV experimental method was developed and applied to a simplified 3D phantom of the LCA bifurcation. The experimental and numerical results prove to be in a good agreement. Implications of a deviation from Murray's law and the effect of different Reynolds numbers in flow behaviour were also explored. A streak line photography method was used to complement the results and analyse the flow patterns. When the deviation from Murray's law is evident, secondary flows are observed and they intensify as the Reynolds number increases. The secondary flows are visible in regions of low wall shear stresses (WSS). The present chapter identifies, from the numerical and experimental perspective, flow patterns that are relevant for prevention and treatment of atherosclerosis.

3.1 Introduction

Bifurcations in the human circulatory system are vulnerable to the development of several medical conditions. In the case of the left coronary artery (LCA), the branching angle and the diameter ratio in coronary artery bifurcations are two important factors for the local hemodynamics and it is believed that they play an important role in atherosclerosis[1] and stenoses[2, 3] development.

Blood is a multiphase fluid with a complex scale dependent rheology. Details of the flow depend of the scale and geometry of the blood vessel as well as of the flow rates and flow division observed *in vivo*. To completely understand the blood hemodynamics in vascular systems a combination of numerical with *in vivo* and *in vitro* experimental studies is required. Several experimental and numerical studies have been published concerning idealized[4-6] or more realistic geometries of coronary artery models[7-10]. Some complex flow patterns are rather difficult to be experimentally studied due to limited spatial and temporal resolution conditions[11]. Therefore, several authors rely on CFD to study the hemodynamics in coronary bifurcations[4, 8, 12-15].

In vitro velocity fields of blood flow have been measured using several techniques, including particle-based methods such as: streak photography, particle tracking velocimetry (PTV), particle image velocimetry (PIV), and micro-particle image velocimetry (µPIV). µPIV is usually applied to study the flow in small diameter vessels (less than 250 µm)[16-18]. An high depth-wise spatial resolution requires sophisticated equipment, for example confocal µPIV[17]. Brunette *el at.*[2] presented 3D velocity fields obtained in a silicon model of a coronary artery, including the three-velocity components, extracted from PIV data. Kabinejadian *et al.*[19] investigated the hemodynamics in a poly(dimethylsiloxane) (PDMS) model of a sequential anastomotic graft design using PIV technique.

Most of the studies in the literature are focused on the primary flow and its effect on wall shear stress (WSS). Less attention has been given to secondary flows, but its importance has been recognized by several authors, mostly through numerical studies. Chen *et al.*[20] found that swirling flow is a relevant factor for stent design since it can suppress flow disturbances. Zhao *et al.*[21] used numerical methods to study realistic configurations of the human carotid arterial bifurcation. They were able to identify a strong helical flow attributed to the asymmetry and curvature of the geometry. Chen *et al.*[22] and Lu *et al.*[23] studied secondary flows, comparing planar bifurcations and bifurcations out of the plane branches. Helical flow is observed in both cases, but while in the planar case symmetric helical patterns form along the daughter branches, in the non-planar case the patterns are asymmetric. In one of the few non-numerical studies, Morbiducci *et al.*[24] used phase-contrast magnetic resonance imaging to quantify *in vivo* aortic helical flows. As far as the present authors know, there are no studies that address the problem of secondary flows in the coronary arteries.

Most of the evidence on helical flow comes from numerical studies. However, CFD is inherently limited, specifically when secondary flows are involved, since limitations of the methods, accuracy of the geometry and mesh density may lead to erroneous numerical solutions. While some evidence was also found using *in vivo* approach, in some specific cases, there have been few attempts to identify and study secondary flows *in vitro*. *In vitro* studies are indispensable to interpret the flow in detail, adding an experimental perspective, allowing the evaluation of idealised geometries with specific features. *In vitro* studies are also important to establish benchmark cases for validation of numerical codes, and presently very few were performed for flows with secondary flows.

In the present chapter, an *in vitro* study is performed to characterize secondary flows (helical flow and vortexes) in a simplified planar model of the bifurcation of the left coronary artery. The flow is characterized by streak photography and μPIV. The experimental approach is complemented with numerical simulations. The numerical data, besides being compared with benchmark experimental data, fill gaps, due to technique limitations, of the experimental results. The design of the bifurcation is based on CT scans and on morphologic parameters available in literature and the 3D PDMS phantom model construction[25] follow a procedure previously described in **Chapter 2**. The effects of flow partition in the flow patterns, taking Murray's law flow partition as reference, are presented and their implications discussed. The effects of Reynolds number in flow behaviour are also analysed. WSS values were obtained from the numerical simulations in order to link them to the presence of secondary flows.

3.2 Materials and Methods

3.2.1 Design of the 3D LCA phantom model

The geometry studied is a simplification of a 3D model of a LCA (Figure 3.1). A significant variety of morphologies have been observed for the branching of the left main stem (LM) of the human LCA. Most frequently, the LM bifurcates into the left anterior descending (LAD) and into the circumflex arteries (LCx)[26-28]. Therefore, the geometry selected was a segment of the left coronary artery comprising LM and its bifurcation into LAD and LCx.

The LM length recorded in the majority of the studies varies from 10 to 15 mm [28-31]. In the present experimental study, it was mandatory to assure, upstream the bifurcation region, a fully developed flow, and, for that reason, the LM length was taken equal to 32.5 mm. Regarding to previous studies, the average LM diameter varies from 4 to 5 mm [28, 31-33], and the LAD diameter from 3.6 to 3.7 mm [30, 32].

The LM and LAD diameters were chosen according to the work of Dodge *et al.*[32], which reports diameters for the LM, LAD and LCx of 4.5 mm, 3.6 mm and 3.4 mm, respectively. To have a perfect match with Murray's law[34]:

$$D_{LM}^3 = D_{LAD}^3 + D_{LCx}^3 \tag{3.1}$$

where, D_{LM}^3, D_{LAD}^3 and D_{LCx}^3 are the diameters of the LM, LAD and LCx arteries, respectively, a small correction was introduced in the LAD diameter, 3.7 mm.

The angle between LAD and LCx branches (α) considered in this study is 90º. The angulation is asymmetrical as is depicted in Figure 3.1.

Due to the limited focal distance needed to perform µPIV, the geometry was downscaled by a factor of 2. Table 3.1 shows the dimensions of the base parameters of the 3D LCA simplified model used in the experimental flow studies.

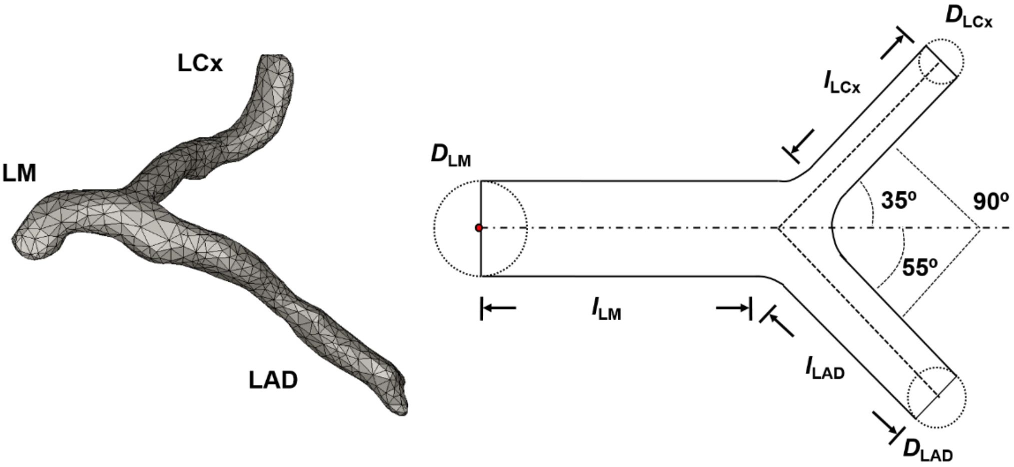

Figure 3.1. On the left, the 3D LCA model from a healthy patient and on the right, the based model for constructing the 3D LCA phantom used in the experimental and numerical studies.

Table 3.1. Dimensions of the 3D LCA phantoms under study.

Parameters		**3D LCA simplified model (mm)**
LM diameter	D_{LM}	2.25
LAD diameter	D_{LAD}	1.85
LCx diameter	D_{LCx}	1.72
Distance between LM and bifurcation	l_{LM}	32.5
Distance between bifurcation and LCx	l_{LCx}	32
Distance between bifurcation and LAD	l_{LAD}	32

3.2.2 3D phantom construction

The model was designed by computer-aided-design (CAD) software, SolidWorks®, and saved in STL format file. This file was used for further processing to produce the experimental model and the numerical mesh. The model material is the polymer poly(dimethylsiloxane), PDMS[35]. The PDMS refractive index was measured in an ABBE® (WYA-1S) digital refractometer, at a controlled temperature of 293 K. The PDMS model (Figure 3.2) was manufactured by the previously reported method (**Chapter 2**) that combines rapid prototyping by sterolithography with molding using sucrose[25]. The method used to convert the STL file into the numerical mesh is explained in the description of the numerical approach.

3.2.3 Fluid characterization

A dimethyl sulfoxide (DMSO)/water mixture was prepared using 52% DMSO and 48% water (*w/w*), in order to match the refractive index of PDMS[25], essential condition to eliminate visual distortion given by the curvature of the model walls. This mixture has also properties (density and viscosity) similar to blood at high shear rates. The viscosity of the solution was measured in an Anton Paar® Physica MCR301 Rotational Rheometer, at a control temperature of 293 K. Table 3.2 shows the relevant properties of the materials used in this study. Figure 3.2 shows the 3D LCA phantom.

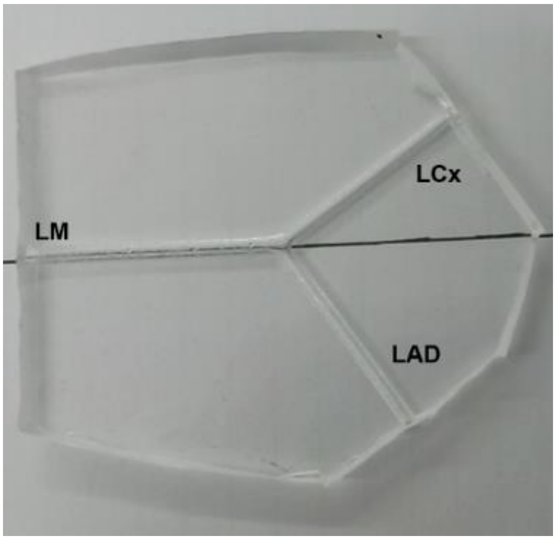

Figure 3.2. 3D LCA PDMS model used in the experiments.

Table 3.2. Relevant properties of the materials used in this study at 293K.

Materials	Refractive index	Density ($kg.m^{-3}$)	Viscosity (Pa·s)
DMSO/Water	1.4125	1057.5	3.08×10^{-3}
PDMS	1.4125	-	-

3.2.4 Flow rate selection

The flow in the bifurcation is characterized by the Reynolds number based on the inlet diameter:

$$Re = \frac{\rho \bar{U} D}{\mu} \tag{3.2}$$

where ρ is the fluid density, $\bar{U}$ the mean inlet velocity (mean velocity in the LM branch), D the main branch diameter and μ the dynamic viscosity.

The coronary flow rate is approximately 250 ml/min[36]. Here it is assumed that about 70% of the coronary flow rate (175 ml/min) passes through the left coronary artery, which, assuming blood viscosity of 0.0035 Pa.s, blood density of 1060 kg·m^{-3} and a LM diameter of 4.5 mm, corresponds to a Reynolds number of 250. A smaller Reynolds number of 50, without physiological relevance, was primarily studied to test the experimental methods with a smooth well behaved flow. A high Reynolds number of 440 was also studied to mimic conditions with accelerated heart rate. In the experiments, the flow rate was adjusted to fit these Reynolds numbers.

The flow partition in the outflow branches, inferred from Murray’s law, is:

$$\frac{Q_{LAD}}{Q_{LCx}} = \left(\frac{D_{LAD}}{D_{LCx}}\right)^3 \tag{3.3}$$

where, Q_{LAD} and Q_{LCx} are the flow rates in the daughter branches, and D_{LAD} and D_{LCx} the corresponding diameters.

In the first set of experiments performed, following Murray’s law, 55% of the inlet flow rate was leaving from LAD and 45 % from LCx. In order to find some relevant behaviour in a noncompliance case to Murray’s law, a distribution flow rate of 80% leaving from LAD and 20 % from LCx was explored. A limiting case, with 100% of the blood flowing through the LAD, was also analysed to clarify the nature of the flow patterns observed in the previous two cases. As explained in the following section, the flow rate in each branch can be independently set. In the limiting case, the flow rate is set to zero in the LCx.

3.2.5 Flow facility and µPIV procedure

To obtain velocity field measurements, the µPIV technique was used. The experimental setup, represented in Figure 3.3, was composed by an inverted epifluorescence microscope (DMI 5000M, Leica Microsystems GMBH), together with a dual ND:YAG (yttrium aluminium garnet) laser (dual Power 65-15, Dantec Dynamics) with a wavelength of 532nm as light source. The microscope objective was a 2.5× (NA = 0.07) to cover the whole bifurcation region under investigation, resulting in a visualization depth of 0.418 mm[37]. Two syringe pumps (Harvard Apparatus PHD ultra) were used to control and impose independently steady flow rates in the two daughter branches. The images were captured by a digital CCD camera (Dantec Dynamics) and processed on a computer with Dinamic Studio software. Flow visualization was performed by streak line photography. The same experimental setup (Figure 3.3) was used with exception of the camera and light source. The camera was a DFC350 Fx (Leica Microsystems GmBH) and the light source a continuous 100W mercury lamp. The experimental fluids used for both µPIV and flow visualization were the same, 52% DMSO/48% water (*w/w*), seeded with 100 ppm (*w/w*) fluorescent polystyrene tracer particles of 2 µm diameter for µPIV studies and 10 µm diameter for visualization studies. For µPIV experiments, for each flow rate, 100 pairs of images were acquired with a resolution of 2048 × 2048 pixels and exposure time in the range of $4 \leq \Delta t$ [µs] ≤ 20. Flow visualizations images were captured with exposure times in the range of $80 \leq \Delta t$ [ms] ≤ 180.

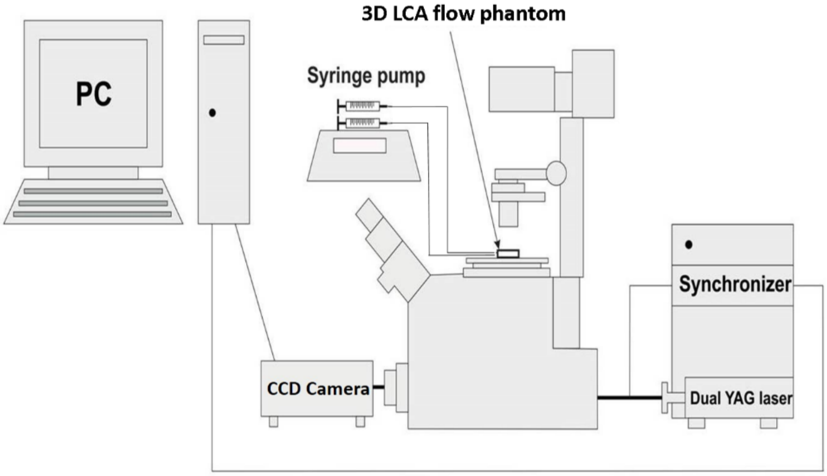

Figure 3.3. Diagram of the experimental setup used for µPIV experiments.

3.2.6 3D velocity fields reconstruction

The µPIV images were post-processed using *Dynamic Studio* V2.3 software (*Dantec Dynamics*). Each velocity field was obtained by averaging 100 pairs of images. The whole volume of the region of interest was divided in slices (6.059 x 6.059 mm). The scanning spatial resolution in the perpendicular direction to the µPIV images (z) was 250 µm.

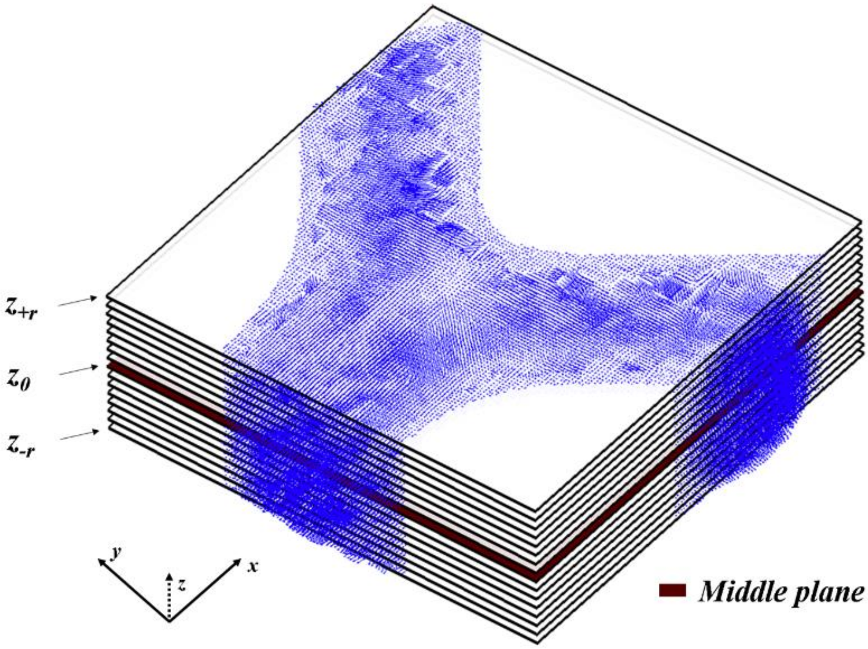

Figure 3.4. Scheme of the 3D velocity vectors reconstruction by a special compilation of 2D µPIV data slices.

The whole 3D volume velocity reconstruction was done stacking all 2D velocity field slices and completing the missing data between them by interpolation, using an R code created for that purpose. In this interpolation, and according to Figure 3.4, z_{-r} represents the reference plane (one of the walls of the phantom) where the interpolation starts, and z_{+r} the closing plane (the other wall of the phantom). The median plane of the phantom is represented by z_0.

3.2.7 Numerical approach

Numerical simulations were performed in the CFD package ANSYS® (version 15). The STL file containing the design of the model was imported into ANSYS® *Design Modeler* and converted into a solid model. In ANSYS® *Meshing*, the solid model was discretized into a mesh grid using the cut cell method. This method allows the creation of a predominantly hexahedral mesh with inflation layers to improve the accuracy in regions with high velocity gradients. The mesh created has 572 912 cells.

Blood was considered to be a Newtonian and incompressible fluid. The no-slip boundary condition was assumed at the artery walls, which were assumed to be rigid and motionless.

The fluid velocity is set at the inlet:

$$\bar{U} = \frac{Q_{LM}}{\pi \frac{D_{LM}^2}{4}} \tag{3.4}$$

where Q_{LM} is the blood flow rate in the LM.

The outflow boundary conditions are set by defining a flow partition based on equation (*3.3*) and by extrapolating the pressure and velocity components from the nodes in the interior of the mesh.

The limiting case, in which 100% of the flow leaves by the LAD, is implemented by using a no-slip boundary condition in the outlet of the LCx.

The Navier-Stokes equations were solved, assuming laminar regime, using the PISO algorithm[38]. The momentum equations were discretized by the QUICK scheme[39] and the pressure equation by the PRESTO! Scheme.

3.2.8 Flow characterization

To check if the inlet flow is fully developed, it was compared with the fully developed laminar velocity profile in a tube:

$$U_x = 2\overline{U}\left(1 - \left(\frac{\boldsymbol{r}}{R_{LM}}\right)^{\mathbf{2}}\right) \tag{3.5}$$

where r is the radial coordinate and R the radius of the LM.

The μPIV was able to determine two velocity components, U_x and U_y, while the CFD simulations were able to determine the three components of the velocity vector, U_x, U_y and U_z. The velocity magnitude, $\left|U_{xy}\right|$, was defined based on the x and y components:

$$\left|U_{xy}\right| = \sqrt{U_x^2 + U_y^2} \tag{3.6}$$

and the velocity magnitude, $|U|$, based on the three components:

$$|U| = \sqrt{U_x^2 + U_y^2 + U_z^2} \tag{3.7}$$

The axial and transversal components of the velocity in each branch were calculated to characterize and compare numerical and experimental velocity profiles. $U_{x_{LAD}}$ and $U_{x_{LCx}}$ represent the axial velocity component in LAD and LCx, respectively, while $U_{y_{LAD}}$ and $U_{y_{LCx}}$ the transversal components.

Helical flow is, by definition, the rotational motion of fluid oriented normal to the mainstream flow[40]. In a cross-section in the LAD branch, the velocity components of the rotational flow are $U_{y_{LAD}}$ and U_z. The magnitude of the rotational velocity,$|U_t|$, in the LAD branch is:

$$|U_t| = \sqrt{U_{y_{LAD}}^2 + U_z^2} \tag{3.8}$$

The analogous definition for the LCx branch is:

$$|U_t| = \sqrt{U_{y_{LCx}}^2 + U_z^2} \tag{3.9}$$

The mean inlet velocity, $\overline{U}$, was chosen as the reference velocity magnitude for the normalization of the velocity fields.

The wall shear stress was evaluated based on the numerically calculated magnitude of the shear stress components:

$$\tau_w = \sqrt{\tau_x^2 + \tau_y^2 + \tau_z^2} \tag{3.10}$$

3.3 Results and discussion

3.3.1 Velocity profiles

Murray's flow rate partition

3D simulation and µPIV data were compared, to evaluate the limitations of both methods and to reinforce the confidence in the results. Although the *z* velocity component was not taken from experimental data, due to the µPIV technique limitations, the other two components were reconstructed in 3D space (Figure 3.5) by the interpolation technique described in section.3.2.6.

According to Figure 3.5, and despite some unavoidable artifacts near the phantom walls, the 3D velocity field extracted from the µPIV data is in good agreement with the numerical results. Note that the velocity magnitude, $|U_{xy}|$, is normalized by the mean inlet velocity, $\overline{U}$.

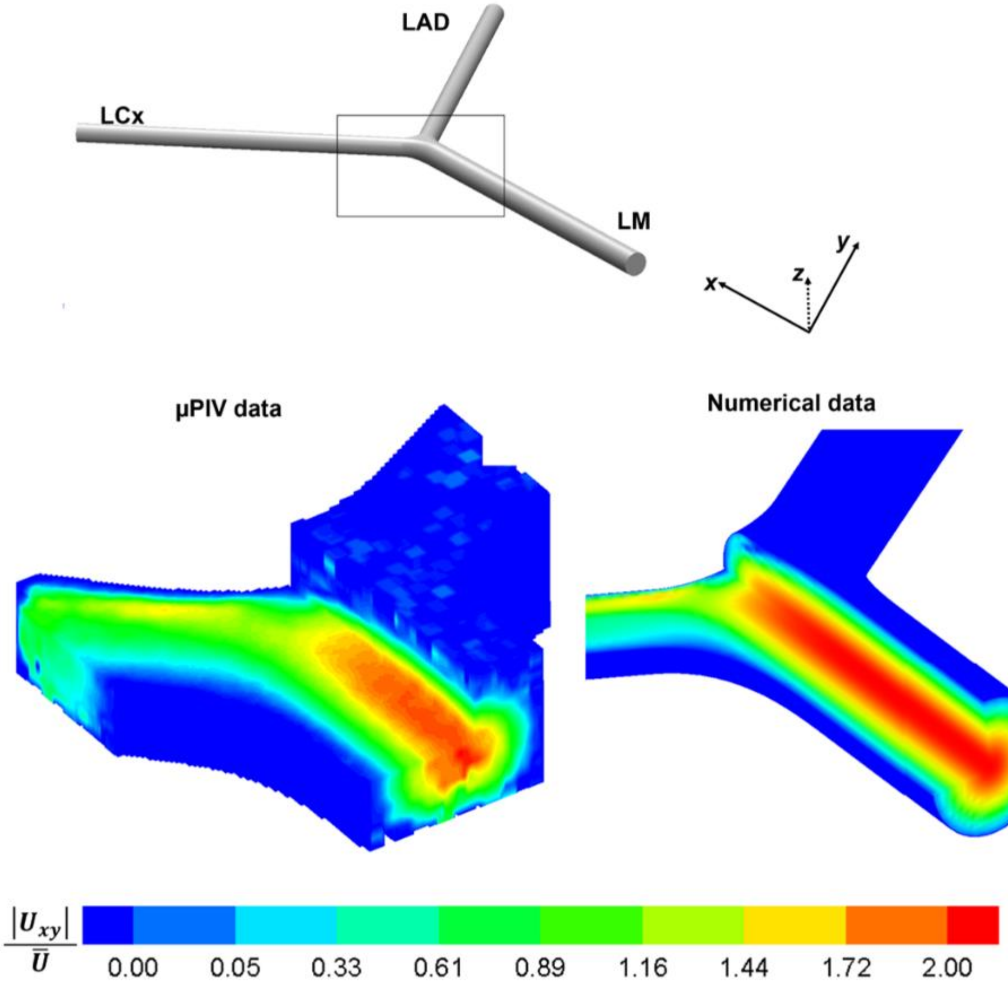

Figure 3.5. Experimental and numerical data of 3D velocity field contours (normalized magnitude of the *x* and *y* components) at the bifurcation region for Re = 440.

In order to verify whether the flow is fully developed upstream the bifurcation, the numerical and experimental data were analyzed in a cross-section 18 mm downstream the inlet and compared with the analytical equation for fully developed laminar flow in a tube. Experimental and numerical data shown in Figure 3.6c are in accordance with each other and with the analytical equation. A test to the quality of the data was done by comparing the flow rate value obtained from numerical data with that obtained by integrating the velocity profile captured in the µPIV measurements. The discrepancy between the values is within 5.9%. This small discrepancy can be attributed to background noise, wall reflection and positioning of the focusing plane, as well as to the uncertainty of syringe pump calibration.

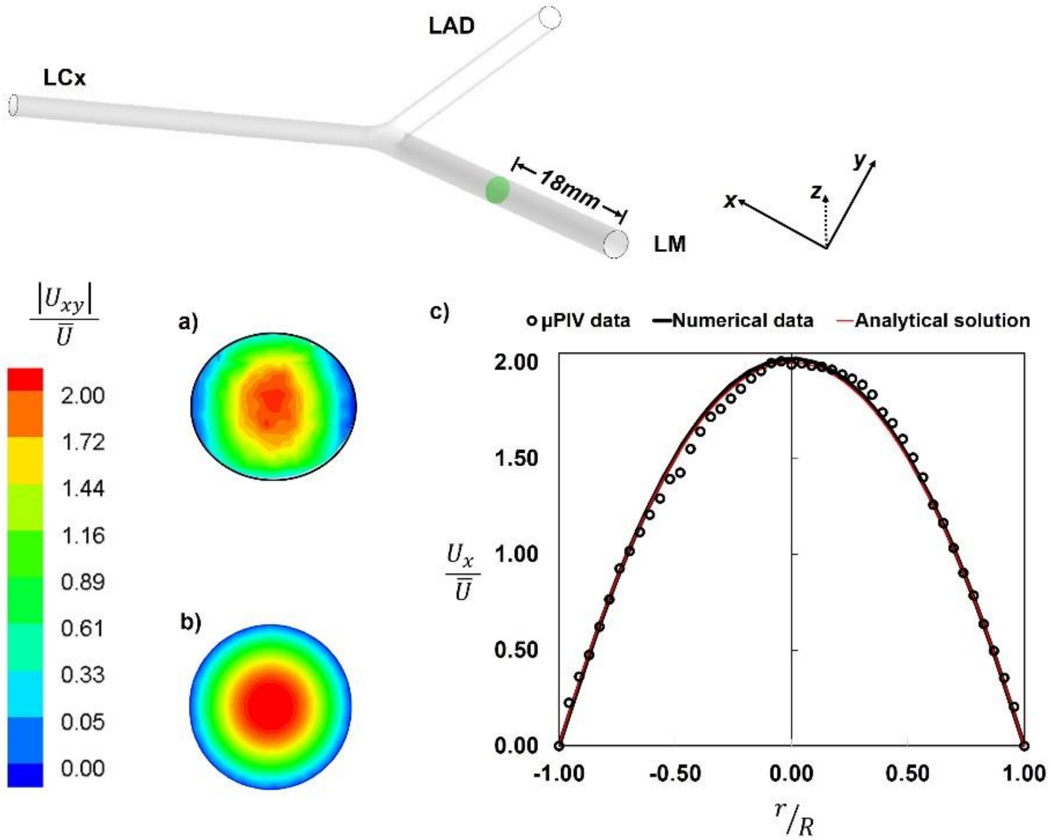

Figure 3.6. Experimental (a) and numerical (b) velocity field contours (normalized magnitude of the *x* and *y* components) in a cross-section extracted from LM branch at Re = 440 and comparison between measured and numerical normalized velocity axial profiles at the middle plane (c).

Effect of Reynolds number

Figure 3.7 shows, for comparison, experimental and numerical velocity contours at the middle plane for different Reynolds numbers. The numerical and µPIV results are in good agreement. The main flow from LM branch maintains its path upon reaching the bifurcation. When it approaches the bifurcation is divided into two streams, forming a stagnation point at the apex. As the Reynolds number increases, the normalized velocity magnitude also increases at the entrance of each branch, in regions close to the apex.

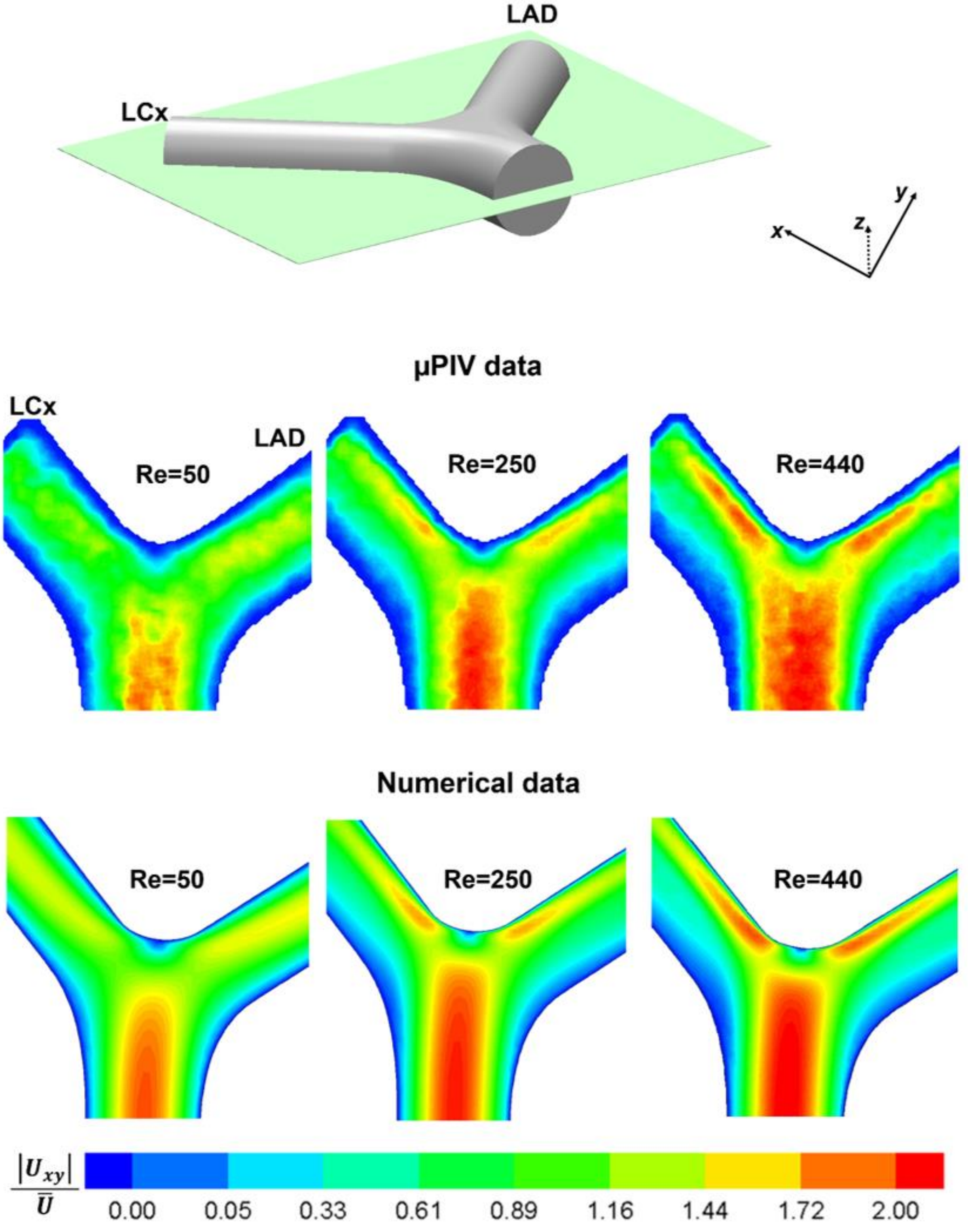

Figure 3.7. Experimental and numerical velocity fields (normalized magnitude of the *x* and *y* components) in the middle plane for different Reynolds number.

Through the velocity profiles presented in Figure 3.8, it is shown, quantitatively, that Reynolds number influences directly the velocity fields in both daughter branches. For the highest Reynolds number, there are, comparatively, more extended regions of low velocity. In blood vessels, these regions are prone to plaque formation and later to atherosclerosis diseases[41, 42].

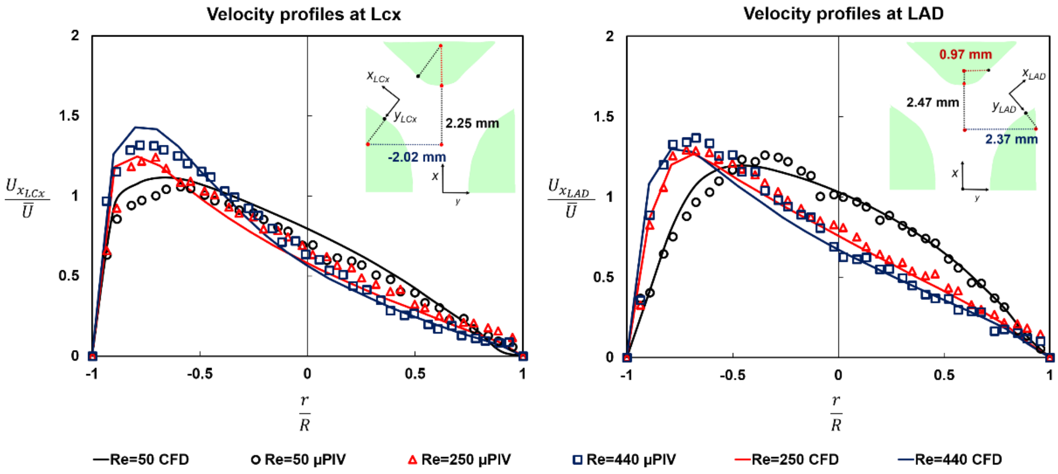

Figure 3.8. Experimental and numerical axial velocity profiles in LCx and LAD branches extracted from the middle plane for different Reynolds number.

Effect of flow rate partition

Although Murray’s law is an important reference in hemodynamics studies, there is a considerable variability among human patients, both in healthy and non-healthy cases. To study the connection between flow disturbances and Murray’s law deviation, numerical and μPIV experiments were conducted, with a flow distribution of 80% leaving from LAD and 20% from LCx at a Reynolds number of 250. Figure 3.9 shows both numerical and experimental velocity fields at the middle plane; an example following Murray’s law flow partition (55% leaving from LAD and 45% from LCx) is also shown for comparison. In the first case (Murray’s law deviation), as the flow approaches the bifurcation, the fluid goes mainly through LAD and by consequence a large region with low velocities at LCx entrance arises. This concomitance can originate the appearance of perceptible vortexes (see flow visualization section - 3.3.2).

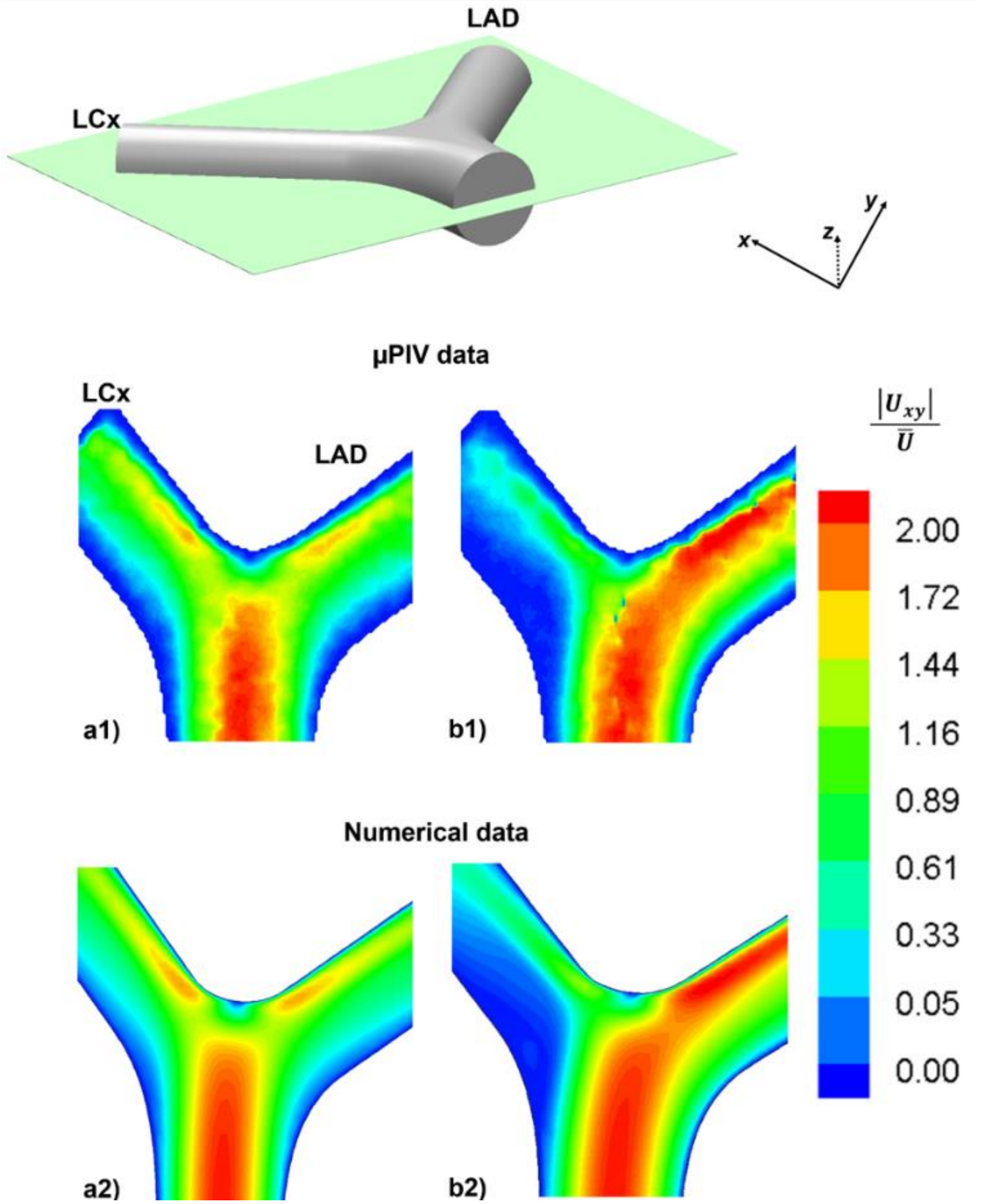

Figure 3.9. Experimental and numerical velocity field (normalized magnitude of the *x* and *y* components) at the middle plane extracted from the bifurcation region with a flow partition: a) according to Murray's law with $Q_{\mathrm{LAD}} = 0.55\ Q_{\mathrm{Inlet}}$ and $Q_{\mathrm{LCx}} = 0.45\ Q_{\mathrm{Inlet}}$ and; b) flow partition of $Q_{\mathrm{LAD}} = 0.8\ Q_{\mathrm{Inlet}}$ and $Q_{\mathrm{LCx}} = 0.2\ Q_{\mathrm{Inlet}}$ for Re=250.

Figure 3.10 shows velocity fields in cross-sections at the entrance of the branches; clearly, there is an uneven velocity distribution when the partition is 20% - 80%. The higher velocities are located in the bifurcation and at the inlet of LAD.

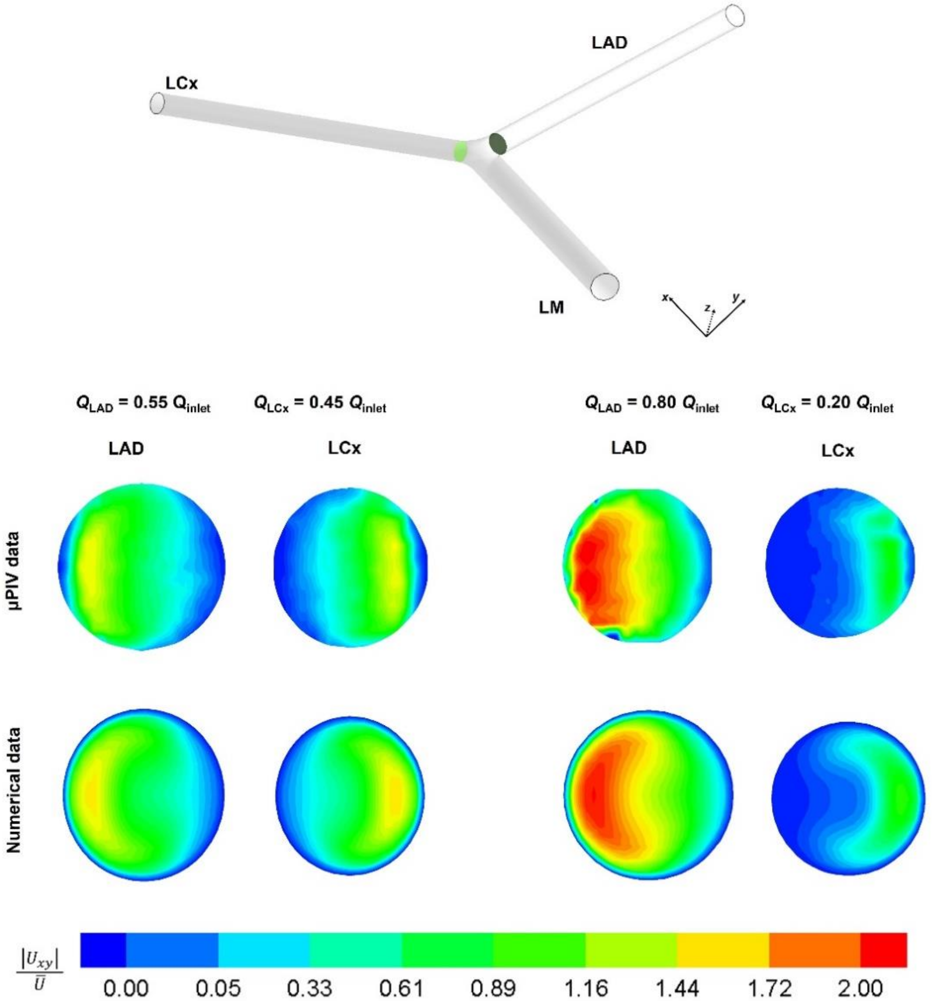

Figure 3.10. Comparison between experimental and numerical velocity fields (normalized magnitude of the *x* and *y* components), for different flow rate distributions, at LAD and LCx inlet cross-sections; Re=250.

In order to get a deeper flow analysis, normalized axial and transversal velocity components were extracted at the middle plane at the entrance of both branches (Figure 3.11 and Figure 3.12); $U_{x_{LAD}}$ and $U_{x_{LCx}}$ represent the axial velocity components in LAD and LCx, respectively, while $U_{y_{LAD}}$ and $U_{y_{LCx}}$ represent the transversal components.

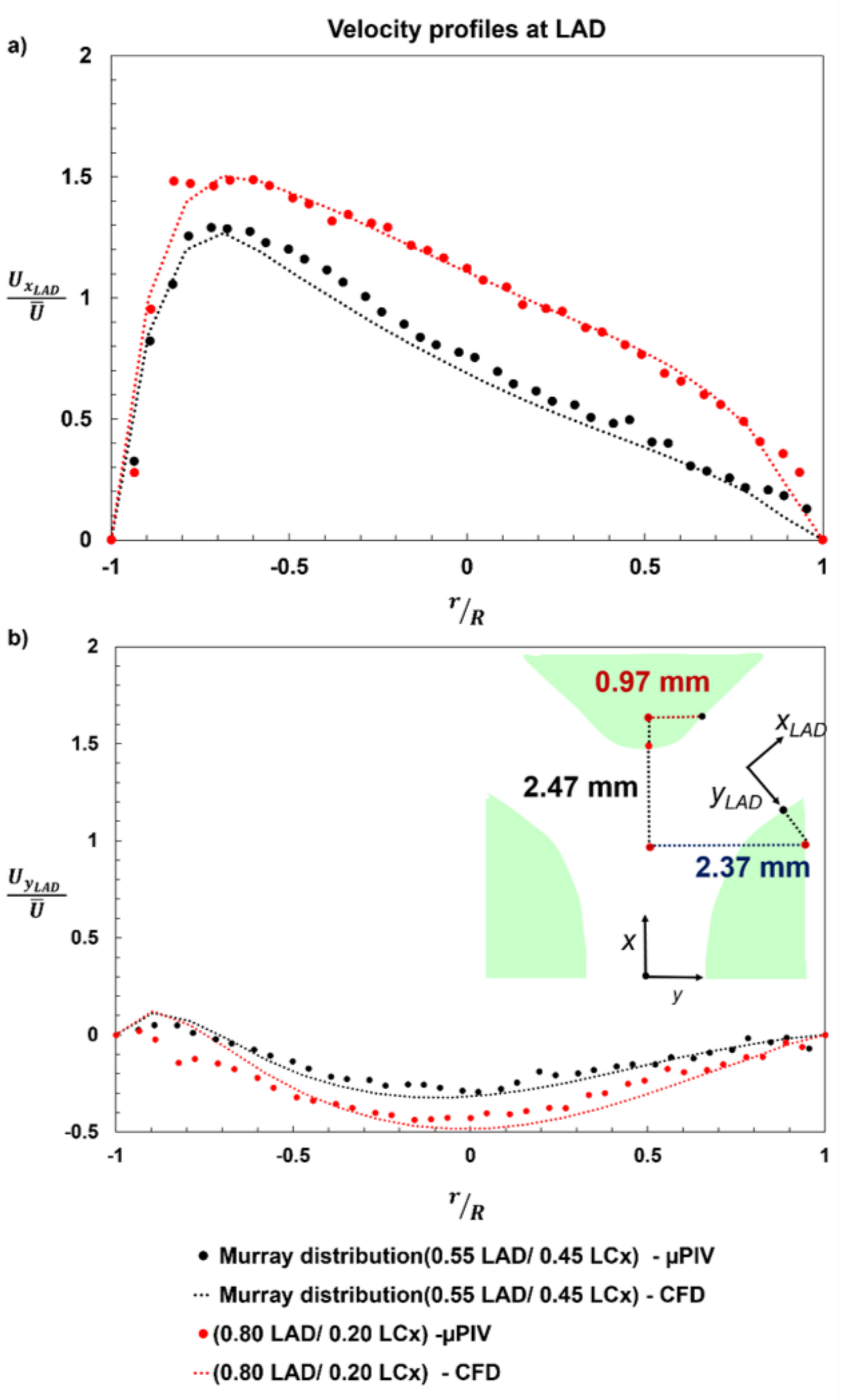

Figure 3.11. Comparison between experimental and numerical normalized velocity profiles at the entrance of LAD: a) axial velocity and b) transversal velocity profiles.

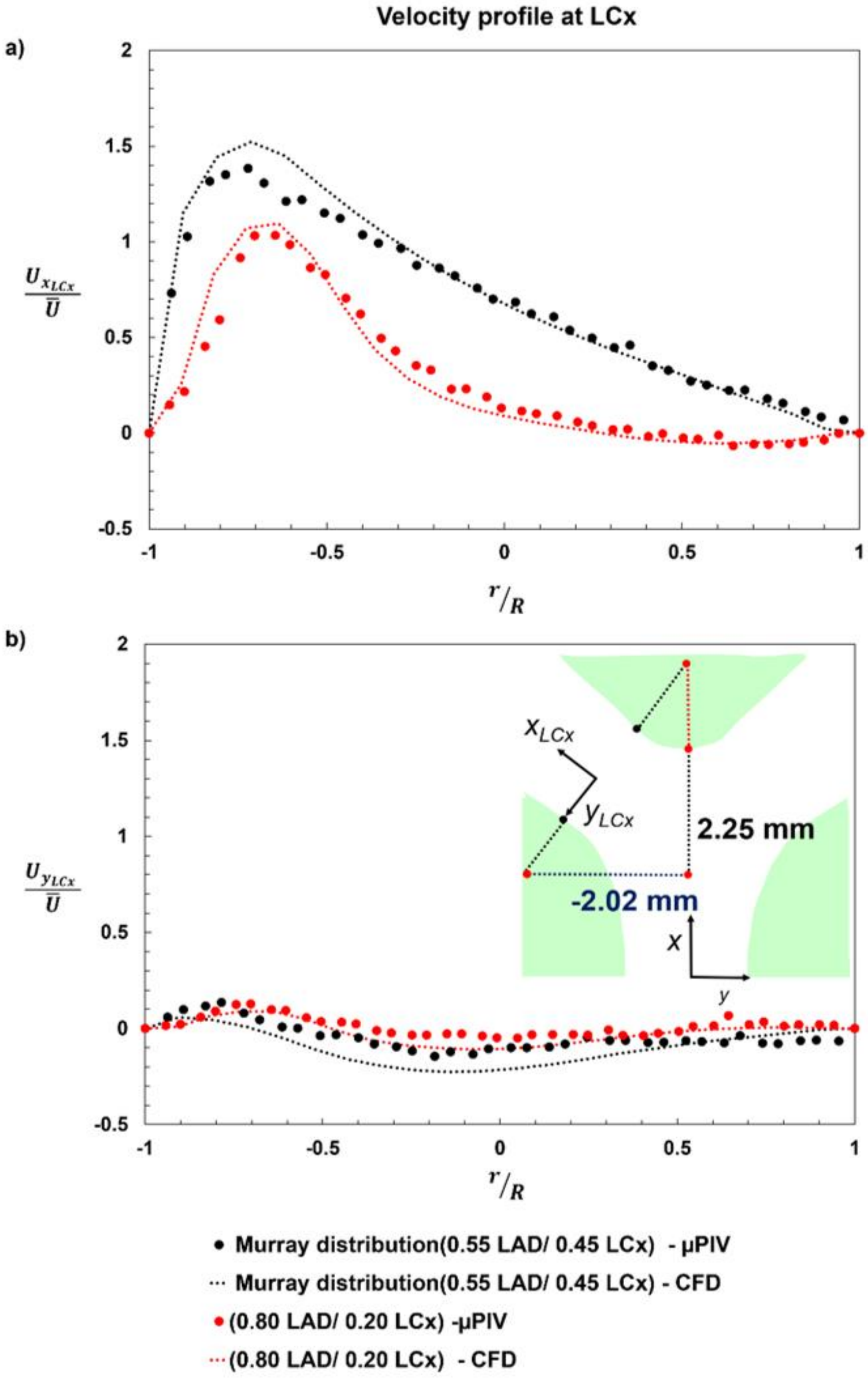

Figure 3.12. Comparison between experimental and numerical normalized velocity profiles at the entrance of LCx: a) axial and b) transversal velocity profiles.

In both flow partitions, the transversal velocity component is significant, particularly in the LAD, suggesting the occurrence of secondary flows. The numerical transversal component compares well with the experimental one, indicating that the numerical method can accurately predict the secondary flow.

The axial velocity component is high, particularly after the apex where the high stagnant pressure contributes to the acceleration of the flow along each branch. At the entrance of LCx, Figure 3.12, the results show that for the Murray's law deviation case, there are some axial negative velocity values, also suggesting the occurrence of secondary flows.

3.3.2 Flow visualization

Flow visualizations, made through streak line photography, were performed to look for secondary flow patterns in the flow at the bifurcation. The pictures for Murray's law flow partition (Figure 3.13) show that when the flow approaches the apex, it slows down and bifurcates. However, in the apex region, the deceleration of the faster flow, which comes from the axis region of the main artery, is not enough to curve in the flow plane and so an ascent trajectory develops, giving origin to a swirling flow. During the swirling path, the flow continues to slow down and reaches the wall of the branch, in the opposite direction of the apex, with low axial velocity. This description becomes unmistakable for increasing Reynolds number, particularly in the LCx, i.e., in the branch with less flow rate (high deceleration).

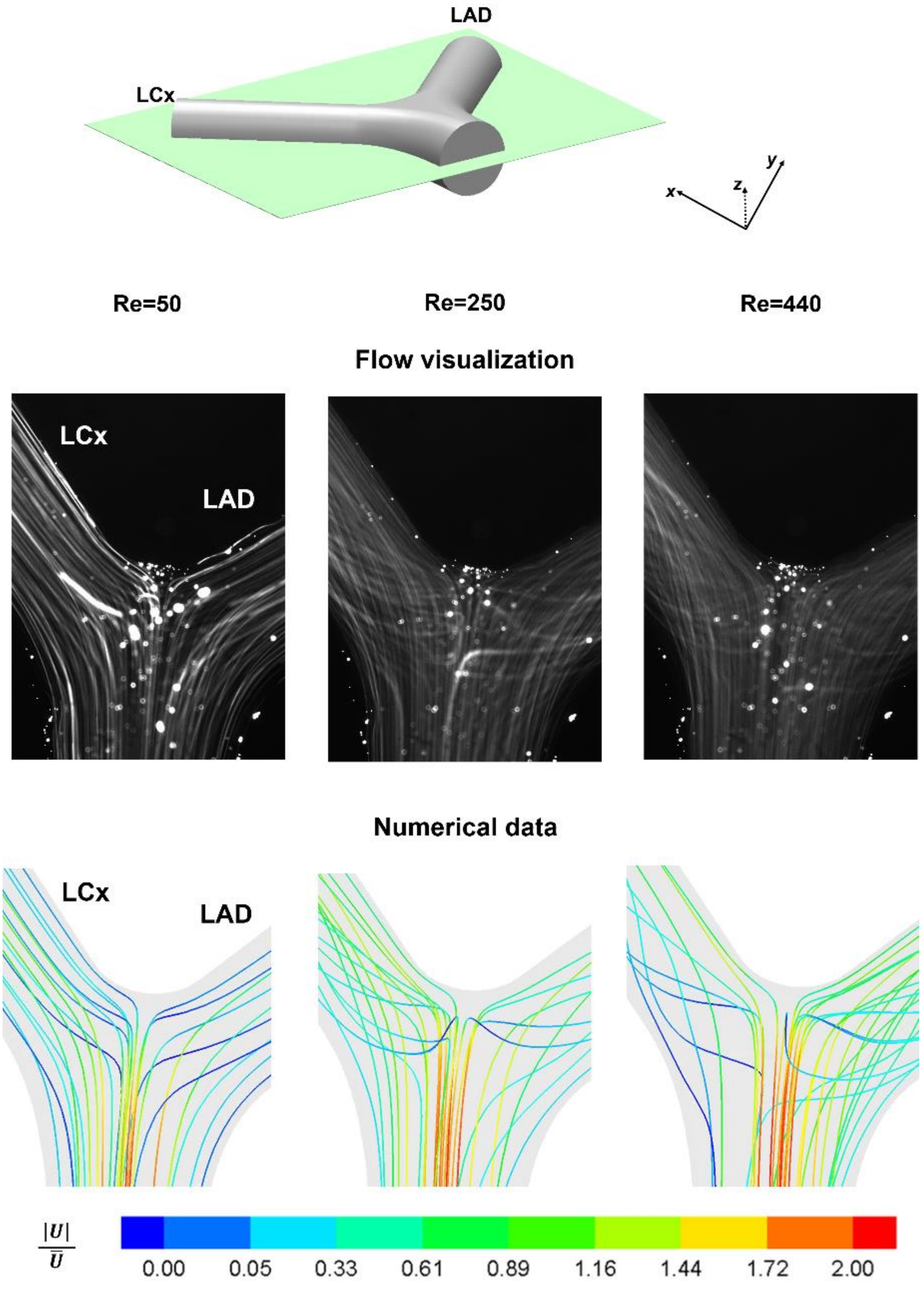

Figure 3.13. Effect of Reynolds number on the flow patterns in the bifurcation region, for the Murray's law flow partition.

Crossing path lines suggest that the fluid, in this trajectory, acquires a helical component. Figure 3.14 shows that the flow rotates around two axis along each branch confirming the occurrence of helical flow.

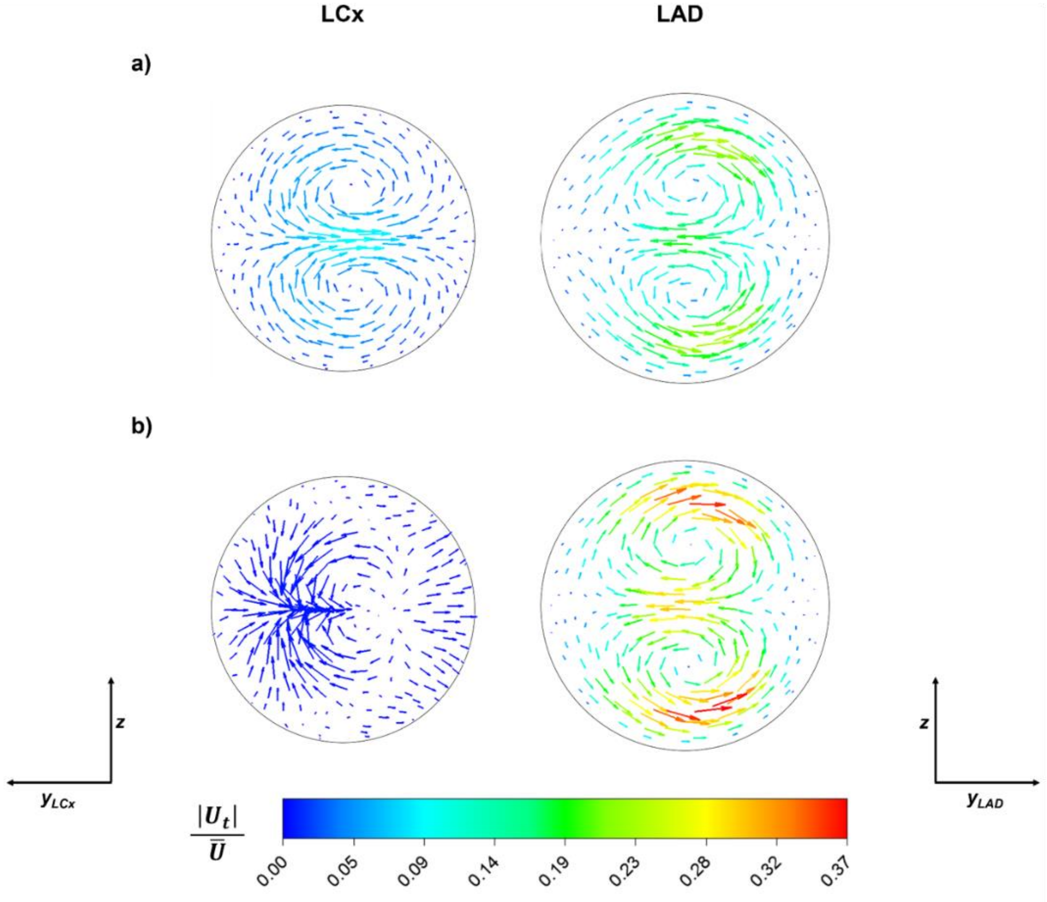

Figure 3.14. Velocity vectors (tangential to the plane) in cross sections of the branches: a) Re=250, Murray’s law flow partition; b) Re=250, flow partition of $Q_{\text{LAD}}=0.8Q_{\text{Inlet}}$. All cross-sections are located 2.1 diameters from the apex.

For the flow rate partition of 80% to LAD and 20 % to LCx (Figure 3.15), the behaviour described above is much more pronounced, in particular in the LCx branch. According to Figure 3.16a), an open vortex appears in the LCx and some fluid that enters the vortex returns to the LAD. For Reynolds number 440, it becomes patent the presence of helical vortices in the flow along LCx.

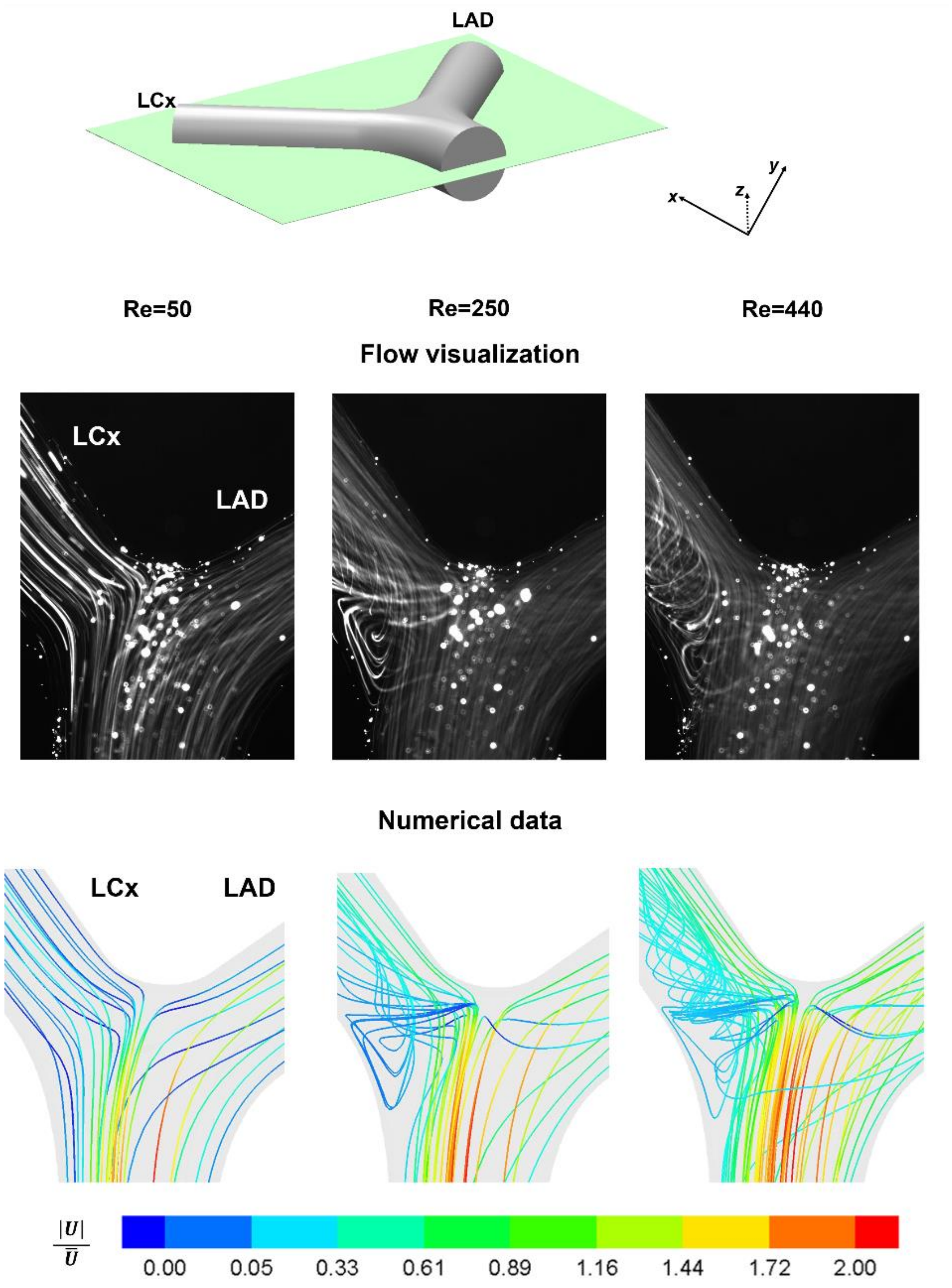

Figure 3.15. Effect of Reynolds number on the flow patterns in bifurcation region, for the distribution $Q_{\mathrm{LAD}}=0.8Q_{\mathrm{Inlet}}$ and $Q_{\mathrm{LCx}}=0.2Q_{\mathrm{Inlet}}$.

For the extreme flow rate distribution, 100% flow to LAD (Figure 3.17), the fluid recirculates inside the closed LCx before emerging into the LAD. For low Reynolds number the vortex is located at the entrance of the LCx while at increasing Reynolds it extends to inside the branch. These are open vortexes and, as in the case of the 20%-80% flow partition, the fluid that enters in the recirculation returns to the LAD. Details of the open vortexes, for Re=250, can be observed in Figure 3.16.

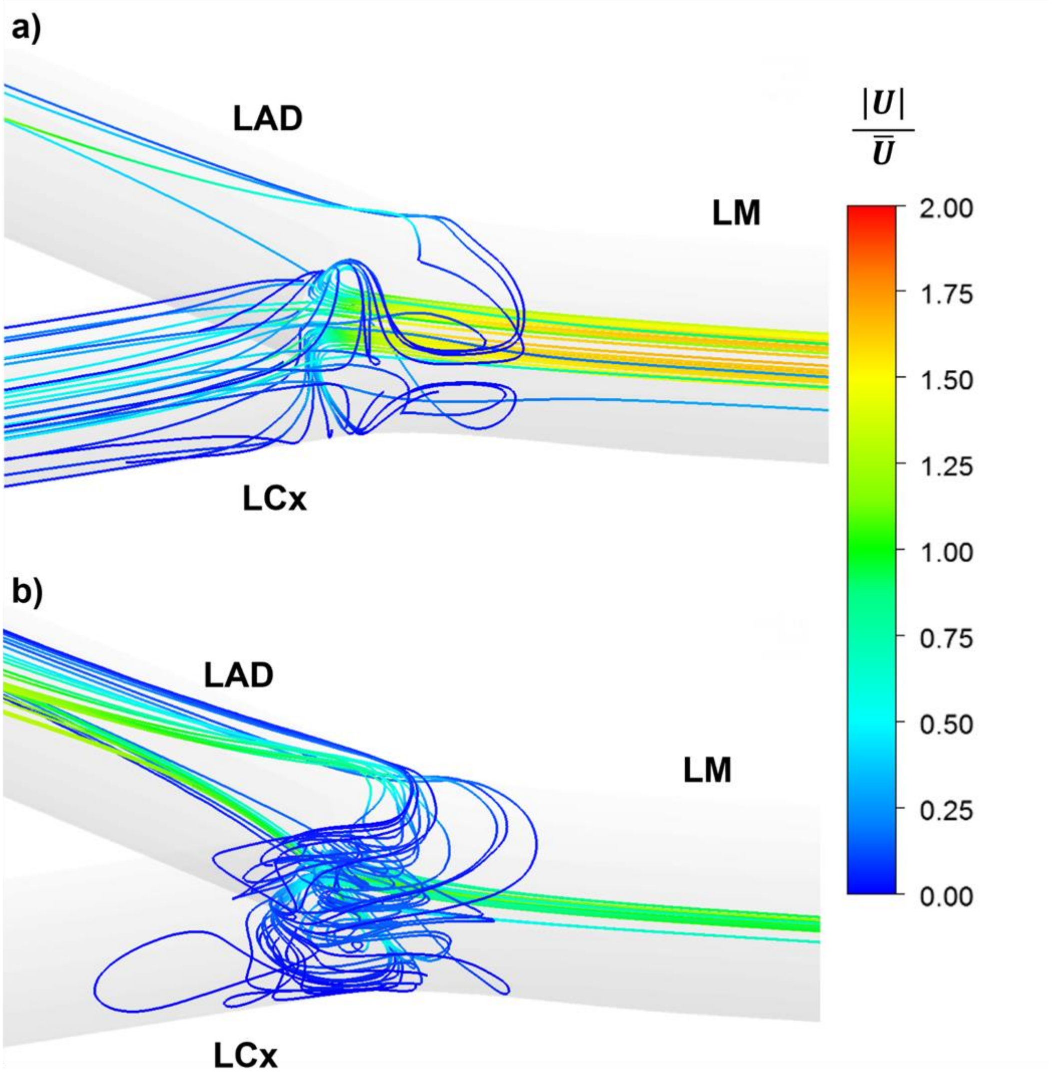

Figure 3.16. Figures showing in detail open vortexes for Re=250: a) flow partition of $Q_{\text{LAD}}=0.8Q_{\text{Inlet}}$; b) flow partition of $Q_{\text{LAD}}=Q_{\text{Inlet}}$.

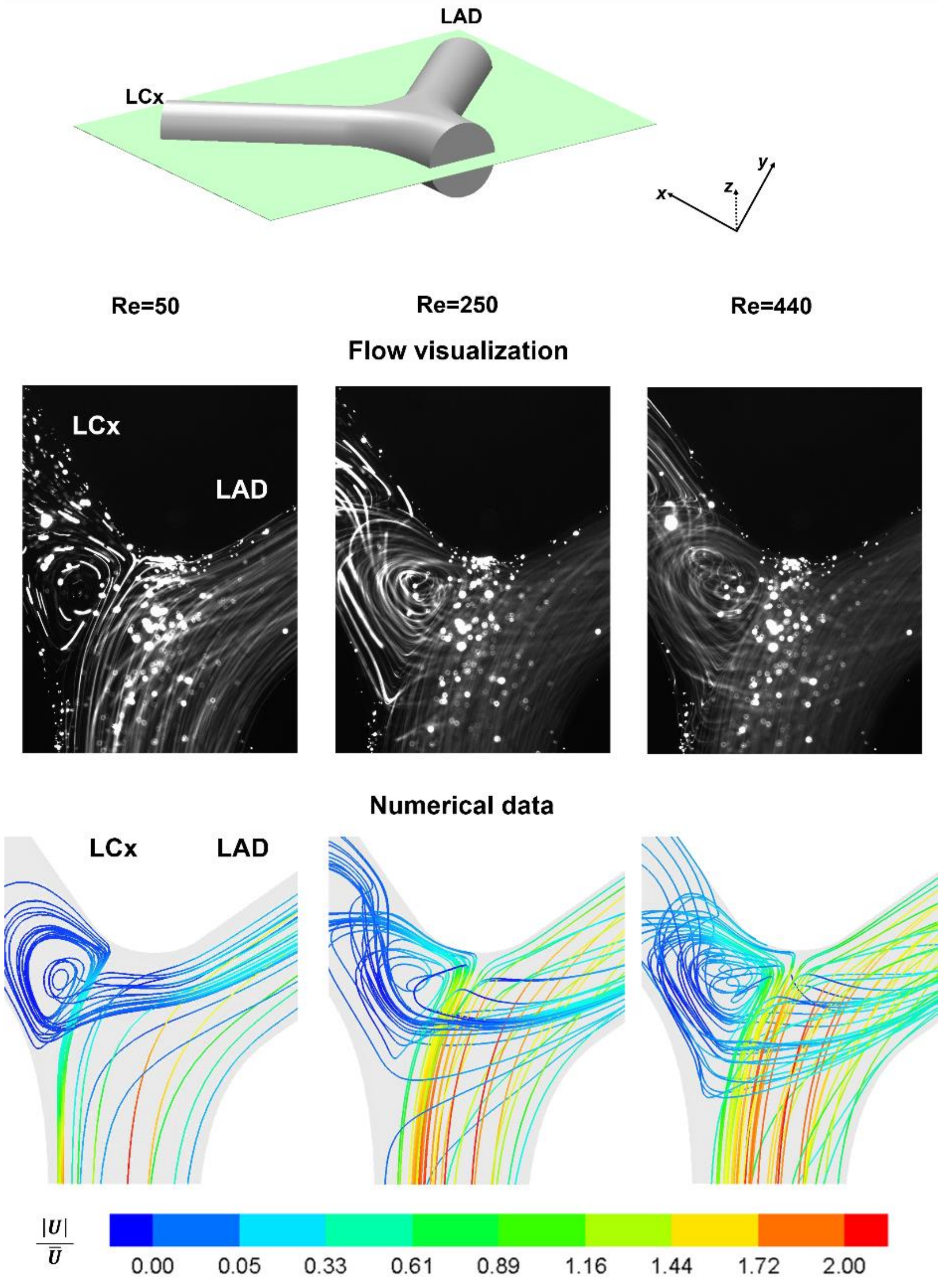

Figure 3.17. Effect of Reynolds number on the flow patterns in the bifurcation region, for the distribution $Q_{\mathrm{LAD}}=Q_{\mathrm{Inlet}}$ and $Q_{\mathrm{LCx}}=0$.

Several authors have been studying the impact of swirling flow in the circulatory system[20, 22, 23, 40]. Coronary bifurcation lesion is one of the main causes of coronary stenosis. Local abnormal blood flow at coronary bifurcation sites and its interaction with cells at the artery wall are important issues to understand how these lesions develop. From the present study, the swirling flow appears to be influenced by the flow distribution between the daughter branches and it is notorious as the Reynolds number increases. In a pathological context, Paul *et al.*[43] state that a strong swirling flow is a potential risk of stroke in stenosed arteries. However, Chen *et al*.[20] proposed that the spiral flow in the ascending aorta can eliminate stagnation flow regions and prevent the accumulation of plaques on the wall. Liu *et al*.[40] also demonstrated that spiral or swirling flows may play a positive role in the transport of oxygen to the arterial wall, having a physiological significance in the aorta wall avoiding atherosclerotic plaques deposition.

The results of the present chapter suggest that, for the typical Reynolds number in the left coronary artery (Re=250) and Murray's Law flow partition, the flow has a helical component in the LCx and in the LAD. In some extreme, but possible situations (high Reynolds numbers and non-Murray partition of the flow rates), open vortexes may appear in the less irrigated branch. These results were observed in steady flow. Numerical simulations (results not shown) demonstrate that oscillatory flow enhances the effects, leading to vortexes that oscillate in size. Wall shear stress has a helical component and an oscillatory pattern, which results from the continuous expansion and recoil of the vortexes.

3.3.3 Wall shear stress

To complement this study, the normalized wall shear stress along the wall of the arteries was studied for different Reynolds numbers. The normalization of the wall shear stress, τ_w, was made taking the undisturbed wall shear stress at the LM branch, τ_{LM}, as reference. Previous *in vitro* and *in vivo* studies locate the atherosclerosis mostly within regions of disturbed blood flow, where WSS is low.

Figure 3.18 shows the normalized WSS contours divided into two different colored zones: a green zone highlighting the region with a normalized WSS below 0.4 and a blue zone for higher values. The results indicate that, at regions opposite to the flow divider, low WSS values occur. Correlating these results with the path lines depicted above, it is possible to state that the region with the lowest WSS coincide with the region where the vortex appears. This becomes more evident as Reynolds number increases, particularly in the LCx branch. For the Murray's law deviation case, the helical flow intensifies along LCx branch (20 % Q_{Inlet}) and this is also the region where the values of WSS are smaller.

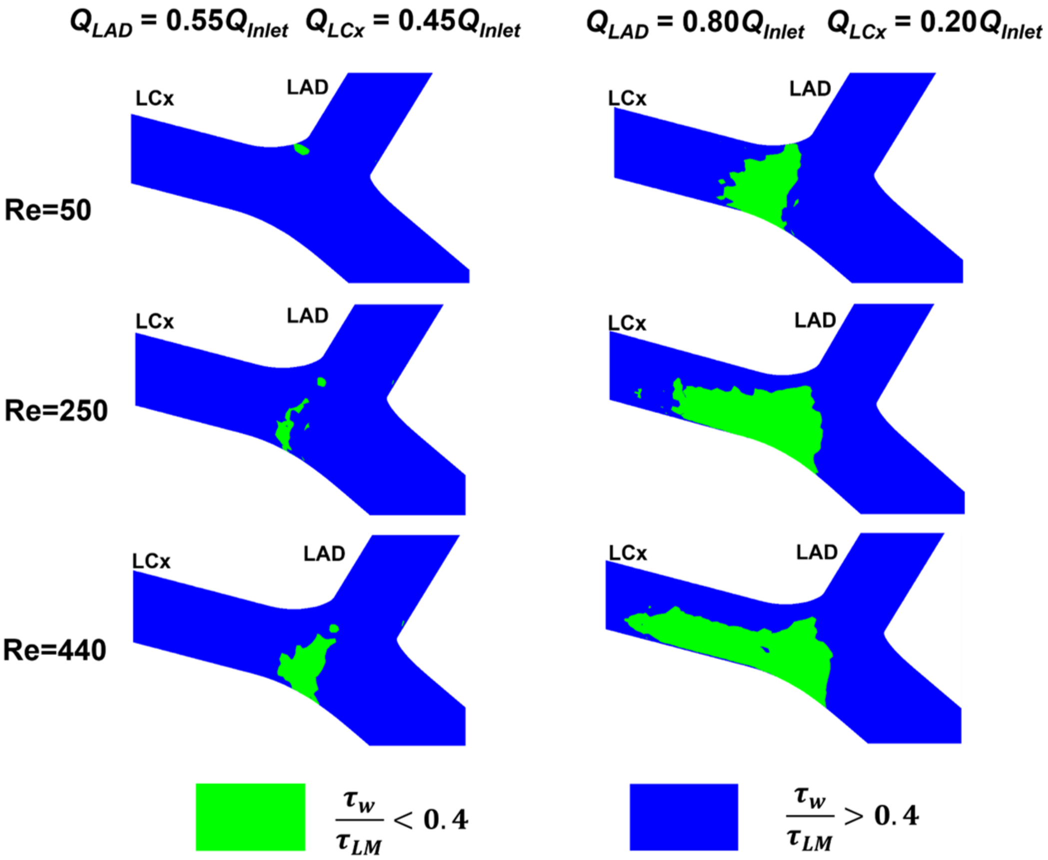

Figure 3.18. Normalized WSS fields for different flow rate distributions and different Reynolds number in the bifurcation region.

3.4 Conclusions

In this chapter, the flow in a simplified model of the left coronary artery bifurcation was studied by numerical methods and by an *in vitro* extensive analysis of the flow pattern through µPIV and streak line photography techniques. Different flow conditions were analysed: different flow distributions, having the Murray's law flow partition as reference, and different Reynolds numbers. Experimental and numerical velocity profiles and contours were extracted and compared and a good agreement was found between both methods. Additionally, vortexes and path line crossing (suggesting the presence of helical flow) were observed in visualization by streak line photography. Detailed numerical results confirmed the presence of an open vortex in the LCx branch and helical flow in both branches.

The present experimental results can be used as a benchmark case to validate numerical simulations of flow in bifurcations. They are also a reference for comparison in future numerical and experimental studies of more complex flows in bifurcations.

When the flow approaches the bifurcation, it is divided into two streams, giving origin to a stagnation point at the apex and creating regions, opposite to the flow divider, of low velocity and WSS values. These regions become larger as the Reynolds number increases, as expected. The deceleration of the main flow, in regions close to the apex, originates an open vortex, visible in the LCx branch for increasing Reynolds number.

When the flow distribution deviates from Murray's law, a remarkable swirling flow occurs in both branches. The swirling flow develops in regions of low WSS. The effect of these secondary flows in regions propitious to plaque formation, and consequently prone to atherosclerosis, should be further investigated. Due to these secondary flows, the wall shear stress direction, distribution and temporal evolution are highly complex and may have an important role in the interaction of blood with the wall cells of the artery, a factor that has been neglected in most studies.

Acknowledgements

The authors gratefully acknowledge the funding by FEDER through the Operational Programme for Competitiveness Factors – COMPETE, ON.2 - O Novo Norte - North Portugal Regional Operational Programme and National Funds through FCT-Foundation for Science and Technology under the projects: PEst-OE/EME/UI0532, NORTE-07-0124-FEDER-000025-RL2_ Environment&Health and PTDC/EME-MFE/102974/2008.

Notation

Symbol	Definition
Δt	Time interval
ρ	Fluid density
D	Main branch diameter
D_{LM}	LM diameter
D_{LAD}	LAD diameter
D_{LCx}	LCx diameter
l_{LM}	Distance between LM inlet and bifurcation
l_{LAD}	Distance between bifurcation and LAD outlet
l_{LCx}	Distance between bifurcation and LCx outlet
μ	Dynamic viscosity
Q_{LM}	Flow rate in the LM
Q_{LAD}	Flow rate in the LAD
Q_{LCx}	Flow rate in the LCx
r	Radial coordinate
R	LM radius
$\bar{U}$	Mean inlet velocity in the LM branch
U_{x}	x velocity component
U_{y}	y velocity component
U_{z}	z velocity component
$\lvert U_{xy} \rvert$	Velocity magnitude based on the x and y components
$\lvert U \rvert$	Velocity magnitude based on the three components (x,y and z)

$U_{\mathrm{x}_{\mathrm{LAD}}}$	Axial velocity at LAD
$U_{\mathrm{x}_{\mathrm{LCx}}}$	Axial velocity at LCx
$U_{\mathrm{y}_{\mathrm{LAD}}}$	Transversal velocity at LAD
$U_{\mathrm{y}_{\mathrm{LCx}}}$	Transversal velocity at LCx
$\lvert U_t \rvert$	The magnitude of the rotational velocity
τ_w	Magnitude of the wall shear stress
z	z-coordinate
z_0	Median plane of the phantom
$z_{-\mathrm{r}}$	Reference plane (phantom wall) where the interpolation starts
$z_{+\mathrm{r}}$	The closing plane (the other phantom wall)

References

1. Ku, D.N., Blood flow in arteries. Annual Review of Fluid Mechanics, 1997. 29: p. 399-434.
2. Brunette, J., R. Mongrain, J. Laurier, et al., 3D flow study in a mildly stenotic coronary artery phantom using a whole volume PIV method. Med Eng Phys, 2008. 30(9): p. 1193-200.
3. Shalman, E., M. Rosenfeld, E. Dgany and S. Einav, Numerical modeling of the flow in stenosed coronary artery. The relationship between main hemodynamic parameters. Computers in Biology and Medicine, 2002. 32(5): p. 329-344.
4. Banerjee, R.K., K.D. Ashtekar, T.A. Helmy, et al., Hemodynamic diagnostics of epicardial coronary stenoses: in-vitro experimental and computational study. Biomed Eng Online, 2008. 7: p. 24.
5. Sayed Razavi, M. and E. Shirani, Development of a general method for designing microvascular networks using distribution of wall shear stress. J Biomech, 2013. 46(13): p. 2303-9.
6. Zhang, J.M., L.P. Chua, D.N. Ghista, et al., Validation of numerical simulation with PIV measurements for two anastomosis models. Med Eng Phys, 2008. 30(2): p. 226-47.

7. Bale-Glickman, J., K. Selby, D. Saloner and O. Savas, Experimental flow studies in exact-replica phantoms of atherosclerotic carotid bifurcations under steady input conditions. J Biomech Eng, 2003. 125(1): p. 38-48.
8. Chiastra, C., S. Morlacchi, D. Gallo, et al., Computational fluid dynamic simulations of image-based stented coronary bifurcation models. J R Soc Interface, 2013. 10(84): p. 20130193.
9. Gijsen, F.J., J.C. Schuurbiers, A.G. van de Giessen, et al., 3D reconstruction techniques of human coronary bifurcations for shear stress computations. J Biomech, 2014. 47(1): p. 39-43.
10. van der Giessen, A.G., H.C. Groen, P.A. Doriot, et al., The influence of boundary conditions on wall shear stress distribution in patients specific coronary trees. J Biomech, 2011. 44(6): p. 1089-95.
11. Buchmann, N.A., C. Atkinson, M.C. Jeremy and J. Soria, Tomographic particle image velocimetry investigation of the flow in a modeled human carotid artery bifurcation. Experiments in Fluids, 2011. 50(4): p. 1131-1151.
12. Banerjee, R.K., L.H. Back, M.R. Back and Y.I. Cho, Physiological flow simulation in residual human stenoses after coronary angioplasty. J Biomech Eng, 2000. 122(4): p. 310-20.
13. Berthier, B., R. Bouzerar and C. Legallais, Blood flow patterns in an anatomically realistic coronary vessel: influence of three different reconstruction methods. J Biomech, 2002. 35(10): p. 1347-56.
14. Chaichana, T., Z. Sun and J. Jewkes, Computation of hemodynamics in the left coronary artery with variable angulations. J Biomech, 2011. 44(10): p. 1869-78.
15. Perktold, K., M. Hofer, G. Rappitsch, et al., Validated computation of physiologic flow in a realistic coronary artery branch. Journal of Biomechanics, 1997. 31(3): p. 217-228.
16. Lima, R., S. Wada, K. Tsubota and T. Yamaguchi, Confocal micro-PIV measurements of three-dimensional profiles of cell suspension flow in a square microchannel. Measurement Science and Technology, 2006. 17(4): p. 797-808.
17. Park, J.S., C.K. Choi and K.D. Kihm, Optically sliced micro-PIV using confocal laser scanning microscopy (CLSM). Experiments in Fluids, 2004. 37(1): p. 105-119.
18. Sugii, Y., R. Okuda, K. Okamoto and H. Madarame, Velocity measurement of both red blood cells and plasma of in vitro blood flow using high-speed micro PIV technique. Measurement Science and Technology, 2005. 16(5): p. 1126-1130.
19. Kabinejadian, F., F. Cui, Z. Zhang, et al., A novel carotid covered stent design: in vitro evaluation of performance and influence on the blood flow regime at the carotid artery bifurcation. Ann Biomed Eng, 2013. 41(9): p. 1990-2002.

20. Chen, Z., Y. Fan, X. Deng and Z. Xu, Swirling flow can suppress flow disturbances in endovascular stents: a numerical study. ASAIO J, 2009. 55(6): p. 543-9.
21. Zhao, S.Z., X.Y. Xu, A.D. Hughes, et al., Blood flow and vessel mechanics in a physiologically realistic model of a human carotid arterial bifurcation. J Biomech, 2000. 33(8): p. 975-84.
22. Chen, J. and X.Y. Lu, Numerical investigation of the non-Newtonian blood flow in a bifurcation model with a non-planar branch. J Biomech, 2004. 37(12): p. 1899-911.
23. Lu, Y., X. Lu, L. Zhuang and W. Wang, Breaking symmetry in non-planar bifurcations: distribution of flow and wall shear stress. Biorheology, 2002. 39(3-4): p. 431-6.
24. Morbiducci, U., R. Ponzini, G. Rizzo, et al., Mechanistic insight into the physiological relevance of helical blood flow in the human aorta: an in vivo study. Biomech Model Mechanobiol, 2011. 10(3): p. 339-55.
25. Doutel, E., J. Carneiro, M.S.N. Oliveira, et al., Fabrication of 3d Mili-Scale Channels for Hemodynamic Studies. Journal of Mechanics in Medicine and Biology, 2015. 15(1): p. 1550004.
26. Angelini, P., Coronary artery anomalies: an entity in search of an identity. Circulation, 2007. 115(10): p. 1296-305.
27. Baptista, C.A., L.J. DiDio and J.C. Prates, Types of division of the left coronary artery and the ramus diagonalis of the human heart. Jpn Heart J, 1991. 32(3): p. 323-35.
28. Reig, J. and M. Petit, Main trunk of the left coronary artery: anatomic study of the parameters of clinical interest. Clin Anat, 2004. 17(1): p. 6-13.
29. Ortale, J.R., J.M. Filho, A. Maria, et al., Anatomy of the lateral , diagonal and anterosuperior arterial branches of the left ventricle of the human heart. 2005. 20(2): p. 149-158.
30. Ballesteros, L.E. and L.M. Ramirez, Morphological expression of the left coronary artery: a direct anatomical study. Folia Morphol (Warsz), 2008. 67(2): p. 135-42.
31. McAlpine, W.A., Heart and Coronary Arteries: An Anatomical Atlas for Clinical Diagnosis, Radiological Investigation, and Surgical Treatment. 1975: Springer-Verlag.
32. Dodge, J.T., Jr., B.G. Brown, E.L. Bolson and H.T. Dodge, Lumen diameter of normal human coronary arteries. Influence of age, sex, anatomic variation, and left ventricular hypertrophy or dilation. Circulation, 1992. 86(1): p. 232-46.
33. Dombe, D.D., T. Anitha, S.D. Dombe and M.V. Ambiye, Clinically relevant morphometric analysis of left coronary artery. International Journal of Biological and Medical Research (IJBMR), 2012. 3: p. 1327-1330.

34. Murray, C.D., The physiologtcal principle of minimom work I The vascular system and the cost of blood volume. Proceedings of the National Academy of Sciences of the United States of America, 1926. 12: p. 207-214.
35. McDonald, J.C., D.C. Duffy, J.R. Anderson, et al., Fabrication of microfluidic systems in poly(dimethylsiloxane). Electrophoresis, 2000. 21(1): p. 27-40.
36. Ramanathan, T. and H. Skinner, Coronary blood flow. Continuing Education in Anaesthesia, Critical Care & Pain, 2005. 5(2): p. 61-64.
37. Fuchs, E., J. Jaffe, R. Long and F. Azam, Thin laser light sheet microscope for microbial oceanography. Opt Express, 2002. 10(2): p. 145-54.
38. Issa, R.I., Solution of the implicitly discretised fluid flow equations by operator-splitting. Journal of Computational Physics, 1986. 62(1): p. 40-65.
39. Leonard, B.P., Order of Accuracy of Quick and Related Convection-Diffusion Schemes. Applied Mathematical Modelling, 1995. 19(11): p. 640-653.
40. Liu, X., Y. Fan and X. Deng, Effect of spiral flow on the transport of oxygen in the aorta: a numerical study. Ann Biomed Eng, 2010. 38(3): p. 917-26.
41. Pielhop, K., M. Klaas and W. Schroder, Analysis of the unsteady flow in an elastic stenotic vessel. European Journal of Mechanics B-Fluids, 2012. 35(0): p. 102-110.
42. Palmen, D.E.M., F.N. Vandevosse, J.D. Janssen and M.E.H. Vandongen, Analysis of the Flow in Stenosed Carotid-Artery Bifurcation Models - Hydrogen-Bubble Visualization. Journal of Biomechanics, 1994. 27(5): p. 581-590.
43. Paul, M.C. and A. Larman, Investigation of spiral blood flow in a model of arterial stenosis. Med Eng Phys, 2009. 31(9): p. 1195-203.

4

Chapter

"*No man is an island.*"

— John Donne

Link between deviations from Murray's Law and occurrence of low WSS regions in LCA[*]

---

[*] E. Doutel, S.IS. Pinto, J. Carneiro, JBLM. Campos, JM. Miranda
Link between deviations from Murray's Law and occurrence of low WSS regions in LCA, **Journal of Theoretical Biology**, http://dx.doi.org/10.1016/j.jtbi.2016.04.038, 2016.

4

Link between deviations from Murray's Law and occurrence of low WSS regions in the LCA

Abstract

Murray developed two laws for the geometry of bifurcations in the circulatory system. Based on the principle of energy minimization, Murray found restrictions for the relation between the diameters and also between the angles of the branches. It is known that bifurcations are prone to the development of atherosclerosis, in regions associated to low wall shear stresses (WSS) and high oscillatory shear index (OSI). These indicators (size of low WSS regions, size of high OSI regions and size of high helicity regions) were evaluated in this chapter. All of them were normalized by the size of the outflow branches. The relation between Murray's laws and the size of low WSS regions was analysed in detail. It was found that the main factor leading to large regions of low WSS is the so called expansion ratio, a relation between the cross-section areas of the outflow branches and the cross-section area of the main branch. Large regions of low WSS appear for high expansion ratios. Furthermore, the size of low WSS regions is independent of the ratio between the diameters of the outflow branches. Since the expansion ratio in bifurcations following Murray's law is kept in a small range (1 and 1.25), all of them have regions of low WSS with similar size. However, the expansion ratio is not small enough to completely prevent regions with low WSS values and, therefore, Murray's law does not lead to atherosclerosis minimization. A study on the effect of the angulation of the bifurcation suggests that the Murray's law for the angles does not minimize the size of low WSS regions.

4.1 Introduction

In advanced countries, cardiovascular diseases are presently the leading cause of morbidity and mortality in humans[1]. Several studies[2] have shown that specific sites in the human circulatory system are particularly sensitive to the development of lesions related to atherosclerosis. These lesions can develop, leading to the formation of an abnormal narrowing in the arteries, a stenosis. Research has linked the development of atherosclerosis to the flow patterns in bifurcations, specifically to low WSS regions and vortexes[3].

Fluid mechanics studies can be an auxiliary tool to the prevention and treatment of lesions related to atherosclerosis. However, knowledge from experimental hemodynamic studies is scarce, not only due to ethical issues, but also due to difficulties to find blood analogue fluids with appropriated non-Newtonian properties (shear thinning and elasticity). Hence, most of the published studies are numerical, performed not only on simple sketch models, but also on models constructed from medical images from patients (*e.g.* CT scans). Simple or more elaborated numerical studies describing velocity and WSS fields and analyzing geometrical effects have been developed.

The left coronary artery (LCA) has been the object of several numerical studies. Several authors have studied the effect of the geometrical characteristics of healthy (non-stenotic) arteries on the flow and wall shear stress field. Chaichana *et al.*[4] and Huo *et al.*[5] studied numerically, on sketch models, the effect of LCA angulation on the flow and WSS fields. Soulis *et al.*[6-9], Hossain *et al.*[10], Malvè *et al.*[11], Olgac *et al.*[12], Evegren *et al.*[13] and Bahaganagar *et al.*[14] performed identical studies, but on models constructed from medical images of patients. Soulis *et al.*[9] and Olgac *et al.*[12] used a diluted lipoprotein (LDL) as tracer in the flow and observed that LDL surface concentration is elevated at locations where WSS is low. Weydahl and Moore Jr[15] studied the effect of LCA curvature on the flow and WSS fields. These studies on healthy LCAs show that angulation and curvature of the bifurcation are relevant parameters to the flow and WSS fields developed. In regions close to the bifurcation, where atherosclerosis frequently occurs, the WSS values are low.

There are also studies reporting hemodynamic flow fields in stenotic LCAs. Chaichana *et al.*[16-18] published several on models from medical images, reporting WSS and velocity fields and also pressure gradients during systolic and diastolic phases.

To better understand blood flow and vessel network architecture, researchers have searched for design principles that rule vessel networks[19]. Murray's law[20] is one of such principles. It establishes restrictions to the size relations and flow distribution in vessel network bifurcations. Murray's laws were derived through two independent optimization approaches, minimization of the energy to pump the fluid and to maintain the blood flowing in the vessels[20, 21] and minimization of the drag force on lumen surface[21]. Both approaches lead to the same results. For laminar flow, the flow rate of a Newtonian fluid must be proportional to the cube of the diameter of the vessel. The same exponent is valid for some non-Newtonian fluid models[22] and a different exponent must be considered for fully developed turbulent flow[19, 23].

While Murray's law is based on general optimizing principles, studies of blood vessel networks show significant statistical variations (see Labarbera[19] for a review on experimental tests to Murray's law), including significant deviations in the carotid bifurcation[24]. Murray's law does not apply exactly to the whole circulatory system[25] or to all species[25]. Despite the complex set of considerations that must be taken into account to interpret deviations (see Reneman *et al.*[25] for a review), Murray's law maintains an important role in hemodynamics studies, as a guiding theoretical principle.

It has been hypothesized that vessel networks that deviate from Murray's law are more prone to health problems. Schoenenberger *et al.*[26] have shown that these deviations are associated to a higher degree of calcification in coronary bifurcations.

One of the implications of Murray's laws is that, for fully developed flow regions, wall shear stress should be the same in all the branches of a blood vessel network. This fact further suggests that an ideal wall shear stress exists. Studies[27, 28] showing associations between low wall shear stress and atherosclerosis reinforce this idea. In their review of the literature, Malek *et al.*[29] conclude that the typical value of wall shear stress varies between 1.5 Pa and 2.0 Pa. Endothelial compensatory response to wall shear stress changes helps to maintain it within this range. The same authors indicate 0.4 Pa as the minimum for a region to avoid atherosclerosis. Reneman *et al.*[25], based on the work of Kamiya *et al.*[30], identify the value of 1.5 Pa as a reference value for typical wall shear stress.

Despite the large number of numerical studies in bifurcations, analyzing diverse geometrical and flow parameters, Murray's laws have been largely ignored. Murray's laws can be useful, for example, to define flow rate partition, helping to solve the problem of outflow boundary conditions definition. Outflow boundary conditions in numerical hemodynamic studies are difficult to establish[31-33] since the flow resistance of the downstream capillary network is unknown and experimental data is usually not available. Murray's laws are also a reference that can be used as a basis for comparison with other, possible more realistic, alternatives.

In this chapter, we study the flow in the left coronary artery bifurcation by numerical methods taking Murray's laws as reference, and we analyze how deviations influence the size of low wall shear stress regions and helical flow development. Based on dimensional analysis, the space of possible outflow branch diameters is studied systematically. Effects of Newtonian and shear thinning fluid properties, as well as the effects of pulsatile flow are considered.

4.2 Numerical Simulations

4.2.1 Geometry

The geometry chosen for this study is an idealized bifurcation which intends to represent a section of the coronary network. The left coronary artery was the reference used to select the diameter of the main branch and the flow Reynolds number. However, the work is sufficiently general so that the conclusions can be applied to other sections of the circulatory system sharing identical flow and geometrical characteristics (*e.g.* flow rate, diameter). Results will be presented, whenever possible, as non-dimensional relations, valid for a large variety of coronary networks.

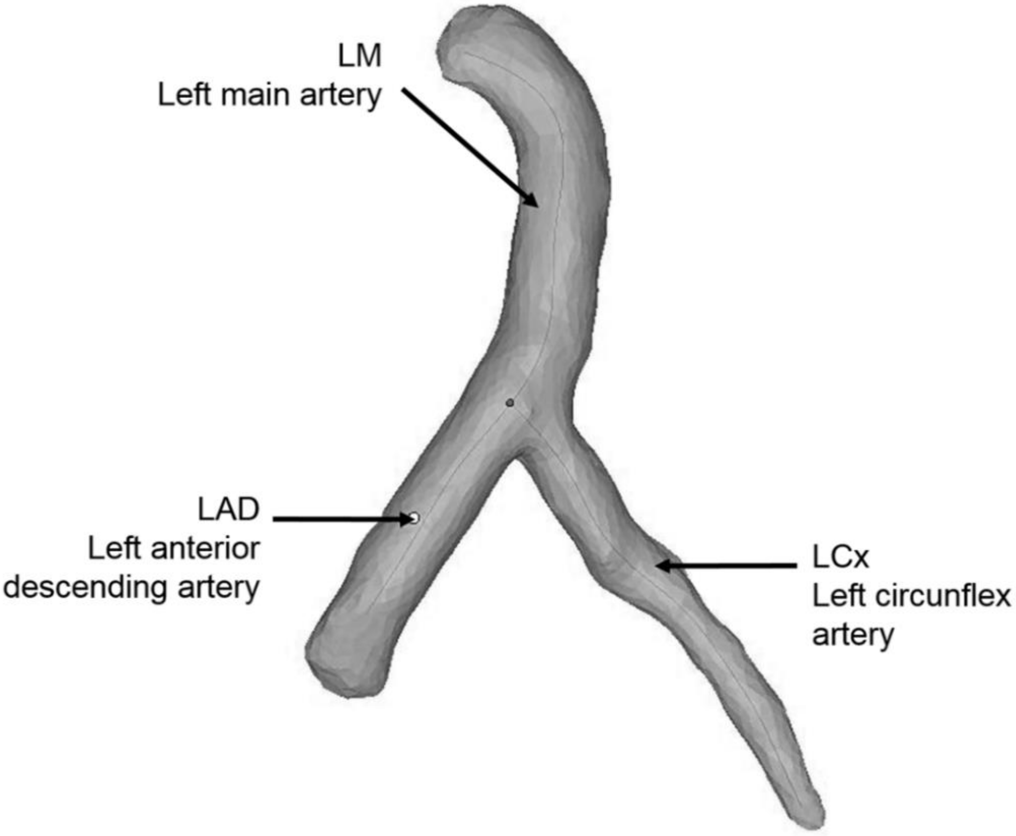

Figure 4.1. Schematic representation of the Left Coronary Artery (LCA) near the main bifurcation, including the Left Main Stem (LM), the Left Anterior Descending Artery (LAD) and the Left Circumflex Artery (LCx).

The left coronary artery (LCA) is sketched in Figure 4.1. The LCA includes the Left Main Stem (LM), which branches into the Left Anterior Descending Artery (LAD) and into the Left Circumflex Artery (LCx).

The shape and dimensions were chosen as close as possible to a human LCA. The average diameter of the LM for healthy individuals varies from study to study: Dodge *et al.*[34] report 4.5 mm, Kiviniemi *et al.*[35] 4 mm, Ballesteros *et al.*[36] 3.6 mm and Dombe *et al.*[37] 3.3 mm. The LM diameter reported by Kiviniemi *et al.*[35] was chosen for reference. These authors found, in agreement with Murray’s law, diameters of 3.5 mm and 2.8 mm for the LAD and LCx, respectively.

The idealized geometries studied followed the design shown in Figure 4.2, with the following restrictions:

- The 3 branches of the skeleton are co-planar;
- The branches of the skeleton intercept in a unique point ($\Delta y_i = 0$);
- The curvatures are defined by an arc of a circumference;
- All the arcs have the same radius $R_{c_1} = R_{c_2} = R_{c_3}$;
- The branches are set to be sufficiently long to assure fully developed flow.

After these assumptions, the geometry has 5 degrees of freedom. The following non-dimensional geometrical parameters left to be freely set:

$$\frac{D_{\mathrm{LAD}}}{D_{\mathrm{LM}}}, \frac{D_{\mathrm{LCx}}}{D_{\mathrm{LM}}}, \frac{R_{c_1}}{D_{\mathrm{LM}}}, \beta, \theta$$

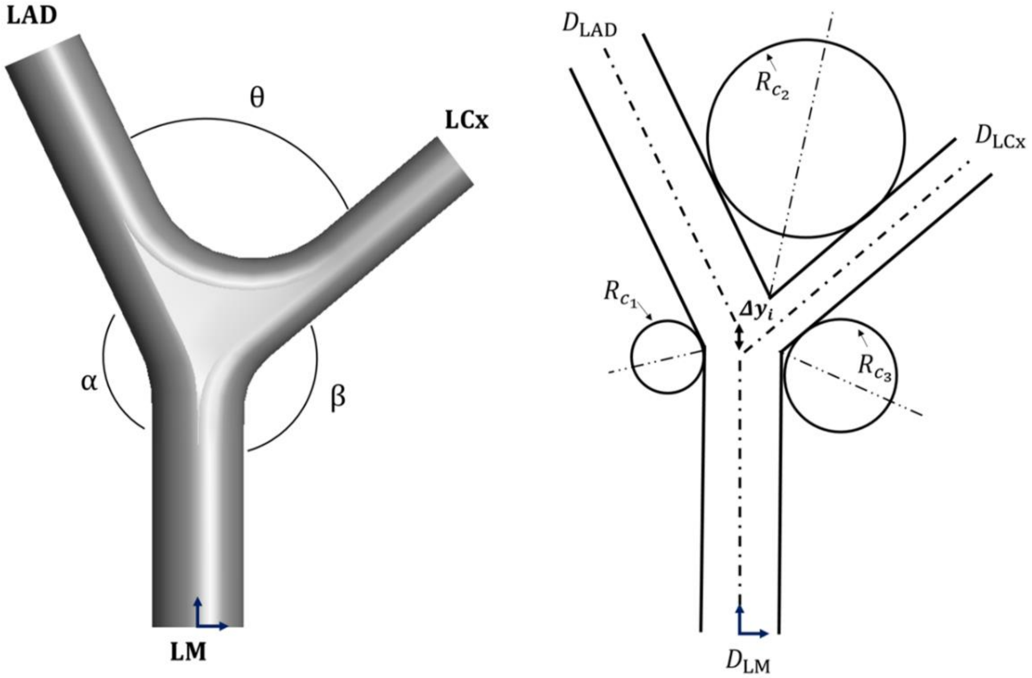

Figure 4.2. LCA 3D geometry created in SolidWorks®.

The geometrical degrees of freedom can further be reduced by introducing Murray's law[20] for laminar flow:

$$Q = kD^3 \tag{4.1}$$

Murray's law, combined with continuity equation, leads to the following restriction to the size of the vessels:

$$D_{LM}^3 = D_{LAD}^3 + D_{LCx}^3 \tag{4.2}$$

It leads also to a restriction in the partition of the flow rate in the bifurcation which will be discussed in detail in boundary conditions section.

The geometrical restriction introduced by Murray's law is best illustrated by Figure 4.3. The diagram represents the space of possible values of D_{LAD} and D_{LCx}. Vessels following Murray's Law are those along the curved solid line. Also represented are isolines for the expansion ratio (dotted line) and for the outflow branches diameter ratio (long dash lines) and several cases studied in the literature[34, 35, 37].

The expansion ratio is defined as the ratio between the sum of the squares of the cross-section areas of the outflow branches and the square of the cross-section area of the inflow branch:

$$A_{ratio} = \frac{D_{LAD}^2 + D_{LCx}^2}{D_{LM}^2} \tag{4.3}$$

The outflow branches diameter ratio is defined by:

$$D_{ratio} = \frac{D_{LAD}}{D_{LCx}} \tag{4.4}$$

The points represented in Figure 4.3 (open circles) are the ones that will be investigated along this work (see also Table 4.1 and Figure 4.4). It was decided to study cases along Murray's law line, as well as cases that deviate from Murray's law, these along two lines of equal outflow branches diameter ratio (1.33 and 0.75). The cases represented along these two lines have distinct expansion ratios.

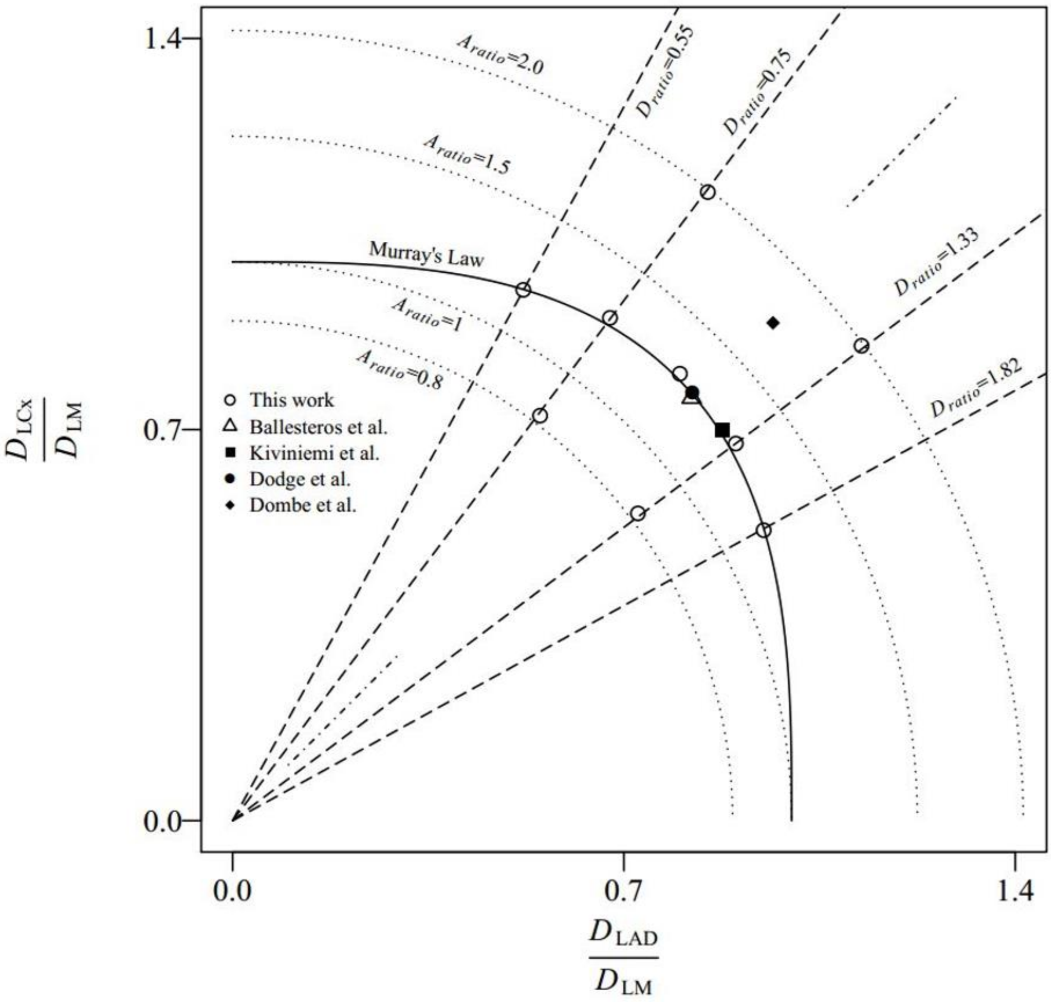

Figure 4.3. Diagram representing the space of possible values of the vessels normalized diameters, showing the Murray's law line (solid line), expansion ratio isolines (dotted lines) and outflow branches diameter ratio isolines (long dash lines). The open circles represent the cases in study. Cases from the literature are also represented.

Already mentioned, the deviation from Murray's law is usually associated to a higher degree of calcification in coronary bifurcations[26]. As can be seen in the diagram, vessels following Murray's law can have a large range of diameter ratio, while the expansion ratio is limited between 1 and 1.25. In turn, large expansion ratios are associated to the development of significant regions of low WSS values, which are usually associated to atherosclerosis[38].

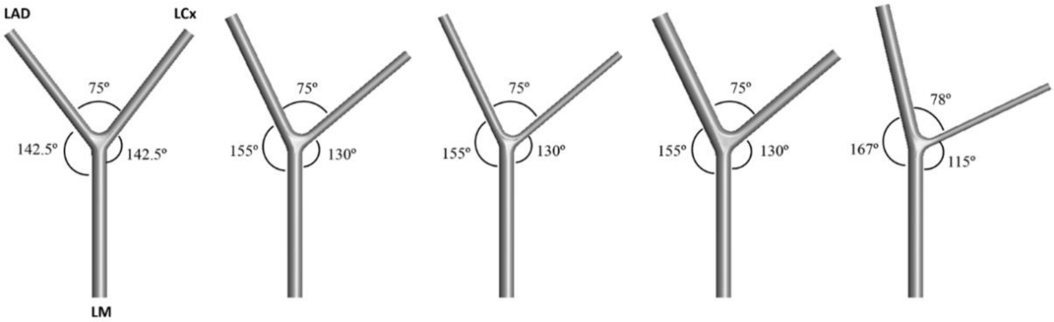

Figure 4.4. LCA geometries with $D_{\text{LAD}} \geq D_{\text{LCx}}$ (points bellow the diagonal of Figure 4.3). The other geometries studied (4) are identical but the diameters of the branches (LAD and LCx) are interchanged ($D_{\text{LAD}} < D_{\text{LCx}}$, points above the diagonal of Figure 4.3).

To further reduce the number of degrees of freedom, for cases following Murray's laws, the angles between the branches were set according to Murray's relation for the angles[39]. According to Murray[39], the optimal angles in a bifurcation follow the equations:

$$cos(\pi - \alpha) = \frac{D_{LAD}^4 + D_{LM}^4 - (D_{LM}^3 - D_{LAD}^3)^{4/3}}{2D_{LM}^2 D_{LAD}^2} \tag{4.5}$$

$$cos(\theta) = \frac{(D_{LCx}^3 - D_{LAD}^3)^{4/3} - D_{LCx}^4 - D_{LAD}^4}{2D_{LCx}^2 D_{LAD}^2} \tag{4.6}$$

For the remaining cases, angles were set identical along D_{ratio} isolines. The use of Murray's relation for the angles is a debatable option, since different diameters will have different angles and so differences in the results may be attributable to changes in both geometric parameters. Conversely, the adoption of a constant angle for all diameter ratios would lead to sub-optimal configurations.

Table 4.1. Geometrical characteristics of the models represented in Figure 4.4.

	$\frac{D_{\mathrm{LAD}}}{D_{\mathrm{LM}}}$	$\frac{D_{\mathrm{LCx}}}{D_{\mathrm{LM}}}$	D_{ratio}	A_{ratio}	$\frac{D_{\mathrm{LAD}}^3 + D_{\mathrm{LCx}}^3}{D_{\mathrm{LM}}^3}$	α (deg.)	β (deg.)	θ (deg.)
a	0.79	0.79	1.00	1.26	1.00	142.5	142.5	75
b	0.89	0.67	1.33	1.24	1.00	155	130	75
c	0.72	0.54	1.33	0.80	0.52	155	130	75
d	1.13	0.85	1.33	2.00	2.06	155	130	75
e	0.96	0.48	2.00	1.16	1.00	167	115	78

An additional study was performed to analyze the effect of the angle. For this study, $D_{\mathrm{ratio}} = 1.33$ was used as reference. The cases studied are represented in Figure 4.5 and the respectively characteristics in Table 4.2.

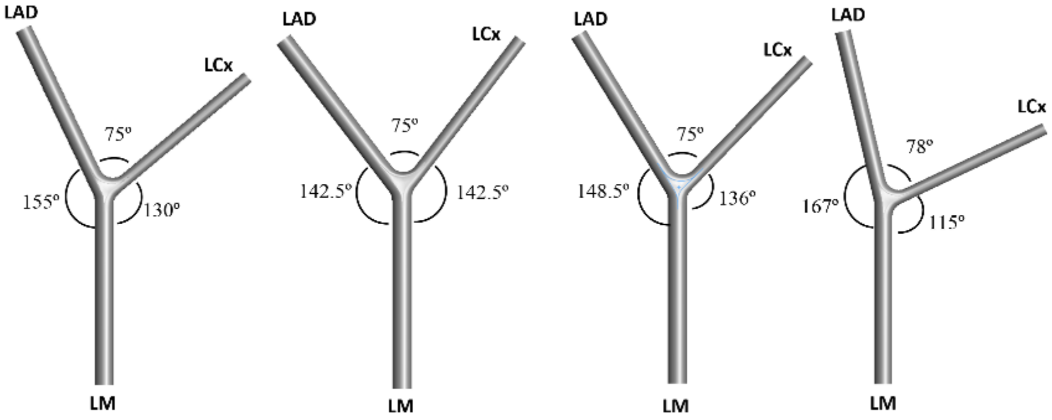

Figure 4.5. LCA geometries for the angles study.

Table 4.2. Geometrical characteristics of the models for the effect of the angles study.

$\frac{D_{\mathrm{LAD}}}{D_{\mathrm{LM}}}$	$\frac{D_{\mathrm{LCx}}}{D_{\mathrm{LM}}}$	D_{ratio}	A_{ratio}	$\frac{D_{\mathrm{LAD}}^3 + D_{\mathrm{LCx}}^3}{D_{\mathrm{LM}}^3}$	α (deg.)	β (deg.)	θ (deg.)
0.89	0.67	1.33	1.24	1.00	155.0	130.0	75.0
0.89	0.67	1.33	1.24	1.00	142.5	142.5	75.0
0.89	0.67	1.33	1.24	1.00	148.5	136.0	75.5
0.89	0.67	1.33	1.24	1.00	167.0	115.5	77.5

4.2.2 Computational grid

SolidWorks® software was used to design the geometries. The solid model was converted into a mesh grid using the cut cell method in ANSYS® v15.0 software. This method allows the creation of a predominantly hexahedral mesh with inflation layers to improve the accuracy in regions with high velocity gradients.

4.2.3 Blood properties

The properties of the blood were obtained from the literature. Blood density[40] was taken constant and equal to 1060 kg/m^3.The effect of shear-thinning blood behaviour on the flow pattern was also analyzed and Carreau model was employed:

$$\mu = \mu_\infty + (\mu_0 - \mu_\infty)[1 + (\lambda\dot{\gamma})^2]^{\frac{n-1}{2}} \tag{4.7}$$

where μ represents the blood viscosity, μ_0 the zero shear viscosity, μ_∞ the infinite shear viscosity, n the power-law index, λ the time-constant and $\dot{\gamma}$ the shear rate magnitude. Table 4.3 shows Carreau model parameters for human blood[41]. Some simulations were performed assuming Newtonian behaviour with viscosity equal to 3.5×10^{-3} Pa·s.

Table 4.3. Carreau model parameters for human blood (reference temperature 37ºC).

Parameters	**Blood**
N	0.3568
μ_0 (Pa.s)	0.0560
μ_∞ (Pa.s)	0.00345
λ (s)	3.313

4.2.4 Navier – Stokes equations

To determine the blood flow in the vessels, the continuity and Navier-Stokes equations for 3D, incompressible flow were considered:

$$\nabla \cdot \boldsymbol{V} = 0 \tag{4.8}$$

$$\rho \frac{\partial \boldsymbol{V}}{\partial t} + \rho(\nabla \cdot \boldsymbol{V})\boldsymbol{V} = -\nabla P + \nabla \cdot \boldsymbol{\tau} \tag{4.9}$$

where $\boldsymbol{V}$ is the velocity vector, ρ the mean density, $\boldsymbol{\tau}$ the shear stress tensor defined by:

$$\boldsymbol{\tau} = \mu[\nabla \boldsymbol{V} + (\nabla \boldsymbol{V})^T] \tag{4.10}$$

4.2.5 Discretization schemes and algorithms

The transient Navier–Stokes equations were solved in ANSYS® *Fluent.* The velocity–pressure equations were solved by PISO algorithm[42]. The QUICK scheme[43] was used to discretize the momentum equations and the PRESTO! scheme for pressure term discretization. For steady flow, the simulation was run for a 0.02 s of physical time with adaptive time step. For oscillatory flow, the simulation was run for 5 cardiac cycles with a time step of 0.001 s.

4.2.6 Boundary conditions

Inlet

Simulations were performed for steady and oscillatory flow. For both, the laminar velocity profile for developed flow was used as inlet boundary condition:

$$v\,(r) = 2\,v_m\left[1 - \left(\frac{r}{R}\right)^2\right] \tag{4.11}$$

where R is the LM radius, r the radial position and v_m the steady flow mean inlet velocity.

For steady flow, the mean inlet velocity is constant. The inlet velocity was chosen in order to have an inlet WSS equal to 1.5 Pa. For Newtonian fluid behaviour, the average velocity was set equal to 0.214 m/s, corresponding to a Reynolds number of 259 for a 4 mm LM diameter and a viscosity of 0.0035 Pa.s, while for non-Newtonian fluid behaviour was set equal to 0.180 m/s.

For oscillatory flow, the instantaneous mean inlet velocity (v_m) of the cardiac cycle is given by:

$$v_m(t) = \frac{\bar{v}_m}{a_0}\left\{a_0 + \sum_{i=1}^{5}\left[a_i\,cos(iwt) + b_i\,sin(iwt)\right]\right\} \tag{4.12}$$

where $\overline{v}_m$ is the average velocity of a complete cycle, w the angular frequency of the cardiac cycle and a_i and b_i parameters of the fitting model. The values of these parameters for the LCA[4] are in Table 4.4 and the cardiac cycle is represented in Figure 4.6. The original velocity profile was normalized so that the time averaged mean inlet velocity is identical to that in steady state flow case.

Table 4.4. Parameters of the pulsatile model.

Parameters	Values	Parameters	Values
a_0(m/s)	0.1308	b_3(m/s)	0.002598
a_1(m/s)	0.05282	a_4(m/s)	0.02509
b_1(m/s)	-0.04866	b_4(m/s)	0.02111
a_2(m/s)	-0.00909	a_5(m/s)	-0.00268
b_2(m/s)	-0.0104	b_5(m/s)	-0.01372
a_3(m/s)	-0.02733	ω	8.483

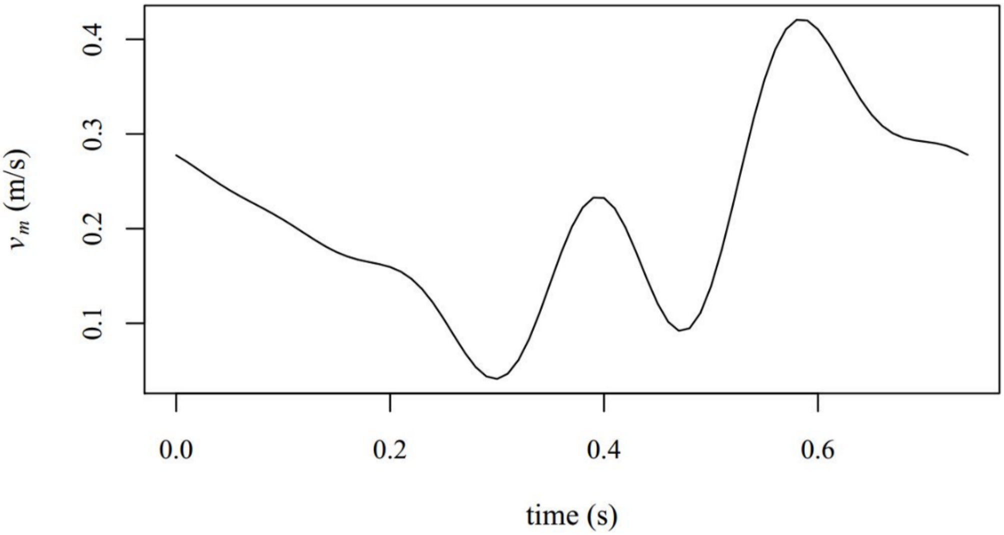

Figure 4.6. Mean velocity rate throughout a cardiac cycle for the Newtonian case.

For the simulation with non-Newtonian fluid behaviour, the following boundary condition was assumed:

$$v\,(r) = \frac{3n+1}{n+1}\,v_m\left[1-\left(\frac{r}{R}\right)^{\frac{n+1}{n}}\right] \tag{4.13}$$

where n is equal to 0.7755. This parameter was obtained by adjusting the velocity profile to the fully developed flow in a tube.

Walls

At the artery wall the velocity was taken zero, the so called no-slip condition.

Outlets

At the outlet sections, the flow rate distribution, according to Murray's law[44, 45] is:

$$\frac{Q_{LAD}}{Q_{LCx}} = \left(\frac{D_{LAD}}{D_{LCx}}\right)^3 \tag{4.14}$$

where Q_{LAD} and Q_{LCx} are, respectively, the flow rate in LAD and LCx branches with diameters D_{LAD} and D_{LCx}.

4.2.7 Flow characterization

The flow was characterized by wall shear stress distribution, size of helical flow regions and surface area with low wall shear stresses. The WSS is a vector tangent to the wall surface that can be obtained by the dot product between the normal unit vector, $\boldsymbol{n}$, and the shear stress tensor[46, 47]:

$$\boldsymbol{\tau_w} = \boldsymbol{n} \cdot \boldsymbol{\tau} \tag{4.15}$$

The magnitude of the WSS is given by:

$$\tau_{\,w} = \sqrt{\tau_x^2 + \tau_y^2 + \tau_z^2} \tag{4.16}$$

Regions of critically low WSS were identified based on the criterion suggested by Malek *et al.*[29]:

$$\boldsymbol{\tau}_w < 0.4\,Pa \tag{4.17}$$

All the cases studied have the same inlet WSS and inlet diameter, but the surface areas of the outflow branches are different. To compensate this effect and to make possible future comparisons a normalization area was defined:

$$A^* = \frac{\pi D_{LM}^2}{4} \times A_{ratio} \tag{4.18}$$

Therefore, the surface normalized area with $\tau_w < 0.4$ is given by:

$$A_{WSS}^L = \frac{A(\boldsymbol{\tau}_w < 0.4)}{A^*} \tag{4.19}$$

The oscillatory cases were characterized by the time averaged wall shear stress:

$$TAWSS = \frac{1}{T}\int_0^T |\boldsymbol{\tau}_w| dt \tag{4.20}$$

and by the oscillatory shear index:

$$OSI = \frac{1}{2}\left(1 - \frac{\left|\int_0^T \boldsymbol{\tau}_w\, dt\right|}{\int_0^T |\boldsymbol{\tau}_w| dt}\right) \tag{4.21}$$

where

$$\left|\int_0^T \boldsymbol{\tau}_w \, dt\right| = \sqrt{\left(\int_0^T \boldsymbol{\tau}_x \, dt\right)^2 + \left(\int_0^T \boldsymbol{\tau}_y \, dt\right)^2 + \left(\int_0^T \boldsymbol{\tau}_z \, dt\right)^2} \tag{4.22}$$

and

$$\int_0^T |\boldsymbol{\tau}_w| dt = \int_0^T \sqrt{\tau_x^2 + \tau_y^2 + \tau_z^2} \, dt \tag{4.23}$$

Regions where the direction of the WSS vector changes during the cardiac cycle have OSI > 0. The surface area with OSI>0.1 normalized by A^* was used to quantify the oscillation of the WSS vector:

$$A_{OSI}^{H} = \frac{A(\text{OSI} > 0.1)}{A^*} \tag{4.24}$$

Helical flow is, by definition, the rotational motion of the fluid oriented normal to the mainstream flow[48]. Helical flow regions are chacterized by high helicity density[49], defined by:

$$H = \boldsymbol{V} \cdot \boldsymbol{\omega} \tag{4.25}$$

where $\boldsymbol{\omega}$ is the vorticity vector:

$$\boldsymbol{\omega} = \nabla \times \boldsymbol{V} \tag{4.26}$$

The normalized helicity density is given by:

$$H_r = \frac{\boldsymbol{V} \cdot \boldsymbol{\omega}}{|\boldsymbol{V}||\boldsymbol{\omega}|} \tag{4.27}$$

The propensity for the appearance of helical flows is associated to regions where the normalized absolute helicity is high. In this work, a threshold of 0.7 was assumed to identify regions of high helicity:

$$|H_r| = \frac{|H|}{|\boldsymbol{V}||\boldsymbol{\omega}|} > 0.7 \tag{4.28}$$

In the present study, the volume of the outflow branches is, in all the cases, dissimilar. To compensate this effect and to make possible future comparisons, a normalization volume was defined:

$$V^* = \frac{\pi D_{LM}^3}{4} \times \frac{D_{LAD}^3 + D_{LCx}^3}{D_{LM}^3} \tag{4.29}$$

Therefore, the normalized volume with $|H_r| > 0.7$ is given by:

$$V_{|H_r|}^H = \frac{V(|H_r| > 0.7)}{V^*} \tag{4.30}$$

4.3 Results

4.3.1 Steady state flow

The normalized size of low WSS regions ($A_{\mathrm{WSS}}^{\mathrm{L}}$) was calculated for steady state flow. As shown in Figure 4.7 the size is constant along Murray's law line and increases with the increase of the expansion ratio. The size is slightly smaller when the fluid with non-Newtonian behaviour (shear-thinning fluid) is simulated. The expansion ratio is determinant for the appearance of low WSS regions. While Murray's law of the diameters results from energy minimization principles, Figure 4.7 suggests that there is no significant cost (in terms of the size of the low WSS regions) of increasing the ratio between the diameters of the branches. The main reason for this is that the maximum expansion ratio under Murray's law is only 1.25, and does not change significantly with changes of the diameter ratio.

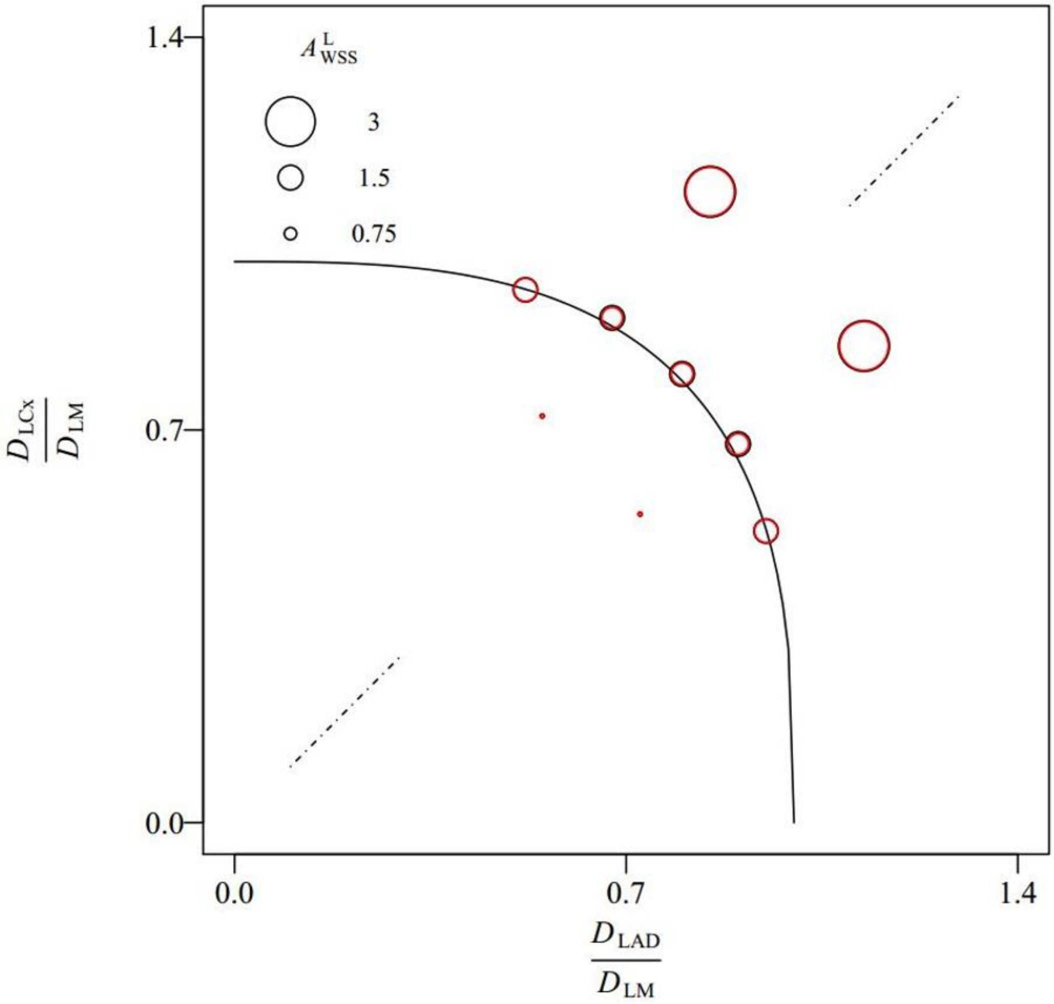

Figure 4.7. $A_{\mathrm{WSS}}^{\mathrm{L}}$ values (eq.(4.19)) for steady state flow. The black and red circles are, respectively, for Newtonian and non-Newtonian behaviours.

Figure 4.8 shows the normalized size of high helicity regions, $V_{|H_r|}^{\mathrm{H}}$, for different geometries, for steady state flow. The normalized size is higher for equal diameter branches $D_{\mathrm{LAD}} = D_{\mathrm{LCx}}$ and decreases as the outflow branches diameter ratio departs from 1. The normalized size of high helicity regions is smaller when the fluid is non-Newtonian. Another important conclusion from the figure is that the normalized volume of the high helicity regions decreases for increasing expansion ratios.

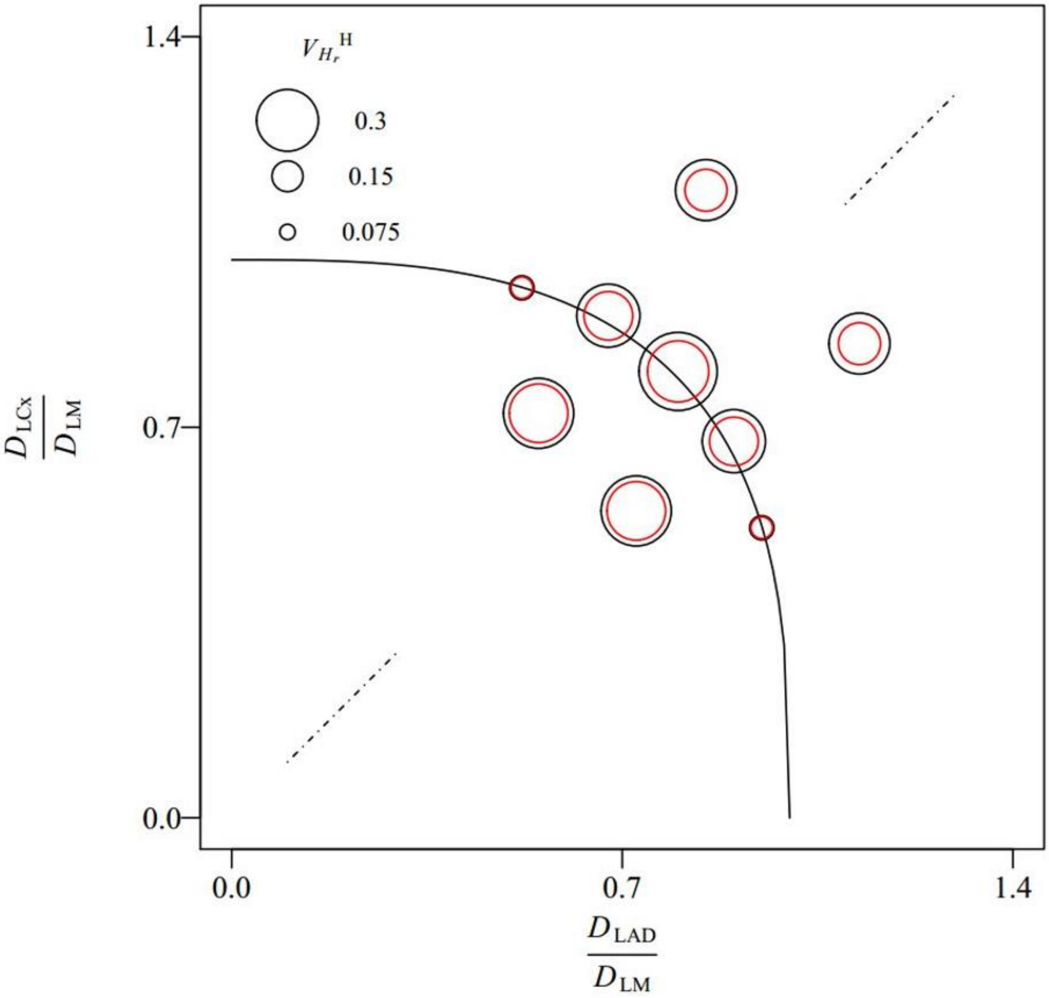

Figure 4.8. $V_{|H_r|}^{\mathrm{H}}$(eq.(4.30)) values for steady state flow. The black and red circles are, respectively, for Newtonian and non-Newtonian behaviours.

It is important to know if data for steady state flow is significantly different from data for oscillatory flow representative of the cardiac cycle. The time averaged wall shear stress (TAWSS) was compared with the WSS for steady state flow. The results are identical (Figure 4.9).

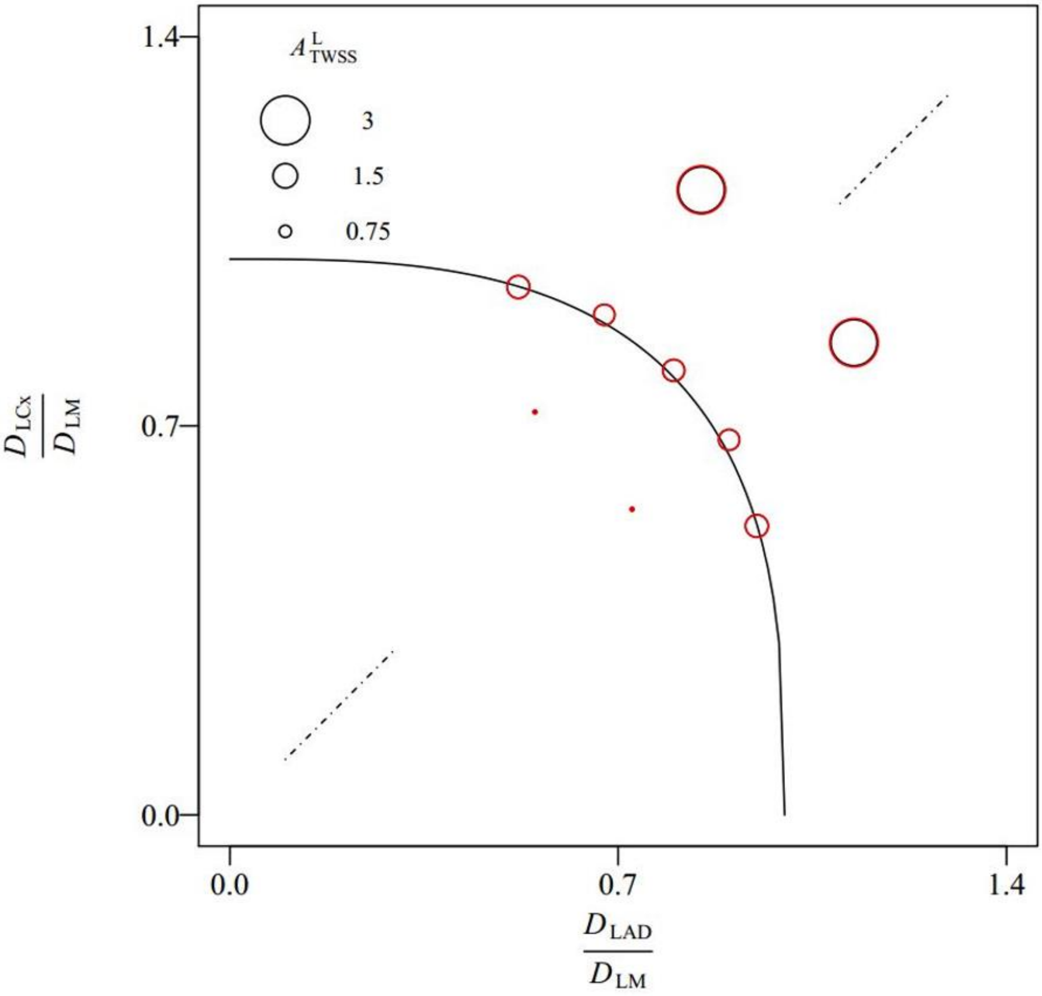

Figure 4.9. $A^{\mathrm{L}}_{\mathrm{TWSS}}$ (eq. (4.19)) values for oscillatory flow (red circles) and steady state flow (black circles), both for Newtonian behaviour.

Figure 4.10 shows the time average normalized size of high helicity regions for the different geometries, for oscillatory flow. As observed for steady state flow, the normalized size is higher for equal diameter branches ($D_{\mathrm{LAD}} = D_{\mathrm{LCx}}$) and decreases as the diameters ratio departs from 1. The normalized volume of high helicity regions also decreases with increasing expansion ratios. The size of high helicity regions is larger for the oscillatory flow case.

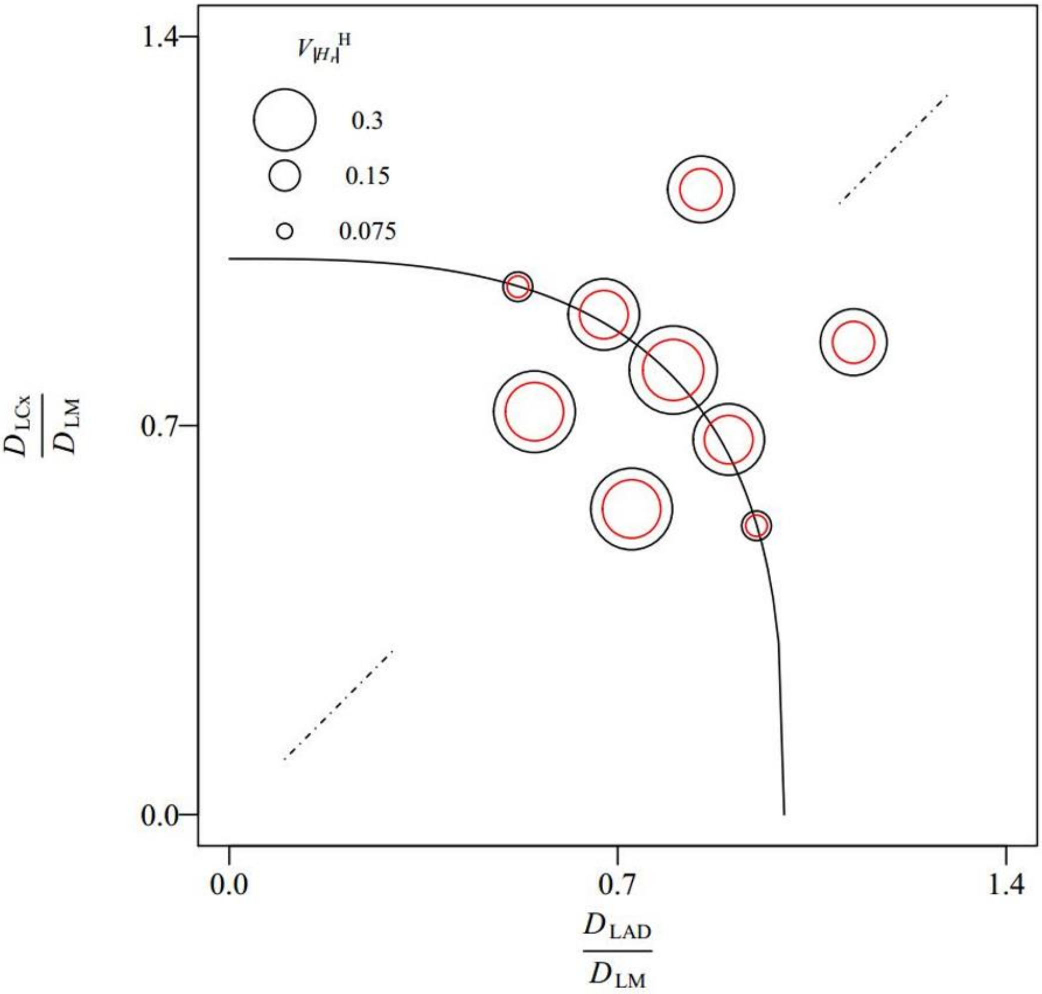

Figure 4.10. $V_{|H_r|}^{\text{H}}$ (eq.(4.30)) values for oscillatory flow (black circles) and steady flow (red circles), both for non-Newtonian behaviour.

The OSI parameter measures the surface area where the shear stress vectors change direction. Regions with OSI>0.1 are more prone to atherosclerosis development because cells do not have a preferential direction to align. The normalization done was identical to that of WSS. The size of these regions for the geometries studied is represented in Figure 4.11. As can be observed, the area of high OSI is higher for symmetric bifurcations and increases with the expansion ratio.

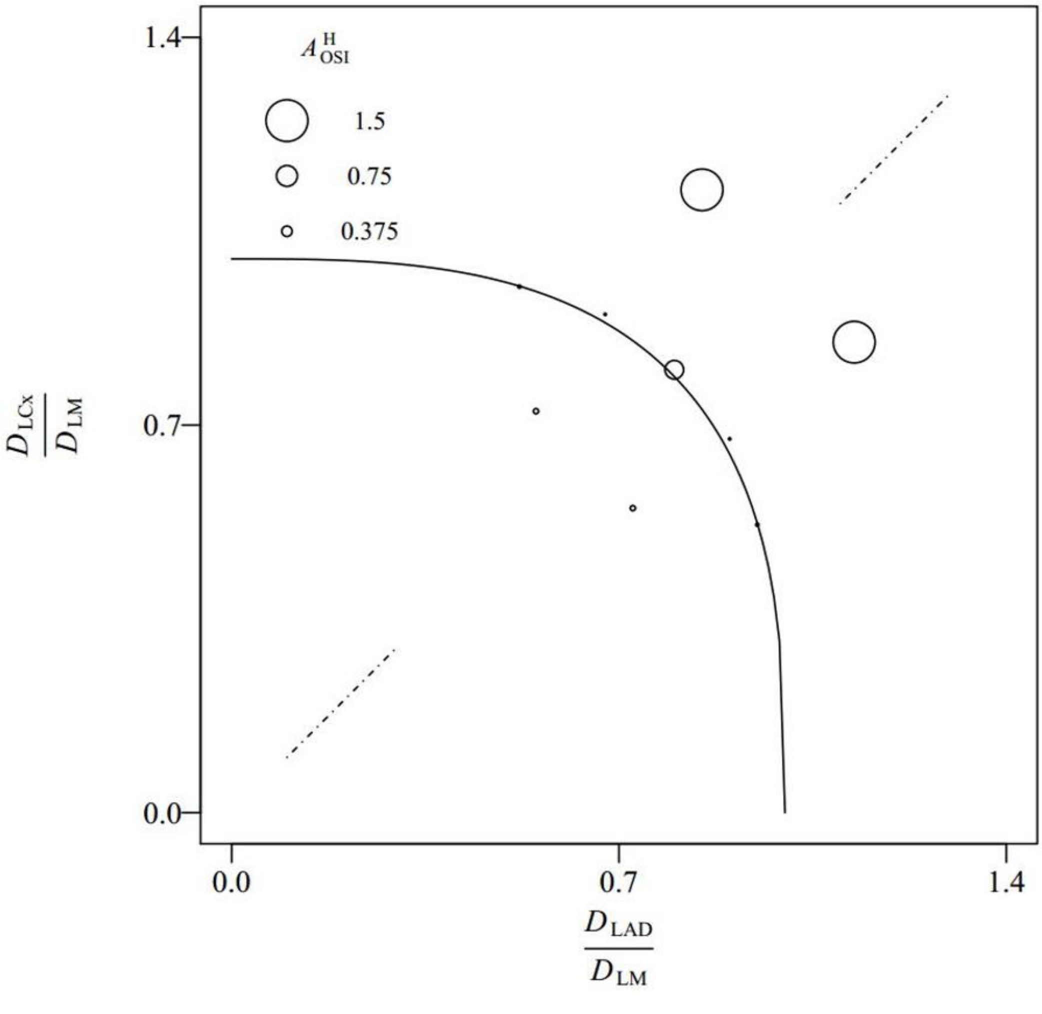

Figure 4.11. $A^{\mathrm{H}}_{\mathrm{OSI}}$ (eq.(4.24)) values for oscillatory flow.

While average indicators have been analyzed until now, instantaneous indicators throughout a complete cardiac cycle are also of interest. Two instantaneous indicators were studied, $A^{\mathrm{L}}_{\mathrm{WSS}}$ and $V^{\mathrm{H}}_{|H_r|}$. Both indicators are shown in Figure 4.12 for a complete cardiac cycle.

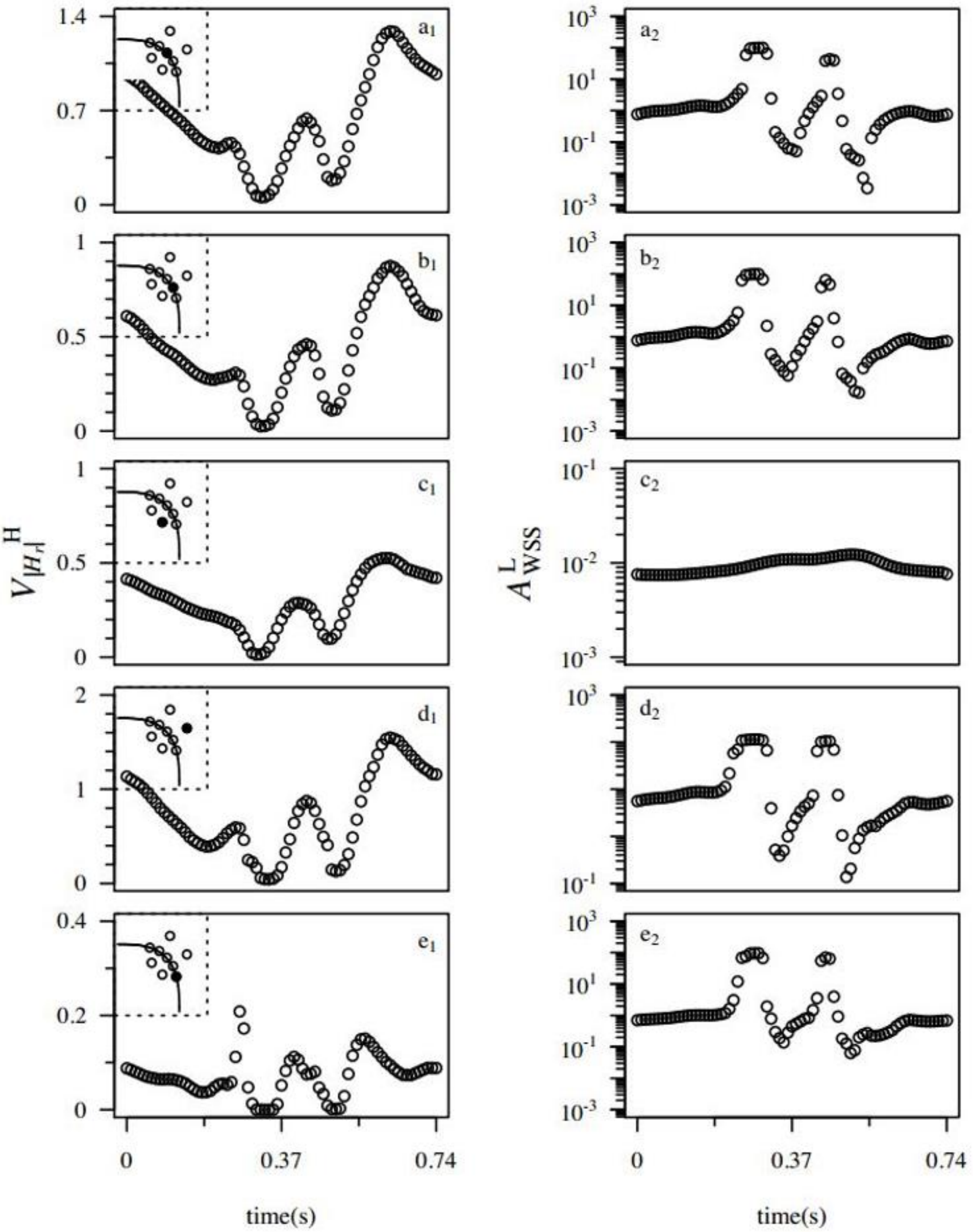

Figure 4.12. $V_{|H_r|}^{\mathrm{H}}$ (left) and $A_{\mathrm{WSS}}^{\mathrm{L}}$ (right) values during a cardiac cycle. The geometrical conditions (from *a* to *e*) are listed in Table 4.1.

The most salient aspect of $A_{\mathrm{WSS}}^{\mathrm{L}}$ data is that this indicator can vary several orders of magnitude during the cardiac cycle. This means that for short periods of the cardiac cycle (coinciding with the down peaks of blood velocity), a large extension of the vessel walls are exposed to low WSS values. In the present study, this is observed for all the cases that follow Murray's law (Figure 4.12 a2, b2 and e2) and for the case of high expansion ratio (Figure 4.12 d2). For the case of low expansion ratio (Figure 4.12 c2), the surface area with low WSS is very small throughout the cycle.

The normalized volume of the regions with high helicity also varies during the cardiac cycle. The normalized volume is almost zero during the down peaks of blood velocity and is high during the periods of high blood velocity. In general, the effects of deviation from Murray's law and of the diameter ratio are similar to the ones already observed for the average values of $V_{|H_r|}^{\mathrm{H}}$(eq.(4.30)).

4.3.2 Effect of the angle

The effect of the angle on the different indicators was analyzed by changing the angle between LAD and LM (α on Figure 4.2). The effect on $A_{\mathrm{WSS}}^{\mathrm{L}}$ (total, in the LAD and in the LCx) is shown in Figure 4.13a.

As it can be observed the angle determined by Murray's law does not minimize the area with low WSS. Smaller regions can be obtained with lower and higher angles. This means that the angle that minimizes energy consumption leads to larger areas of low shear stress that otherwise would be possible.

Figure 4.13b shows that $A_{\mathrm{OSI}}^{\mathrm{H}}$ (eq.24) is constant between 142.5° and 155° and significantly lower for 167°. These results also suggest that Murray's law of the angles leads to larger regions prone to atherosclerosis than otherwise would be possible.

Figure 4.13c shows that $V_{|H_r|}^{\mathrm{H}}$ is constant between 142.5° and 155° and decreases for larger angles, indicating that Murray's law of the angles is associated to significant helicoidal flows.

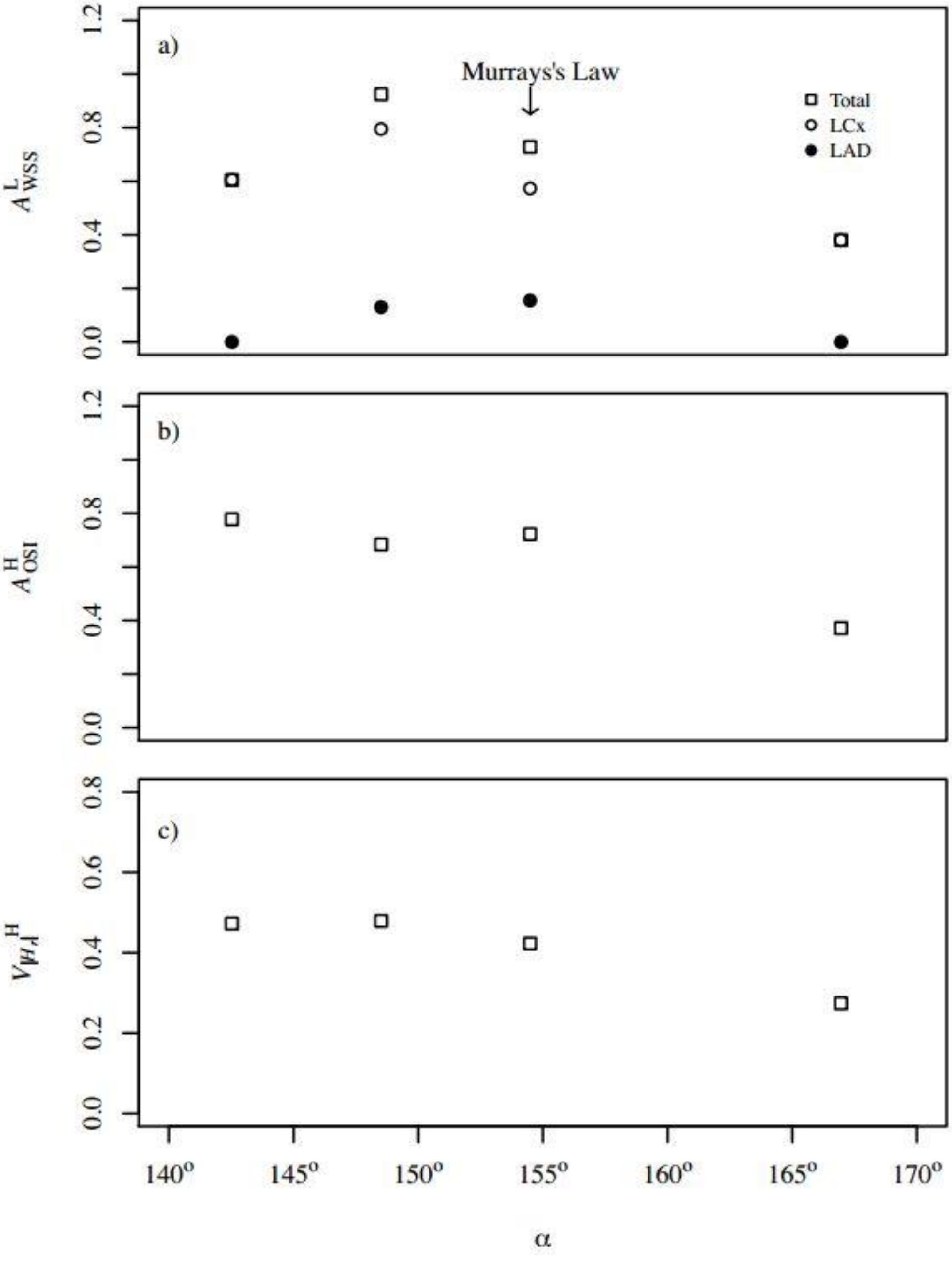

Figure 4.13. Effect of the angulation between LAD and LM on the different indicators: (a) $A^{\mathrm{L}}_{\mathrm{WSS}}$ (eq.(4.19)); (b) $A^{\mathrm{H}}_{\mathrm{OSI}}$ (eq. (4.24)); (c) $V^{\mathrm{H}}_{|H_r|}$(eq.(4.30)).

4.4 Conclusion

A numerical study about Murray’s laws was performed comparing indicators for different configurations of the left coronary artery. The results are represented in diagrams with two degrees of freedom corresponding to both diameters of the outflow branches in the bifurcation. The diagrams allow the immediate visualization of the effects of two of the most important non-dimensional numbers that influence indicators relevant for medical conditions, the branch diameter ratio and the expansion ratio.

Geometries following Murray’s law minimize the energy cost to maintain and keep the blood flow in circulation. This study demonstrates that in configurations following Murray’s law the expansion ratio is kept small (around 1.25), but not small enough to completely prevent regions with low WSS values. Since the geometries following Murray’s law have a downstream total cross-section area larger than the cross-section area of the parent vessel, the fluid decelerates originating adverse pressure gradients and favouring flow separation and low – pressure regions. Atherosclerosis risk would be smaller in geometries with an expansion ratio smaller than those Murray’s law imposes. In geometries with expansion ratio smaller than 1 the fluid accelerates minimizing the appearance of low – pressure regions.

The extension of regions with helical flow primarily depends on the outflow branches diameter ratio; these regions are prominent when the ratio is nearby 1. The regions where the WSS vector changes direction (OSI > 0.1) increase with the expansion ratio and decrease when the diameter ratio moves away from 1.

The angles determined by Murray’s law does not minimize the area with low WSS, these results suggest that atherosclerosis is a cost imposed to organisms given that energy minimization is the main driver of natural selection.

Several studies in the literature have shown that not all real arteries follow Murray’s law. Power laws similar to the Murray’s law with exponents between 2 and 3 have been reported. A power law with 2 has an expansion ratio of 1, with no deceleration of the fluid, which is preferable from the point of view of atherosclerosis minimization. While an exponent of around 2 could be explained by turbulent flow, a significant fraction of the results reported are inconsistent with energy minimization. The findings of the present chapter may provide a theoretical explanation for this inconsistency. Energy minimization leads to an exponent of 3 in laminar flow, but smaller exponents may be favored by natural selection because they have smaller regions with low WSS and, consequently, a lower susceptibility to atherosclerosis.

Acknowledgements

The authors gratefully acknowledge the funding by FEDER through the Operational Programme for Competitiveness Factors – COMPETE ON.2 - O Novo Norte - North Portugal Regional Operational Programme and National Funds through FCT-Foundation for Science and Technology under the projects: PEst-OE/EME/UI0532, NORTE-07-0124-FEDER-000025-RL2_ Environment&Health and PTDC/EME-MFE/102974/2008.

Notation

Symbol	**Definition**
$\mathrm{A}_{\mathrm{ratio}}$	Area expansion ratio
$A_{\mathrm{WSS}}^{\mathrm{L}}$	Surface normalized area with $\tau_w < 0.4$
$A_{\mathrm{OSI}}^{\mathrm{H}}$	Surface normalized area with OSI > 0.1
A^*	Normalization area
D_{ratio}	Diameter ratio of the outflow branches
D_{LM}	Diameter of LM
D_{LAD}	Diameter of LAD
D_{LCx}	Diameter of LCx
H	Helicity density
H_r	Normalized helicity
k	Murray’s law constant
n	Power-Law Index
$\boldsymbol{n}$	Normal unit vector
OSI	Oscillatory shear index
P	Pressure
Q_{LM}	Flow rate in LM
Q_{LAD}	Flow rate in LAD
Q_{LCx}	Flow rate in LCx
r	Radial position
R	Vessel radius
R_C	Curvature radius, see Figure 4.2

t	Time – instant of the cardiac cycle
T	Total time of the cardiac cycle
TAWSS	Time averaged wall shear stress
$\boldsymbol{V}$	Velocity vector
V^*	Normalization volume
v_m	Mean inlet velocity at the LM
$\bar{v}_m$	Average mean inlet velocity of a complete cycle at the LM
$V_{\lvert H_r\rvert}^{\mathrm{H}}$	Normalized volume with normalized helicity above 0.7
w	Frequency of the cardiac cycle
α	Angle between LM and LAD
β	Angle between LM and LCx
Δy_i	Mismatch in the interception of the vessel branches
θ	Angle between LAD and LCx
$\dot{\gamma}$	Shear rate magnitude
λ	Time-constant (Carreau model)
ρ	Blood density
$\boldsymbol{\tau}$	Shear stress tensor
τ_w	Wall shear stress magnitude
$\boldsymbol{\tau_w}$	Wall shear stress vector
μ	Blood viscosity
μ_0	Zero shear viscosity
μ_∞	Infinite shear viscosity
ω	Vorticity

References

1. Lozano, R. and M. Naghavi and K. Foreman, *et al.*, *Global and regional mortality from 235 causes of death for 20 age groups in 1990 and 2010: a systematic analysis for the Global Burden of Disease Study 2010.* Lancet, 2012. **380**(9859): p. 2095-128.
2. Chatzizisis, Y.S., A.U. Coskun, M. Jonas, *et al.*, *Role of endothelial shear stress in the natural history of coronary atherosclerosis and vascular remodeling: molecular, cellular, and vascular behavior.* J Am Coll Cardiol, 2007. **49**(25): p. 2379-93.
3. Gibson, C.M., L. Diaz, K. Kandarpa, *et al.*, *Relation of vessel wall shear stress to atherosclerosis progression in human coronary arteries.* Arterioscler Thromb, 1993. **13**(2): p. 310-5.
4. Chaichana, T., Z. Sun and J. Jewkes, *Computation of hemodynamics in the left coronary artery with variable angulations.* J Biomech, 2011. **44**(10): p. 1869-78.
5. Huo, Y., G. Finet, T. Lefevre, *et al.*, *Which diameter and angle rule provides optimal flow patterns in a coronary bifurcation?* Journal of biomechanics, 2012. **45**(7): p. 1273-1279.
6. Soulis, J.V., G.D. Giannoglou, G.E. Parcharidis and G.E. Louridas, *Flow parameters in normal left coronary artery tree. Implication to atherogenesis.* Computers in biology and medicine, 2007. **37**(5): p. 628-636.
7. Soulis, J.V., T.M. Farmakis, G.D. Giannoglou and G.E. Louridas, *Wall shear stress in normal left coronary artery tree.* J Biomech, 2006. **39**(4): p. 742-9.
8. Soulis, J.V., G.D. Giannoglou, Y.S. Chatzizisis, *et al.*, *Non-Newtonian models for molecular viscosity and wall shear stress in a 3D reconstructed human left coronary artery.* Med Eng Phys, 2008. **30**(1): p. 9-19.
9. Soulis, J.V., G.D. Giannoglou, V. Papaioannou, *et al.*, *Low-Density Lipoprotein concentration in the normal Left Coronary Artery tree.* Biomed Eng Online, 2008. **7**(1): p. 26.
10. Hossain, S.S., Y. Zhang, X. Liang, *et al.*, *In silico vascular modeling for personalized nanoparticle delivery.* Nanomedicine (Lond), 2013. **8**(3): p. 343-57.
11. Malvè, M., A. Garcia, J. Ohayon and M. Martínez, *Unsteady blood flow and mass transfer of a human left coronary artery bifurcation: FSI vs. CFD.* International Communications in Heat and Mass Transfer, 2012. **39**(6): p. 745-751.
12. Olgac, U., D. Poulikakos, S.C. Saur, *et al.*, *Patient-specific three-dimensional simulation of LDL accumulation in a human left coronary artery in its healthy and atherosclerotic states.* Am J Physiol Heart Circ Physiol, 2009. **296**(6): p. H1969-82.

13. Evegren, P., L. Fuchs and J. Revstedt, *Wall shear stress variations in a 90-degree bifurcation in 3D pulsating flows.* Med Eng Phys, 2010. **32**(2): p. 189-202.
14. Bhaganagar, K., C. Veeramachaneni and C. Moreno, *Significance of plaque morphology in modifying flow characteristics in a diseased coronary artery: Numerical simulation using plaque measurements from intravascular ultrasound imaging.* Applied Mathematical Modelling, 2013. **37**(7): p. 5381-5393.
15. Weydahl, E.S. and J.E. Moore, *Dynamic curvature strongly affects wall shear rates in a coronary artery bifurcation model.* J Biomech, 2001. **34**(9): p. 1189-96.
16. Chaichana, T., Z. Sun and J. Jewkes, *Computational fluid dynamics analysis of the effect of plaques in the left coronary artery.* Comput Math Methods Med, 2012. **2012**: p. 504367.
17. Chaichana, T., Z. Sun and J. Jewkes, *Haemodynamic analysis of the effect of different types of plaques in the left coronary artery.* Comput Med Imaging Graph, 2013. **37**(3): p. 197-206.
18. Chaichana, T., Z. Sun and J. Jewkes, *Impact of plaques in the left coronary artery on wall shear stress and pressure gradient in coronary side branches.* Comput Methods Biomech Biomed Engin, 2014. **17**(2): p. 108-18.
19. LaBarbera, M., *Principles of design of fluid transport systems in zoology.* Science, 1990. **249**(4972): p. 992-1000.
20. Murray, C.D., *The physiologtcal principle of minimom work I The vascular system and the cost of blood volume.* Proceedings of the National Academy of Sciences of the United States of America, 1926. **12**: p. 207-214.
21. Gafiychuk, V.V. and I.A. Lubashevsky, *On the principles of the vascular network branching.* J Theor Biol, 2001. **212**(1): p. 1-9.
22. Revellin, R., F. Rousset, D. Baud and J. Bonjour, *Extension of Murray's law using a non-Newtonian model of blood flow.* Theoretical Biology & Medical Modelling, 2009. **6**: p. 7-7.
23. Uylings, H.B., *Optimization of diameters and bifurcation angles in lung and vascular tree structures.* Bull Math Biol, 1977. **39**(5): p. 509-20.
24. Beare, R.J., G. Das, M. Ren, *et al.*, *Does the principle of minimum work apply at the carotid bifurcation: a retrospective cohort study.* BMC Med Imaging, 2011. **11**(1): p. 17.
25. Reneman, R.S., H. Vink and A.P.G. Hoeks, *Wall shear stress revisited.* Artery Research, 2009. **3**(2): p. 73-78.
26. Schoenenberger, A.W., N. Urbanek, S. Toggweiler, *et al.*, *Deviation from Murray's law is associated with a higher degree of calcification in coronary bifurcations.* Atherosclerosis, 2012. **221**(1): p. 124-30.
27. Eshtehardi, P., M.C. McDaniel, J. Suo, *et al.*, *Association of coronary wall shear stress with atherosclerotic plaque burden, composition, and distribution*

in patients with coronary artery disease. J Am Heart Assoc, 2012. **1**(4): p. e002543.

28. Samady, H., P. Eshtehardi, M.C. McDaniel, *et al.*, *Coronary artery wall shear stress is associated with progression and transformation of atherosclerotic plaque and arterial remodeling in patients with coronary artery disease.* Circulation, 2011. **124**(7): p. 779-88.
29. Malek, A.M., S.L. Alper and S. Izumo, *Hemodynamic shear stress and its role in atherosclerosis.* JAMA, 1999. **282**(21): p. 2035-42.
30. Kamiya, A., R. Bukhari and T. Togawa, *Adaptive regulation of wall shear stress optimizing vascular tree function.* Bull Math Biol, 1984. **46**(1): p. 127-37.
31. Figueroa, C.A., I.E. Vignon-Clementel, K.E. Jansen, *et al.*, *A coupled momentum method for modeling blood flow in three-dimensional deformable arteries.* Computer Methods in Applied Mechanics and Engineering, 2006. **195**(41-43): p. 5685-5706.
32. Vignon, I.E. and C.A. Taylor, *Outflow boundary conditions for one-dimensional finite element modeling of blood flow and pressure waves in arteries.* Wave Motion, 2004. **39**(4): p. 361-374.
33. Vignon-Clementel, I.E., C.A. Figueroa, K.E. Jansen and C.A. Taylor, *Outflow boundary conditions for 3D simulations of non-periodic blood flow and pressure fields in deformable arteries.* Computer Methods in Biomechanics and Biomedical Engineering, 2010. **13**(5): p. 625-640.
34. Dodge, J.T., Jr., B.G. Brown, E.L. Bolson and H.T. Dodge, *Lumen diameter of normal human coronary arteries. Influence of age, sex, anatomic variation, and left ventricular hypertrophy or dilation.* Circulation, 1992. **86**(1): p. 232-46.
35. Kiviniemi, T.O., M. Saraste, J.W. Koskenvuo, *et al.*, *Coronary artery diameter can be assessed reliably with transthoracic echocardiography.* Am J Physiol Heart Circ Physiol, 2004. **286**(4): p. H1515-20.
36. Ballesteros, L.E. and L.M. Ramirez, *Morphological expression of the left coronary artery: a direct anatomical study.* Folia Morphol (Warsz), 2008. **67**(2): p. 135-42.
37. Dombe, D.D., T. Anitha, S.D. Dombe and M.V. Ambiye, *Clinically relevant morphometric analysis of left coronary artery.* International Journal of Biological and Medical Research (IJBMR), 2012. **3**: p. 1327-1330.
38. Asakura, T. and T. Karino, *Flow patterns and spatial distribution of atherosclerotic lesions in human coronary arteries.* Circ Res, 1990. **66**(4): p. 1045-66.
39. Murray, C.D., *The Physiological Principle of Minimum Work Applied to the Angle of Branching of Arteries.* J Gen Physiol, 1926. **9**(6): p. 835-41.
40. Frauenfelder, T., E. Boutsianis, T. Schertler, *et al.*, *In-vivo flow simulation in coronary arteries based on computed tomography datasets: feasibility and initial results.* Eur Radiol, 2007. **17**(5): p. 1291-300.

41. Yilmaz, F. and M.Y. Gundogdu, *A critical review on blood flow in large arteries; relevance to blood rheology, viscosity models, and physiologic conditions.* Korea-Australia Rheology Journal, 2008. **20**(4): p. 197-211.
42. Issa, R.I., *Solution of the implicitly discretised fluid flow equations by operator-splitting.* Journal of Computational Physics, 1986. **62**(1): p. 40-65.
43. Leonard, B.P., *Order of accuracy of QUICK and related convection-diffusion schemes.* Applied Mathematical Modelling, 1995. **19**(11): p. 640-653.
44. Sherman, T.F., *On connecting large vessels to small. The meaning of Murray's law.* J Gen Physiol, 1981. **78**(4): p. 431-53.
45. van der Giessen, A.G., H.C. Groen, P.A. Doriot, *et al.*, *The influence of boundary conditions on wall shear stress distribution in patients specific coronary trees.* J Biomech, 2011. **44**(6): p. 1089-95.
46. Murphy, J.B. and F.J. Boyle, *A full-range, multi-variable, CFD-based methodology to identify abnormal near-wall hemodynamics in a stented coronary artery.* Biorheology, 2010. **47**(2): p. 117-32.
47. Reddy, J.N., *Principles of continuum mechanics: a study of conservation principles with applications*. 2010: Cambridge University Press.
48. Liu, X., A. Sun, Y. Fan and X. Deng, *Physiological significance of helical flow in the arterial system and its potential clinical applications.* Ann Biomed Eng, 2015. **43**(1): p. 3-15.
49. Grigioni, M., C. Daniele, U. Morbiducci, *et al.*, *A mathematical description of blood spiral flow in vessels: application to a numerical study of flow in arterial bending.* J Biomech, 2005. **38**(7): p. 1375-86.

5

Chapter

"Simplicity is the ultimate sophistication."

— Leonardo da Vinci

Artificial stenoses for computational hemodynamics[*]

---

[*] E. Doutel, J. Carneiro, J.B.L.M. Campos, J. M. Miranda.
Artificial stenoses for computational hemodynamics, **Journal of Computer Methods in Applied Mechanics and Engineering**, March 2016, under review.

5

Artificial stenoses for computational hemodynamics

Abstract

Atherosclerosis is the leading cause of death in developed countries. Mass accumulation in artery walls causes obstruction to the blood flow, stenoses, giving origin to life threatening events. This chapter focuses on the use of a simple and effective methodology for creating three-dimensional irregular stenosis in artery models for *in vitro* hemodynamic studies. The developed model infers the artery geometry prone to stenoses appearance by identifying areas of low wall shear stress. Then, by using a heat/mass-diffusional process, the stenoses growth is controlled. The method was tested using different artery models, being one of them taken from a healthy patient CT scan. The generated stenoses are irregular shaped and are highly dependent on the flow patterns developed on each artery type. The method disclosed allows a fast hemodynamic comparison between healthy and a stenotic case for a given artery geometry.

5.1 Introduction

Atherosclerosis pathological complications, namely heart attacks and thromboses, are the leading cause of mortality in the western world[1, 2]. One of early atherosclerosis hallmarks is the accumulation of high molecular weight lipoproteins within the artery intima. This abnormal accumulation, which causes obstruction to the free blood circulation, is commonly designated by stenosis. Stenosis formation and development involve complex cascades of interactions among many factors, such as biological, chemical and genetics. Mass transport between the blood and the artery wall plays also a key role in the development of atherosclerotic lesions[3-7]. Additionally, numerous studies state that there is a tendency for the development of atherosclerotic lesions at specific regions of the arterial tree, in particular at the curvatures of the arterial bifurcations and lateral walls of the respective branches. For this reason, hemodynamic factors are believed to be a cause of the focal nature of this disease[8-10].

One of these hemodynamic factors is the wall shear stress (WSS), which expresses the tangential force per unit area exerted by the blood on the surface of the vascular wall. Over the last three decades, observations and studies have validated that atherosclerosis lesions tend to be localized in regions of low WSS all over the arterial tree[11-13]. Malek and Alper [13] associated specific regions of the arterial tree prone to atherosclerosis with low wall shear stress magnitude (< 0.4 Pa) and concluded that the typical value of WSS in blood vessels varies between 1.5 and 2.0 Pa.

For both normal and stenosed vessels, analytical, numerical, and experimental studies were recognized to help in the prediction, prevention and better understanding of atherosclerosis disease[10, 14-17]. There are several studies based on idealized geometries using stenoses with idealized shapes (e.g. half spheres, ellipsoids, toroids)[15, 18-20]. Most of these are in two-dimensions (2D), not taking into account 3D hydrodynamic phenomena such as secondary flows[20]. Moreover, the flow predictions lose accuracy and realism if stenosis severity is expressed only by the diameter reduction of the vessel (2D). Therefore, it is necessary to have a good representation of the stenosis profile and evolution to make accurate predictions of the fluid flow in the arteries[21, 22].

The physical, chemical and biological mechanisms involved in the plaques deposition are complex, not completely understood and, by consequence, difficult to be modelled[23, 24]. For example, Caro *et al.* [25] suggested that atherosclerosis depends of the mass transfer rate of cholesterol between blood and the arterial wall. However, according to the authors, the fundaments of the mass transfer mechanism are not fully understood.

Although some studies use real shaped stenoses based on medical images, stenotic and non-stenotic images of a given patient are not available simultaneously[14, 16, 26, 27]. A long-term study, through medical images of a specific patient, can give important information about the evolution disease, but most of the times over dated for patient survival. The statistical information of stenosis development, taken from large samples of previous cases, is also a valuable material, however, is not enough for a correct diagnostic of the disease evolution of other patients, due to the specificity of the artery geometry of each patient. Whereas, mechanisms that generate artificial but realistic stenoses are a promising approach to the systematic and in time understanding of the hemodynamic in blood vessels.

This chapter proposes a procedure to create artificial stenoses, with irregular shapes, based on diffusional mechanisms. The diffusional process depends only on one non-dimensional parameter, the Fourier number (Fo). Three different artery geometries were chosen to implement the method. Two of them are simplified geometries of the Left Coronary Artery (LCA) and the third is an LCA artery reconstructed from a CT scan of a healthy patient. The method proposed is characterized and the advantages and limitations are discussed.

5.2 Development of stenosis growth model

The procedure for the onset of an artificial stenosis and subsequent growth in the lumen artery is schematically presented in Figure 5.1.

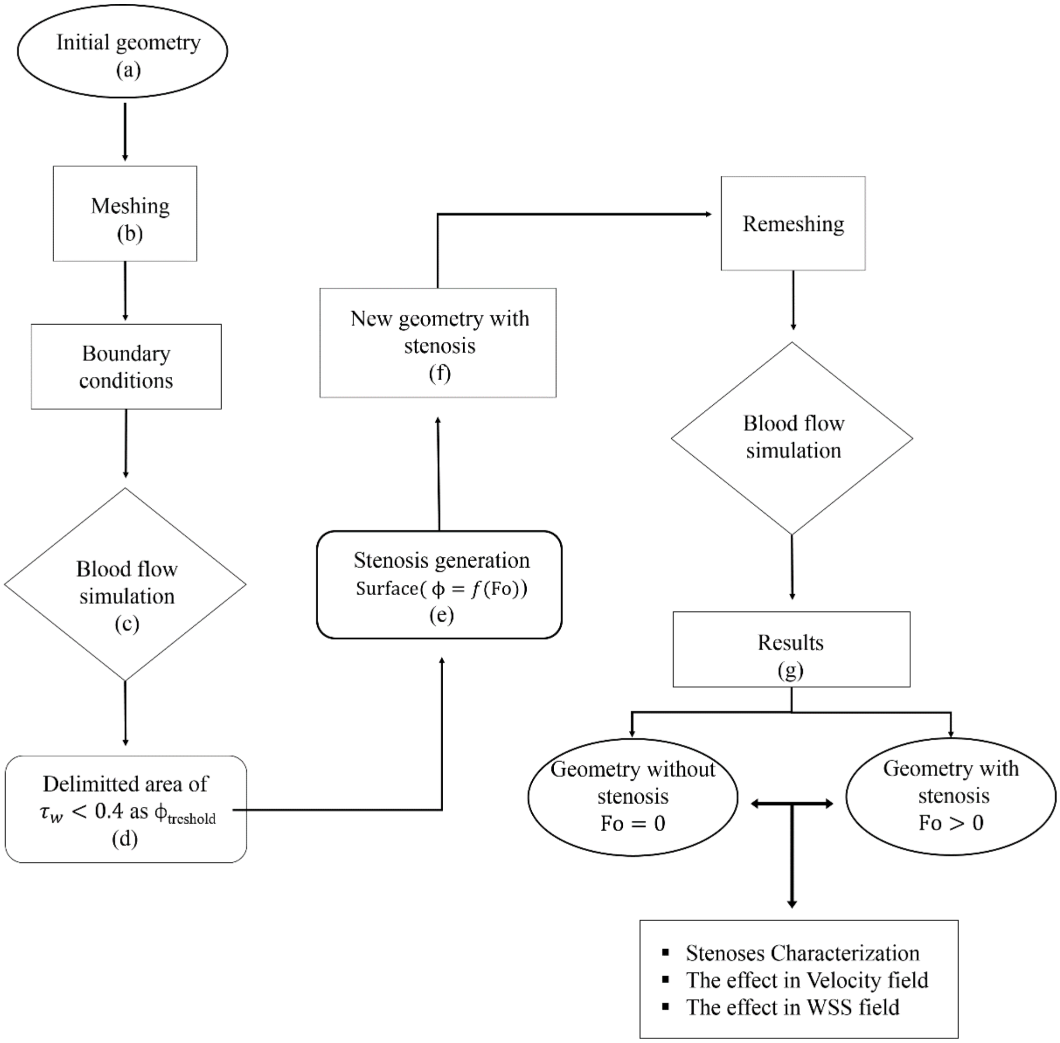

Figure 5.1. Block diagram of the stages involved in the stenosis generation process.

The procedure for stenosis creation assumes that stenosis develop in regions of low wall shear stress. Therefore, and according to the literature studies, a WSS threshold for the onset of a stenosis in healthy arteries was adopted (< 0.4 Pa[13]).

The first step is the numerical simulation of blood flow in the domain of a healthy artery model — Figure 5.1(a-c). Since the purpose of the present chapter is to demonstrate the method to produce stenoses, the blood is presumed to behave as a Newtonian fluid, in order to simplify the analysis. The method can be easily applied to non-Newtonian blood rheology. Owing to the predominant high shear rates in the arteries, this simplification does not change significantly the size and extension of the stenosis. The flow is assumed steady, incompressible and in laminar regime. The governing equations are the Navier-Stokes and the continuity equation. After solving these equations, by the commercial CFD software – ANSYS® Fluent, regions of different WSS are identified. Figure 5.2 shows an example of a region of low WSS separated from the remaining domain based on the WSS threshold ($\tau_{\text{treshold}} < 0.4$ Pa).

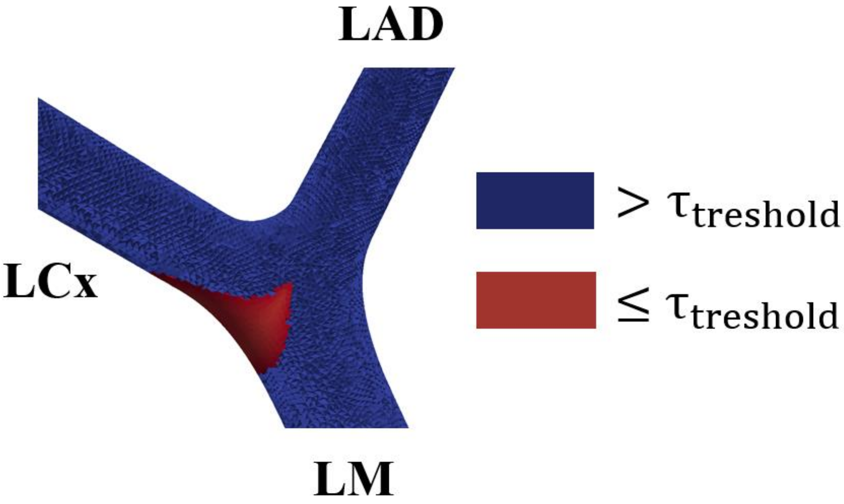

Figure 5.2. Example of low WSS region separated from the remaining domain.

The second step, Figure 5.1 (d-f), is the solution of a non-steady heat/mass diffusional model based on the 2^{a} Fourier/Fick law to generate the stenoses.

The regions with WSS below the threshold are identified as a source of the property ϕ. The stenosis growth, for each case under study, is governed by the Fourier number and a threshold value for the property ϕ.

A constant threshold value is used for all simulations. As a result, for a given geometry, different stenoses are obtained according to the Fourier number chosen, which can be indirectly defined by setting the duration of the transient simulation, Figure 5.1 (f).

In this chapter, through different Fourier numbers, five scenarios were selected: a) $\text{Fo} = 0$, representing a healthy artery without stenosis; b) $\text{Fo} = 0.004$, artery with mild stenosis; c) $\text{Fo} = 0.0320$, moderate stenosis; d) $\text{Fo} = 0.0640$, severe stenosis and; e) $\text{Fo} = 0.1280$, critical stenosis. After the stenosis formation, the new geometry was re-meshed to perform blood flow simulations with the boundary conditions of the first step. The flow, in all the geometries with and without stenosis, was analysed and characterized to evaluate the efficiency of the method developed, Figure 5.1 (g).

5.2.1 Blood flow

Governing equations and boundary conditions

As the flow was assumed steady, incompressible and laminar and the blood with a Newtonian behaviour, the governing equations are the Navier Stokes equations:

$$\rho \frac{\partial \boldsymbol{V}}{\partial t} + \rho(\boldsymbol{V} \cdot \nabla)\boldsymbol{V} = -\nabla P + \nabla \cdot \boldsymbol{\tau} \tag{5.1}$$

and the continuity equation:

$$\nabla \cdot \boldsymbol{V} = 0 \tag{5.2}$$

where $\boldsymbol{V}$ is the velocity vector, ρ the mean density, P the pressure, $\boldsymbol{\tau}$ the stress tensor. Assuming a fully developed flow, a parabolic velocity profile was imposed at the inlet of the artery:

$$v(r) = 2\, v_m \left[1 - \left(\frac{r}{R}\right)^2\right], \tag{5.3}$$

where, v_m is the mean inlet velocity, R the radius of the artery and r a radial position.

The v_m is constant (steady flow) and it was determined assuring a WSS of 1.5 Pa at the LM inlet artery[13, 28, 29] corresponding to a different Reynolds number for the three geometries under study (see Figure 5.3):

$$v_m = \frac{D_{LM}\ \tau_w}{8\ \mu} \tag{5.4}$$

The artery wall was assumed rigid and a no-slip condition was applied, *i.e.*, zero velocity at the wall. The outflow boundary conditions are difficult to establish and experimental data is non-existent due to scarce knowledge of the flow resistance of the downstream capillary network[30-32]. Therefore, outflow boundary conditions were set defining a flow partition $Q_{\mathrm{LAD}}/Q_{\mathrm{LCx}}$, where Q_{LAD} and Q_{LCx} are the flow rates in LAD and LCx branches. The flow partition implied in the Murray's law[33, 34] was used in two of the cases studied.

$$\frac{Q_{LAD}}{Q_{LCx}} = \left(\frac{D_{LAD}}{D_{LCx}}\right)^3 \tag{5.5}$$

In the other case studied, the flow partition does not follow this law and the flow rate relations $Q_{\mathrm{LAD}} = 0.7\ Q_{\mathrm{LM}}$ and $Q_{\mathrm{LCx}} = 0.3\ Q_{\mathrm{LM}}$ were assumed (see details in Table 5.1).

5.2.2 Stenosis growth by diffusional process

Governing equations and initial condition

The equation representing the non-steady transport of the dimensionless property ϕ for stagnant fluid and constant properties is:

$$\frac{\partial \phi}{\partial t^*} = Fo\left(\frac{\partial^2 \phi}{\partial {x^*}^2} + \frac{\partial^2 \phi}{\partial {y^*}^2} + \frac{\partial^2 \phi}{\partial {z^*}^2}\right) \tag{5.6}$$

where Fo is the Fourier number:

$$Fo = \frac{t_D \mathcal{D}}{D^2} \tag{5.7}$$

Here $t_{\mathcal{D}}$ is the duration of the diffusive process, D the characteristic dimension of the inlet vessel and $\mathcal{D}$ the diffusivity. The variable t^* is the time normalized by $t_{\mathcal{D}}$ and the variables x^*, y^* and z^* are the Cartesian coordinates normalized by the characteristic dimension. In a Fourier Law framework the diffusivity is defined by:

$$\mathcal{D} = \frac{k}{\rho Cp} \tag{5.8}$$

where, k is the thermal conductivity, Cp the heat capacity and ρ the density.

For the boundary conditions, the dimensionless property ϕ is set to zero in all boundaries, except in the wall regions with $\tau_w < 0.4$ Pa where ϕ is set to 1. For $t^* = 0$, ϕ is set to 0 in the interior of the domain. The solution of equation (5.6) is a ϕ field that depends on t^* and Fo. The field for $t^* = 1$ is a function of the Fourier number only:

$$\phi(t^* = 1) = f(Fo) \tag{5.9}$$

The stenosis is defined as the regions for which:

$$\phi(t^* = 1) > 0.5 \tag{5.10}$$

As described above, after the stenoses creation, the geometries are exported and re-meshed to perform new blood flow simulations. This final step allows studying the effects of the different generated stenoses on WSS and flow fields in the respective arteries.

5.3 Methods

5.3.1 Cases under study

The selection of the geometries to be studied had the Murray's law as reference:

$$D_{LM}^3 = D_{LCx}^3 + D_{LAD}^3 \tag{5.11}$$

The geometries were characterized by the expansion ratio, defined as the ratio between the sum of the squares of the cross-section areas of the daughter branches and the square of the main branch:

$$A_{ratio} = \frac{D_{LAD}^2 + D_{LCx}^2}{D_{LM}^2} \tag{5.12}$$

A volume ratio V_{ratio} was also defined by:

$$V_{ratio} = \frac{D_{LAD}^3 + D_{LCx}^3}{D_{LM}^3} \tag{5.13}$$

Geometries that follow the Murray's law have an expansion ration between 1 and 1.25. Usually, conditions for the formation of large stenoses emerge for high expansion ratios.

To test the procedure in vessels encompassing a significant range of geometrical characteristics, three different geometries (Figure 5.3), were studied:

(I) Simplified LCA bifurcation (Murray's law geometry);
(II) Simplified LCA bifurcation (has a high expansion ratio and does not follow Murray's law);
(III) A Patient-specific LCA.

Idealized models – Cases (I) and (II)

The models (I) and (II) under study represent a segment of the left coronary artery comprising LM and its bifurcation into LAD and LCx. The geometries were constructed using Solidworks® software and their main properties are listed in Table 5.1. These two geometries were chosen in order to assess the ability of the method when it is applied to different arteries, and also to study the effects of different stenoses in the blood flow.

Real model - Case (III)

The third model is a real artery extracted from a CT scan of a LCA of a healthy patient. The CT scans come from collaboration with a hospital center (*Vila Nova de Gaia and Espinho Hospita*l, Portugal), which provided CT scans from several patients in DICOM format. The DICOM data from one random patient with healthy coronary arteries was selected then the original DICOM data were transferred to a separate workstation equipped with a medical imaging program, the Mimics® version 16.0, for image post-processing and segmentation. The 3D LCA model was saved in STL format and afterwards, rearranged by SolidWorks® software in order to isolate the region of interest: the LCA with its branches (left anterior descending artery, LAD, and left circumflex artery, LCx). All LAD and LCx ramifications were removed. Anatomic measurements were performed at the LCA in order to provide suitable dimensions for the models (I and II). The inlet of the extracted artery was elongated to ensure a fully developed velocity profile (blue region in Figure 5.3- III).

Table 5.1. Geometrical characteristics of the cases under study

Characteristics	**Cases under study**		
	I	**II**	**III**
D_{LM} (mm)	4.5	4.00	4.00
D_{LCx} (mm)	3.4	3.39	1.48
D_{LAD} (mm)	3.7	4.53	2.95
Murray' Law diameters	yes	no	no
α	145º	155º	150º
β	125º	130º	143º
$D_{\mathrm{LCx}}/D_{\mathrm{LAD}}$	0.92	0.75	0.50
$Q_{\mathrm{LAD}}/Q_{\mathrm{LM}}$	0.70	0.70	0.89
Murrays law flow partition	no	yes	yes
Re	329	260	247
$\mathrm{A}_{\mathrm{ratio}}$	1.25	2.00	0.70
$\mathrm{V}_{\mathrm{ratio}}$	1.00	2.10	0.50

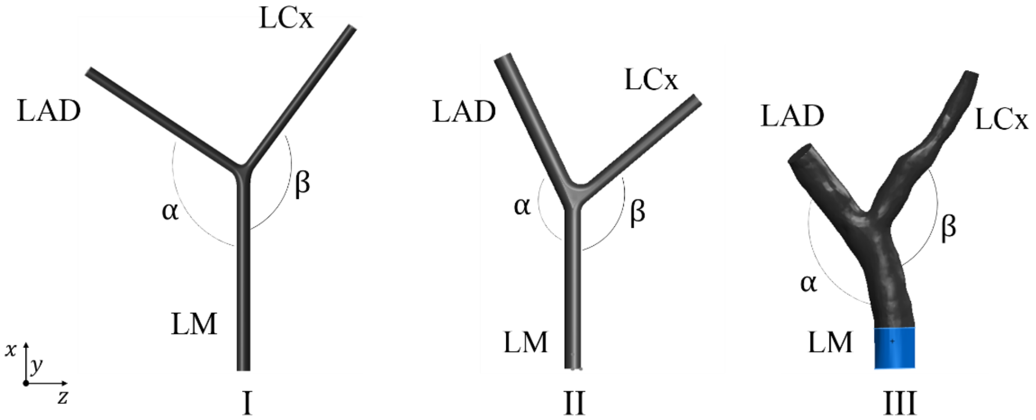

Figure 5.3. Geometries of the cases under study. In blue the tube inserted to assure a developed velocity profile.

5.3.2 Discretization schemes and algorithms

To perform the numerical flow simulations, CFD package ANSYS® Fluent (version 15) was used. The solid models from the STL files, with the design of the geometries under study, were discretized in *Fluent Meshing*®. A hybrid mesh, composed of regular Cartesian cells in the core of the artery and tetrahedral cells near the wall allowing a major refinement in the boundary layer, was created. Grid tests were made by re-running simulations and refining the number of cells. Simulations with a refined grid with ~8 million cells were performed and no significant differences in the results were observed. These tests were done for the three LCA geometries. The grids adopted are in Figure 5.4 and their properties listed in Table 5.2.

Table 5.2. Details of the grids for the three cases under study.

Cases	**No. of nodes**	**No. of cells**
I - Simplified LCA (Murray's Law)	470486	565679
II-Simplified LCA bifurcation (with expansion)	172844	909221
III-Patient-specific LCA	195611	1043677

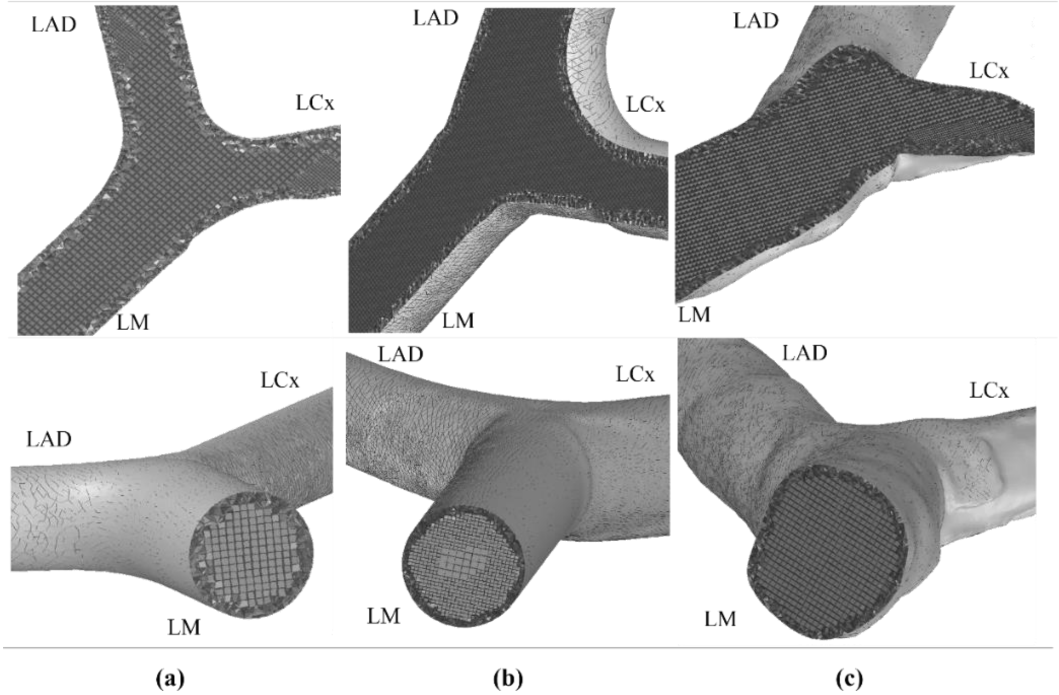

Figure 5.4. Mesh representation for the three cases under study: (a) I -Simplified LCA bifurcation (Murray's Law), (b) II - Simplified LCA bifurcation (with expansion) and (c) III – A patient-specific LCA.

The Navier Stokes velocity-pressure coupled equations were solved by the PISO algorithm[35]. The QUICK scheme[36] was used for the discretization of the momentum equations and the PRESTO! scheme for the discretization of the pressure equation.

5.3.3 Stenosis characterization

In order to characterize the stenoses, several dimensionless parameters were defined: normalized volume (V^*), normalized average thickness (L_s) and occlusion fraction (O_{cc}). The purpose of each parameter is to represent specific geometrical characteristics of the stenosis.

The normalized volume (V^*) evaluates the volume of the stenosis compared with the volume of a segment of the artery. To compensate the volume difference between the three cases and to allow future comparisons, a normalized volume was calculated by:

$$V^* = \frac{V_{stenosis}}{\frac{\pi D_{LM}^3}{4} V_{ratio}} \tag{5.14}$$

where, V_{stenosis} is the volume of the stenosis created, and V_{ratio} is given by equation (5.13).The normalized average thickness, L_{s} , evaluates the average thickness of the stenosis normalized by the inlet diameter.

$$L_s = \frac{\frac{V_{stenosis}}{A(\tau_w < 0.4)}}{D_{LM}} \tag{5.15 }$$

The occlusion fraction is defined by:

$$O_{cc} = \frac{A_{stenosis}}{A_{flow}} \tag{5.16}$$

where, A_{stenosis} is the stenosis area extracted from a cross-section perpendicular to the flow direction and A_{flow} the area of the same cross-section without stenosis.

5.3.4 Wall shear stress characterization

In order to compare the wall shear stress of different stenotic vessels two dimensionless parameters were defined: normalized area of critical WSS (A_{WSS}) and dimensionless WSS peak value ($\mathrm{WSS_p}$) along the stenosis x-coordinate.

The normalized area of critical WSS compares the size of the regions with low WSS of a stenotic artery with the size of the regions with low WSS of the corresponding healthy artery:

$$A_{WSS} = \frac{A(\tau_w < 0.4)_{Fo}}{A(\tau_w < 0.4)_{Fo=0}} \tag{5.17}$$

The dimensionless WSS peak value along the stenosis x-coordinate is defined by:

$$\tau_w^p = \left[\frac{\left(\tau_w^p\right)_{Fo} - \left(\tau_w^p\right)_{Fo=0}}{\left(\tau_w^p\right)_{Fo=0.128}}\right] \tag{5.18}$$

where, $\left(\tau_w^p\right)_{\mathrm{Fo=0}}$ is the peak WSS value for the initial Fourier number, $\left(\tau_w^p\right)_{\mathrm{Fo}}$ the peak WSS value for a given Fourier number and $\left(\tau_w^p\right)_{\mathrm{Fo=0.128}}$ the peak WSS value for the maximum Fourier number studied.

5.4 Results

5.4.1 Stenosis characterization

From a purely qualitative perspective, the morphologies obtained look more natural and smooth than the geometries usually obtained by the insertion of perfect geometrical solids – (See Figure 5.5). The shape of the stenosis by a simply insertion of an elliptic cut (Figure 5.5a) has a shape less natural and realistic than the shape obtained by the diffusional method developed (Figure 5.5b).

In the diffusional method, Figure 5.6, the stenosis originates at the surface of the vessel where the WSS is smaller than 0.4 Pa and progresses to the interior of the vessel by diffusion. The size of the stenosis can be controlled by the WSS threshold and by the Fourier number. The shape of the arteries obtained for the three cases under study are represented in Figure 5.6. Figure 5.7 shows, for the three cases, a cross–section perpendicular to blood flow. The different lines represent the stenosis progression, from the geometry without stenosis ($\mathrm{Fo} = 0$) until the final stage ($\mathrm{Fo} = 0.1280$).

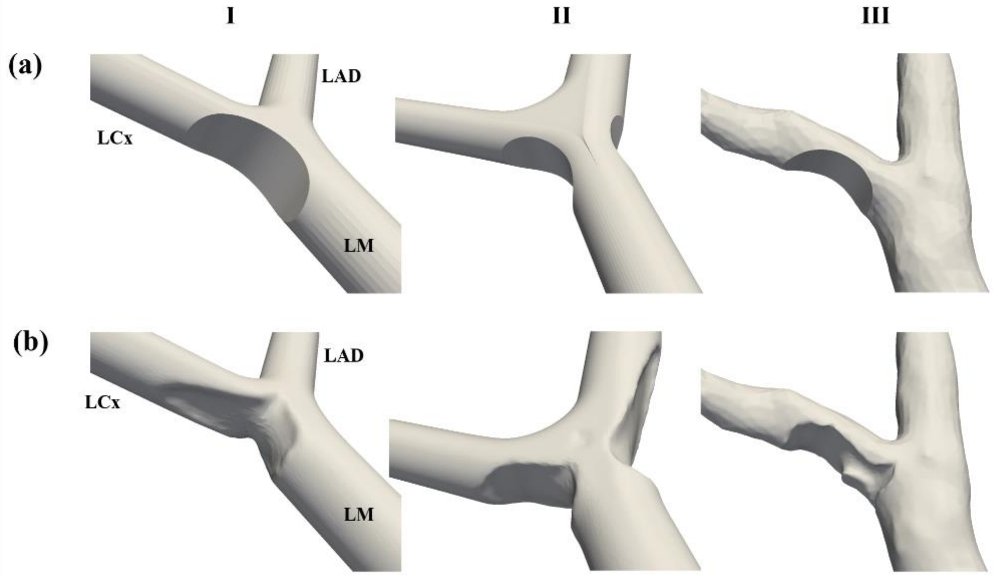

Figure 5.5. Comparison of the stenosis formation for all models under study by: a) Insertion of a perfect geometrical solid (ellipse) and b) diffusional process under study for Fo=0.064.

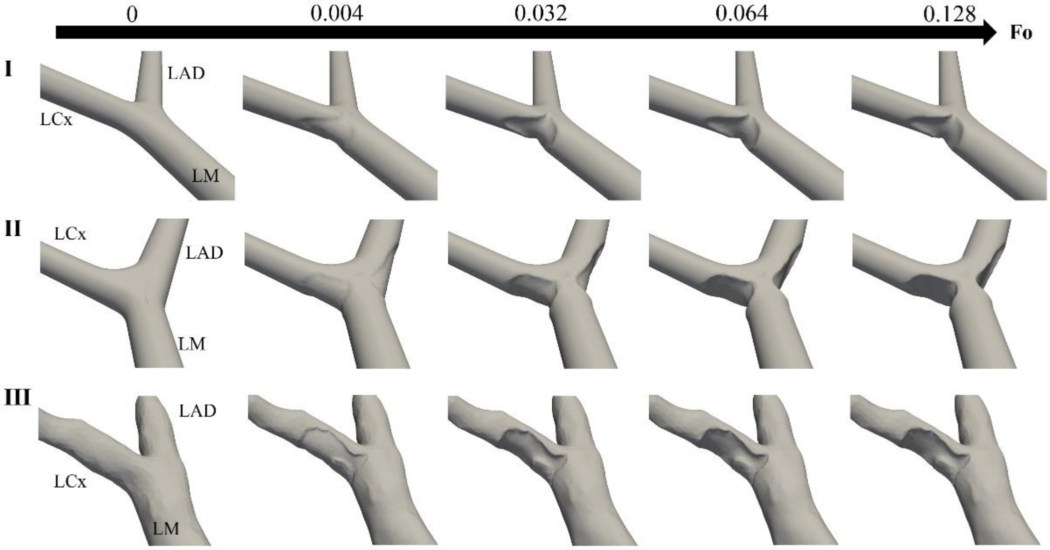

Figure 5.6. Evolution of the vessel shape with increasing Fourier numbers. I – Simplified LCA (Murray's Law), II – Simplified LCA bifurcation (with expansion) and III – A patient-specific LCA.

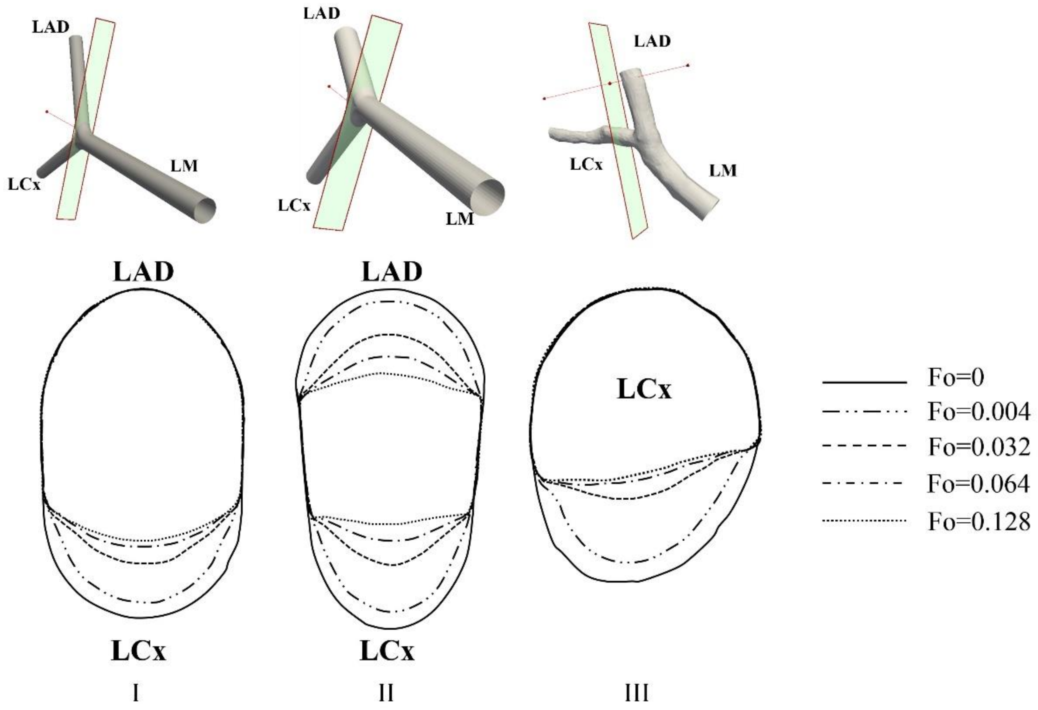

Figure 5.7. Cross-section representation, for several Fourier numbers: I – Simplified LCA (Murray's Law), II – Simplified LCA bifurcation (with expansion) and III – A patient-specific LCA.

According to Figure 5.7, in cases (I) and (III) only one branch (LCx) is affected by the stenosis, while in case (II) both branches are generating a bilateral stenosis.

Figure 5.8 summarizes the characterization of the stenosis progression for all cases. The normalized volume, normalized average thickness and occlusion fraction are presented for all the Fourier numbers.

Case (II), for all the defined variables, has the highest values. This occurrence can be explained by the formation of a bilateral stenosis, affecting both branches, and, subsequently, generating a larger stenotic region.

Although case (III) has a larger occlusion fraction than case (I), the later has a larger stenosis average thickness. This result is explained by the stenosis location on the real LCA (case III), LCx branch, which has a smaller cross-section area compared to the bifurcation region, where the stenosis in case (I) is located.

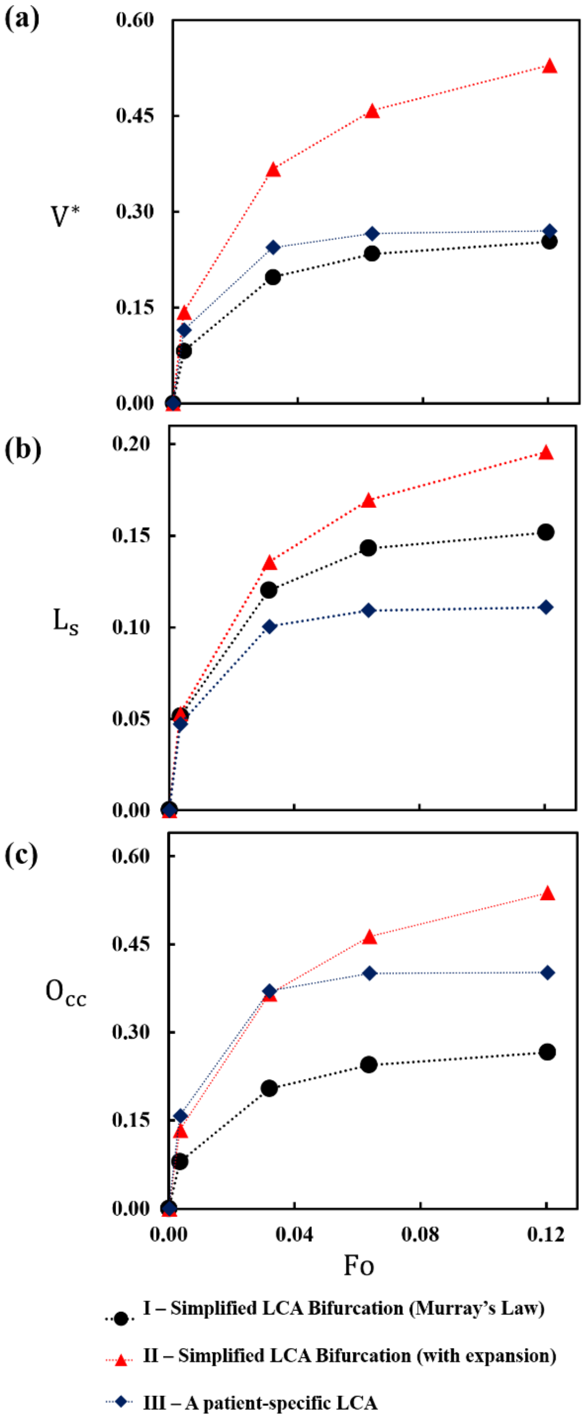

Figure 5.8. Stenosis characterization by the: a) normalized volume, b) average thickness and c) occlusion fraction for the three cases under study, I – Simplified LCA (Murray's Law), II – Simplified LCA bifurcation (with expansion) and III – A patient-specific LCA.

These results indicate that the dimensions of the stenosis, as measured by the different parameters, depend on the specific geometry of the vessel. Specific studies must be performed, in a case-by-case basis, to establish the relation between the stenosis size and the Fourier number. When this task is completed, it is possible to produce the stenosis with the desired size by setting the corresponding Fourier number.

5.4.2 Blood flow

Figure 5.9 shows the velocity fields in the cross-section obtained with the purpose of analyzing the impact of the several obstructions on blood flow. As expected, a progressive increase of the velocity in the vessel region without obstruction is patent.

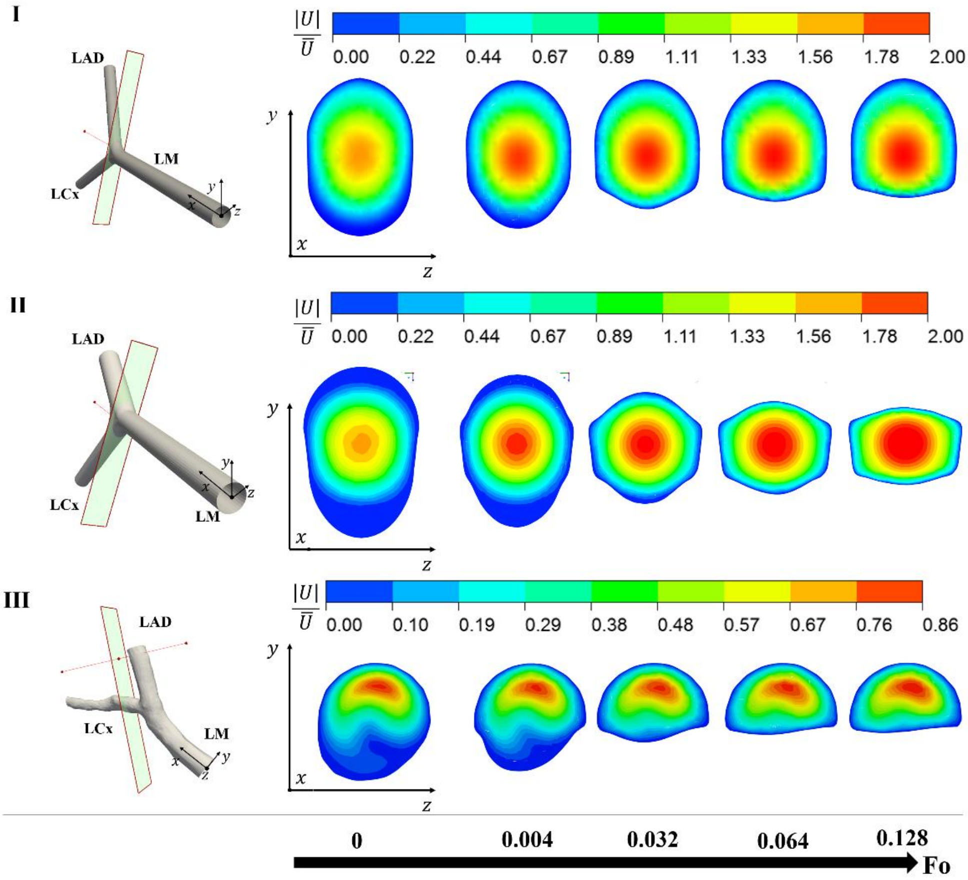

Figure 5.9. Velocity fields in the cross-section at several Fourier numbers for: I – Simplified LCA (Murray's Law), II – Simplified LCA bifurcation (with expansion) and III – A patient-specific LCA. The velocity was normalized by the inlet mean velocity for each case.

5.4.3 Wall shear stress

Figure 5.10 depicts the 3D WSS map contours for the different stenosis. This map is divided in two different colored regions: red color highlighting the critical region ($\tau_w \leq 0.4$ Pa) and blue color representing regions of higher WSS values, ($\tau_w > 0.4$ Pa).

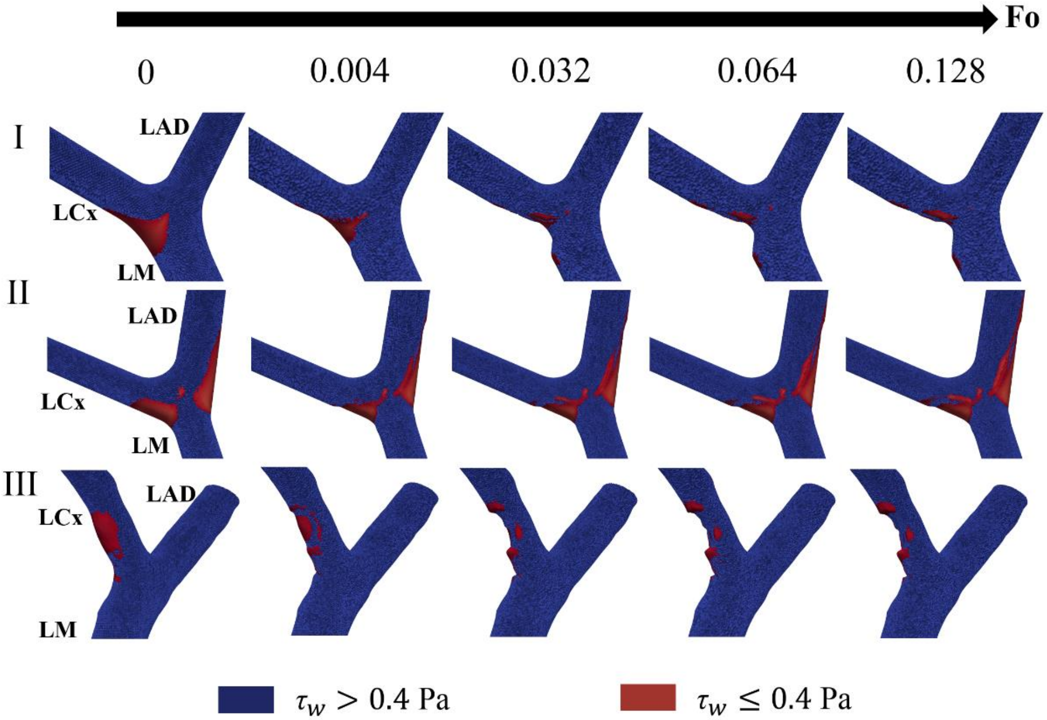

Figure 5.10. 3D WSS map contours for the stenosis generated. I – Simplified LCA (Murray's Law), II – Simplified LCA bifurcation (with expansion) and III – A patient-specific LCA.

In Figure 5.11 the normalized area of critical WSS, A_{WSS}, is plotted *vs*. the Fourier number for each case under study.

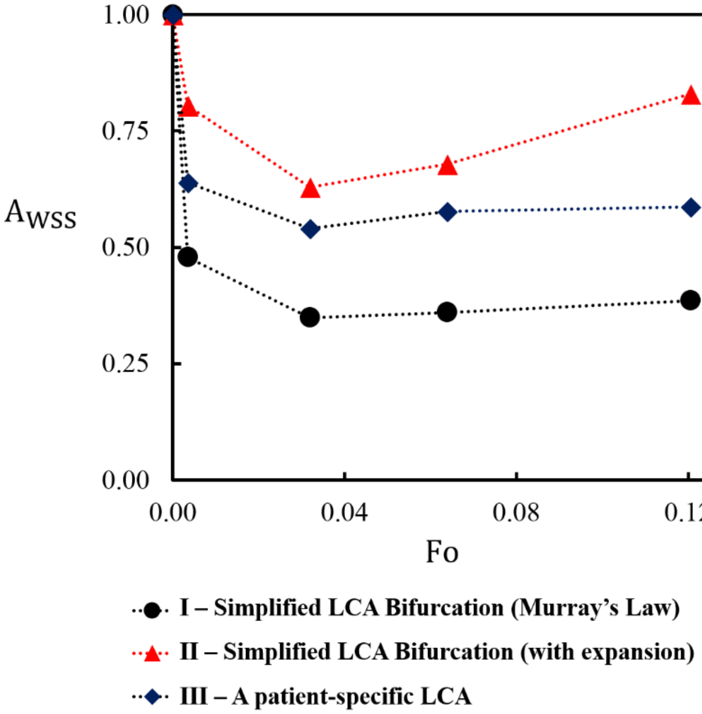

Figure 5.11. Normalized area of critical WSS for the cases under study *vs* Fourier number.

In cases (I) and (III), after the stenosis creation, A_{WSS} decreases and stabilizes for increasing Fourier numbers. In case (II), after an initial decrease, A_{WSS} increases. These results highlight the fact that, after a certain Fo number, the stenosis development and flow patterns in the blood vessels should be characterized independently.

In order to analyze in depth the effect of the stenosis in the wall sheer stress, WSS in the artery branches was plotted along *x*-coordinate for several Fourier numbers (cases (I), (II) and (III) - Figure 5.12, 13 and 14, respectively). For each figure, two lines were defined: a) the line resulting from the intersection of the middle plane with the external wall of the LAD branch and b) the line resulting from the intersection of the middle plane with the external wall of the LCx branch.

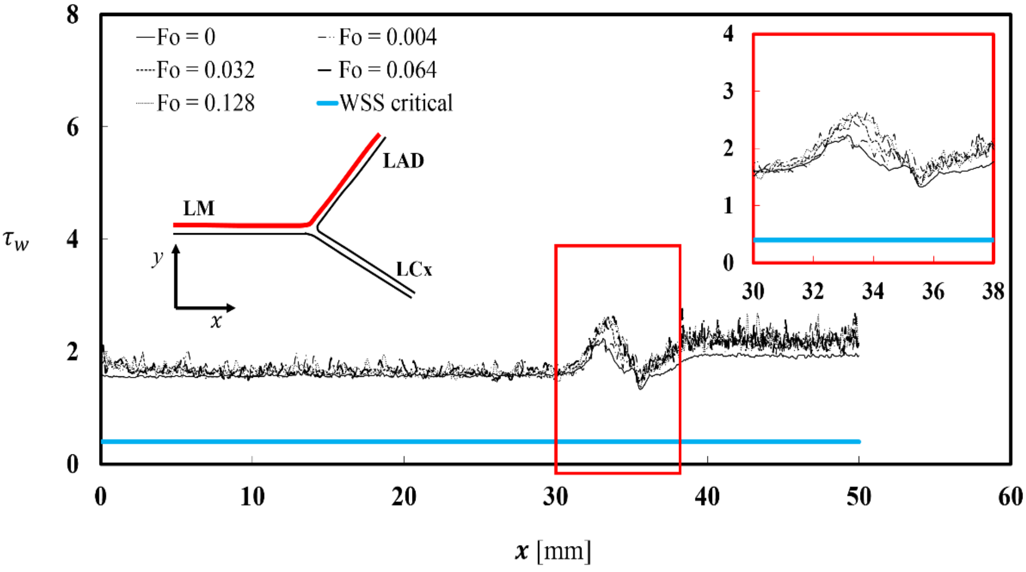

(a)

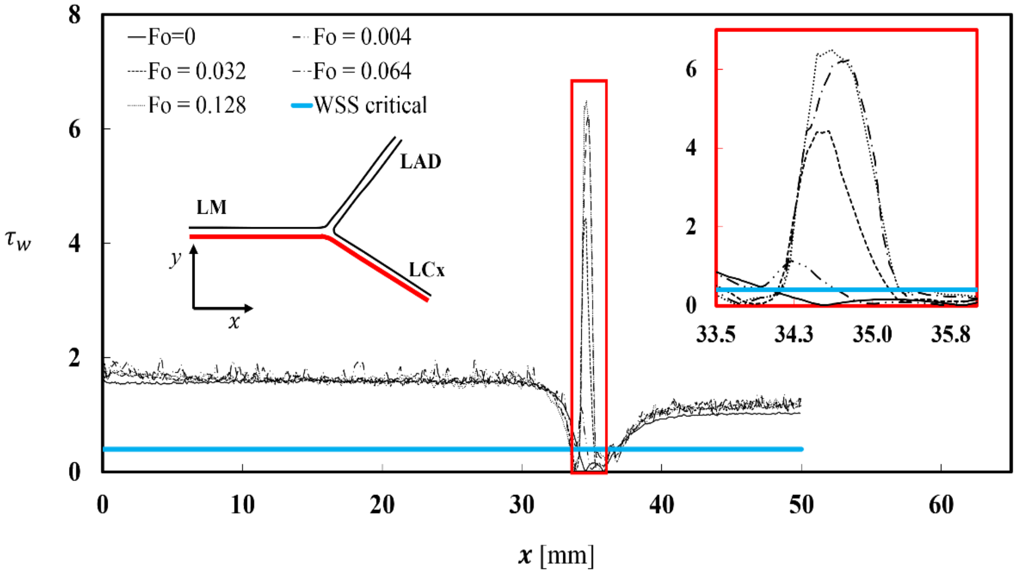

(b)

Figure 5.12. WSS along the x-coordinate: a) from LM to LAD and; b) from LM to LCx, for different Fourier numbers, for case I - Simplified LCA bifurcation (Murray's Law).

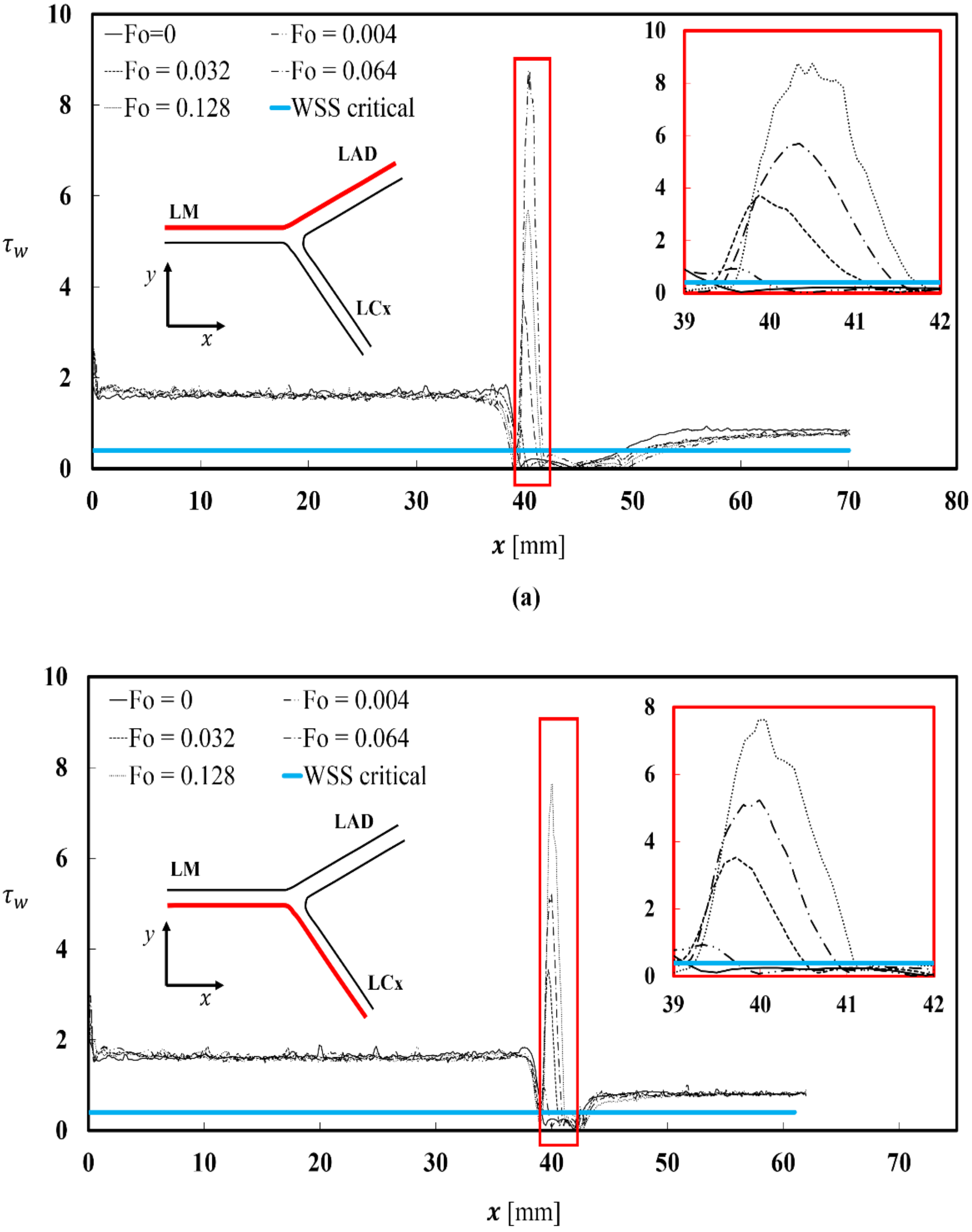

(a)

(b)

Figure 5.13. WSS along the x-coordinate: a) from LM to LAD and; b) from LM to LCx, for different Fourier numbers, for case II - Simplified LCA bifurcation (with expansion).

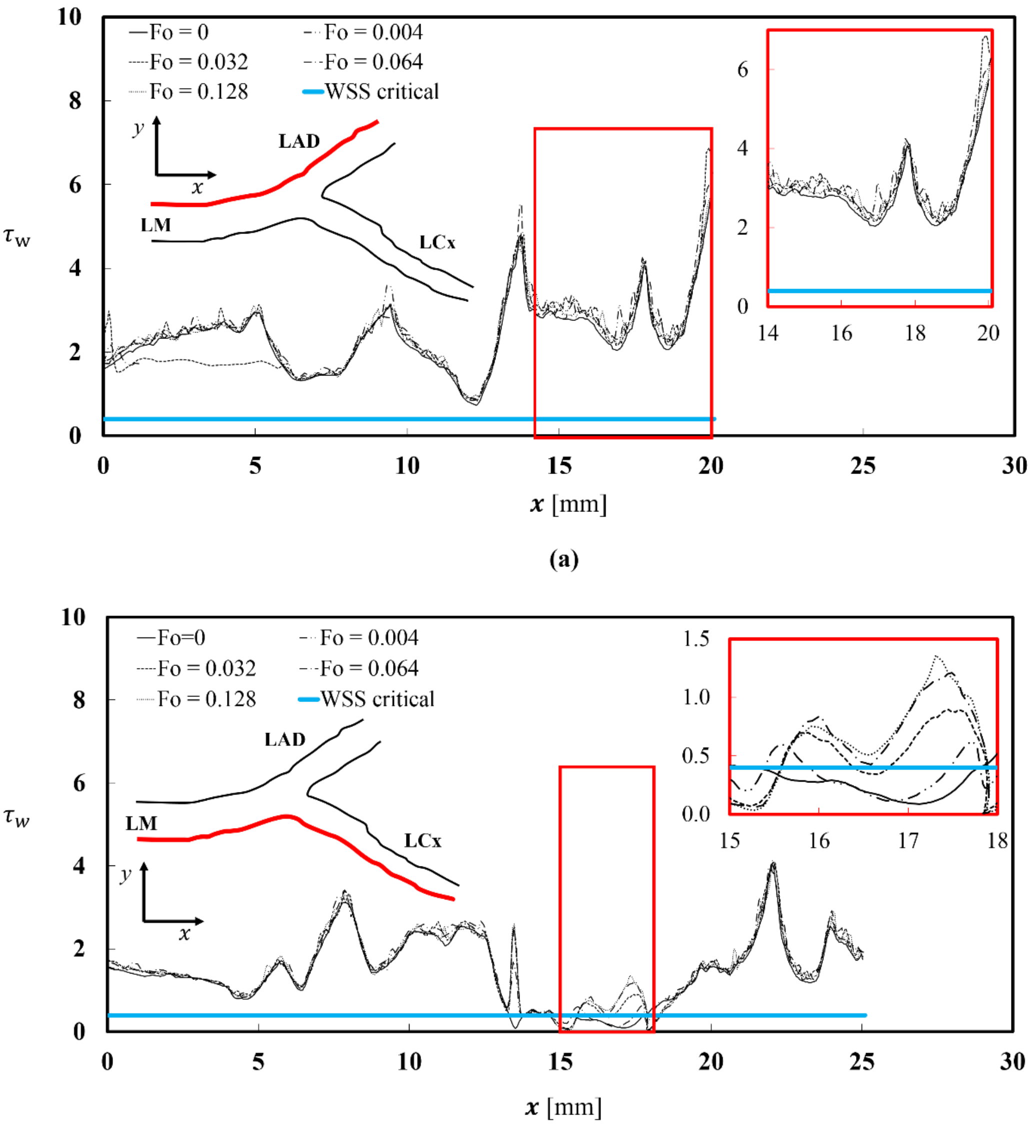

(a)

(b)

Figure 5.14. WSS along the x-coordinate: a) from LM to LAD and; b) from LM to LCx, for different Fourier numbers, for case III – A patient-specific LCA

Figure 5.12 to 14 show, in some wall region near the stenoses, a sudden WSS increase, which can cause damages in the wall tissues and eventually wall rupture. In cases (I) and (III), only one branch is exposed to high WSS values, while in case (II) both branches are. This effect along stenosis development on WSS field was analysed by plotting peak WSS, in each case under study, versus Fourier number — Figure 5.15.

The data clearly show that the stenosis growth causes a constant increase in the dimensionless peak WSS. In cases (I) and (III) an artery rupture can occur in only one of the branches, while in case (II), it can in both branches.

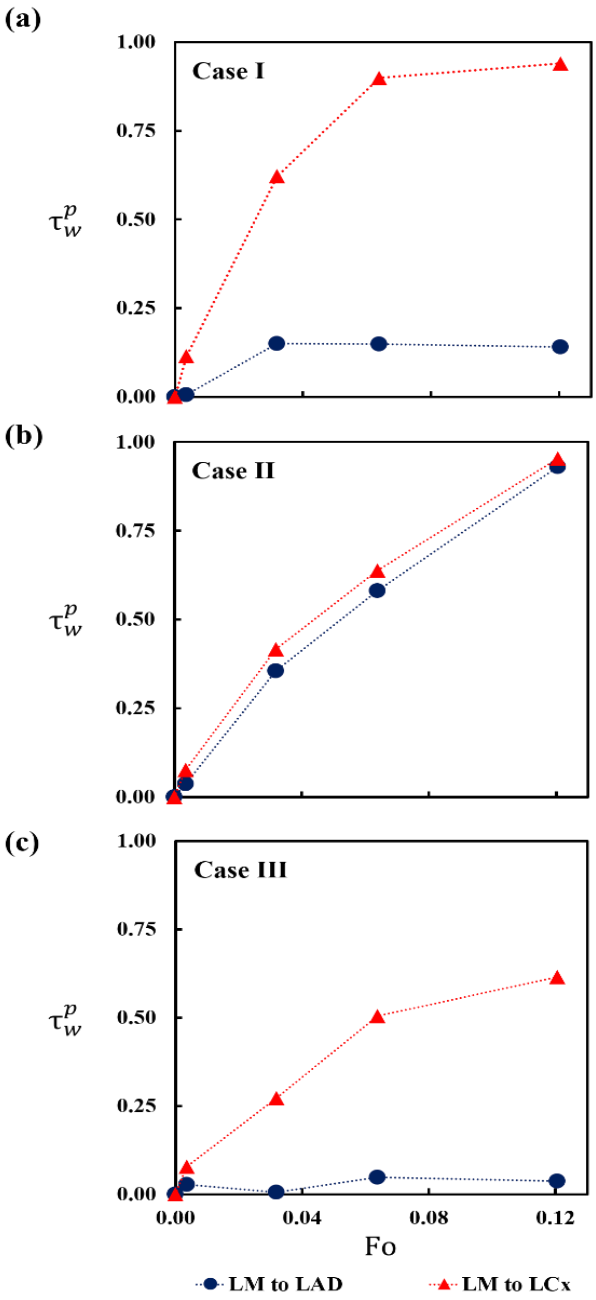

Figure 5.15. Dimensionless peak WSS values versus Fourier number for: I – Simplified LCA bifurcation (Murray's Law), II – Simplified LCA bifurcation (with expansion) and III – A patient-specific LCA.

5.5 Discussion

To the present date, there are no diagnostic tools allowing the identification of blood vessels vulnerable to atherosclerosis or plaque rupture. The accumulation of cholesterol and stenosis growth is a slow process, taking place during several years; making any clinical investigation very time consuming and expensive[37]. Therefore, mathematical models are particularly interesting for studying atherosclerosis disease and in particular stenosis formation. Several theoretical studies have considered mass transport through the blood flow for studying cholesterol accumulation in artery walls[4, 37, 38]. The best models describing mass transport process consider several layers in the artery wall due its heterogeneity. These complex models require several physical properties of the lumen artery that are very difficult to measure on real patients, making them mainly theoretical and difficult to validate. Prosi *et al.*[38] reviewed and discussed the use of mathematical models to describe the transport of low density lipoproteins (LDL) through the artery walls. These authors established that the accumulation of cholesterol highly depends on morphological characteristics of the artery, such as curvature and roughness of the lumen section. Besides, in the case of stenotic arteries regions with low shear stress and recirculation regions, the non-Newtonian behaviour of blood flow is important and should be considered, making these models even more complex [39]. Shukla *et al.*[40], Chaturani *et al.*[41] and Misra *et al.*[42] concluded that the accumulation of cholesterol increases with the severity of the stenosis, considering blood as a non-Newtonian fluid.

In this chapter, the main goal was to develop a relatively simple model that could easily produce irregular and three-dimensional stenoses based on the artery wall shear stress (WSS). Although the developed model does not consider biological processes that influence the stenosis growth kinetics, it considers the clinical hypothesis that correlates areas of low WSS with the occurrence of atherosclerosis lesions. Thus, this methodology allows creating irregular shaped stenoses in areas of the artery prone to the atherosclerosis disease. Additionally, the stenosis growths by a diffusional process, allowing a smooth progressive *in situ* development. The process mimics aspects of the growth of real stenoses and the shape of the stenosis adapts to local geometrical boundaries, leading to shapes more realistic than the ideal solids such as ellipsoids and spheres. This way, it allows hemodynamic studies in any geometry, even in real artery models. To validate this strategy, the model was used to three different arteries, one of them taken from a healthy patient CT scan. While the stenoses were generated for artery models used in computational simulations, an STL version can also be created allowing its rapid prototyping in order to proceed to *in vitro* experimental studies. This approach grants realistic stenoses, allowing a solid ground for hemodynamic studies in any type of healthy artery.

The WSS values obtained along the artery wall match the findings of other studies[43-45], reinforcing the idea that vessel rupture may occur due to high WSS at the stenosis throat. In regions before and after the stenosis, new regions with low velocities appear increasing the risk of restenosis, furthering the atherosclerosis disease.

The approach presented in this work allows increasing the robustness of hemodynamic studies in real artery models. A better understanding between the arteries morphology and stenosis formation could allow prediction of a more accurate atherosclerosis progression in the future.

The present approach can be modified, with the aim of improving its realism, by changing the boundary conditions or the diffusion equation. For example, different shapes could be obtained by using boundary condition dependent of the local WSS or by adding reaction and/or convection terms to the diffusion equation. Presently the size of the stenosis can be controlled by adjusting the Fourier number. By extending the model, new degrees of freedom can be added.

5.6 Conclusions

In this study, a procedure for creating three-dimensional irregular stenoses was developed. The proposed method does not take into account the usually complex and therefore unpredictable physiological factors. The stenosis generation is based on a diffusional process that depends on only one factor, the Fourier number. This method produces irregular shaped stenoses that are highly dependent on the flow patterns, and in particular on areas of low wall shear stress. Therefore, the implemented method links the arterial geometrical factors with the onset and growth of the stenosis.

Three different geometrical cases were selected in order to validate the effect of irregular stenosis shapes in the flow field. Different geometries have different low

WSS patterns originating case-specific sites prone to the development of atherosclerosis.

The results showed that the irregular shape of the stenosis and their particular morphology affects the flow field, originating diverse values of WSS for each case. This diffusional process allows a fast comparison between a healthy and a stenotic case. The proposed methodology is a simple but effective route that easily generates realistic stenoses suitable for hemodynamic studies.

Acknowledgements

The authors gratefully acknowledge the support of the medical team from the Hospital center of Vila Nova de Gaia and Espinho, Portugal, especially to Dr. Nuno Bettencourt and to the cardiovascular imaging specialist, Daniel Leite.

Financial support from FEDER through the Operational Programme for Competitiveness Factors – COMPETE, ON.2 – O Novo Norte – North Portugal Regional Operational Programme and National Funds through FCT – Foundation for Science and Technology under grant FCT/3013/10/2/2016/S and projects PEst-OE/EME/UI0532, NORTE-07-0124-FEDER-000025-RL2_ Environment&Health and PTDC/EME-MFE/102974/2008.

Notation

Symbol	**Definition**
A_{flow}	Initial area of the cross-section where the stenosis will growth
$A_{(\tau_w<0.4)_{\text{Fo}}}$	Critical WSS area depending of the Fourier number
$A_{(\tau_w<0.4)_{\text{Fo}=0}}$	Critical WSS area for Fo = 0
$\mathrm{A}_{\text{ratio}}$	Area expansion ratio
A_{stenosis}	Area of the cross-section where is located the stenosis

$\mathrm{A}_{\mathrm{WSS}}$	Normalized area of critical WSS
Cp	Heat capacity
D	Characteristic dimension of the inlet vessel
$\mathcal{D}$	Diffusivity coefficient
D_{LM}	Diameter of LM
D_{LAD}	Diameter of LAD
D_{LCx}	Diameter of LCx
Fo	Fourier number
k	Thermal conductivity
L_{s}	Normalized average thickness
O_{cc}	Normalized occlusion factor
P	Pressure
Q_{LAD}	Flow rate in LAD
Q_{LCx}	Flow rate in LCx
r	Radial position
R	Inlet vessel radius
t	Time
t^*	Normalize time
$t_{\mathcal{D}}$	Duration of the diffusive process
$\boldsymbol{V}$	Velocity vector
V^*	Normalized volume
V_{stenosis}	Volume of stenosis created
$\mathrm{V}_{\mathrm{ratio}}$	Volume expansion ratio

v_m	Steady flow mean velocity inlet
$\mathrm{WSS_p}$	Normalized WSS peak value along the stenosis axial coordinate
$(WSS_{\mathrm{p}})_{\mathrm{Fo=0}}$	Peak value of WSS for Fo = 0
$(WSS_{\mathrm{p}})_{\mathrm{Fo=n}}$	Peak value of WSS depending of the Fourier number
$(WSS_{\mathrm{p}})_{\mathrm{Fo=0.128}}$	Peak value of WSS for Fo = 0.128
x, y, z	Cartesian coordinate system
x^*, y^*, z^*	Normalized Cartesian coordinate system
α	Angle between LM and LAD
β	Angle between LM and LCx
ρ	Blood density
μ	Blood viscosity
ϕ	Property which identifies the regions that will develop the stenosis
$\boldsymbol{\tau}$	Shear stress tensor
τ_w	Wall shear stress magnitude
τ_{treshold}	WSS threshold value

References

1. Chatzizisis, Y.S., A.U. Coskun, M. Jonas, *et al.*, *Role of endothelial shear stress in the natural history of coronary atherosclerosis and vascular remodeling: molecular, cellular, and vascular behavior.* J Am Coll Cardiol, 2007. **49**(25): p. 2379-93.
2. Lozano, R. and M. Naghavi and K. Foreman, *et al.*, *Global and regional mortality from 235 causes of death for 20 age groups in 1990 and 2010: a systematic analysis for the Global Burden of Disease Study 2010.* Lancet, 2012. **380**(9859): p. 2095-128.
3. Sarifuddin, S. Chakravarty, P.K. Mandal and H.I. Andersson, *Mass transfer to blood flowing through arterial stenosis.* Zeitschrift für angewandte Mathematik und Physik, 2008. **60**(2): p. 299-323.
4. Cilla, M., E. Pena and M.A. Martinez, *Mathematical modelling of atheroma plaque formation and development in coronary arteries.* J R Soc Interface, 2014. **11**(90): p. 20130866.
5. Gessaghi, V.C., M.A. Raschi, D.Y. Tanoni, *et al.*, *Growth model for cholesterol accumulation in the wall of a simplified 3D geometry of the carotid bifurcation.* Computer Methods in Applied Mechanics and Engineering, 2011. **200**(23-24): p. 2117-2125.
6. Lee, R.T., A.J. Grodzinsky, E.H. Frank, *et al.*, *Structure-dependent dynamic mechanical behavior of fibrous caps from human atherosclerotic plaques.* Circulation, 1991. **83**(5): p. 1764-70.
7. Wellnhofer, E., J. Osman, U. Kertzscher, *et al.*, *Flow simulation studies in coronary arteries-Impact of side-branches.* Atherosclerosis, 2010. **213**(2): p. 475-481.
8. VanderLaan, P.A., C.A. Reardon and G.S. Getz, *Site specificity of atherosclerosis: site-selective responses to atherosclerotic modulators.* Arterioscler Thromb Vasc Biol, 2004. **24**(1): p. 12-22.
9. Berk, B.C., *Atheroprotective signaling mechanisms activated by steady laminar flow in endothelial cells.* Circulation, 2008. **117**(8): p. 1082-9.
10. Ku, D.N., D.P. Giddens, D.J. Phillips and D.E. Strandness, Jr., *Hemodynamics of the normal human carotid bifurcation: in vitro and in vivo studies.* Ultrasound Med Biol, 1985. **11**(1): p. 13-26.
11. Asakura, T. and T. Karino, *Flow patterns and spatial distribution of atherosclerotic lesions in human coronary arteries.* Circ Res, 1990. **66**(4): p. 1045-66.
12. Zarins, C.K., D.P. Giddens, B.K. Bharadvaj, *et al.*, *Carotid bifurcation atherosclerosis. Quantitative correlation of plaque localization with flow velocity profiles and wall shear stress.* Circ Res, 1983. **53**(4): p. 502-14.
13. Malek, A.M., S.L. Alper and S. Izumo, *Hemodynamic shear stress and its role in atherosclerosis.* JAMA, 1999. **282**(21): p. 2035-42.
14. Bale-Glickman, J., K. Selby, D. Saloner and O. Savas, *Experimental flow studies in exact-replica phantoms of atherosclerotic carotid bifurcations under steady input conditions.* J Biomech Eng, 2003. **125**(1): p. 38-48.
15. Walker, A.M., J. Scott, D.E. Rival and C.R. Johnston, *In vitro post-stenotic flow quantification and validation using echo particle image velocimetry (Echo PIV).* Experiments in Fluids, 2014. **55**(10).
16. Caiazzo, A., G. Montecinos, L.O. Muller, *et al.*, *Computational haemodynamics in stenotic internal jugular veins.* J Math Biol, 2015. **70**(4): p. 745-72.

17. Park, S.M., Y.U. Min, M.J. Kang, *et al.*, *In Vitro Hemodynamic Study on the Stenotic Right Coronary Artery Using Experimental and Numerical Analysis.* Journal of Mechanics in Medicine and Biology, 2010. **10**(4): p. 695-712.
18. Javadzadegan, A., Y. Shimizu, M. Behnia and M. Ohta, *Correlation between Reynolds number and eccentricity effect in stenosed artery models.* Technol Health Care, 2013. **21**(4): p. 357-67.
19. Marsden, A.L., J.A. Feinstein and C.A. Taylor, *A computational framework for derivative-free optimization of cardiovascular geometries.* Computer Methods in Applied Mechanics and Engineering, 2008. **197**(21-24): p. 1890-1905.
20. Barakat, A.I. and E.T. Cheng. *Numerical simulation of fluid mechanical disturbance induced intravascular stents*. in *CMMB-11: Int Conf Mechanics in Medicine and Biology*. 2000. Maui, Hawaii.
21. Nosovitsky, V.A., O.J. Ilegbusi, J. Jiang, *et al.*, *Effects of curvature and stenosis-like narrowing on wall shear stress in a coronary artery model with phasic flow.* Comput Biomed Res, 1997. **30**(1): p. 61-82.
22. Andersson, H.I., R. Halden and T. Glomsaker, *Effects of surface irregularities on flow resistance in differently shaped arterial stenoses.* J Biomech, 2000. **33**(10): p. 1257-62.
23. Kaazempur-Mofrad, M.R., S. Wada, J.G. Myers and C.R. Ethier, *Mass transport and fluid flow in stenotic arteries: Axisymmetric and asymmetric models.* International Journal of Heat and Mass Transfer, 2005. **48**(21-22): p. 4510-4517.
24. Sarifuddin, S. Chakravarty and P.K. Mandal, *Effect of heat and mass transfer on non-Newtonian flow – Links to atherosclerosis.* International Journal of Heat and Mass Transfer, 2009. **52**(25-26): p. 5719-5730.
25. Caro, C.G., J.M. Fitz-Gerald and R.C. Schroter, *Atheroma and arterial wall shear. Observation, correlation and proposal of a shear dependent mass transfer mechanism for atherogenesis.* Proc R Soc Lond B Biol Sci, 1971. **177**(1046): p. 109-59.
26. Chaichana, T., Z. Sun and J. Jewkes, *Impact of plaques in the left coronary artery on wall shear stress and pressure gradient in coronary side branches.* Comput Methods Biomech Biomed Engin, 2014. **17**(2): p. 108-18.
27. Cloutier, G., G. Soulez, S.D. Qanadli, *et al.*, *A multimodality vascular imaging phantom with fiducial markers visible in DSA, CTA, MRA, and ultrasound.* Med Phys, 2004. **31**(6): p. 1424-33.
28. Kamiya, A., R. Bukhari and T. Togawa, *Adaptive regulation of wall shear stress optimizing vascular tree function.* Bull Math Biol, 1984. **46**(1): p. 127-37.
29. Reneman, R.S., H. Vink and A.P.G. Hoeks, *Wall shear stress revisited.* Artery Research, 2009. **3**(2): p. 73-78.
30. Figueroa, C.A., I.E. Vignon-Clementel, K.E. Jansen, *et al.*, *A coupled momentum method for modeling blood flow in three-dimensional deformable arteries.* Computer Methods in Applied Mechanics and Engineering, 2006. **195**(41-43): p. 5685-5706.
31. Vignon, I.E. and C.A. Taylor, *Outflow boundary conditions for one-dimensional finite element modeling of blood flow and pressure waves in arteries.* Wave Motion, 2004. **39**(4): p. 361-374.
32. Vignon-Clementel, I.E., C.A. Figueroa, K.E. Jansen and C.A. Taylor, *Outflow boundary conditions for 3D simulations of non-periodic blood flow and pressure fields in deformable arteries.* Comput Methods Biomech Biomed Engin, 2010. **13**(5): p. 625-40.

33. van der Giessen, A.G., H.C. Groen, P.A. Doriot, *et al.*, *The influence of boundary conditions on wall shear stress distribution in patients specific coronary trees.* J Biomech, 2011. **44**(6): p. 1089-95.
34. Sherman, T.F., *On connecting large vessels to small. The meaning of Murray's law.* J Gen Physiol, 1981. **78**(4): p. 431-53.
35. Issa, R.I., *Solution of the implicitly discretised fluid flow equations by operator-splitting.* Journal of Computational Physics, 1986. **62**(1): p. 40-65.
36. Leonard, B.P., *Order of Accuracy of Quick and Related Convection-Diffusion Schemes.* Applied Mathematical Modelling, 1995. **19**(11): p. 640-653.
37. Bulelzai, M.A. and J.L. Dubbeldam, *Long time evolution of atherosclerotic plaques.* J Theor Biol, 2012. **297**: p. 1-10.
38. Prosi, M., P. Zunino, K. Perktold and A. Quarteroni, *Mathematical and numerical models for transfer of low-density lipoproteins through the arterial walls: a new methodology for the model set up with applications to the study of disturbed lumenal flow.* J Biomech, 2005. **38**(4): p. 903-17.
39. Nematollahi, A., E. Shirani, M.R. Sadeghi and I. Mirzaee, *Effects of shear-dependent transport properties on lumen surface concentration of LDL particles in stenosed carotid artery.* Meccanica, 2015. **50**(7): p. 1733-1746.
40. Shukla, J.B., R.S. Parihar and S.P. Gupta, *Effects of Peripheral Layer Viscosity on Blood-Flow through the Artery with Mild Stenosis.* Bulletin of Mathematical Biology, 1980. **42**(6): p. 797-805.
41. Chaturani, P. and R.P. Samy, *A study of non-Newtonian aspects of blood flow through stenosed arteries and its applications in arterial diseases.* Biorheology, 1985. **22**(6): p. 521-31.
42. Misra, J.C. and S. Chakravarty, *Flow in arteries in the presence of stenosis.* J Biomech, 1986. **19**(11): p. 907-18.
43. Sarifuddin, *Simulation of Casson Fluid Flow and Heat Transport in Differently Shaped Stenoses.* Journal of Mechanics in Medicine and Biology, 2014. **14**(2): p. 1450024.
44. Chaichana, T., Z. Sun and J. Jewkes, *Hemodynamic impacts of various types of stenosis in the left coronary artery bifurcation: a patient-specific analysis.* Phys Med, 2013. **29**(5): p. 447-52.
45. Chaichana, T., Z. Sun and J. Jewkes, *Haemodynamic analysis of the effect of different types of plaques in the left coronary artery.* Comput Med Imaging Graph, 2013. **37**(3): p. 197-206.

6

Chapter

"To err is human and blame it on a computer

is even more so"

— Robert Orben

Geometrical effects in the hemodynamics of healthy and stenotic left coronary arteries– numerical and in vitro approaches*

---

*E. Doutel, N.Viriato, J. Carneiro, JBLM. Campos, JM. Miranda
Geometrical effects in the hemodynamics of healthy and stenotic left coronary arteries– numerical and in vitro approaches, **Journal of Biomechanics and Modeling in Mechanobiology,** May 2016, under review.

6

Geometrical effects in the hemodynamics of healthy and stenotic left coronary arteries – numerical and in vitro approaches

Abstract

Atherosclerosis is a common cardiovascular disease found in the left coronary artery (LCA). The development of this disease is believed to be closely linked to local hemodynamics, which in turn is highly influenced by the artery geometry. The hemodynamics in the LCA was studied in a healthy and stenotic patient-specific geometry using both numerical and *in vitro* approaches. The influence of non-planarity was evaluated in a patient-specific LCA model by considering two ideal models that deviate from its original geometry in their planarity. In all models, irregular stenoses were created by a previously developed procedure in which the stenosis emerges by diffusion from low wall shear stress (WSS) areas. The WSS distribution and flow patterns were evaluated in healthy and stenotic models. The experimental results validate the numerical code developed to study the blood flow assuming a steady state Newtonian behaviour. The results between the planar and non-planar idealized LCA revealed no significant differences in low WSS regions forming equal stenotic shaped regions. In the patient-specific LCA, the low WSS regions are not consistent with the idealized models leading to a different stenosis shape. The results revealed that the non-planarity has a positive effect in helicity, which is believed to have beneficial effects for atherosclerosis control. It was also demonstrated that eccentricity of the vessels cross-section and the position of the apex in relation to the axis of the parent branch have an important contribution to the flow patterns observed. Numerical results of pulsatile blood flow assuming a non-Newtonian behaviour, in the patient-specific LCA healthy and stenotic model, reinforce the non-planarity effect in local hemodynamics.

6.1 Introduction

Physiological description of blood flow has received considerable attention in recent decades due to cardiovascular diseases, the leading cause of death in developed countries[1, 2]. The study of the tangential force between the fluid and the endothelial cells of the arterial wall and the description of the velocity field contribute to understand the development of atherosclerosis (one of the leading cardiovascular diseases) and the formation of stenoses.

A stenosis in a blood vessel is an obstruction to the free circulation of blood, which, in the majority of the cases, is caused by plaques accumulation in the arterial lumen[3]. Several studies indicate that their formation is related to geometrical characteristics of the artery, such as curvatures and bifurcations, usually regions with local low wall shear stresses (WSS)[4, 5]. The diversity of plaques composition and their irregular shape hinder the prediction of the hemodynamic parameters in the stenosis region[6]. Most of the times, the hemodynamic characteristics in stenotic arteries involve high WSS at the stenosis throat and low WSS (and in some cases flow separation) upstream and downstream the stenosis[3].

The coronary arteries are non-planar at the bifurcations[7]. The non-planarity in arteries is believed to affect local hemodynamics. As a result of the non-planarity, some studies report swirling and/or helical flows in the out-of-plane branch[7-9]. Studies concerning helical and swirling flows show that they have a beneficial effect in inhibiting atherosclerosis development by increasing the strength of secondary flows near the vessel wall[10, 11]. Also, they can be beneficial to the transport of oxygen [10].

Another important geometric factor to the local hemodynamics is the detailed shape of the stenosis. Some theoretical studies apply idealized stenosis shapes, such as half spheres or ellipses to the flow phantoms, ignoring the real irregular shape of the stenosis[12-16]. Other studies make use of artery stenotic models based on medical images from CT scans and MRI[17, 18]. The contraction of the blood vessel diameter can promote disturbances in the flow field as it passes through the stenosis region [19]. The study of secondary flows in stenotic arteries is particularly important. Experimental and numerical procedures have been presented focusing on the hemodynamics in stenotic and non-stenotic arteries. Ha and Lee[20] studied experimentally the effect of pulsatile swirling flow in a stenotic artery using particle image velocimetry (PIV) technique. However, geometrical properties are not the only factor that influences local hemodynamics, the unsteady blood flow and blood rheological properties are also determinant[8, 21, 22].

In this chapter an analysis of geometrical effects on blood flow is performed comparing a LCA model from a CT scan of a healthy patient and two derived models, one planar and another non-planar. Additionally, stenotic versions of all models were also studied. 3D irregular shaped stenoses were created using a previously developed method[23] detailed in **Chapter 5**. To study the influence of the non-planarity in LCA hemodynamics, velocity fields, low WSS regions and high helicity regions were analysed in detail. To validate the numerical code an experimental analysis performed by µPIV technique and streak photography was applied to the patient-specific LCA. The effects of shear thinning blood behaviour and pulsatile flow mimicking the cardiac cycle were studied and the effect of non-planarity and the implications of irregular stenoses were analysed and discussed.

6.2 Materials and methods

6.2.1 Patient-specific and idealized LCA models

This study focuses on a specific segment of the left coronary artery comprising the left main stem (LM) and its bifurcation into left anterior descending (LAD) and left circumflex arteries (LCx). CT scans from several patients were provided in DICOM format from a collaborating medical center (*Vila Nova de Gaia and Espinho Hospital*, Portugal). A multislice CT scan from a random healthy patient was used. The patient-specific geometry was imported into SolidWorks® after post-processing and segmentation of the CT scan slices using Mimics® software (version 16.0)[23], as detailed in previous chapter. Figure 6.1a) shows the SolidWorks® three-dimensional representation of the patient-specific LCA with its centerline colored according to the respective branches. To study the influence of geometrical effects, such as non-planarity and other morphological irregularities in the hemodynamics of the LCA, two extra models were derived from the original patient-specific artery. These models, from henceforth called idealized, were designed using SolidWorks® software.

The idealized models have as main reference plane the projection of the patient-specific artery in *xy* plane, illustrated in Figure 6.2b). The angles between the branches and the main stem (*cf*. Figure A1 and Table A1 shown in Appendix) are those of the original patient-specific artery, but the diameter along the branches is constant. One of these idealized models is coplanar, *i.e.*, all three branches have their centerline in the reference plane ($z=0$), as presented in Figure 6.2b1) and b2). The other model is non-planar, with LAD and LCx centerlines deviated from the reference plane by 15º and 10º, respectively Figure 6.2c1) and c2); these inclinations are approximately those of the original patient-specific LCA, as shown in Figure 6.2a1) and a2). In the idealized models the wall surfaces are assumed to be smooth.

In order to eliminate geometrical artefacts that could lead to erroneous disturbances in the flow measurements and to assure a fully developed velocity profile, both in the experimental model and in the numerical simulations, the LM branch was artificially extended by 8 times its diameter (*cf*. Figure A1 and Table A1 shown in Appendix).

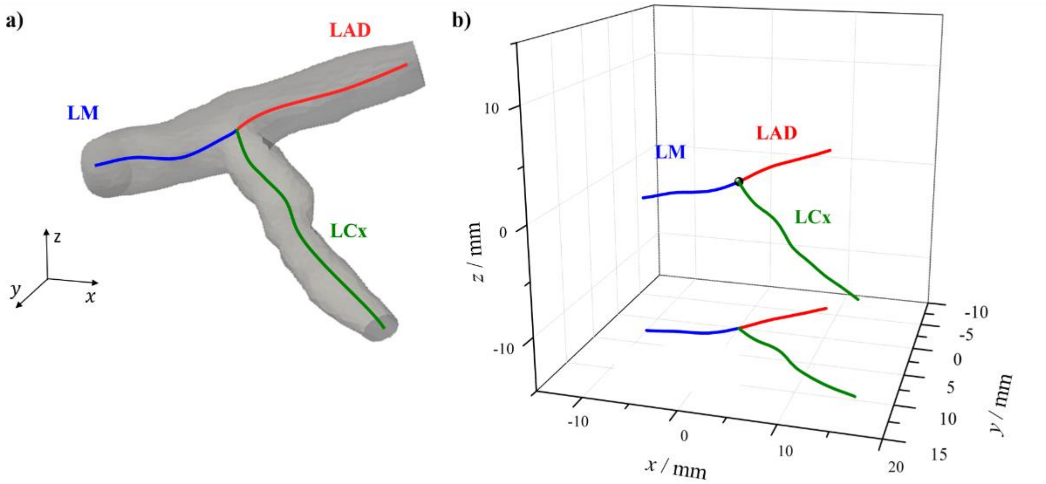

Figure 6.1. Patient-specific LCA: a) three-dimensional representation and b) centerline representation with *xy* plane projection.

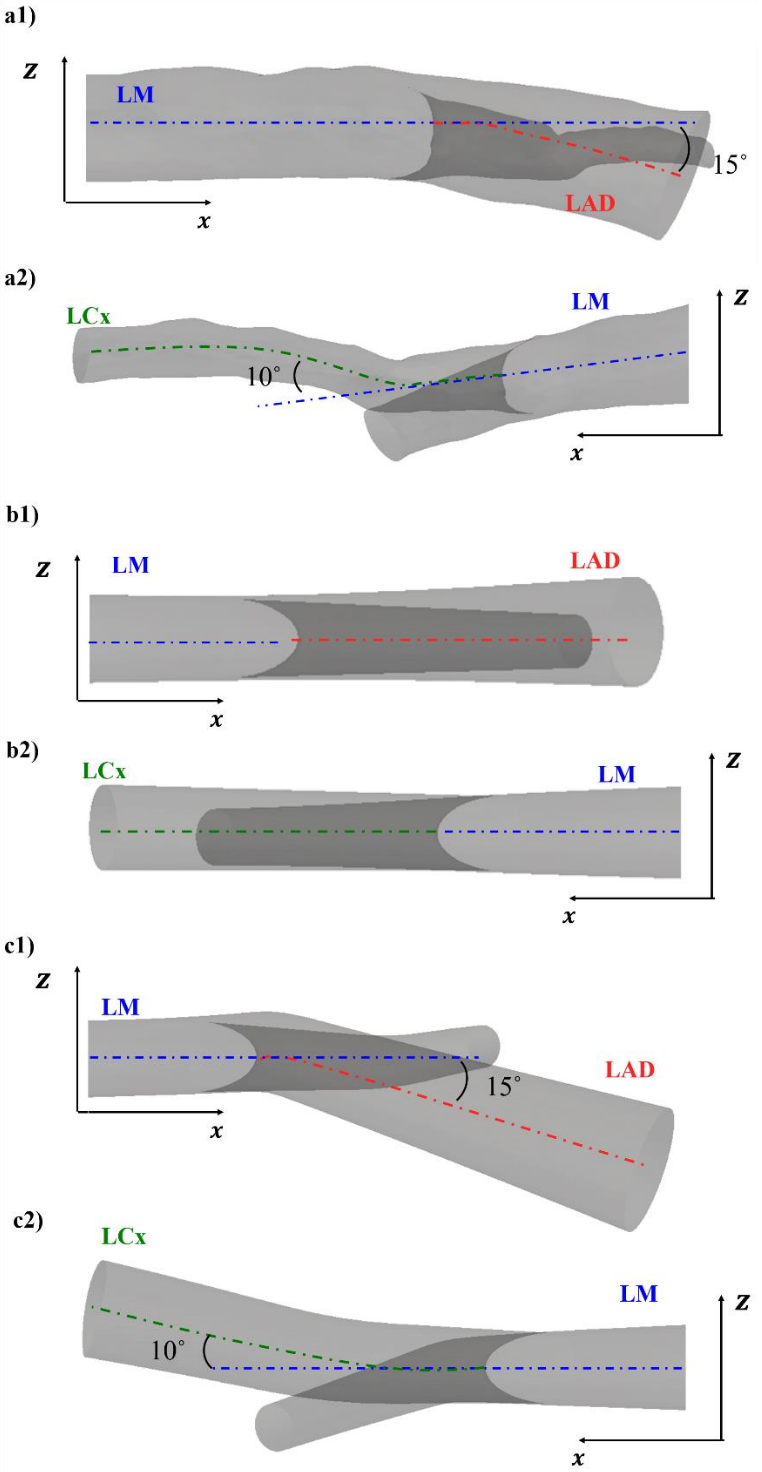

Figure 6.2. LAD and LCx lateral views of the three LCA models under study: a1) and a2) patient-specific LCA, b1) and b2) coplanar idealized LCA and, c1) and c2) non-planar idealized LCA.

Geometrical characteristics

Figure 6.3a) shows how the vessel diameter changes along LM, LAD and LCx branches of the patient-specific and idealized LCA models. As described in the previous section the idealized models have constant diameters along their branches.

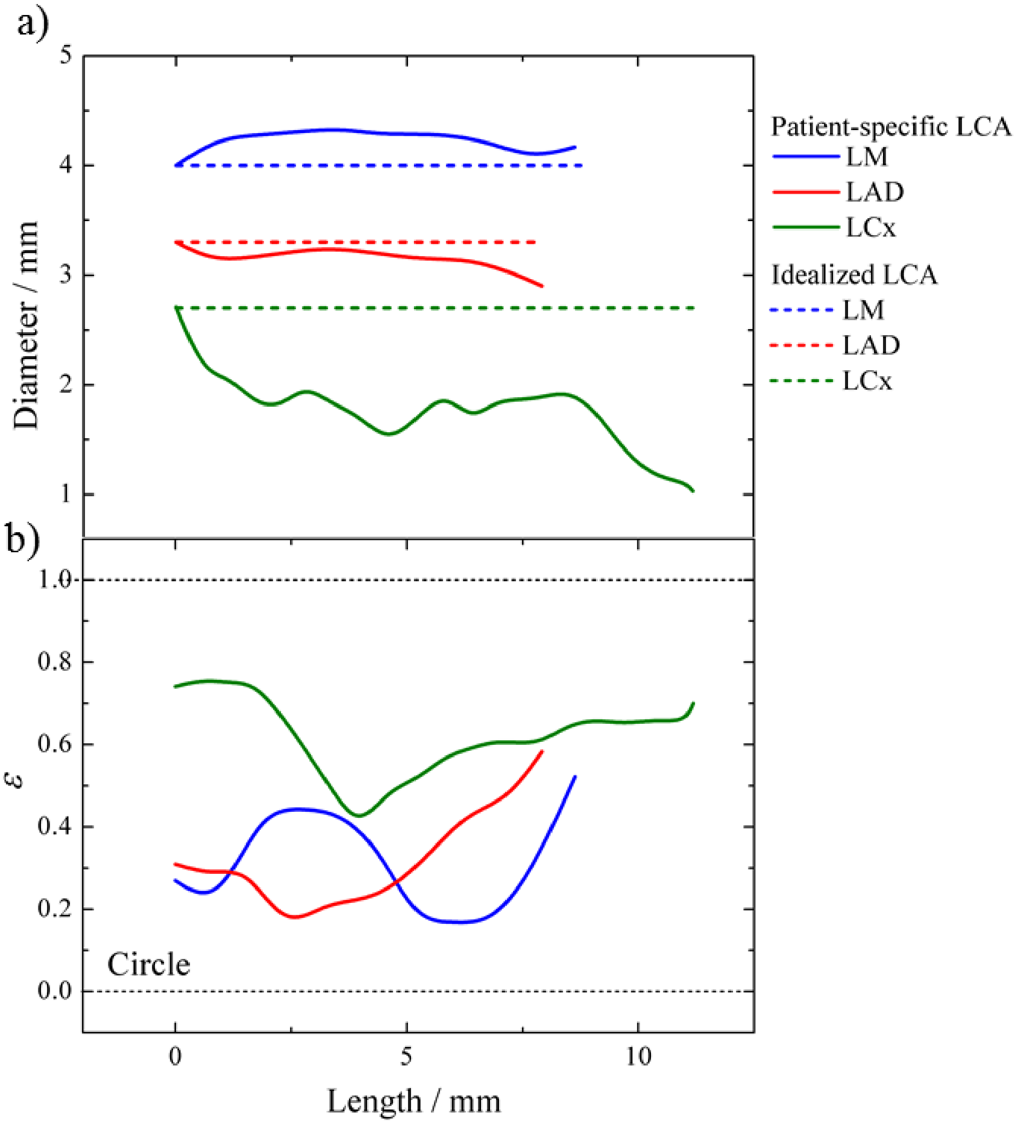

Figure 6.3. Geometrical characteristics of the models: a) LCA diameter along LM, LAD and LCx branches of the patient-specific and idealized LCA models and b) ellipticity (ε) along LM, LAD and LCx of the patient-specific LCA.

The patient-specific LCA shows variable diameter along the branches, particularly in LCx where there is a severe diameter reduction of *ca.* 3 mm to 1 mm. Figure 6.3b) depicts the ellipticity (ε) along LM, LAD and LCx of the patient-specific LCA. The ellipticity (mathematical formula, eq. A1, shown in Appendix) describes the deviation from a circular shape ($\varepsilon = 0$) towards an increasingly elliptic shape (the maximum possible value of ε is 1). As can be seen by Figure 6.3b) the LCA branches deviate considerably from the circular shape, particularly the LCx, highlighting the difference in geometrical characteristics to the idealized models, in which there is no ellipticity ($\varepsilon = 0$). Although LAD and LM present small diameter variation along its length, their shape deviates from the ideal circular shape as shown by their ε values – Figure 6.3b).

Stenosis implementation

The methodology previously developed[23] in **Chapter 5**, was used to introduce artificial stenoses in the LCA models. This methodology uses a diffusional process to generate stenoses in regions of low wall shear stresses. The stenosis grows by diffusion from the wall regions with WSS smaller than 0.4 Pa until it reaches the desired size. The generated stenosis, represented in Figure 6.4, are irregular shaped and highly dependent on the flow patterns developed on each artery. All stenoses in this work have a maximum occlusion factor (O_{cc}) of 0.4.

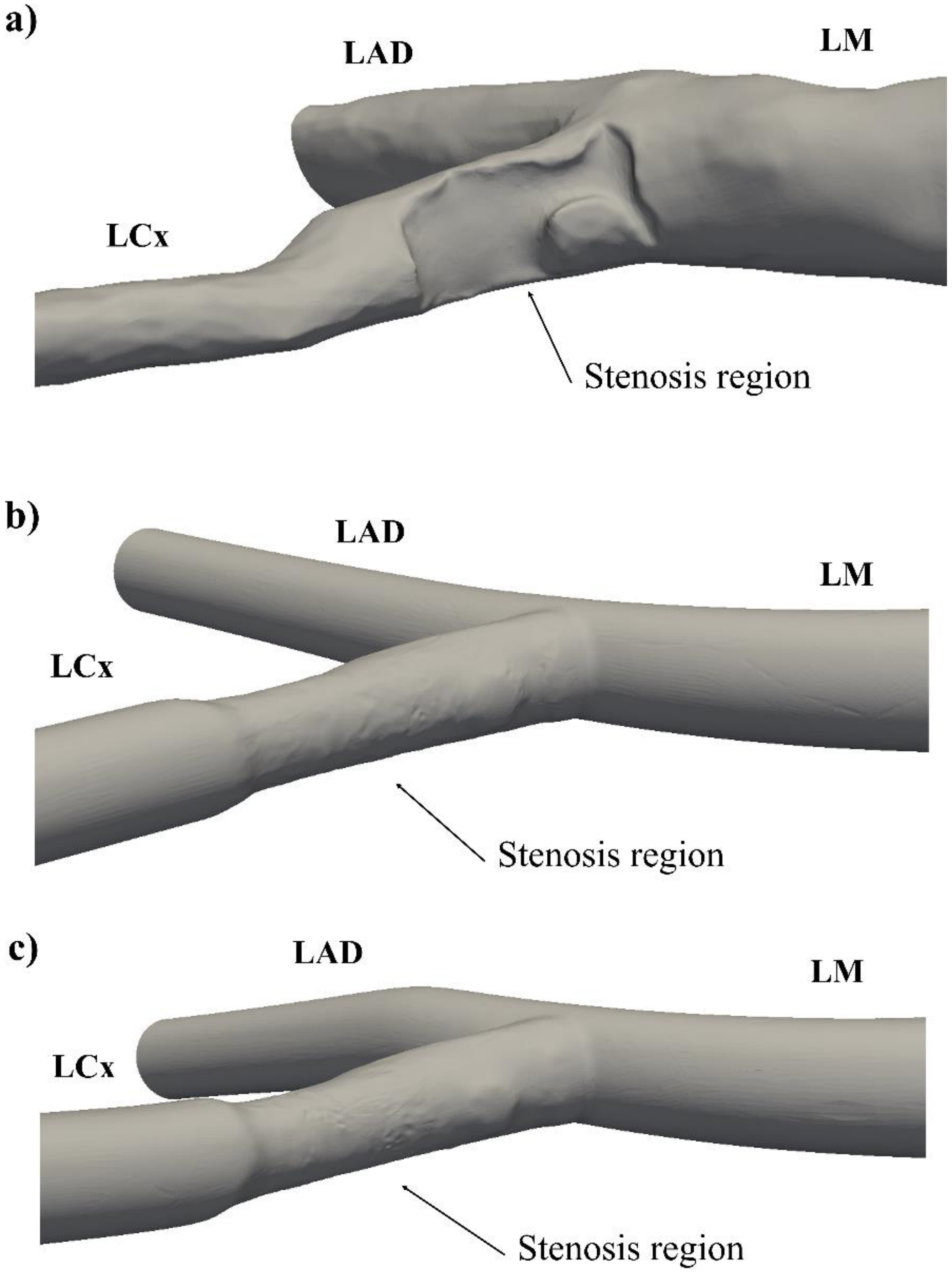

Figure 6.4. 3D irregular shaped stenosis implemented in: a) Patient-specific LCA model; b) coplanar idealized model and c) non-planar idealized model.

6.2.2 Experimental flow study

Flow phantom preparation

The more complex case (patient-specific LCA) was selected for the experimental validation by using µPIV and streak photography techniques. Due to the limited focal distance needed to perform µPIV, the patient-specific model was scaled down by a factor of 0.75. The 3D geometry designs were saved in STL format file for both numerical meshing and for constructing the experimental phantoms by rapid prototyping. The flow phantoms were prepared using the previously process[24] developed and described in **Chapter 2.** This method combines rapid prototyping (sterolithography) with sucrose molding, and allows obtaining 3D poly(dimethylsiloxane) (PDMS) flow phantoms with any desired geometry. PDMS is a widely used polymer in microfluidics and has a refractive index of approximately 1.4125 at 293 K[25]. Figure A2, shown in Appendix, illustrates this methodology by showing the fabrication steps of the LCA patient-specific flow phantom with and without stenosis.

Blood analogue fluid and flow rate selection

The fluid selected as blood analogue was a dimethyl sulfoxide (DMSO)/water mixture (52% / 42% - *w/w*), μ = 0.0035 Pa.s and ρ = 1057.5 kg.m^{-3}. This mixture eliminates the visual distortion given by the curvature of the phantoms walls by matching the refractive index of the PDMS[24]. Although in small arteries and capillaries the blood exhibits non-Newtonian behaviour, in vessels of larger diameter, such as the coronary artery tree, the non-Newtonian behaviour is small due to the predominant high shear rates[26-29]. Nevertheless, the non-Newtonian behaviour will be assessed by the numerical approach.

The flow rate used in the experimental steady flow characterization corresponds to a Reynolds number (Re) of 248. In a normal scale vessel, a Reynolds number of 248 corresponds to a WSS of 1.5 Pa at the LM inlet artery, which is a widely accepted WSS value in blood vessels[5, 23]. The flow partition was based in Murray's Law[30]. Selecting the smallest diameter of each daughter branch (see Figure 6.3a) Murray's law leads to a flow rate ratio of $Q_{\mathrm{LAD}} = 0.89\, Q_{\mathrm{LM}}$ and $Q_{\mathrm{LCx}} = 0.11\, Q_{\mathrm{LM}}$, where Q_{LAD} and Q_{LCx} are the flow rates in LAD and LCx branches. The same flow rate partition was used for the stenotic arteries. It was also assumed that the additional resistance to the flow due to the stenosis is negligible in comparison with the resistance to the flow of the capillary network downstream to the LCA.

Experimental setup for flow characterization

The experimental setup was centred on an epifluorescence microscope (DMI 5000M, Leica Microsystems GmbH) equipped with two light sources for the µPIV measurements: Nd:YAG (yttrium aluminum garnet) laser (Dual Power 65-15, Dantec); and a mercury lamp (100W) for flow visualization. The microscope objectives used were 2.5× and 5× for flow visualizations, and 2.5× for µPIV analysis. The experimental apparatus and flow visualization procedure[29] are described in detail in **Chapter 2** and **Chapter 3**. The particles used for seeding the blood analogue fluid were 8 µm fluorescent polystyrene tracer particles (Red, Molecular Probes, Invitrogen, Ex/Em: 580/605 nm, density: 1.06g/mL) at a concentration of 100 ppm (*w*/*w*). For µPIV measurements, the time interval between pulses was set to ~75 µs; for flow visualizations the exposure time ranged between 80 ms and 180 ms. The whole volume µPIV images were constructed by stacking multiple 2D velocity field slices[29] as described in **Chapter 3**. The distance between each slice was ~ 50 µm. Note that only *x* and *y* velocity components were reconstructed from the 2D slices.

6.2.3 Numerical approach

The numerical meshing and simulations were performed in the CFD package ANSYS® Fluent (version 15). In *Fluent Meshing®* an unstructured hybrid mesh was created, composed of tetrahedral cells near the walls and hexahedral cells in the core. Approximately 500.000 elements were needed for the non-stenotic models, and 1 million for the stenotic ones. To assure a mesh independent solution, grid tests were made by refining the mesh and re-running the simulations until no significant differences were observed.

Two kinds of simulations were performed, for Newtonian fluid and steady flow (matching the experimental conditions) and for pulsatile blood flow (matching more accurately the physiological conditions). The Newtonian steady flow simulations were performed for the Reynolds number of the experimental study. For the pulsatile non-Newtonian blood flow simulations, a Carreau model shear-thinning blood behaviour and a pulsatile blood flow was introduced[31] as described in **Chapter 4**. The parameter values of the cardiac cycle were those of Chaichana *et al.* [32] and the velocity profile was normalized by the time averaged inlet velocity. The time averaged inlet velocity was 0.18 m/s, corresponding to a WSS in the LM branch of 1.5 Pa, on average. Details on the implementation of the inlet boundary condition[31] that specifies the cardiac cycle can be found on the **Chapter 4**. Four consecutive cardiac cycles were simulated and the results from the last cycle were collected. A constant time-step of 0.001 s and a residual target of 10^{-6} were considered.

The blood flow simulations were based on the Navier–Stokes equations[23], assuming incompressible and laminar flow through rigid artery walls with no-slip conditions, *i.e.* zero velocity at the walls. The outflow boundary conditions were defined according to the flow partition used in the *in vitro* experiments. The Navier-Stokes equations were solved by the PISO algorithm[33]; the discretization of the momentum and pressure equations was done according to QUICK[34] and PRESTO! schemes.

6.2.4 Flow characterization

Two velocity components, U_x and U_y, were determined by µPIV. The velocity magnitude, $|U_{xy}|$, was defined based on the *x* and *y* components:

$$|U_{xy}| = \sqrt{U_x^2 + U_y^2} \tag{6.1}$$

In the CFD simulations the three components, U_x, U_y and U_z of the velocity vector were calculated.

Based on these components, the velocity magnitude $|\boldsymbol{U}|$ is definded as:

$$|U| = \sqrt{U_x^2 + U_y^2 + U_z^2} \tag{6.2}$$

The mean inlet velocity, $\overline{U}$, was chosen as the reference velocity magnitude for the normalization of the velocity fields. The WSS magnitude is given by:

$$\tau_w = \sqrt{\tau_x^2 + \tau_y^2 + \tau_z^2} \tag{6.3}$$

where τ_x, τ_y and τ_z are the WSS components. Regions of critical low WSS, $\tau_w < 0.4$ Pa, were identified based on the criterion suggested by Malek and Alper [5]. In order to analyse the areas of low WSS in all models, a surface normalized area with $\tau_w < 0.4$ Pa was calculated[31]:

$$A_{\mathrm{WSS}}^{\mathrm{L}} = \frac{A(\boldsymbol{\tau}_w < 0.4)}{\frac{\pi D_{\mathrm{LM}}^2}{4}} \tag{6.4}$$

Helical flow[11] is characterized by high helicity density[35]. The normalized helicity density is given by:

$$H_r = \frac{\boldsymbol{U} \cdot \boldsymbol{\omega}}{|\boldsymbol{U}||\boldsymbol{\omega}|} \tag{6.5}$$

where $\boldsymbol{U}$ is the velocity vector and $\boldsymbol{\omega}$ the vorticity vector. To determine the regions where the normalized absolute helicity is high, a threshold of 0.7 was assumed[31]:

$$|H_r| = \frac{|H|}{|\boldsymbol{U}||\boldsymbol{\omega}|} > 0.7 \tag{6.6}$$

Therefore, the normalized volume with $|H_r| > 0.7$ is given by:

$$V^H_{|H_r|} = \frac{V(|H_r| > 0.7)}{\frac{\pi D^3_{\mathrm{LM}}}{4}} \tag{6.7}$$

6.3 Results

6.3.1 Experimental validation of the numerical simulations

Due to the geometrical complexity of the patient-specific LCA, a reference plane (Figure 6.5b) was chosen in order to display the broadest bifurcation area. The µPIV and numerical simulations are presented for the reference plane and for planes above (Figure 6.5a) and below (Figure 6.5c) the reference plane (Figure 6.5b).

The flow goes mainly to the LAD and, consequently, the LCx exhibits the lowest velocities, as expected. These regions of low velocities originate low WSS and consequently are regions prone to the development of stenosis[36-38]. When a stenosis is placed in the LCA model, the principal features of the flow change. The extension of regions of low velocity is smaller than in their healthy counterparts and the artery diameter reduction causes higher velocities, which cause high WSS at stenosis throat. The low velocity regions are particularly prone to three-dimensional secondary flows [3, 37], while those with high velocity are susceptible to wall rupture. Since the flow patterns and the velocity magnitude are similar in the simulations and in the experimental results, it can be concluded that the experimental results validate the numerical approach.

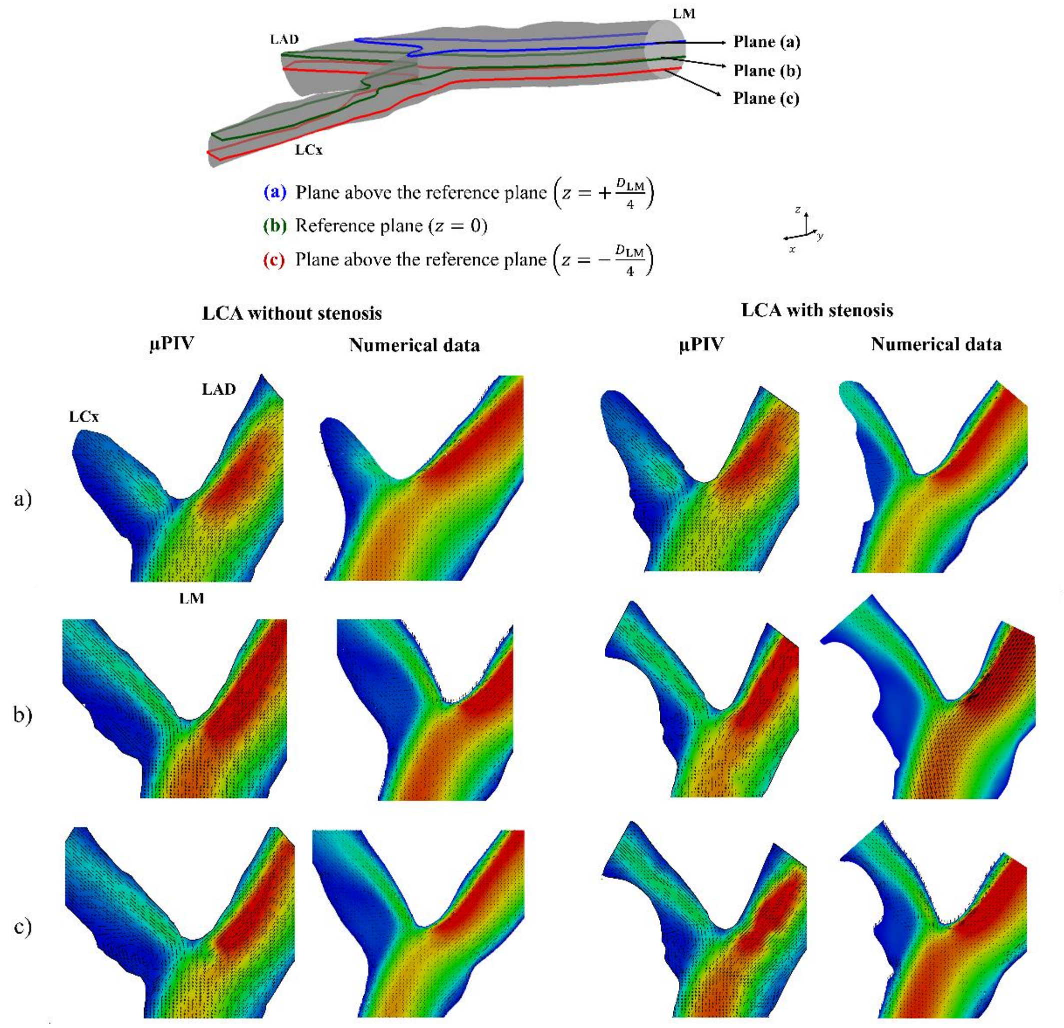

Figure 6.5. Experimental and numerical data for steady flow and Newtonian blood analogue fluid representing the normalized vector velocity fields for patient-specific LCA without stenosis (left) and with stenosis (right): a) above $(+D_{\mathrm{LM}}/4)$ the reference plane; b) in the reference plane and; c) below$(-D_{\mathrm{LM}}/4)$ the reference plane.

µPIV analysis is not sufficient for a correct hemodynamic characterization due to the three-dimensional behaviour of the phenomena. To characterize the secondary flows developed in the patient-specific LCA model, a streak photography technique was used. This technique permits the visualization of the tracer path-lines along the analysis region, describing qualitatively any secondary flows that may occur. Figure 6.6 shows, for the patient-specific LCA model, the streak photography results and the streamlines obtained by CFD simulation. The numerical data describes well the experimental results, showing that the healthy artery has an open vortex at LCx that is smaller in volume for the case with stenosis.

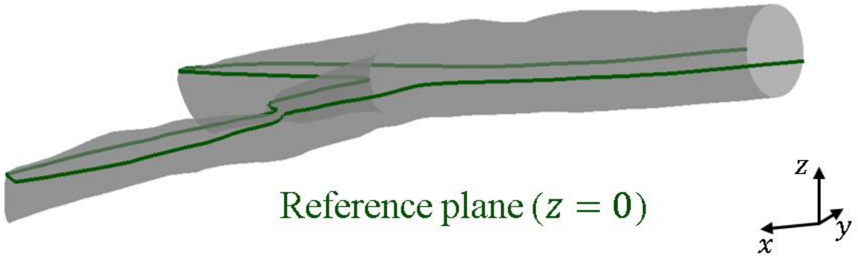

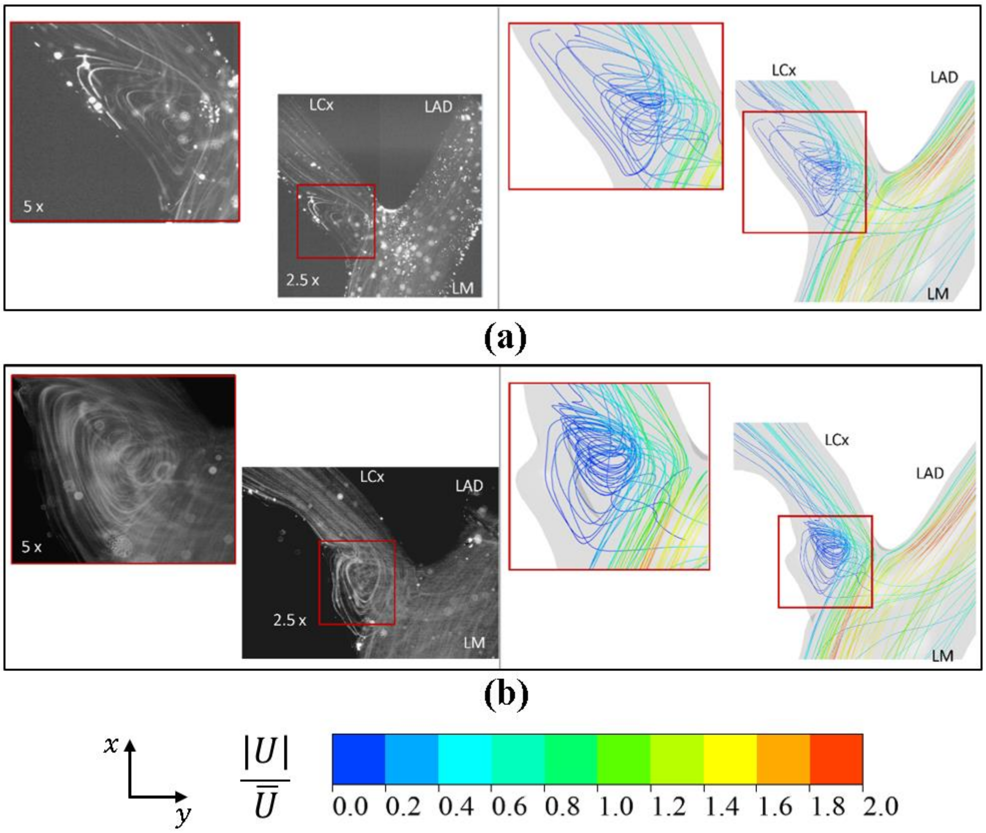

Figure 6.6. Top view of the experimental and numerical path-lines in the patient-specific LCA for steady flow and Newtonian blood analogue fluid: a) without stenosis and b) with stenosis.

To further study the flow pattern in the patient-specific LCA model, the CFD numerical data were represented at the 3D volume model, alongside with the artery

WSS values - Figure 6.7. For the healthy case (Figure 6.7a1) and a2)), there is an open vortex at LCx associated to a large zone of low WSS values ($\tau_w < 0.4$ Pa). The highest WSS values ($\tau_w > 2.5$ Pa) are observed at the apex, mostly due to the velocities of the faster flow that comes from LM bifurcating and curving mainly to the LAD branch (flow partition of 0.89 of the main flow). When the stenosis is introduced (Figure 6.7 b1 and b2), the volume of the open vortex is reduced. Although the WSS region at the apex does not change considerably, there is a reduction in the extension of regions with low WSS, located mainly downstream and upstream, *cf*. Figure 6.7b1) and Figure 7b2) the stenosis.

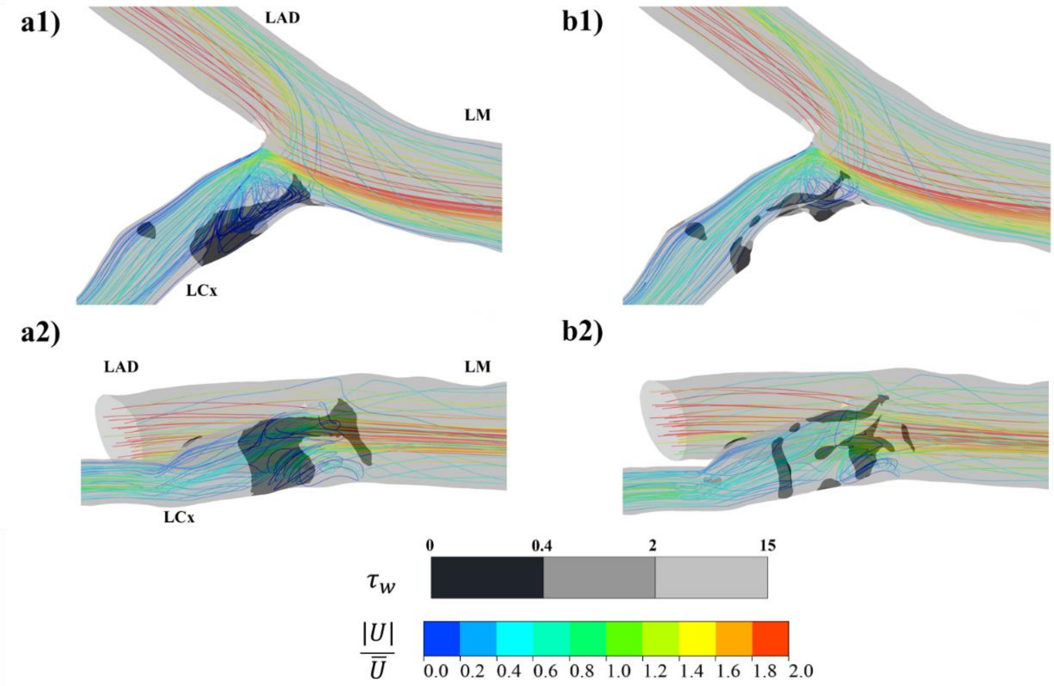

Figure 6.7. 3D streamlines and WSS distribution (greyscale colour) in the patient-specific LCA model for steady flow and Newtonian blood analogue fluid without (a1 and a2) and with (b1and b2) stenosis. 1-Top view and 2- 3D lateral view.

6.3.2 Effect of non-planarity in the flow field

In the patient-specific LCA, LCx diameter decreases along the flow direction, while both ideal models have a constant diameter along this branch. This diameter contraction causes a velocity increase, and therefore the only sizable zone at low WSS is located in the larger diameter region, as observed in Figure 6.8a). In the idealized models this contraction is absent, causing a larger area of low WSS values.

Comparing the results in the idealized models, the effect of coplanarity has no consequence in the appearance of low WSS regions in stenotic and non-stenotic arteries. - Figure 6.8b) and c).

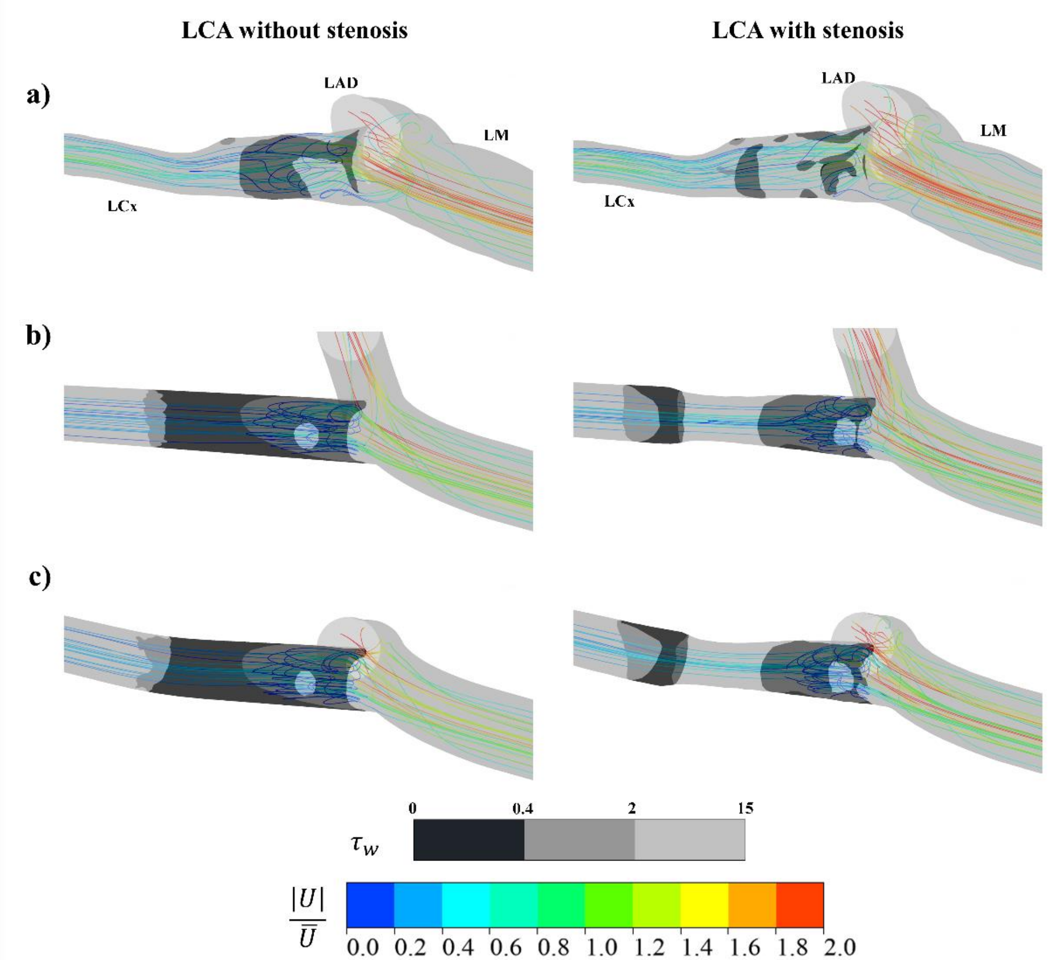

Figure 6.8. 3D streamlines and WSS field (greyscale colour) without (left) and with (right) stenosis: a) patient-specific LCA; b) coplanar LCA; and c) non-planar LCA models. Numerical results obtained for the steady state and Newtonian blood behaviour.

To better characterize the non-planarity effects, the velocity vectors tangential to 8 cross-sections normal to the main flow direction along LAD and LCx branches in all LCA models were analyzed (Figure 6.9): five cross-sections where located at LCx branch, three of them in the stenotic region (Figure 6.9 – (1) (2) and (3), red) and the other two where the LCx deviates from the main plane (Figure 6.9 – (4) and (5), green). The remaining cross-sections are located at the LAD in the region where this branch deviates from the main plane (Figure 6.9 – (6), (7) and (8), blue).

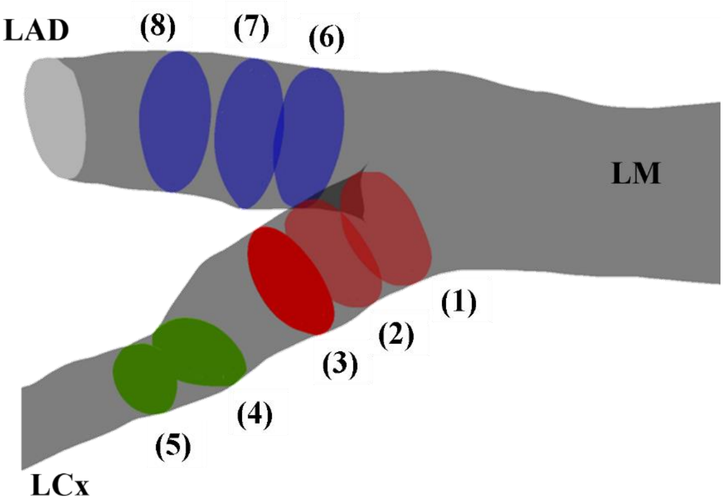

Figure 6.9. Cross-sections perpendicular to the flow along LAD an LCx branches.

The cross-sections along LCx, displayed in Figure 6.10, show that the flow in the patient-specific LCA is mainly asymmetric along the cross-sections 1 to 3. Conversely, in the idealized models the flow is symmetric, rotating around two axes. The asymmetric flow behaviour observed in the patient-specific LCA is mainly caused by geometrical irregularities, particularly the LCx ellipticity variation (Figure 6.3b), which is clearly seen in the shape of the cross-sections in Figure 6.10. The idealized models are circular shaped along the LCx branch, therefore a symmetrical behaviour is observed.

The influence of non-planarity in flow pattern can be observed at cross-sections 4 and 5, Figure 6.10. The velocity vectors show that in the non-planar idealized model the flow pattern progressively becomes asymmetric, which is in line with the 10° inclination of the LCx branch. This contrasts with the coplanar one, where the lack of inclination between branches causes perfect symmetry in the flow pattern.

Figure 6.11 shows the velocity vectors in cross-sections at LCx branch in LCA models with stenosis.

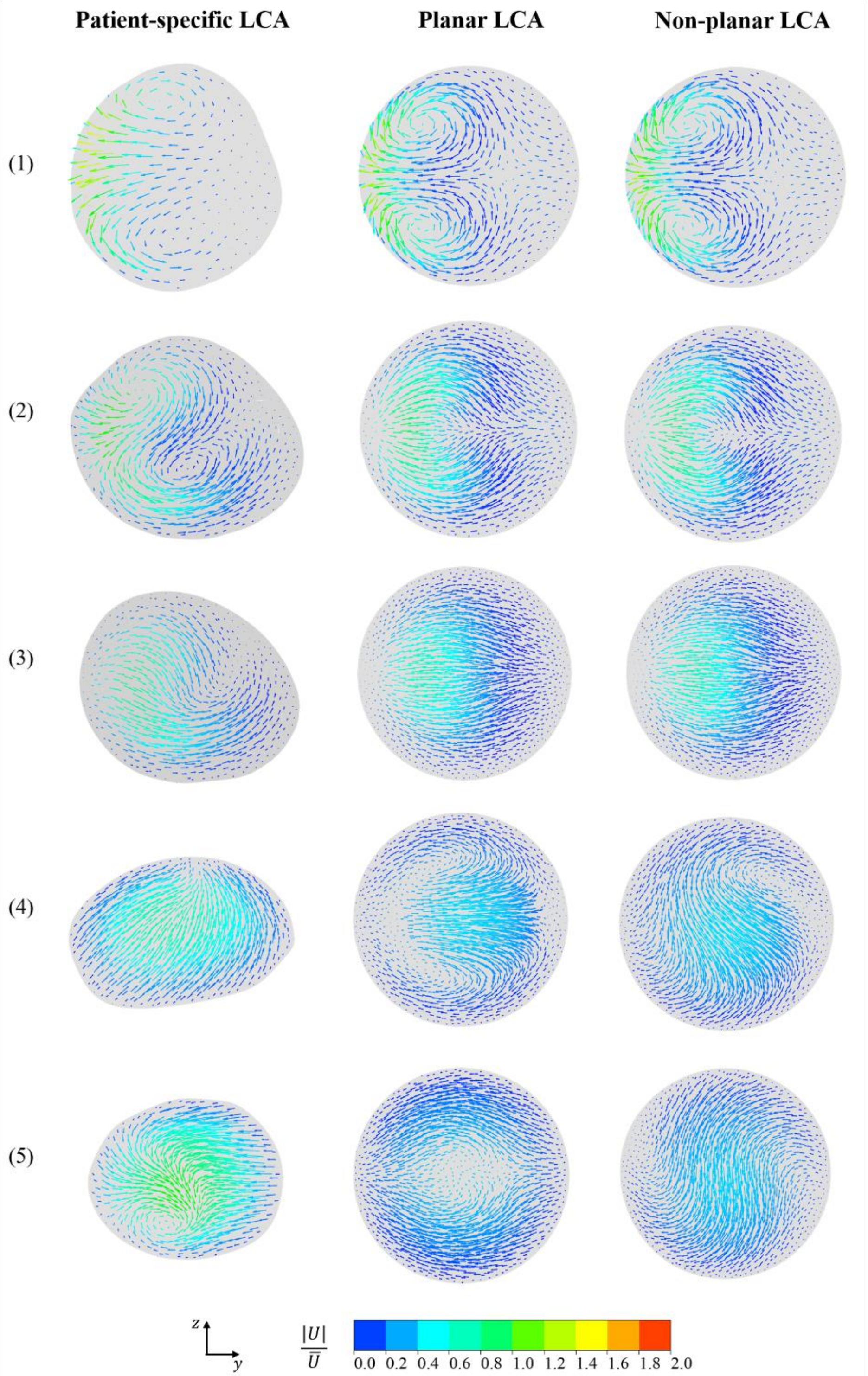

Figure 6.10. Velocity vectors (components tangential to the plane) at the LCx branch in models without stenosis. Numerical results obtained for the steady state and Newtonian blood behaviour.

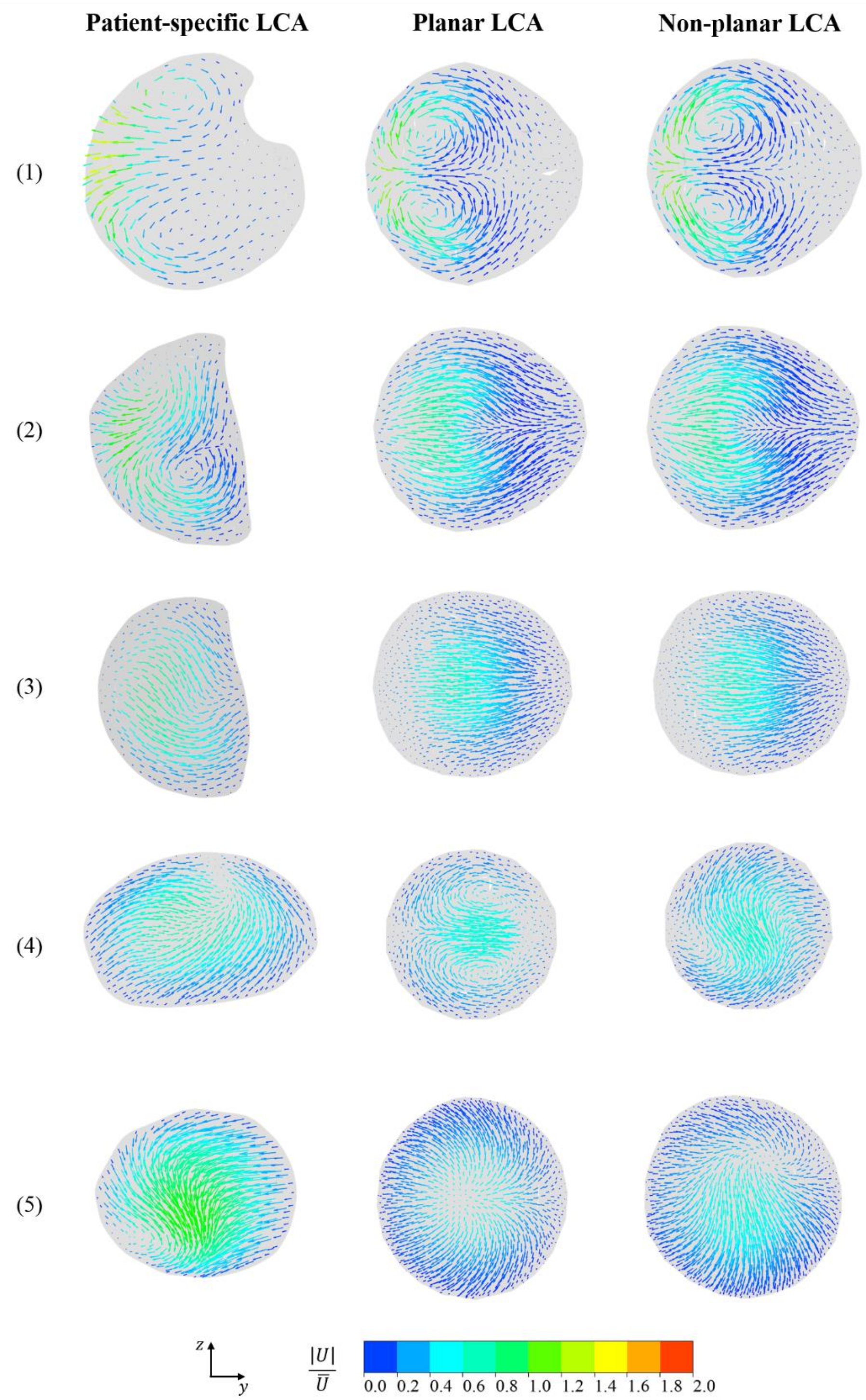

Figure 6.11. Velocity vectors (components tangential to the plane) at the LCx branch in models with stenosis. Numerical results obtained for the steady state and Newtonian blood behaviour.

Stenotic and non-stenotic cases differ mainly in the flow velocity which increases in the stenotic region, as expected. The stenosis presence does not influence the flow symmetry/asymmetry observed in the non-stenotic cases. The stenoses emerge in regions of low WSS and occupy a region of the arteries where the flow velocity is low. For this region, their effect on the flow patterns tends to be small. Since the occlusion factor is moderate (only 0.4), the stenoses create a smooth transition in a region previously with more sudden variations of shape.

The effect of non-planarity is also observed at the LAD, as displayed in Figure 6.12.

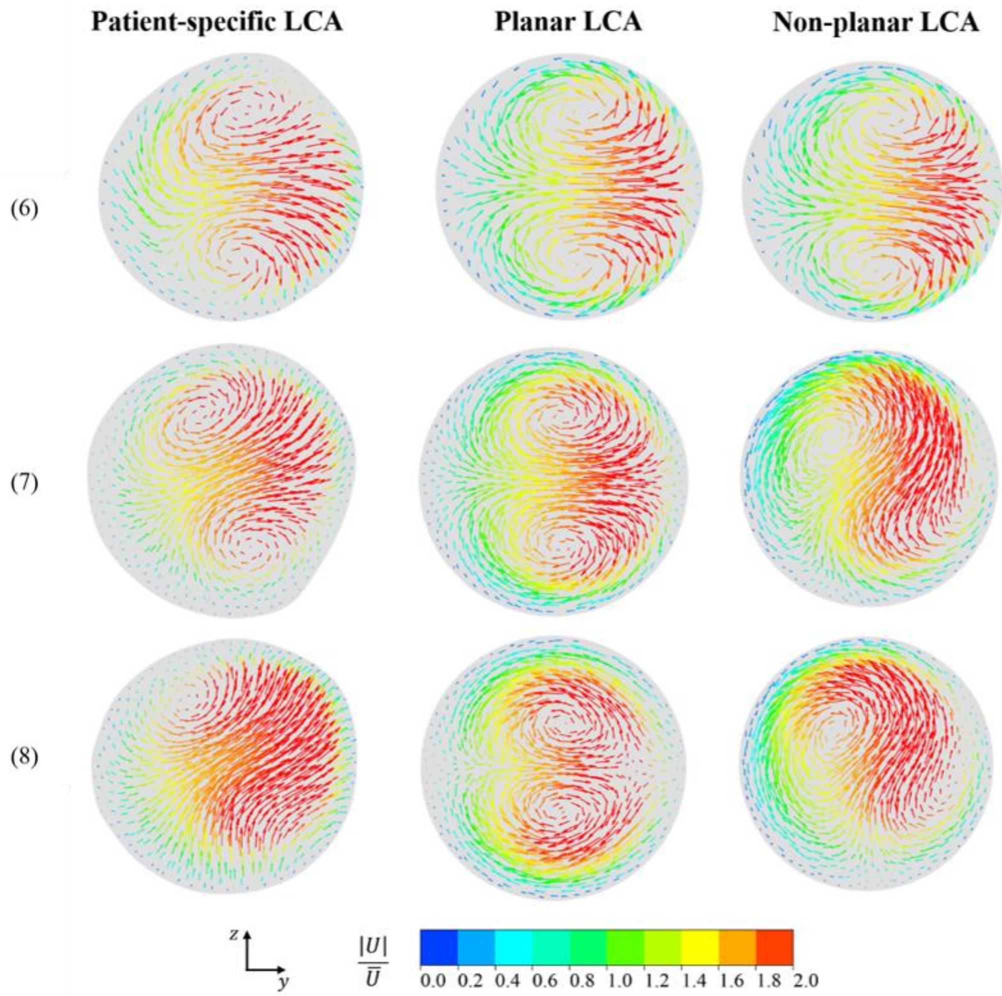

Figure 6.12. Velocity vectors (components tangential to the plane) at the LAD branch in models without stenosis. Numerical results obtained for the steady state and Newtonian blood behaviour.

The non-planar model presents asymmetrical flow behaviour, similarly to the patient-specific model, in contrast with the symmetric flow in the planar model - Figure 6.12 (7). In summary, these results show that small deviations from idealised models, caused either by inclination of branches or shape irregularities (ellipticity) originate asymmetries in the flow leading to distinct hemodynamic behaviour.

Figure 6.13 shows the normalized size of low WSS regions, $A_{\mathrm{WSS}}^{\mathrm{L}}$, and the normalized size of high helicity regions, $V_{|H_r|}^{\mathrm{H}}$, for all models studied. As previously observed, the normalized size of low WSS regions, $A_{\mathrm{WSS}}^{\mathrm{L}}$ shown in Figure 6.13a), is equal in both idealized models, stenotic and non-stenotic cases. The $A_{\mathrm{WSS}}^{\mathrm{L}}$ of the idealized models is also higher than that of the patient-specific LCA, mostly because the diameter in the idealized models is higher (and constant along the LCx branch), as seen in Figure 6.3.

In turn, helicity is affected by the non-planarity, as seen in Figure 6.13b). Non-planar models exhibit higher values of $V_{|H_r|}^{\mathrm{H}}$ since this system forces the flow to rotate while changing its direction through the different planes. Thus, these results indicate that an artery with non-planar geometry presents a stronger helical blood flow. The patient-specific model exhibits higher $V_{|H_r|}^{\mathrm{H}}$ values than the idealized models. In the patient-specific model the apex is aligned with the LM axis and the main flow goes directly into the apex region; conversely, in the idealised models the flows curves more smoothly due to the lack of geometrical irregularities in the bifurcation. Therefore, in the patient-specific model the amount of fluid that has to rotate is higher, causing higher values of$V_{|H_r|}^{\mathrm{H}}$. Figure 6.14 helps to understand this effect showing the three-dimensional locations with high values of helicity ($V_{|H_r|}^{\mathrm{H}}$).

When the stenosis is introduced, the size of low WSS regions decreases for all models. Once more, the diameter contraction caused by stenosis itself increases the velocity in that region, originating an increase of WSS. In terms of helicity, the stenosis causes a slight decrease in $V_{|H_r|}^{\mathrm{H}}$ for all models – Figure 6.13b). In this case, the low influence of stenosis in $V_{|H_r|}^{\mathrm{H}}$ is mainly due to the fact that most flow goes through LAD (Q_{LAD}=0.89 Q_{LM}) , where the high values of helicity are present, as seen in Figure 6.14.

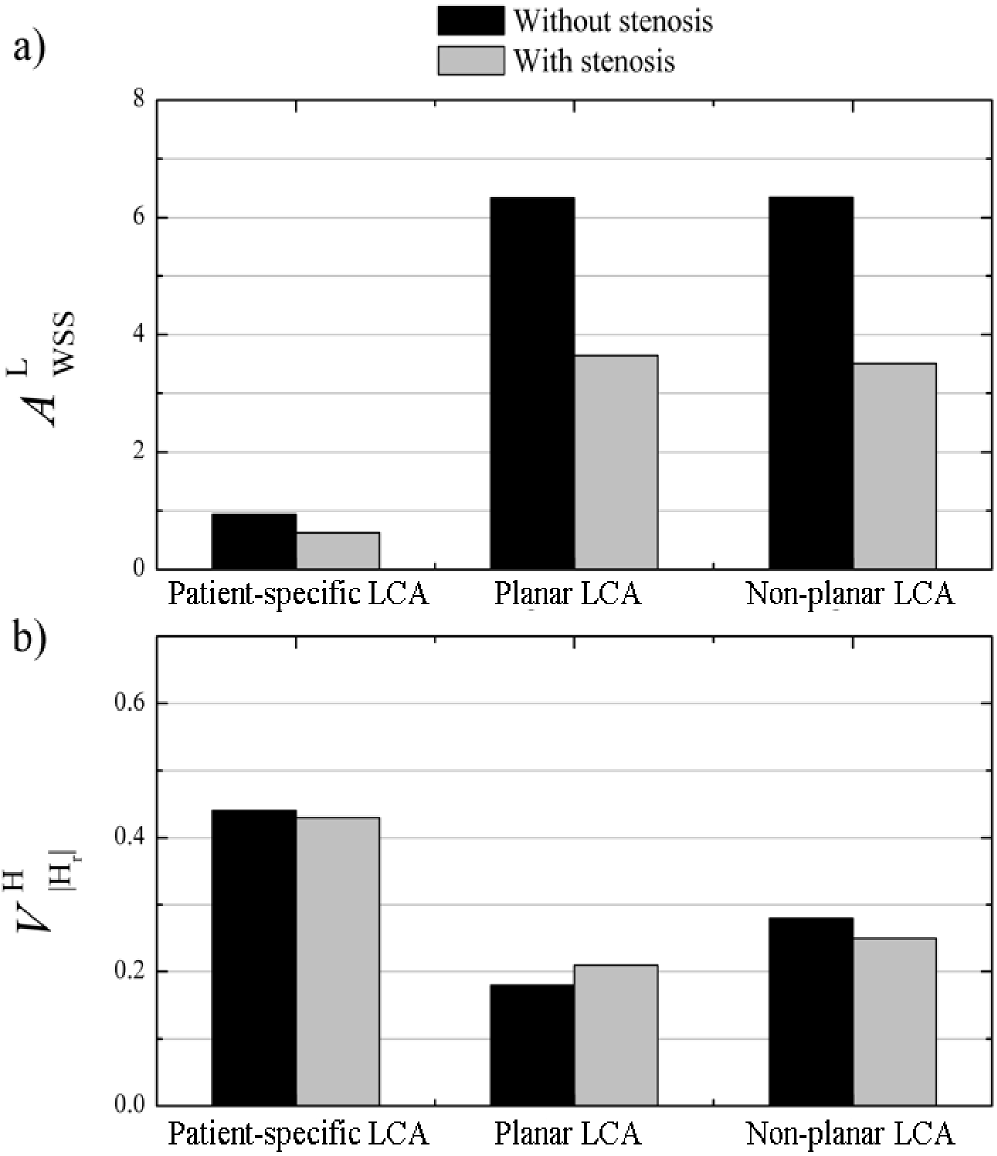

Figure 6.13. $A_{\mathrm{WSS}}^{\mathrm{L}}$ (top) and $V_{|H_r|}^{\mathrm{H}}$ (bottom) values without (black) and with stenosis (grey) for all models under study. Numerical results obtained for the steady state and Newtonian blood behaviour.

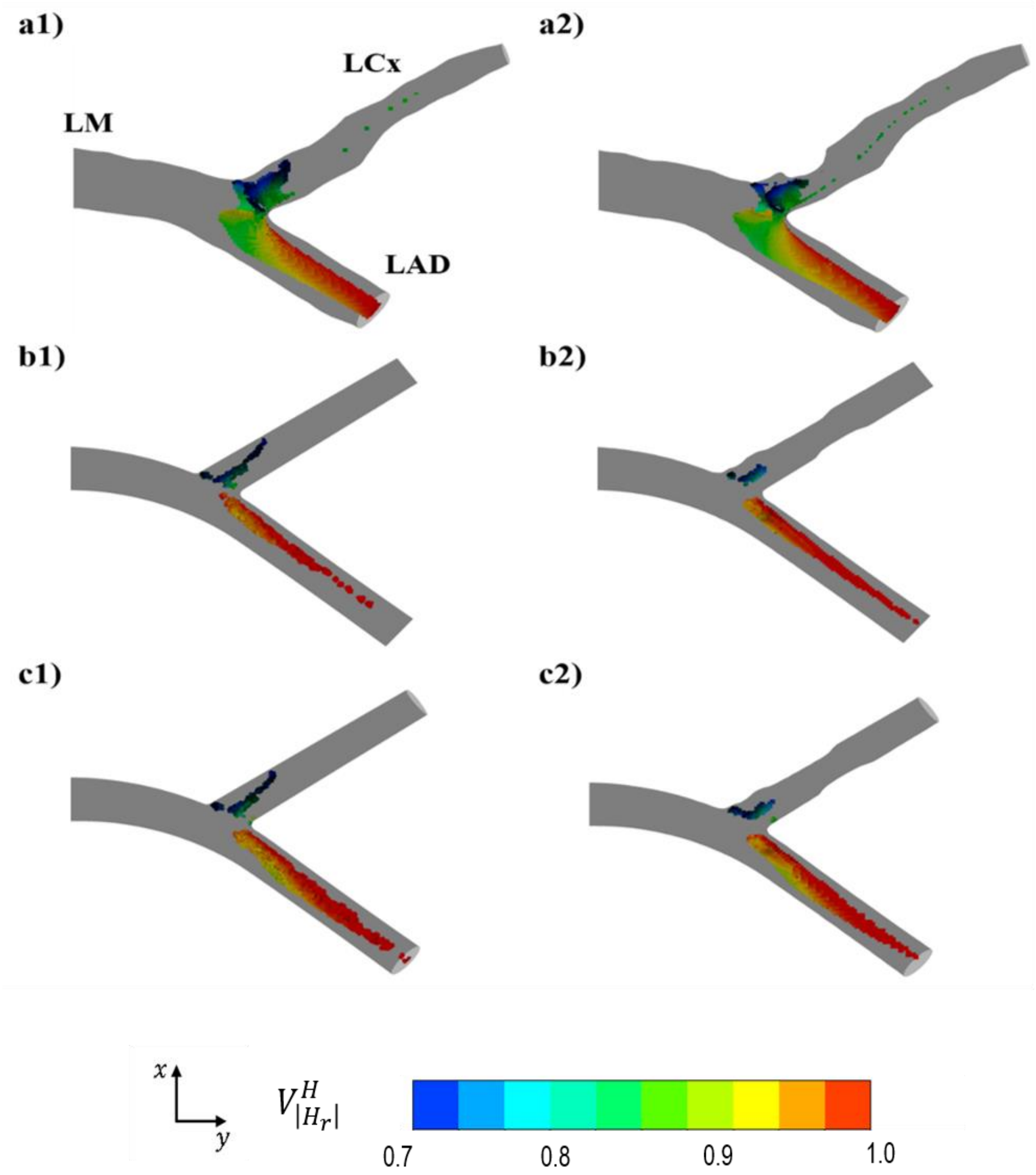

Figure 6.14. Three-dimensional regions with high values of helicity ($V^{\mathrm{H}}_{|H_r|}$) coloured by normalized velocity magnitude for non-stenotic (1) and stenotic (2) cases: a) patient-specific LCA, b) idealized coplanar model and c) idealized non-planar model. Numerical results obtained for the steady state and Newtonian blood behaviour.

6.3.3 Pulsatile flow

Although the average indicators analysed until now are helpful, instantaneous indicators throughout the cardiac cycle are also important. With this purpose, for the patient-specific LCA (stenotic and non-stenotic), the effects of shear thinning blood behaviour (Carreau model) and pulsatile flow were analysed mimicking the physiological conditions of the cardiac cycle in the LCA.

Figure 6.15 shows the 3D streamlines and WSS distribution at the lowest and at the highest velocity of a complete cardiac cycle (see also Figure A3 with the top view data, shown in Appendix). The figure also shows results for steady state with an inlet velocity equal to the time averaged velocity of the pulsatile flow. At the average velocity, the low WSS regions were located at the outer wall of the LCx branch (dark grey) in the stenotic and non-stenotic LCA – Figure 6.15a2) and b2). At the lowest down peak coronary flow (initiation of the systole), $A_{\mathrm{WSS}}^{\mathrm{L}}$ extends to cover nearly the whole daughter vessels surface, even when a stenosis is present - Figure 6.15a1) and b1). At the highest peak of coronary blood flow (during diastole), the LCA surface has predominantly values of WSS above 0.4 Pa and just a small area (at outer wall of LCx) exhibits critical values of WSS- Figure 6.15a3). Here, when a stenosis is present, the regions of low WSS are concentrated upstream and downstream the contraction - Figure 6.15b3).

The normalized size of high helicity regions also varies during the cardiac cycle. Figure 6.16 shows, for extreme instantaneous velocities during the cardiac cycle, the normalized volume of high helicity regions for the patient-specific LCA with and without stenosis. $V_{|H_r|}^{\mathrm{H}}$ is almost zero at the beginning of the systole while is higher at the peak of the diastole. The $V_{|H_r|}^{\mathrm{H}}$ extension is a direct consequence of high Reynolds number at the diastole velocity peak, since when inertial forces are dominant the rotation of the fluid extends for larger volumes.

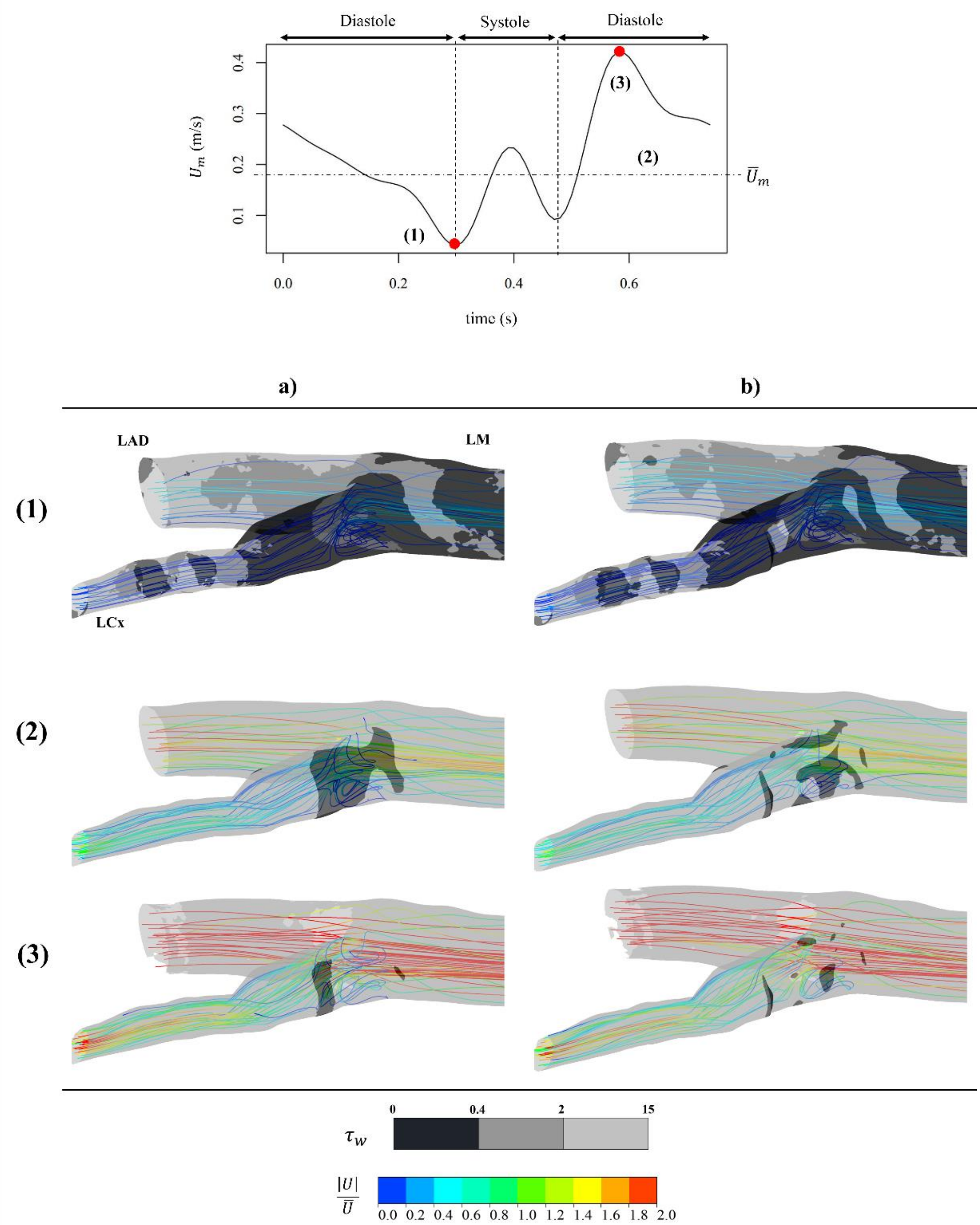

Figure 6.15. 3D streamlines and WSS field (greyscale colour) of patient-specific LCA a) without stenosis and b) with stenosis: (1) lowest instant velocity at beginning of systole, (2) steady state flow and (3) highest instant velocity during diastole. Numerical results obtained for the Carreau model.

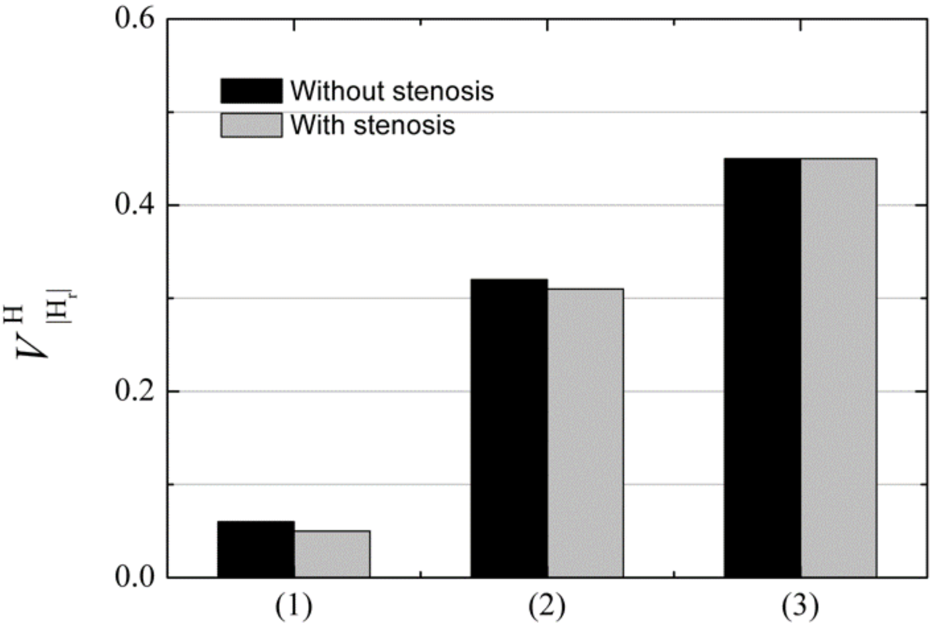

Figure 6.16. $V^{\mathrm{H}}_{|H_r|}$ values without (black) and with stenosis (grey) in the patient-specific LCA for the: (1) lowest instantaneous velocity at beginning of systole, (2) steady state flow and (3) highest instantaneous velocity during diastole. Numerical results obtained for the Carreau model.

6.4 Conclusions

The experimental results validate the numerical code assuming steady state Newtonian blood flow behaviour. The µPIV technique proves to be an invaluable technique for validating the CFD numerical results, and particularly in identifying areas of low velocities, which are prone to stenosis development. However, streak photography has demonstrated to be a more effective imaging analysis in identifying secondary flows, such as vortex and helical flows. In particular, the patient-specific LCA results show that the presence of the irregular shaped stenosis causes an increase of the flow velocities, reducing the volume of the open vortex present in the healthy artery.

Low WSS regions don’t coincide with the regions affected by the presence of non-planarity and therefore no significant differences were observed between planar and non-planar idealized models. Since the low WSS regions pin point the regions for the stenosis appearance, the irregular shaped stenosis originated in both idealized models are equivalent. The irregular shape of the patient-specific LCA, observed by ellipticity variation along its branches, affected its hemodynamics particularly in the appearance of asymmetric flow patterns. For the patient-specific LCA, the stenosis shape is different from the idealized models due to the presence of a diameter contraction downstream that reduces the size of low WSS regions. Non-planarity does not have a role in the formation of the stenosis. Helicity results have a more direct link with non-planarity system since there is evidence of an increase in the helical flow when flow is forced to change its direction following the curvatures induced by the non-planarity.

When pulsatile blood flow conditions are studied in patient-specific LCA, both instantaneous indicators of low WSS and high helicity vary. For the lowest peak of coronary blood flow (at beginning of the systole) low WSS regions are predominant and high helicity regions are almost inexistent. The opposite occurs at the highest peak coronary blood flow (during diastole) presenting the highest normalized size for the high helicity regions and the lowest for the areas of low WSS regions.

The results presented here show that care should be taken when hemodynamic effects are studied in ideal artery models. For the most part, ideal models do not describe the morphological irregularity of real arteries, and diameter and cross-section shape variations along the vessels are usually neglected. Also, pulsatile blood flow conditions are of utmost importance since instantaneous changes during the cardiac cycle can have cumulative effects in local hemodynamics. Thus patient-specific models with physiological conditions should be used for hemodynamic studies whenever possible.

Acknowledgments

The authors gratefully acknowledge the funding by FEDER through the Operational Program for Competitiveness Factors – COMPETE, ON.2 - O Novo Norte - North Portugal Regional Operational Program and National Funds through FCT-Foundation for Science and Technology under the projects: PEst-OE/EME/UI0532, NORTE-07-0124-FEDER-000025-RL2_ Environment&Health and PTDC/EME-MFE/102974/2008.

Notation

Symbols	Definition
$A_{\mathrm{WSS}}^{\mathrm{L}}$	Surface normalized area with $\tau_w < 0.4$
D_{LM}	Diameter of LM
D_{LAD}	Diameter of LAD
D_{LCx}	Diameter of LCx
H	Helicity density
H_r	Normalized helicity
l_{LM}	LM branch length
O_{cc}	Normalized occlusion factor
P	Pressure
Q_{LAD}	Flow rate in LAD
Q_{LCx}	Flow rate in LCx
r	Radial position
R	Inlet vessel radius
$\boldsymbol{U}$	Velocity vector
$\overline{U}$	Mean inlet velocity in the LM branch
$\overline{U}_m$	Average mean inlet velocity of a complete cycle at the LM
U_x	*x* velocity component
U_y	*y* velocity component
U_z	*z* velocity component
$\lvert U_{xy} \rvert$	Velocity magnitude based on the *x* and *y* components

$\lvert U\rvert$	Velocity magnitude based on the three components (x,y and z)
$V_{\lvert H_r\rvert}^{\mathrm{H}}$	Normalized volume with normalized helicity above 0.7
x, y, z	Cartesian coordinate system
α	Angle between LM and LAD
β	Angle between LM and LCx
θ	Angle between LAD and LCx
ε	Ellipticity
ρ	Blood density
μ	Blood viscosity
τ_w	Wall shear stress magnitude
ω	Vorticity magnitude
$\boldsymbol{\omega}$	Vorticity vector

References

1. Chatzizisis, Y.S., A.U. Coskun, M. Jonas, *et al.*, *Role of endothelial shear stress in the natural history of coronary atherosclerosis and vascular remodeling: molecular, cellular, and vascular behavior.* J Am Coll Cardiol, 2007. **49**(25): p. 2379-93.
2. Lozano, R. and M. Naghavi and K. Foreman, *et al.*, *Global and regional mortality from 235 causes of death for 20 age groups in 1990 and 2010: a systematic analysis for the Global Burden of Disease Study 2010.* Lancet, 2012. **380**(9859): p. 2095-128.
3. Ku, D.N., *Blood Flow in Arteries.* Annual Review of Fluid Mechanics, 1997. **29**(1): p. 399-434.
4. Takeuchi, S. and T. Karino, *Flow patterns and distributions of fluid velocity and wall shear stress in the human internal carotid and middle cerebral arteries.* World Neurosurg, 2010. **73**(3): p. 174-85; discussion e27.
5. Malek, A.M., S.L. Alper and S. Izumo, *Hemodynamic shear stress and its role in atherosclerosis.* JAMA, 1999. **282**(21): p. 2035-42.
6. Bale-Glickman, J., K. Selby, D. Saloner and O. Savas, *Experimental flow studies in exact-replica phantoms of atherosclerotic carotid bifurcations under steady input conditions.* J Biomech Eng, 2003. **125**(1): p. 38-48.
7. Caro, C.G., D.J. Doorly, M. Tarnawski, *et al.*, *Non-planar curvature and branching of arteries and non-planar-type flow.* 2008. **452**(1944): p. 185-197.
8. Chen, J. and X.Y. Lu, *Numerical investigation of the non-Newtonian blood flow in a bifurcation model with a non-planar branch.* J Biomech, 2004. **37**(12): p. 1899-911.
9. Lu, Y., X. Lu, L. Zhuang and W. Wang, *Breaking symmetry in non-planar bifurcations: distribution of flow and wall shear stress.* Biorheology, 2002. **39**(3-4): p. 431-6.
10. Liu, X., Y. Fan and X. Deng, *Effect of spiral flow on the transport of oxygen in the aorta: a numerical study.* Ann Biomed Eng, 2010. **38**(3): p. 917-26.
11. Liu, X., A. Sun, Y. Fan and X. Deng, *Physiological significance of helical flow in the arterial system and its potential clinical applications.* Ann Biomed Eng, 2015. **43**(1): p. 3-15.
12. Walker, A.M., J. Scott, D.E. Rival and C.R. Johnston, *In vitro post-stenotic flow quantification and validation using echo particle image velocimetry (Echo PIV).* Experiments in Fluids, 2014. **55**(10).
13. Javadzadegan, A., Y. Shimizu, M. Behnia and M. Ohta, *Correlation between Reynolds number and eccentricity effect in stenosed artery models.* Technol Health Care, 2013. **21**(4): p. 357-67.
14. Marsden, A.L., J.A. Feinstein and C.A. Taylor, *A computational framework for derivative-free optimization of cardiovascular geometries.* Computer

Methods in Applied Mechanics and Engineering, 2008. **197**(21-24): p. 1890-1905.

15. Nosovitsky, V.A., O.J. Ilegbusi, J. Jiang, *et al.*, *Effects of curvature and stenosis-like narrowing on wall shear stress in a coronary artery model with phasic flow.* Comput Biomed Res, 1997. **30**(1): p. 61-82.
16. Barakat, A.I. and E.T. Cheng. *Numerical simulation of fluid mechanical disturbance induced by intravascular stents*. in *Proceedings of the 11th International Conference on Mechanics in Medicine and Biology*. 2000.
17. Chiastra, C., S. Morlacchi, D. Gallo, *et al.*, *Computational fluid dynamic simulations of image-based stented coronary bifurcation models.* J R Soc Interface, 2013. **10**(84): p. 20130193.
18. Andersson, H.I., R. Halden and T. Glomsaker, *Effects of surface irregularities on flow resistance in differently shaped arterial stenoses.* J Biomech, 2000. **33**(10): p. 1257-62.
19. Hye, M.A. and M.C. Paul, *A computational study on spiral blood flow in stenosed arteries with and without an upstream curved section.* Applied Mathematical Modelling, 2015. **39**(16): p. 4746-4766.
20. Ha, H. and S.J. Lee, *Effect of pulsatile swirling flow on stenosed arterial blood flow.* Med Eng Phys, 2014. **36**(9): p. 1106-14.
21. Ku, D.N., D.P. Giddens, C.K. Zarins and S. Glagov, *Pulsatile flow and atherosclerosis in the human carotid bifurcation. Positive correlation between plaque location and low oscillating shear stress.* Arteriosclerosis, 1985. **5**(3): p. 293-302.
22. Perktold, K., M. Hofer, G. Rappitsch, *et al.*, *Validated computation of physiologic flow in a realistic coronary artery branch.* J Biomech, 1998. **31**(3): p. 217-28.
23. Doutel, E., J. Carneiro, J.B.L.M. Campos and J.M. Miranda, *Artificial stenoses for computational hemodynamics.* Computer Methods in Applied Mechanics and Engineering (under review), 2016.
24. Doutel, E., J. Carneiro, M.S.N. Oliveira, *et al.*, *Fabrication of 3d Mili-Scale Channels for Hemodynamic Studies.* Journal of Mechanics in Medicine and Biology, 2015. **15**(01): p. 1550004.
25. McDonald, J.C., D.C. Duffy, J.R. Anderson, *et al.*, *Fabrication of microfluidic systems in poly(dimethylsiloxane).* Electrophoresis, 2000. **21**(1): p. 27-40.
26. Gijsen, F.J., F.N. van de Vosse and J.D. Janssen, *The influence of the non-Newtonian properties of blood on the flow in large arteries: steady flow in a carotid bifurcation model.* J Biomech, 1999. **32**(6): p. 601-8.
27. Perktold, K., R.O. Peter, M. Resch and G. Langs, *Pulsatile non-Newtonian blood flow in three-dimensional carotid bifurcation models: a numerical study of flow phenomena under different bifurcation angles.* J Biomed Eng, 1991. **13**(6): p. 507-15.

28. Cho, Y.I. and K.R. Kensey, *Effects of the non-Newtonian viscosity of blood on flows in a diseased arterial vessel. Part 1: Steady flows.* Biorheology, 1991. **28**(3-4): p. 241-62.
29. Doutel, E., J. Carneiro, J.B.L.M. Campos and J.M. Miranda, *Experimental and numerical characterization of secondary flows in a coronary bifurcation.* Experiments in Fluids (under review), 2016.
30. Murray, C.D., *The Physiological Principle of Minimum Work: I. The Vascular System and the Cost of Blood Volume.* Proceedings of the National Academy of Sciences, 1926. **12**(3): p. 207-214.
31. Doutel, E., S.I. Pinto, J.B. Campos and J.M. Miranda, *Link between deviations from Murray's Law and occurrence of low wall shear stress regions in the left coronary artery.* J Theor Biol, 2016.
32. Chaichana, T., Z. Sun and J. Jewkes, *Computation of hemodynamics in the left coronary artery with variable angulations.* J Biomech, 2011. **44**(10): p. 1869-78.
33. Issa, R.I., *Solution of the implicitly discretised fluid flow equations by operator-splitting.* Journal of Computational Physics, 1986. **62**(1): p. 40-65.
34. Leonard, B.P., *Order of accuracy of QUICK and related convection-diffusion schemes.* Applied Mathematical Modelling, 1995. **19**(11): p. 640-653.
35. Grigioni, M., C. Daniele, U. Morbiducci, *et al.*, *A mathematical description of blood spiral flow in vessels: application to a numerical study of flow in arterial bending.* J Biomech, 2005. **38**(7): p. 1375-86.
36. Berger, S.A. and L.D. Jou, *Flows in Stenotic Vessels.* Annual Review of Fluid Mechanics, 2000. **32**(1): p. 347-382.
37. Soulis, J.V., G.D. Giannoglou, G.E. Parcharidis and G.E. Louridas, *Flow parameters in normal left coronary artery tree. Implication to atherogenesis.* Comput Biol Med, 2007. **37**(5): p. 628-36.
38. Rikhtegar, F., J.A. Knight, U. Olgac, *et al.*, *Choosing the optimal wall shear parameter for the prediction of plaque location-A patient-specific computational study in human left coronary arteries.* Atherosclerosis, 2012. **221**(2): p. 432-7.

7

Chapter

> *"Agir, eis a inteligência verdadeira. Serei o que quiser. Mas tenho que querer o que for. O êxito está em ter êxito, e não em ter condições de êxito. Condições de palácio tem qualquer terra larga, mas onde estará o palácio se não o fizerem ali?"*
>
> **— Fernando Pessoa**

Conclusions and Outlook

7

Conclusions and Outlook

This chapter summarizes the contributions of this thesis to the field, and discusses possible extensions and future work.

7.1 Main Conclusions

This thesis studied the hemodynamics in the Left Coronary Artery (LCA). For this purpose two main pathways were followed: numerical simulations using computational fluid dynamics (CFD) and experimental flow analysis using µPIV and streak photography techniques. The CFD code was validated with experimental data obtained from *in vitro* tridimensional flow phantoms that mimic the arterial morphology. The flow phantoms are made of a commonly used polymer in microfluidics, poly(dimethylsiloxane) (PDMS), and were fabricated using a newly developed process allowing hemodynamic studies using optical techniques. The developed process is based on lost-sucrose mold casting; it is based on a sequential method that employs a sacrificial material, sucrose, which can be removed by dissolution, shaping the desired arterial geometry. This methodology fulfilled all the requirements, in terms of transparency, exhibiting excellent optical properties. The developed fabrication method was found to be superior to the commonly employed method in literature (lost-wax casting method) due to the lower level of contamination of the final flow phantom.

An approach combining numerical (CFD) and experimental methods (µPIV and streak photography) was followed to investigate the local hemodynamics in an idealized LCA bifurcation. Different flow conditions were considered, such as different flow distributions, having as reference the Murray's flow partition law, and different Reynolds numbers. The numerical and experimental data identifies flow patterns that are relevant for prevention and treatment of atherosclerosis. Both results allow the observations of secondary flows, *i.e.* open vortexes, and helical flow. These results were used as a benchmark case to validate the numerical code implemented and also as a reference for comparison with the more complex studies developed throughout this thesis.

The outflow boundary conditions in LCA bifurcation are hard to establish, mainly because the flow resistance of the downstream capillary network is unknown and experimental data is usually not available. Murray’s flow partition is useful to solve this problem. It was analyzed how deviations from Murray’s laws (Murray’s diameter law and Murray’s law for the angles) influence the indicators relevant to atherosclerosis development. A CFD study was implemented to evaluate regions of low WSS and other indicators associated with atherosclerosis. These indicators were shown to be influenced by the bifurcation shape. The geometries following Murray’s laws minimize the energy required to maintain blood flow circulation. However, these configurations do not minimize the size of low WSS regions that can lead to atherosclerosis. While energy minimization is probably the main driver of natural selection shaping the arteries geometry, these findings suggest that atherosclerosis is a cost imposed to organisms, which may explain why deviations from Murray’s law have been identified in several studies.

A methodology was developed for allowing a fast hemodynamic comparison between healthy and stenotic cases for a given artery geometry. The method developed is based on a relatively simple mass/heat diffusional process and can easily produce irregular three-dimensional stenoses on areas of low WSS. The implemented method links arterial geometrical factors with the onset and growth of the stenosis. In order to validate the effect of irregular stenosis shapes in the flow field, three different geometrical cases were selected: two different idealized models and a real LCA obtained by a CT scan of a healthy patient. Different geometries have different low WSS patterns originating case-specific sites prone to the development of atherosclerosis. The irregular shape of the stenosis affects the flow field, originating different values of WSS for each case. This methodology mimics the growth of real stenosis, and its shape adapts to local geometrical boundaries, leading to shapes more realistic than in cases of regular shaped stenosis such as ellipsoids and spheres.

This methodology allowed a numerical and *in vitro* hemodynamic study in healthy and stenotic patient-specific LCA models. The results showed that the presence of the irregular shaped stenosis caused an increase of the flow velocities, reducing the volume of the open vortex present in the healthy artery. The experimental and simulated results are in good agreement, demonstrating the viability of hemodynamic analysis using CFD tools in patient-specific left coronary arteries. Specific arterial characteristics, such as non-planarity and diameter irregularities (*i.e.* ellipticity) were shown to be the major cause of disturbed flow originating distinct hemodynamic phenomena. These geometric features cause higher helical flows which introduce disturbances in blood flow inhibiting plaque accumulation which may help inhibit atherosclerosis development.

Shear thinning blood behaviour and pulsatile flow mimicking the cardiac cycle in a healthy and stenotic patient-specific LCA were also studied. At beginning of the systolic phase, low WSS regions are predominant contrasting to the high helicity regions which are almost inexistent. Oppositely, the highest peak coronary blood flow occurs during diastole and presents the highest helicity regions and the lowest WSS regions.

The results show that care should be taken when hemodynamic effects are studied in ideal artery models. For the most part, ideal models do not describe the morphological irregularity of the arteries therefore the real hemodynamics cannot be accurately described. Also physiological conditions should be considered since instantaneous changes during the cardiac cycle can have cumulative effects in local hemodynamics. Thus patient-specific models with physiological conditions should be used for hemodynamic studies whenever possible.

The main achievement of this PhD thesis was the creation of a flexible framework which enables to cover several aspects of patient-specific flow analysis problem. The approach disclosed in this thesis allows the design of ideal and patient-specific models with subsequent rapid prototyping for experimental flow studies alongside with mesh generation for implementation of the numerical code. This thesis also make possible inserting realistic shaped stenosis in the both models types allowing having a deeper understanding of atherosclerosis initiation. The numerical code used was validated by experimental data, allowing using CFD simulations for flow analysis in any patient-specific artery. This approach can be used either as an early diagnosis tool or as an auxiliary tool before and after medical interventions.

7.2 Outlook

The CFD work developed assumes both Newtonian and non-Newtonian blood behaviour in steady and unsteady flow conditions. However, the *in vitro* study only considered Newtonian and steady state blood flow. In the future, it would be interesting to experimentally consider the non-Newtonian blood behaviour alongside with pulsatile flow. To accomplish this, the *in vitro* analysis should implement the pulsatile flow conditions in the pump in order to mimic the cardiac cycle. To replicate the non-Newtonian behaviour of blood, it will be necessary to find a reliable blood analogue. Meanwhile, once the secondary flows are tridimensional phenomena, rather than use µPIV technique to obtain the 2D components of velocity, a stereo PIV system should be used. This technique allows to extract the third velocity component, and in this way obtaining a more reliable validation of the unsteady simulations.

A broader variety of artery geometrical characteristics such as, bifurcation angles and diameter contractions along the LCA branches could be taken into account in order to establish a more accurate relation between artery geometries and atherosclerosis.

The major limitation of the methodology implemented to create 3D irregular shaped stenoses is the static region of low wall shear stress that originates the different stenosis. In each time step a dynamic motion solver should be implemented in order to update the geometry mesh modifying the low WSS region as the stenosis is growing. By doing this, the stenosis growth along time is continually dependent of WSS and a more realistic stenosis growth will be accomplished. The artificial stenosis should be compared with real stenosis taken from patient’s CT scans provided by the medical unit. This should allow validating the proposed methodology and if needed to optimize the implemented model.

Finally, an interesting extension of the developed work is in the stent design. The work disclosed in this thesis allows to easily introducing stents in the artery models, either numerically or experimentally. The hemodynamic results should bring helpful insights not only for the stent design but also in their positioning inside the artery.

This thesis shows that flow analysis by CFD in patient-specific arteries can be used as an auxiliary tool for medical teams, either before or after surgical intervention in arteries affected by atherosclerosis. Regular CT scans of the affected artery with CFD flow analysis allow checking either the disease progression or to predict the success of stent implementation and medical intervention.

Appendix

Appendix A. Supporting information for **Chapter 6**

Supporting information for Chapter 6

Geometry

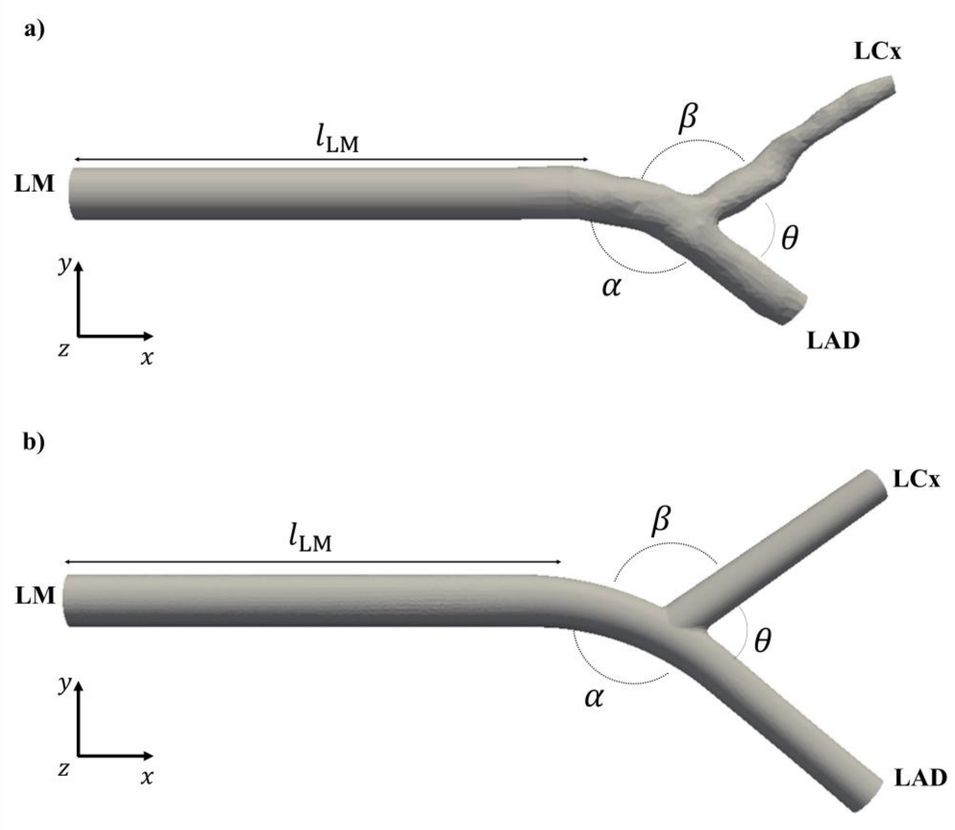

Figure A1. Top view of 3D LCA models: a) patient-specific model and b) idealized models.

Table A1. Geometrical features of the *xy* plane projection of the LCA models under study.

Parameters	**Value**
$\mathbf{l_{LM}}$	$8 \cdot \boldsymbol{D}_{\mathbf{LM}}$
$\boldsymbol{\theta}$	73°
$\boldsymbol{\alpha}$	167°
$\boldsymbol{\beta}$	120°

Ellipticity

$$\varepsilon = \sqrt{\frac{a^2 - b^2}{a^2}} \tag{A1}$$

Where a is the length of the semimajor axis and b the length of the semiminor axis.

Model Fabrication

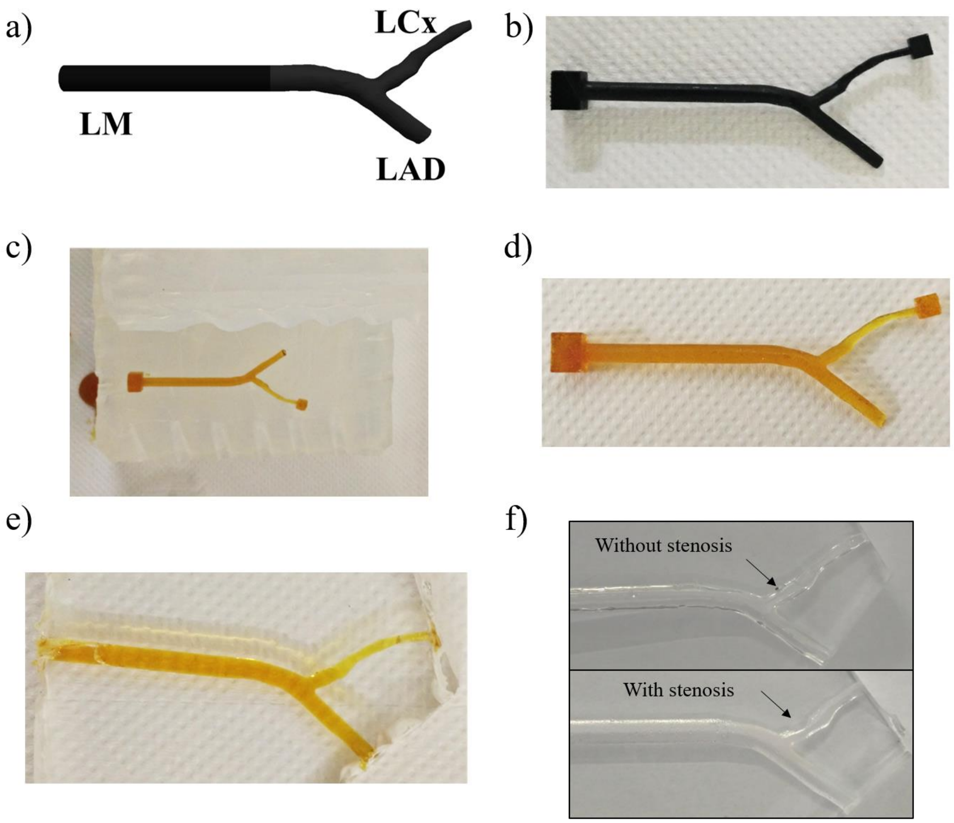

Figure A2. Lost-sucrose casting method used to construct the 3D flow phantom of the patient-specific LCA. The steps involved in this methodology are: a) STL LCA geometry used in a 3D printer by rapid prototyping; b) Epoxy resin mold made by rapid prototyping; c) Non-transparent silicon mold with the negative version of the geometry made of sucrose; d) Sucrose negative mold of 3D patient-specific LCA; 3D PDMS flow phantom after curing stage and before the sucrose removal step by dissolution and f) 3D PDMS flow phantoms, after sucrose dissolution, with and without stenosis.

Flow patterns

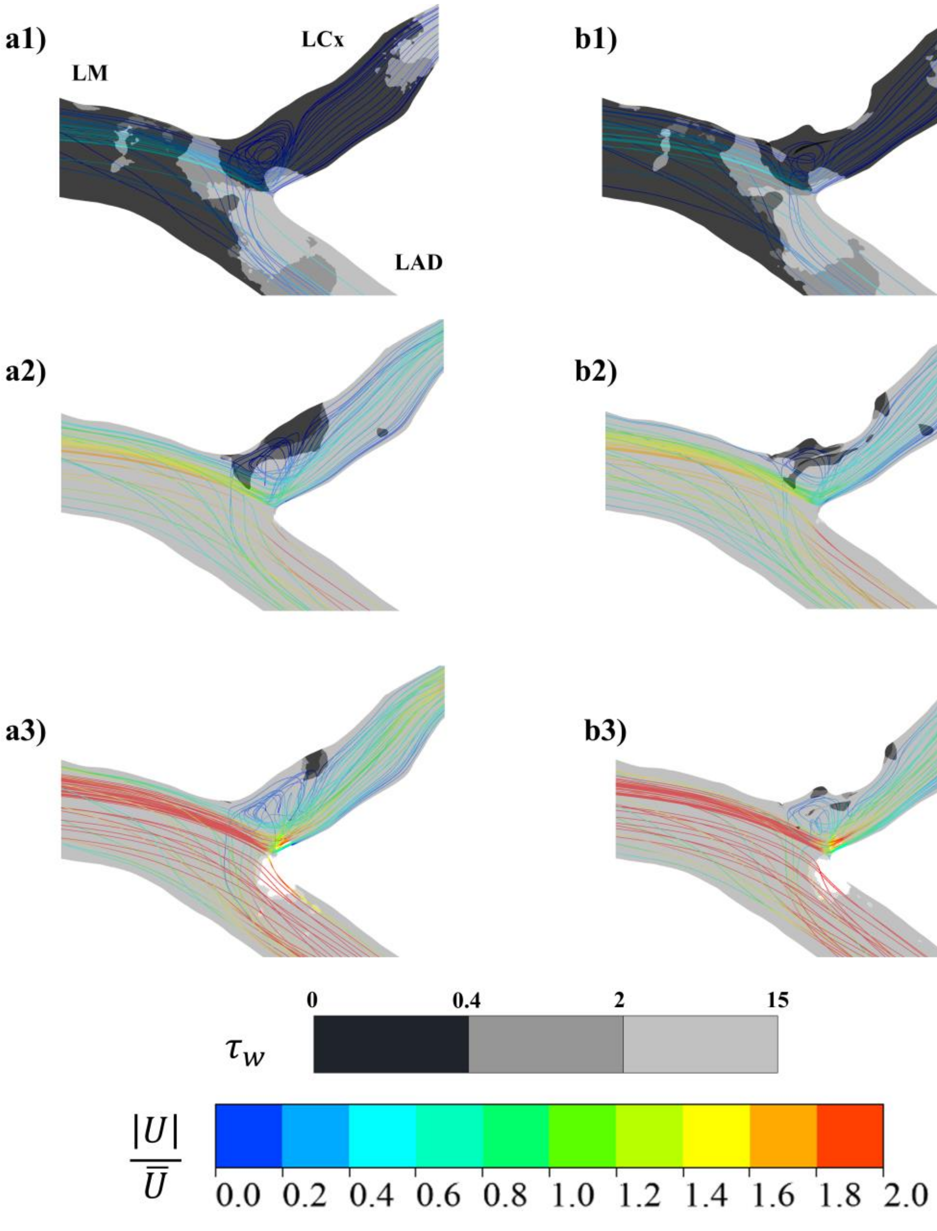

Figure A3. Top view of 3D streamlines and WSS distribution (greyscale color) of patient-specific LCA a) without stenosis and b) with stenosis: (1) lowest instant velocity at beginning of systole, (2) steady state and (3) highest instant velocity during diastole. Numerical results obtained for the Carreau model.